University of Navarra

School of Engineering

Donostia-San Sebastián

INFLUENCE OF THE LOCAL CURVATURE ON THE ABDOMINAL AORTIC ANEURYSM WALL STRESS AND NEW METHODOLOGIES FOR MANUFACTURING REALISTIC PHANTOMS

DISSERTATION

submitted for the Degree of Doctor of Philosophy

of the University of Navarra by

Sergio Ruiz de Galarreta Moriones

under the supervision of

Raúl Antón Remírez and

Aitor Cazón Martín

Donostia-San Sebastián, November 2016

Al tío y a la Yaya,

Agradecimientos

Es un tópico, pero la mejor forma con la que empezar esta tesis es mostrando un dato, cuando menos, llamativo: *en una vida media de 78.5 años llegamos a conocer a alrededor de 1700 personas*. Después de unos cálculos no muy laboriosos, he podido deducir que durante esta etapa he conocido a 86.6 personas más. De todas ellas, sois muchas las que directa o indirectamente habéis colaborado o me habéis acompañado estos años y me gustaría aprovechar este apartado para agradecéroslo aunque sea con unas pocas palabras.

Las primeras palabras van dirigidas como no puede ser de otra manera a mis directores de tesis *Raúl* y *Aitor*. Gracias por darme la oportunidad de emprender este proyecto y por haber dedicado vuestro tiempo a lo largo de éste para aportar ideas, consejos, apoyo y demás; os estaré siempre agradecido. De igual forma quiero dar las gracias a mi paisano *Joaquin* por todo el asesoramiento de estos últimos años.

También quiero agradecer a todos los compañeros de Igara (Multiusos) y CEIT por ser los responsables de algo que considero muy valioso en Tecnun: ese 'buen rollo' en el trabajo. En especial a mis compañeros del café (con pintxo), tanto a los que no os hacen gracia mis chistes, como a los que no os hacen gracia pero aun así os reís: J*on, Juan, Asier, Amaia, Pablo, Xabi, Ainitze, Mikel, Itziar*; y los recientes: *Wilmer, Sofía, Leire* y *Ángel*; compartir estos años con vosotros ha sido un

verdadero placer; hacéis que escuchar el pitido del despertador siga costando, pero menos.

Y si el ambiente de trabajo es importante, también lo es el de fuera. Deporte, cañas, escapadas, dardos, una vuelta tonta… cualquier opción es buena para desconectar y en este aspecto muchos sois los que me habéis acompañado: *Mikel*, *Alex* y demás vitorianos; *Juan*, *Oier*, amigos de la carrera y otros cuantos de Tecnun-CEIT que repetís, gracias por tan buenos momentos en estos años.

Mención aparte merecen todas esas personas que durante 7 meses me acogieron en territorio 'vaquero' de una forma espectacular. En primer lugar *Ender*, gracias por acogerme en el VBBL y por todos los consejos en estos cuatro años de tesis. Gracias a todos los compañeros de laboratorio, pero de forma muy especial a *Miru*, *Matt*, *Ruban* y *Rita*, será difícil olvidaros. También quiero acordarme de los que podría denominar mis tíos de San Antonio, *Antonio* y *Luisa*, con vosotros he llegado a cenar en el aparcamiento de los Spurs mejor que en los nueve años que llevo viviendo sólo, gracias por todo.

Y dejo para el final a las cuatro personas más importantes: mis padres *Jesús* e *Isabel*, si no es por vosotros y por vuestra excelente educación yo no podría haber llegado hasta aquí; mi hermano *Iñaki* con el que he podido plantarme estos años en platós de televisión, radios, teatros…quién pudiese tener un hermano así, incluso de vez en cuando solía interesarse por cómo me iba la investigación "¿y ahora qué estás investigando?"; y por último *Irantzu*, simplemente por hacerme feliz. Mil gracias.

<div align="right">Sergio Ruiz de Galarreta Moriones</div>

Abstract

An abdominal aortic aneurysm (AAA) is a focal dilation of the
abdominal aorta that is at least 1.5 times its normal diameter. AAA
rupture causes around 1.3% of deaths in developed countries among
men aged 65-85. In clinical practice, uncertainty still remains about
the correct time to operate, but the criterion of maximum diameter is
commonly accepted as a rupture prediction factor. The general
consensus is that patients with AAA diameters bigger than 5 cm
warrant elective repair if they are reasonable operative candidates.
However, the failure rate of this criterion is high, ranging from 10% to
25% of cases: 13% of aneurysms with a maximum diameter under 50
mm ruptured, while 60% of aneurysms with diameters over 50 mm
remained intact. Several numerical studies have attempted to find
new parameters that can help physicians estimate AAA rupture risk.
In contrast, few experimental studies have been carried out due to the
cost and time-consuming nature of manufacturing patient-specific
AAA replicas.

This thesis comprises both numerical and experimental studies. The
numerical approach investigates new geometric parameters that
influence AAA wall stress distribution, while the experimental
approach studies new methodologies for manufacturing AAA replicas.

In the numerical studies, 30 patient-specific AAA geometries were analyzed, and it was found that the local curvature significantly affects the wall stress distribution, which in turn affects the risk of AAA rupture. The results suggest that considering this parameter in future AAA rupture estimations can assist in clinical decision-making.

In terms of the experimental studies, a new methodology for manufacturing more realistic AAA phantoms was developed via vacuum casting technique. This new methodology considers the regionally varying wall thickness and the anisotropic behavior of the AAA. Additionally, the multi-material additive manufacturing technology has been used to fabricate idealized AAA phantoms with anisotropic properties. The results of uniaxial and biaxial tests verify the suitability of both methodologies in manufacturing AAA replicas with properties similar to AAA tissue.

Finally, an experimental study was run on the fabricated AAA phantoms and the AAA wall stress distribution was verified. This study was carried out at the University of Texas at San Antonio (UTSA) in collaboration with Dr. Ender Finol.

Laburpena

Sabelako aorta aneurisma, AAA (ingelesez 'abdominal aortic aneurysm' esan nahi duena) sabelako aortaren zabalkuntza da, gutxienez, 1.5 aldiz bere ohiko diametroa. Herrialde garatuetan AAAren hausturak 65 eta 85 urte bitarteko gizonezkoen %1.3 heriotza eragiten du. Oraindik praktikan, ebakuntza egiteko noiz den momento egokia zalantza handiak daude. Hala ere, normalean, hausturako iragarpenaren faktore gisa gehienezko diametroaren irizpidea onartu da; orokorrean, AAAren diametroa 5 cm baino handiagoa daukaten pazientei AAA kompontzea gomendatzen zaie baldin eta horretarako gai badira. Dena den, hutsegiteen portzentajea nabarmena da (%10 eta %25 ingurukoa): 50 mm baino diametro txikiagoko aneurismaren %13 hautsi egin ziren eta 50 mm baino diametro handiagoko aneurismaren %60 bere horretan jarraitu zuten. Zenbakizko ikerketa batzuk, haustura arriskuaren estimaziorako lagungarri izan daitezkeen parametroen aurkikuntzan oinarritu dira. Hala ere, ez daude hainbat ikerketa esperimental. Arrazoia da gaixoen AAA erreplikak fabrikatzeko denbora asko behar dela eta garestia dela. Tesi honek esperimental eta zenbakizko ikerketak barne hartzen ditu. Alde batetik, parametro geometriko berriak eta bere esfortzuengan eragina ikertu da. Beste aldetik, metodo berriak AAA erreplikak fabrikatzeko ikertzen dira.

Zenbakizko ikerketei dagokienez, 30 gaixoen AAA geometriak analizatu ondoren, kurbadura lokala ikertzea garrantzitsua dela ondoriuztatu da. Kurbadura lokalak esfortzu-banaketari, eta ondorioz AAAren haustura arriskuari erasaten dio. Emaitzen arabera, parametro hau kontuan hartuta AAAren haustura estimatzeko lagungarria izan daiteke etorkizunean.

Atal esperimentalari dagokionez, metodologia berria garatu da AAA erreplikak errealistagoak fabrikatzeko; hutsean injekzio teknika erabili da. Metodologia honek lodiera aldagarri eta anisotropia kontuan hartzen ditu. Gainera, aditiboa-fabrikazio teknologia (multi-materiala) erabili da eta ideal AAA erreplikak anisotropiko portaerarekin fabrikatzen dira. Uniaxial eta biaxial entseguen emaitzak kontuan hartuta, bi metodologiekin AAA erreplikak AAA ehun propietate antzekoak fabrika daitezkela esan daiteke.

Azkenean, fabrikatzen diren AAA erreplikekin ikerketa esperimentala bat egin da eta AAAren paretan esfortzu-banaketa egiaztatu da. Azken ikerketa hau Texasko Unibertsitatean, San Antonion (UTSA) burutu da Dr. Ender Finol lankidetzari esker.

Resumen

El aneurisma de aorta abdominal (AAA) es una dilatación focalizada de la aorta abdominal de al menos 1.5 veces su diámetro habitual. La rotura de AAA causa alrededor de 1.3% de muertes en países desarrollados en hombres con una edad comprendida entre 65 y 85 años. En la práctica todavía existe incertidumbre con respecto al momento correcto de llevar a cabo la operación, sin embargo, el criterio de diámetro máximo es aceptado habitualmente como el factor de predicción de rotura; generalmente a aquellos pacientes cuyo diámetro del AAA supera los 5 cm se les recomienda reparar el AAA siempre y cuando estén en condiciones para ello. No obstante, el porcentaje de fallo de este criterio es considerable y falla en torno al 10% y 25% de los casos: 13% de los aneurismas con diámetros inferiores a 50 mm rompieron, mientras que el 60% de aneurismas con diámetros superiores a 50 mm permanecieron intactos. Varios estudios numéricos han intentado encontrar nuevos parámetros que puedan ayudar a los médicos a la hora de estimar el riesgo de rotura del AAA. Por el contrario, se han realizado pocos estudios experimentales debido al alto coste y tiempo que lleva la fabricación de réplicas de AAAs de pacientes.

Esta tesis abarca tanto el estudio numérico como el experimental. Por un lado se ha estudiado la influencia de nuevos parámetros

geométricos en la distribución de esfuerzos en la pared del AAA. Por otro lado se han investigado nuevas metodologías para la fabricación de réplicas de AAA.

Con lo referido a los estudios numéricos, después de analizar 30 geometrías de AAAs de pacientes, se ha descubierto que la curvatura local afecta de forma considerable a la distribución de esfuerzos en la pared, y consecuentemente al riesgo de rotura del AAA. Los resultados sugieren que considerar este parámetro en un futuro para estimar la rotura de AAA puede ayudar a las decisiones clínicas.

Con respecto al apartado experimental, se ha definido una nueva metodología para fabricar réplicas de AAA más realistas mediante la técnica de inyección al vacío. Esta metodología nueva tiene en cuenta el espesor variable de la pared y el comportamiento anisótropo del AAA. Asimismo, la tecnología de fabricación aditiva multi-material se ha utilizado para fabricar réplicas de AAA ideales con propiedades anisótropas. Los resultados de los ensayos uniaxiales y biaxiales certifican la idoneidad de las dos metodologías para la fabricación de réplicas de AAA con propiedades similares a las del tejido del AAA.

Por último, se ha realizado un estudio experimental con las réplicas de AAA fabricadas y se ha verificado la distribución de esfuerzos en la pared del AAA. Este último estudio se llevó a cabo en la Universidad de Texas en San Antonio (UTSA) gracias a la colaboración con el Dr. Ender Finol.

Table of contents

List of figures

List of tables

Chapter 1:

Introduction

1.1 Motivation

The term aneurysm, derived from the Greek "aneurusma" (widening), can be defined as a permanent and irreversible localized dilatation of a vessel. Nearly all aneurysms are present in the aorta, which is the main artery that runs from the heart through the chest and abdomen, and depending on the region the aneurysm is located in, they are classified as thoracic aortic aneurysm (TAA), abdominal aortic aneurysm (AAA) or thoracoabdominal aortic aneurysms (TAAA) (Figure 1-1).
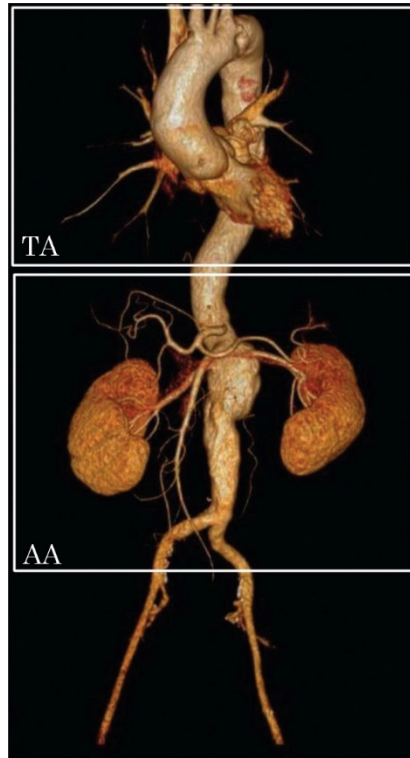
Figure 1-1 Aorta artery regions: thoracic aorta (TA) and abdominal aorta (AA) [1].

An AAA is defined by the Society for Vascular Surgery as a permanent focal dilatation of the abdominal aorta to 1.5 times its normal diameter (15-24 mm depending on age, sex and body weight) [2,3] (Figure 1-2). It is diagnosed especially in elderly people: in the USA, the prevalence of AAAs for patients between the ages of 75-84 is 12.5% in men and 5.2% in women [4]; while in Europe, between 4% and 8% of men aged 65-80 have AAA [5].
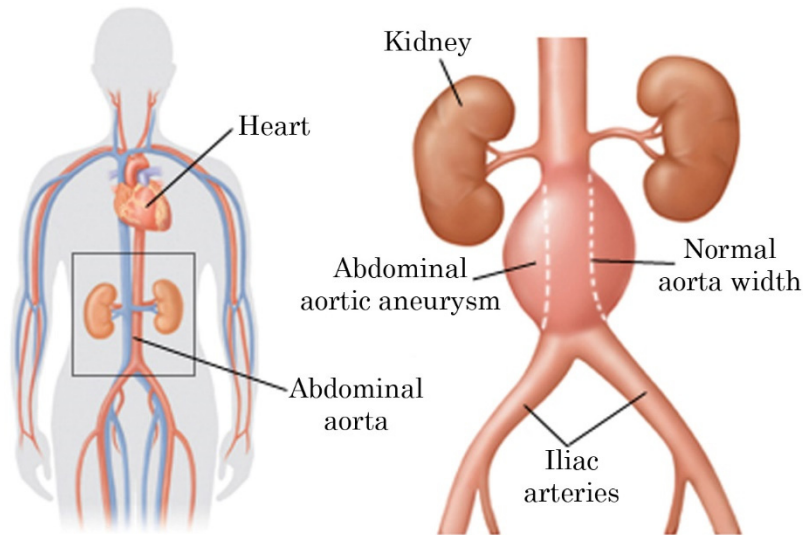
Figure 1-2 Infrarenal abdominal aortic aneurysm [6].

Each blood vessel of the circulatory system has a three-layer structure [7] that provides the elastic recoil required in a closed circulatory system [8]: the intima, made of a single layer of endothelial cells lining the lumen; the media, consisting of concentric layers rich in elastin and collagen fibers, smooth muscle cells (SMC) and non-fibrous matrix, and the adventitia, made of a loose collagen-rich tissue containing fibroblasts (Figure 1-3). Within this structure, the elastin and collagen are the elements responsible for providing aortic wall strength: elastin contributes dominantly at low strains, while collagen fibers become gradually engaged at higher strain ranges.
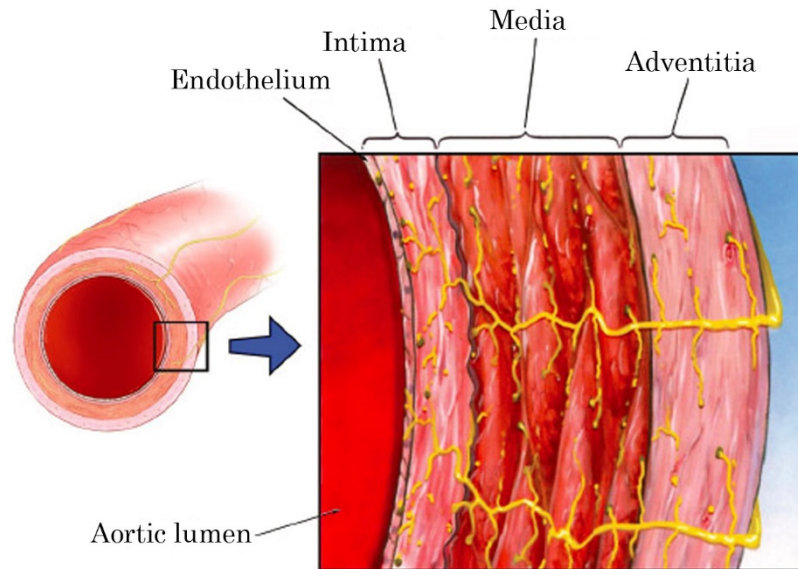
Figure 1-3 Layers of the artery [9].

The development of AAAs is associated with a significant loss of elastin, which is adversely affected by natural issues (aging and gender) or pathologic process (smoking, hypertension, etc.). Macrophages and lymphocytes present in the aneurysmal wall secrete a cascade of cytokines that results in activation of many proteases. Specific proteases defined as matrix metalloproteinases (MMPs) degrade elastin and collagen fibers [10–12]. To combat these proteases, the aortic wall contains tissue inhibitors of matrix metalloproteinases (TIMPs). An increase of TIMPs in the aneurysmal wall [13] has been found during aneurysm development; however, the proteases/antiproteases balance favors proteolysis (breakdown of proteins) [14]. Elastin degradation, together with the decrease in elastin synthesis due to SMC apoptosis, results in a decrease in elastin concentration.

Due to the absence of a competent medial-layer (considering the decrease in elastin concentration), the adventitia tissue, which predominantly contains collagen, may provide some mechanical resistance to the aorta by increasing the collagen concentration. Before rupture, an increase in MMP activity causes the collagen degradation

to exceed collagen production, which finally results in focal wall weakening and rupture. The whole process is summarized in Figure 1-4.
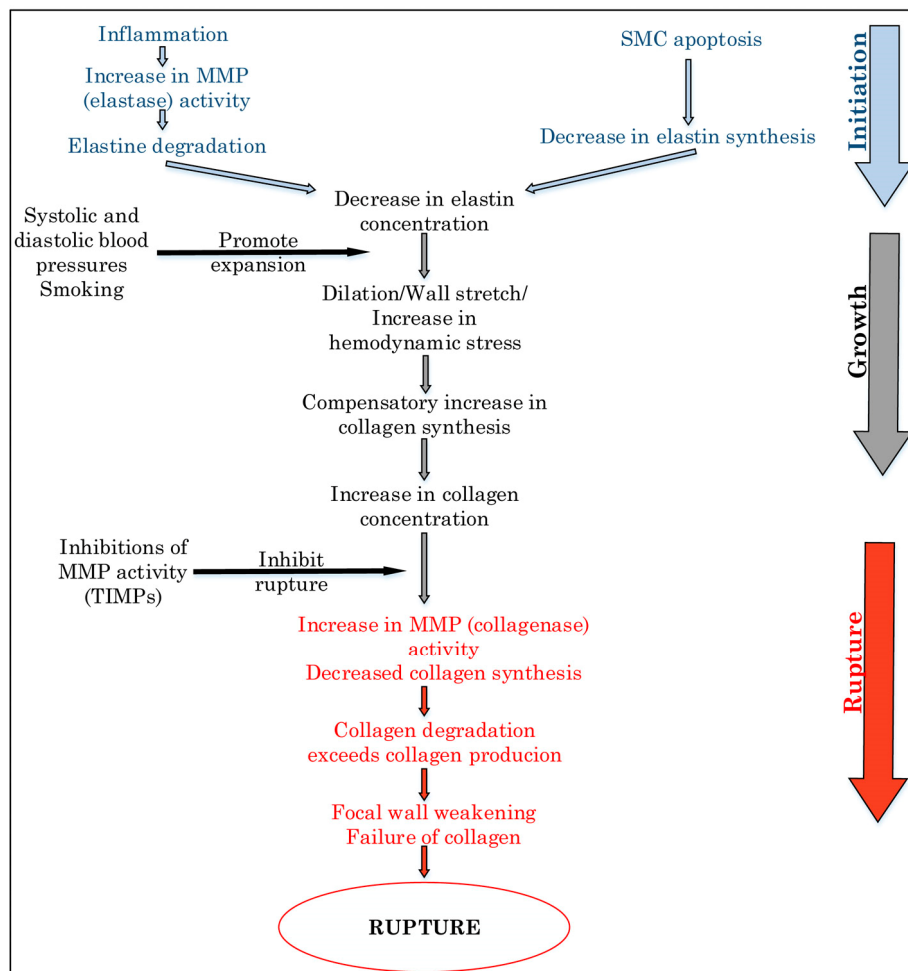
Figure 1-4 Succession of biological events related to AAA rupture. Reproduced in modified form from [15].

As explained above, everything indicates that the particular strength properties of the media, as a result of elastin degradation and excessive collagen deposition [16–18], are extremely important to understanding the biomechanical behavior of AAA tissues.

AAA is risky once rupture occurs, since the mortality rate is high: in the United States, AAA rupture accounts for over 10,000 deaths each

year [19], and it is estimated that when rupture occurs one third of patients die before reaching a hospital [20]. In order to avoid AAA rupture, two strategies are currently available to physicians for excluding blood flow from the aneurysm sac and eliminating pressure from the aneurysm wall: open repair or endovascular repair.

Open repair requires an abdominal incision in the sac of the AAA in order to place a synthetic graft that replaces that section of the artery. The whole process is illustrated in the top row of Figure 1-5.
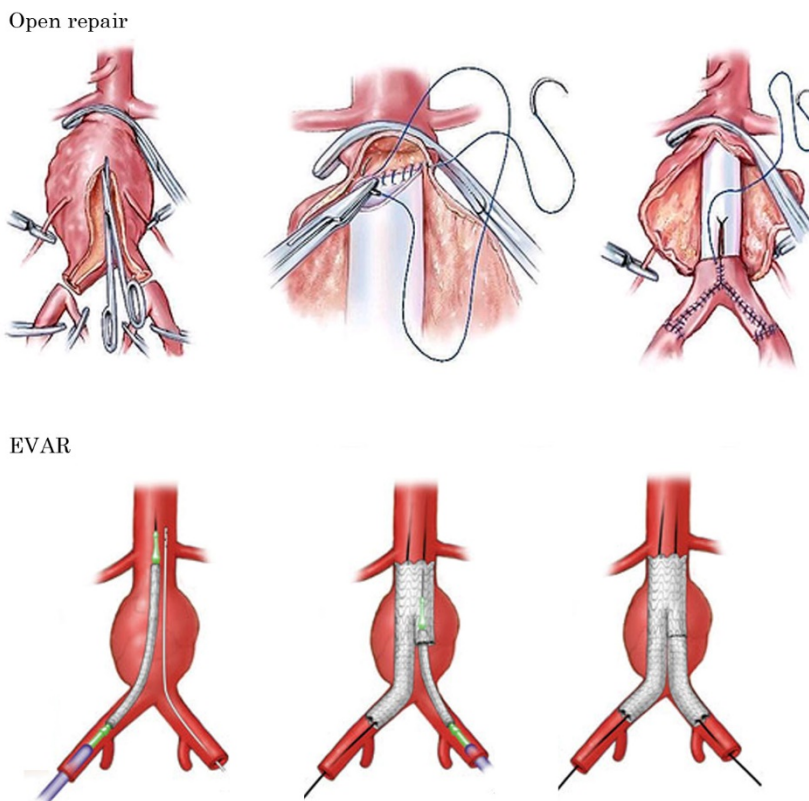
Figure 1-5 AAA intervention process: open repair (top) [21] and EVAR (bottom) [22].

Endovascular repair, or EVAR, is a less invasive approach that is currently performed in more than 75% of patients undergoing surgical intervention. It involves the intraluminal introduction of an endograft (composed of fabric and metal stents) through the iliac arteries by means of catheters and guidewires until the endograft is positioned

correctly, anchoring it in the normal aorta above the aneurysm and in the iliac arteries below the aneurysm. The whole process is illustrated in the bottom row of Figure 1-5.

These two strategies improve patients' survival rates but additional interventions may be required [23,24]. A brief comparison between open repair and EVAR is shown in Table 1-1.

Table 1-1: Open repair and EVAR comparison.

	Open Repair	EVAR
Survival rate after 1 year [24]	89%	96%
Survival rate after 3 years [24]	82%	92%
Reinterventions [23]	10%	20-30%

Although these two approaches help improve a patient's life, there are risks associated with surgery. In order to minimize these risks, physicians only operate on AAAs that are close to the rupture point and on patients who are expected to have a long-term benefit from elective aneurysm repair.

In order to evaluate the risk of aneurysm rupture, the diameter of the aneurysm is a universally recognized factor: as the diameter increases, so does the risk of rupture [25]. The general consensus is that patients with AAA diameters ranging 5-5.5 cm warrant elective repair if such patients are also reasonable operative candidates. For patients with AAA diameters greater than 6 cm, they should be considered for undergoing surgical repair, even if they have an elevated cardiac risk. However, this parameter, despite being the most extended predictor, fails in 10-24% of cases in one of two ways. Either AAAs that had a diameter smaller than 5.5 cm ruptured, or AAAs larger than 5.5 cm never ruptured [26–30].

Aside from this widely extended parameter, other indicators are being incorporated into decisions regarding whether surgical intervention is necessary:

- The rate of growth: Aneurysms that expand by more than 0.5 cm in diameter over a period of 6 months should be considered for repair regardless of the absolute size [31].
- Serum MMP-9: This is significantly higher in patients with abdominal aortic aneurysm [32].
- α1-antitrypsin (α1-AT): The importance of this marker in abdominal aortic aneurysm has contradictory findings [33,34].
- Patients with abdominal or back pain without other obvious causes in the presence of an AAA should undergo repair.

In conclusion, AAA rupture carries a high mortality risk and it has to be avoided via interventions. However, interventions also present their own risk during and after intervention, and therefore it is critical to estimate when an AAA is going to rupture. Currently, the diameter criterion and the aneurysm expansion rate are the most popular criteria followed by physicians. However, reports show that these two metrics are not a reliable measure of rupture risk in all cases, since there is evidence that aneurysms smaller than 55 mm fail and that some larger aneurysms do not rupture during the lifespan of the patient. Therefore, a general indication based on diameter measurements alone may not be sufficient in order to discriminate whether AAAs are close to rupture. Instead, individually tailored rupture predictors that take into account the local and global geometric and mechanical properties of the aneurysm wall are necessary.

1.2 Main contributions of this thesis

The main objectives of this thesis were to:

- Analyze new geometric parameters that may affect AAA wall stress distribution and consequently AAA rupture risk.
- Develop new methodologies to manufacture more realistic patient-specific AAA replicas for further experimentation and clinical help.

This research project has made the following contributions:

- Highlight a non-studied parameter, the local curvature, which significantly influences the wall stress distribution in patient-specific AAA geometries.
- Develop a new and affordable methodology for fabricating patient-specific AAA replicas with regionally varying wall thickness. The methodology can be used to manufacture AAA phantoms with isotropic and anisotropic properties.
- Apply the multi-material additive manufacturing technology to the manufacture of idealized AAA replicas with anisotropic properties.
- Experimentally verify the numerically predicted AAA wall stress distribution.

1.3 Contents and structure of this thesis

The thesis is divided into nine chapters. A brief description of the remaining chapters is given here:

- Chapter 2 aims to place the reader in the context of this thesis by presenting the main findings related to AAA rupture risk. The complex mechanical behavior of the AAA tissue is described, as well as some numerical and experimental studies which are directed at helping physicians estimate rupture risk.
- Chapter 3 statistically analyzes the influence of wall curvature and wall thickness in synthetic AAA geometries, while in Chapter 4 this study is extended to patient-specific AAA geometries.
- A methodology for manufacturing patient-specific AAA phantoms with regionally varying wall thickness and isotropic properties is described in Chapter 5. Then, in Chapter 6, this methodology is modified in order to enable the manufacture of AAA phantoms with a defined anisotropic.
- The multi-material additive manufacturing technology is used in Chapter 7 to manufacture idealized AAA replicas with anisotropic behavior.
- Chapter 8 describes an experimental methodology for verifying AAA wall stress distribution. Additionally, the geometric

parameters studied in Chapter 3 and Chapter 4 are analyzed once again.

- Finally, in Chapter 9, the main conclusions reached by the research carried out and described in this thesis are summarized, and some future lines of research are suggested.

Chapter 2:

State of the art

2.1 Introduction

This chapter collects the most relevant studies related to the AAA rupture. The state of the art is divided into five main subjects. In the first part the basic background regarding elasticity and continuum mechanics is provided. In the second part the mechanical properties of the AAA tissue are described. The third and fourth part summarize the main contribution of numerical and experimental studies, respectively. And finally, the fifth part describes the main biomechanical factors that influence the AAA wall stress distribution.

2.2 Elasticity and continuum mechanics

This section aims to provide some theoretical background regarding mechanical properties of materials that will later be used as reference to represent and characterize the mechanical properties of AAAs.

2.2.1 Elasticity

Elasticity is the main mechanical property for solids. When an elastic material is deformed due to an external force, it experiences internal forces that oppose the deformation and restore it to its original state if the external force is no longer applied. This effect is called elasticity.

The elastic modulus measures the resistance of an object or substance to be deformed elastically (i.e. non-permanently) when a force is applied to it. Depending on the type of loading (shown in Figure 2-1), different elastic modulus are defined.
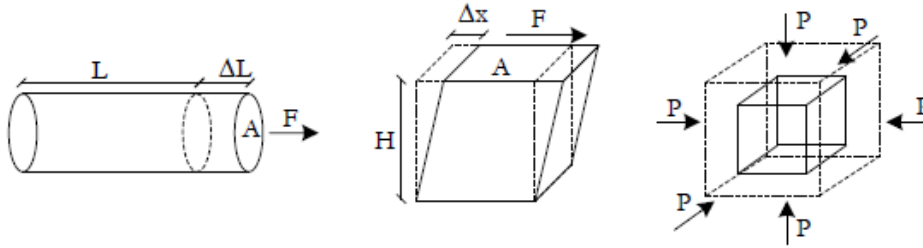
Figure 2-1 Longitudinal deformation (left), simple shear deformation (middle) and uniform compression (right).

- Young's modulus, E, describes the elastic properties of a solid undergoing uniaxial tension or compression (left of Figure 2-1). It is defined as stress, σ, divided by strain, ε, as Equation 2-1.

$$E = \sigma/\varepsilon \qquad (2\text{-}1)$$

where tensile stress is the normal force per area $\sigma = F/A$ and tensile strain is the fractional increase in length $\varepsilon = \Delta L/L$.

- Shear modulus, G, is a measure of the ability of a material to resist tangential deformation (middle of Figure 2-1). Elasticity in shear is defined as the ratio of shear stress, τ, and the corresponding shear strain, γ (Equation 2-2).

$$G = \tau/\gamma \qquad (2\text{-}2)$$

being shear stress the tangential force per area $\tau = F/A$ and shear strain $\gamma = \Delta x/H$.

- Bulk modulus, K, measures the substance's resistance to uniform compression (right of Figure 2-1). It is associated with volume changes experienced by a material under the action of forces acting perpendicularly to its surfaces. The bulk modulus is defined by Equation 2-3.

$$K = -V \, \Delta p / \Delta V \qquad\qquad (2\text{-}3)$$

  where V is the volume and Δp and ΔV are pressure and volume changes respectively.

The stress-strain relationship of materials can be differentiated into linear elastic materials (Hookean elastic solids) or non-linear elastic solids. A Hookean elastic solid is an ideal solid that obeys Hooke's law, which states that the stress tensor is linearly proportional to the strain tensor. In contrast, in non-linear elastic solids the stress-strain relationship is not linear. To model non-linear elastic solids, hyperelasticity is commonly used and the stress-strain relationship is derived from a strain energy density function (SEF).

2.2.2 Continuum mechanics

Continuum mechanics' approach establishes the constitutive equations necessary to model the mechanical behavior of a solid.

Being a solid in a reference configuration presented in Figure 2-2 the position of a particle in the body is defined by the vector $\boldsymbol{X} = (X_1, X_2, X_3)^T$ in the reference configuration and vector $\boldsymbol{x} = (x_1, x_2, x_3)^T$ in the current configuration, called the material and spatial coordinates, respectively. The description in terms of the material variables is called the material (or Lagrangian) description, and the one in terms of the spatial variables is called the spatial (or Eulerian) description.
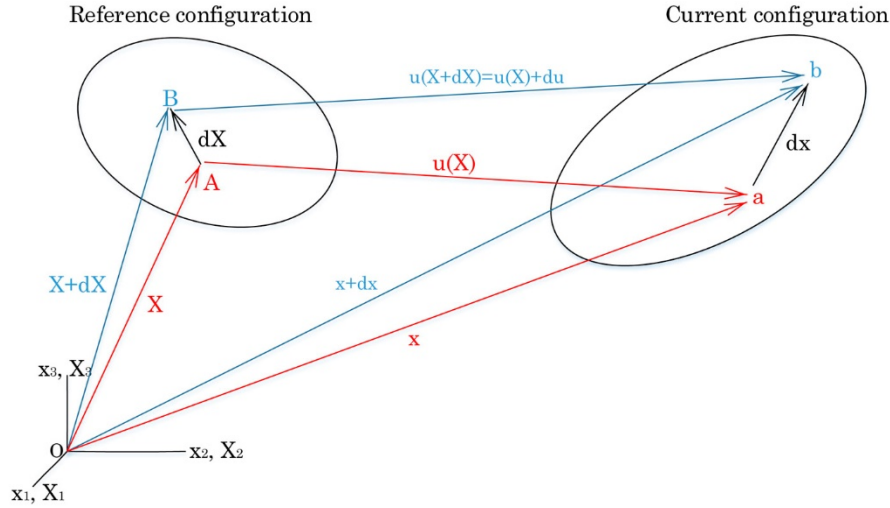
Figure 2-2 Reference and current configuration of a solid.

Let's suppose two points initially close, A and B, separated by d**X**. The final position of these points can be written as:

- Point a: $\boldsymbol{x} = \boldsymbol{X} + \boldsymbol{u}(\boldsymbol{X}, t)$
- Point b: $\boldsymbol{x} + d\boldsymbol{x} = \boldsymbol{X} + d\boldsymbol{X} + \boldsymbol{u}(\boldsymbol{X} + d\boldsymbol{X}, t)$

The deformation in non-linear continuum mechanics is measured by the deformation gradient (Equation 2-4).

$$\boldsymbol{F} = \partial \boldsymbol{x} / \partial \boldsymbol{X} \tag{2-4}$$

$J = det(\boldsymbol{F})$ is the Jacobian determinant, a measure of volume change. Materials which keep the volume constant throughout a motion (incompressible materials) are characterized by the incompressibility constraint, $J = det(\boldsymbol{F}) = 1$.

Strain tensors

Different finite deformation tensors are defined in continuum mechanics:

- Green-Lagrange finite strain tensor:

$$\boldsymbol{E} = \frac{1}{2}(\nabla\boldsymbol{u} + \nabla\boldsymbol{u}^T + \nabla\boldsymbol{u}^T\nabla\boldsymbol{u}) = \frac{1}{2}(\boldsymbol{F}^T\boldsymbol{F} - \boldsymbol{I}) \tag{2-5}$$

- Right Cauchy-Green deformation tensor:

$$\boldsymbol{C} = \boldsymbol{F}^T \boldsymbol{F} \tag{2-6}$$

- Left Cauchy-Green deformation tensor:

$$\boldsymbol{B} = \boldsymbol{F}\boldsymbol{F}^T \tag{2-7}$$

Strain energy function

The strain energy function (SEF), *W*, describes how the material stores the deformation energy. Most constitutive laws specify the strain energy density per unit reference volume to avoid introducing the mass density, ρ_0. The SEF is independent of translations and rotations of the body; it is only dependent on the deformation gradient $\boldsymbol{F}$ via the three invariants (I_1, I_2, I_3) of the Right Cauchy-Green deformation tensor, $\boldsymbol{C}$. The three strain invariants of $\boldsymbol{C}$ are:

$$I_1 = tr(\boldsymbol{C}) \tag{2-8}$$

$$I_2 = \frac{1}{2}(tr(\boldsymbol{C})^2 - tr(\boldsymbol{C}^2)) \tag{2-9}$$

$$I_3 = det(\boldsymbol{C}) = J \tag{2-10}$$

Noteworthy is that the invariants of the Left Cauchy-Green deformation tensor are the same.

Stress tensors

Different stress tensors are defined in continuum mechanics and the most notables are described below.

- Cauchy (true) stress tensor, $\boldsymbol{\sigma}$, relates the forces in the current (deformed) configuration to areas in the current configurations. It is defined by Athanasiou and Natoli [35] as:

$$\boldsymbol{\sigma} = 2J^{-1}\boldsymbol{F}\frac{\partial W}{\partial \boldsymbol{C}}\boldsymbol{F}^T \tag{2-11}$$

Using the chain rule,

$$\frac{\partial W}{\partial \boldsymbol{C}} = \frac{\partial W}{\partial I_1}\frac{\partial I_1}{\partial \boldsymbol{C}} + \frac{\partial W}{\partial I_2}\frac{\partial I_2}{\partial \boldsymbol{C}} + \frac{\partial W}{\partial I_3}\frac{\partial I_3}{\partial \boldsymbol{C}} \tag{2-12}$$

one can reach Equation 2-13:

$$\boldsymbol{\sigma} = 2J^{-1}\left(I_3\frac{\partial W}{\partial I_3}\boldsymbol{I} + \left(\frac{\partial W}{\partial I_1} + I_1\frac{\partial W}{\partial I_2}\right)\boldsymbol{B} - \frac{\partial W}{\partial I_2}\boldsymbol{B}^2\right) \tag{2-13}$$

- First Piola-Kirchhoff stress tensor, $\boldsymbol{P}$, also called the Lagrangian stress tensor, relates forces in the current configuration with areas in the initial configuration. It can be obtained from

$$\boldsymbol{P} = \frac{\partial W(\boldsymbol{F})}{\partial \boldsymbol{F}} \tag{2-14}$$

and is related with the Cauchy stress tensor as follows

$$\boldsymbol{P} = J\boldsymbol{\sigma}\boldsymbol{F}^{-T} \tag{2-15}$$

- Second Piola-Kirchhoff stress tensor, $\boldsymbol{S}$, relates forces in the initial configuration to areas in the initial configurations and is defined as

$$\boldsymbol{S} = 2\frac{\partial W(\boldsymbol{C})}{\partial \boldsymbol{C}} \tag{2-16}$$

and can be written as

$$\boldsymbol{S} = 2\left[\left(\frac{\partial W}{\partial I_1} + I_1\frac{\partial W}{\partial I_2}\right)\boldsymbol{I} - \frac{\partial W}{\partial I_2}\boldsymbol{C} + I_3\frac{\partial W}{\partial I_3}\boldsymbol{C}^{-1}\right] \tag{2-17}$$

The Second Piola-Kirchhoff stress tensor is related with the First Piola-Kirchhoff and the Cauchy stress tensors as follows

$$\boldsymbol{S} = \boldsymbol{F}^{-1}\boldsymbol{P} \tag{2-18}$$

$$\boldsymbol{S} = J\boldsymbol{F}^{-1}\boldsymbol{\sigma}\boldsymbol{F}^{-T} \tag{2-19}$$

2.3 Mechanical behavior of AAA

The mechanical properties of an engineering material (ex. steel) are derived by capturing the relationship between forces and constraints on the entity in experimental tests: specimens of the solid entity are

subjected to controlled loads while measuring the resulting motion (load-controlled tests) or vice versa (motion-controlled tests).

The mechanical properties of biological tissues, including AAAs, can be calculated by means of in vivo or ex vivo experiments depending if that tissue is still on the living body or not. Ex vivo testing is an approach easier than in vivo testing and the experimental outcomes can be used to better characterize the mechanical properties of the AAA tissue. However, it must be pointed out that specimens are isolated from their physiological environment inducing unknown changes to their behavior.

This section introduces the different approaches followed to acquire the mechanical behavior of the tissue.

2.3.1 In vivo studies

Noninvasive techniques such as ultrasound and computed tomography have long been used in the detection and treatment of AAAs. Measures of the motion of the wall under pulsatile blood pressure provide a first look at its in vivo behavior. These measures usually capture the relationship between the pressure pulse and resulting change in size. The challenge with this approach is in the ability to accurately determine the true force and the displacement distribution in the biological entity, which is not devoid of errors.

In 1992 Lanne et al. [36] used a phase-locked ultrasound tracking system to derive the size of the AAA in vivo. They quantified in vivo distensibility of the AAA wall using the pressure-strain elastic modulus (E_p) and what they termed, the stiffness parameter (β) based on the following equations:

$$E_p = D_d(P_s - P_d)/(D_s - D_d) \qquad\qquad (2\text{-}20)$$

$$\beta = D_d Ln(P_s/P_d)/(D_s - D_d) \qquad\qquad (2\text{-}21)$$

where D is diameter, P is pressure and the subscripts, s and d refer to systolic and diastolic time points. They found that E_p was higher on

average and more widely dispersed in aneurysmal abdominal aorta compared to the nonaneurysmal aorta group. Similar to these results, Mac Sweeney et al. [37] reported an increase in the pressure-strain elastic modulus in patients with AAA using M-mode ultrasonography.

Later on, Sonesson et al [38] measured the artery stiffness (β) of 121 individuals using an ultrasonic echo-tracking system. They reported an increase in stiffness for patients with AAA compared with data reported for healthy subjects. Later work by this group showed that ultrasonographically measured stiffness was not significantly different between ruptured AAA and electively repaired AAA [39].

In 1996 Vorp et al. [40] performed ultrasound imaging of nine AAA subjects to study the wall distensibility, which they quantified using compliance defined as,

$$C = (A_{max} - A_{min})/[A_{max}(P_{max} - P_{min})] \qquad (2\text{-}22)$$

where A is cross sectional area measured from ultrasound image, P is blood pressure, with subscripts, max and min referring to the maximum and minimum values. They found that the compliance of the AAA wall is decreased as compared with that of the luminal-thrombus, suggesting the incompressibility of this tissue (ILT).

Wilson et al. concluded that large aneurysms tended to be less compliant, or stiffer [41]. This group later investigated serum markers in AAA and concluded that increased elastolysis is associated with decreased AAA wall stiffness [42].

Long et al. [43] employed tissue Dopler imaging (an ultrasonographic modality which allows wall motion measurements along an arterial segment) of 56 AAA patients. In contrast to previous results, they did not find a significance correlation between AAA size and E_p and β, but they reported that compliance, C, correlated positively to AAA size.

More recently, Ganten et al. [44] investigated also the relation between aneurysm size and compliance (they called it distensibility). In this case they used time-resolved electrocardiogram (ECG) gated

CT imaging data from 67 patients and found that the compliance of AAA did not differ between small (D<5 cm) and large (D>5 cm) lesions.

These are some of the studies that represent the evolution of reports on the topic of in vivo AAA distensibility and are summarized in Table 2-1.

Table 2-1: Findings of in vivo studies

Author	Noninvasive technique	Measured parameters	Findings
Lanne, 1992	Phase-locked ultrasound tracking system	E_p and β	E_p is higher in aneurysmatic aortas compared to healthy aortas.
MacSweeney, 1992	M-mode ultrasonography	E_p	E_p increases with age and in aneurysmatic aortas
Sonesson, 1997	Ultrasonic echo-tracking system	β	β is higher in anerysmatic aortas
Wilson, 1999	Diamové echo-tracking system	E_p and β	Large aneurysms tend to be less compliant
Long, 2005	Tissue Doppler imaging	E_p , β and C	C is significantly correlated with aneurysm size, but E_p and β are not
Ganten, 2008	ECG-gated CT	C	C does not differ between large and small lesions

The advantage of in vivo analysis is that the AAA structure is being studied undisturbed (i.e., it is not isolated from its surrounding environment and undergoes deformation in its natural physiological environment) and provides valuable information on the in vivo motion of the AAA. However, the physical meaning are unclear, for instance,

the physical distinction between E_p and β pose difficulties in explaining findings where one is different between two groups but not the other [41]. In addition, a continuum-based constitutive model required when using finite element analysis cannot be derived from these studies. In order to solve this drawback, Trabelsi et al. [45] have recently published a new work in which they identified the patient-specific material properties of AAA tissue using in vivo gated CT. They proposed an inverse method to identify the patient-specific material properties of the AAA using volume variations of the dynamics CT scans. Briefly, this method consists in minimizing the difference between the model predictions and the CT measurements of the aneurysm volume change between the systolic and diastolic pressure. To minimize this difference, the material properties are varied in each simulation.

2.3.1.1 *In vivo wall strength estimation*

A small number of studies have analyzed in vivo the patient-specific wall strength due to methodological reasons. A very relevant assessment and often used in numerical studies, is the estimation of the AAA wall strength distribution described by Vande Geest et al. [46]. They identified in this study that gender, local thrombus thickness, local AAA diameter and AAA family history have statistically significant influence on AAA wall strength and were employed in a statistical model for patient-specific wall strength distribution. There were two methods for measuring the local ILT thickness and local diameter for a given AAA wall specimen. In the first method a wedge of ILT with AAA wall attached was cut and removed from the intact aneurysm and measurements were done (bench top), while the second method uses CT for measurements. The model was defined as follows

$$STRENGTH = \beta_0 + \beta_1 ILT + \beta_2 AGE + \beta_3 SIZE + \beta_4 NORD \\ + \beta_5 HIST + \beta_6 SMK + \beta_7 SEX + \beta_8 METHOD + \varepsilon \quad (2\text{-}23)$$

where β_0, β_1,..., β_8 are regression coefficients. STRENGTH is the predicted strength of a point on the AAA wall in N/cm², ILT is local attached ILT thickness in cm, AGE is patient's age in years, SIZE is the maximum cross-sectional diameter of the AAA in cm, NORD is the

local diameter normalized to the diameter of nonaneurysmal aorta estimated from the patient's age and sex [47], HIST is a family history (1/2=with, -1/2=without), SMK is patient's smoking status (1/2=smoker, -1/2=non-smoker), SEX is patient's gender (1/2=male, -1/2=female), METHOD is the method used for local variable measurement (1/2=CT, -1/2=bench top) and ε is the residual, i.e. the difference between the model predicted wall strength and the measured local wall strength.

More recently, Kontopodis et al. [48] suggested that the AAA wall strength could be estimated using modern image techniques as ECG-gated CT scans. The hypothesis is based on previous studies [49,50] which found that AAA wall strength is significantly correlated with tissue properties. Therefore, obtaining the tissue elasticity via ECG-gated CT scan would be useful to estimate the AAA wall strength distribution. However, this technique has not been applied yet.

2.3.2 Ex vivo studies: uniaxial tests

Uniaxial extension testing is the simplest and most common of ex vivo elastic property testing methods. Commonly, a rectangular planar sample is subjected to extension along its length at a constant displacement rate in a tensile machine while the force is recorded during extension (Figure 2-3). Typically, these tests are conducted until failure of the specimen. Prior to tensile tests, the specimens are preconditioned for 10 cycles to avoid Mullins effect [51]. From the resulting force-extension data, some elastic properties may be inferred.
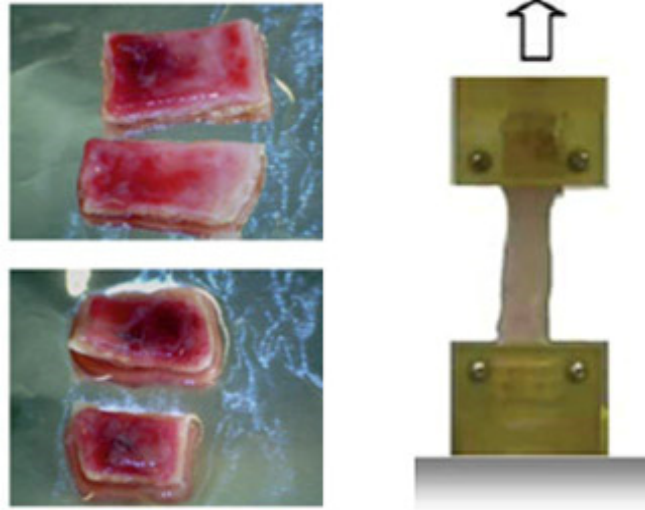
Figure 2-3 AAA tissue uniaxial testing: specimen (left) and uniaxial test (right) [52].

He and Roach [53] obtained rectangular specimen strips during surgical resection of eight AAA patients and subjected them to uniaxial extension tests. The recorded force-extension data was converted to Cauchy stress-strain data assuming incompressibility. They showed that the stress-strain behavior of AAA tissue was non-linear and they fit their data to the exponential functional form

$$\sigma = a e^{b\varepsilon} \qquad (2\text{-}24)$$

where σ is Cauchy stress, ε is strain and a and b are material parameters. They found that both the composition and mechanical properties of AAAs are different from those of nonaneurysmal aortas. The aneurysms were stiffer, with an increase in volume fraction of collagen and a decrease in volume fraction of elastin.

Later Raghavan et al. [54] uniaxially tested 78 AAA specimen strips harvested from 69 patients. The specimen strips were cut along the circumferential and longitudinal direction in this study and tested separately. The data was fit to

$$\varepsilon = [K + A/(B + \sigma)]\sigma \qquad (2\text{-}25)$$

where *K, A* and *B* are material parameters. This model is thought to transition through three phases:

- Phase 1: an initial low-strain phase where load is borne only by elastin fibers, resulting in a linear stress-strain curve whose slope maybe thought of the stiffness of elastin in the tissue.
- Phase 2: at medium strains, some collagen fibers start to straighten out and contribute to load bearing. As a result, the slope of the stress-strain curve starts to increase gradually.
- Phase 3: all collagen fibers contribute to load bearing.

Then, this group used the stress-strain data to fit it to a more robust finite strain constitutive model and estimated its material parameters [55]. The strain energy function (SEF) accounts for a hyperelastic and isotropic material behavior and was defined as

$$W = \alpha(I_B - 3) + \beta(I_B - 3)^2 \tag{2-26}$$

where α and β are the material parameters and I_B is the first invariant of the left Cauchy-Green tensor ***B***. This constitutive model and the mean parameter values have been extensively used for the aneurysm wall in the computational stress analyses of individual AAA [56–61].

More recently, in 2012, Marini et al. [62] obtained experimental data by uniaxial tensile tests of 8 freshly harvested AAA wall samples. They slightly modified the SEF defined by Raghavan and Vorp [55] accounting also for the slightly compressibility of the tissue, i.e. they added a volumetric contribution to the isochoric part of the SEF proposed by Raghavan and Vorp. In order to account for the slight compressibility of the material in the isochoric part, instead of using the right Cauchy-Green strain tensor ***C***, they used a modified right Cauchy-Green strain tensor $(\overline{\boldsymbol{C}} = J^{\frac{-2}{3}}\boldsymbol{C})$ when calculating the first invariant. For the volumetric part of the SEF, a model by Ogden was utilized [63]:

$$U(J) = \frac{k}{\eta}(\eta lnJ + J^{-\eta} - 1) \tag{2-27}$$

where k is the bulk modulus and η is an additional parameter. Note that for incompressible materials J is equal to 1 and the volumetric part of the SEF would disappear.

Later on, in 2013 Reeps et al. [64] harvested 163 AAA wall specimens from 50 patients and tested them using uniaxial tensile tests. They utilized the same model as Raghavan and Vorp but dividing α by 6. Their findings indicated a more distinct nonlinear elastic behavior for AAA wall than previously reported. They also found a correlation between thickness and α and β stiffness.

All the data from these studies is summarized in Table 2-2.

Although the biomechanical response of normal and pathologic human abdominal aortic tissue to uniaxial loading condition is useful in many ways, several drawbacks must be mentioned:

- The in vivo tissue is loaded in multiple directions, and therefore uniaxial loading may be insufficient for characterizing its multi-axial mechanical response.
- Additionally, uniaxial extension testing is not well suited for studying AAA wall tissue anisotropy. For investigating the apparent anisotropy, biaxial testing is a more appropriate alternative.

2.3.2.1 *Ex vivo wall strength estimation*
Researchers have easily assessed AAA wall strength performing ex vivo experimental testing on excised normal and pathological aortic tissue, specifically carrying out uniaxial tests of harvested specimens until failure. Some of the most remarkable findings are cited below.

In 1996, Raghavan et al. [54] noted in the failure properties large differences between normal and aneurysmal tissue in the longitudinal direction, being the ultimate strength for aneurysmal tissue significantly lower (σ_u=0.86MPa) than normal tissue (σ_u=2.01MPa). Later on, Di Martino et al. [49] found that the tensile strength of the ruptured tissue (σ_u=0.54MPa) was significantly lower than that for the electively repaired tissue (σ_u=0.82MPa). They also found that wall strength was negatively correlated with the wall thickness and

positively correlated with the tissue maximum tangential modulus (maximum slope of the stress-strain curve). The latter findings were corroborated in the study by Iliopoulos et al. [50], in which they also reported lower longitudinal tensile strength with aneurysm enlargement. Unlike the earlier study by Di Martino, Raghavan et al. [65] and Xiong et al. [66] did not find a significant difference of failure stress between ruptured (σ_u=0.95 MPa) and non-ruptured groups (σ_u=0.98 MPa).

Summarizing, the AAA wall strength is significantly lower than normal aortic tissue wall strength. However, this difference between ruptured and non-ruptured groups is still not clear. Noteworthy is that the wall strength distribution along the AAA is not homogeneous and there has been reported values of failure stress ranging from 0.34 MPa up to 2.35 MPa [52].

2.3.3 Ex vivo studies: biaxial tests

Biaxial testing is essential for detecting anisotropy and accurately determine the material coefficients for nonlinear constitutive models where multiple test protocols, spanning the entire range of physiological stresses, are carried out.

The preparation of specimens are similar to the uniaxial tests, but in this case square specimens are commonly cut for testing. The square samples are mounted in a biaxial test system as shown in Figure 2-4. Each specimen is submerged in isotonic saline and stretched in the circumferential and longitudinal directions. The samples are tested using a series of circumferential to longitudinal displacement (or nominal stress) ratios, i.e., λ_θ:λ_L=1:1, 0.75:1, 1:0.75, 0.5:1, 1:0.5. Prior to tensile tests the specimens are preconditioned for 10 cycles. From the resulting force-extension data, the stress-strain data for each direction and test is derived.
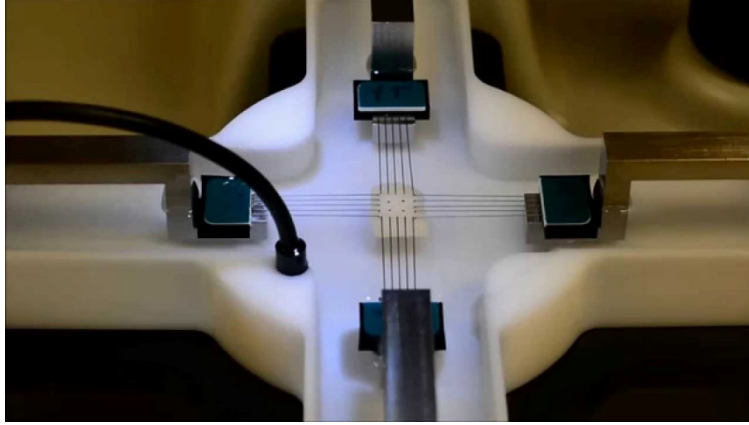
Figure 2-4 Biaxial test system [67].

There are not many studies that have investigated the biaxial properties of the AAA tissue. Vande Geest et al. [68] reported that the AAA was anisotropic. They observed a reduction in AAA extensibility and an increase in AAA stiffness in the circumferential direction compared to the nonaneurysmal abdominal aorta (AA). They fitted the experimental data to the model developed by Choi and Vito [69] for canine pericardium

$$W = b_0(e^{(1/2)b_1 E_{\theta\theta}^2} + e^{(1/2)b_2 E_{LL}^2} + e^{b_3 E_{\theta\theta} E_{LL}} - 3) \qquad (2\text{-}28)$$

where b_0, b_1, b_2 and b_3 are material parameters; and $E_{\theta\theta}$ and E_{LL} the Green strain in the circumferential and longitudinal direction respectively. They also calculated the anisotropic factor

$$AI = \sqrt{b_1/b_2} \qquad (2\text{-}29)$$

and indicated a larger degree of anisotropy for AAA tissue compared to AA tissue.

Similar results were observed by Tong et al. [70]. They biaxially tested 43 AAA samples of thrombus-covered wall and they fit their experimental data to a model developed for arterial walls [71,72]

$$\psi = \mu(I_1 - 3)\frac{k_1}{k_2}(\exp\{k_2[(1-\rho)(I_1 - 3)^2 + \rho(I_4 - 1)^2]\} - 1) \qquad (2\text{-}30)$$

where μ and k_1 are stress-like parameters with dimension (kPa), and $\rho \in [0,1]$ and k_2 are dimensionless. I_1 is the first invariant (described above) and I_4 can be written as

$$I_4 = \lambda_\theta^2 cos^2\varphi + \lambda_L^2 sin^2\varphi \qquad (2\text{-}31)$$

where λ_θ and λ_L are the principal stretches in the circumferential and longitudinal directions; and φ is a geometrical parameter that represents the angle between some fiber reinforcement and the circumferential direction. They also found in this study that when the thrombus gets older, there is an increase in the wall anisotropy and wall is much weaker.

Recently, O'Leary et al. [73] found as previous studies, that the AAA tissue is anisotropic with a greater tendency to stiffen in the circumferential direction. In this study 34 specimens were biaxially tested and the biomechanical response was represented with the anisotropic hyperelastic constitutive model used by Vande Geest et al. [68]. Material coefficients derived from this study were comparable to the ones derived in Vande Geest work, but lower.

A summary of these studies is represented in Table 2-2.

Table 2-2: AAA uniaxial and biaxial tensile tests studies.

Authors	Test	Constitutive model	Material Parameter Values
He and Roach, 1994	Uniaxial	$\sigma = ae^{b\varepsilon}$	a=319 Pa b=38.7
Raghavan, 1996	Uniaxial	$\varepsilon = [K + A/(B + \sigma)]\sigma$	Klong=0.39 MPa-1 Along=0.091 Blong=0.039 MPa Kcirc=0.25 MPa-1 Acirc=0.103 Bcirc=0.047 MPa
Raghavan, 2000	Uniaxial	$W = \alpha(I_B - 3) + \beta(I_B - 3)^2$	α=0.174 MPa β=1.881 MPa
Marini, 2012	Uniaxial	$\psi = \alpha(\overline{I_B} - 3) + \beta(\overline{I_B} - 3)^2 + \frac{k}{\eta}(\eta lnJ + J^{-\eta} - 1)$	α=0.088 MPa β=5.803 MPa k=1.56 MPa η= -2

Authors	Test	Constitutive model	Material Parameter Values
Reeps, 2013	Uniaxial	$W = \dfrac{\alpha}{6}(I_B - 3) + \beta(I_B - 3)^2$	α=0.339 MPa β=4.329 MPa
Vande Geest, 2006	Biaxial	$W = b_0(e^{(1/2)b_1 E_{\theta\theta}^2} + e^{(1/2)b_2 E_{LL}^2} + e^{b_3 E_{\theta\theta} E_{LL}} - 3)$	b0=0.14 MPa b1=477.0 b2=416.4 b3=408.3
Tong, 2011	Biaxial	$\psi = \mu(I_1 - 3) + \dfrac{k_1}{k_2}(\exp\{k_2[(1-\rho)(I_1 - 3)^2 + \rho(I_4 - 1)^2]\} - 1)$	μ=6.0 kPa k_1=97.4 kPa k_2=173.7 φ=35.8° ρ=0.25
O'Leary, 2014	Biaxial	$W = b_0(e^{(1/2)b_1 E_{\theta\theta}^2} + e^{(1/2)b_2 E_{LL}^2} + e^{b_3 E_{\theta\theta} E_{LL}} - 3)$	b0=0.44 MPa b1=297.0 b2=219.9 b3=184.3

2.3.4 Other factors influencing wall mechanical properties

2.3.4.1 Incompressibility

A material which can undergo changes of volume is said to be compressible. However, there are numerous materials that can sustain finite strains without noticeable volume changes (incompressible materials). In these types of material only isochoric (volume preserving) motions are possible. Materials which keep the volume constant throughout a motion are characterized by the incompressibility constraint, $J = \det(F) = 1$. Soft tissues and rubber are good examples of incompressible or nearly incompressible materials.

Carew et al. [74] proved that under physiological strains, the walls of blood vessels behave as an incompressible material. In the literature, it is commonly assumed that under mechanical loads, the walls of abdominal aortic aneurysms are almost incompressible [49,75]. Moreover, Kobielarz et al. [76] demonstrated recently the incompressibility of the AAA tissue. Even so, there exist models that consider a possible compressibility of the tissue as the one developed by Marini, defined previously.

2.3.4.2 Intraluminal thrombus (ILT)

Intraluminal thrombus (ILT) is defined as a clot of blood formed within the lumen of a blood vessel remaining attached to its place of origin. The ILT is found in most AAAs of clinically-relevant size [77] and an appropriate model for the ILT is also necessary to accurate estimate the wall stress distribution in AAAs. The ILT, as the AAA wall, is also composed of three layers: luminal, media and abluminal (Figure 2-5). The mechanical properties of these layers have been studied in the literature.

In 1998 Di Martino et al. [78] uniaxially tested 21 AAA thrombus specimens (from the luminar layer). They found a linear stress-strain relationship for all the thrombus specimens with an average Young's modulus equal to 0.131 MPa. Later on, in 2001 Wang et al. [79] uniaxially tested 50 specimens in both, longitudinal and

circumferential directions (from the luminal and medial layers). Their results suggested that ILT is inhomogeneous and possibly isotropic. Vande Geest et al. [80] corroborated these findings investigating the multi-axial biomechanical behavior of the ILT luminal layer of 9 specimens. They concluded that the use of an isotropic SEF (Equation 2-26) for ILT is appropriate. In contrast, Tong et al. [70] found that while the medial and the abluminal layers are isotropic materials, the luminal layers of the ILT exhibit anisotropic stress responses. The anisotropic model defined previously in Equation 2-30 was able to fit the three individual layers of ILT very well. More recently, O'Leary et al. [81] biaxially tested the three layers of the ILT from 19 patients. In this study they reported that all ILT have isotropic and inhomogeneous properties, finding consistent with Wang and Vande Geest studies. Also compressive studies have been carried out in the three layers of the ILT reporting inhomogeneous between layers, with significant higher compressive stiffness for the abluminal layer [82].
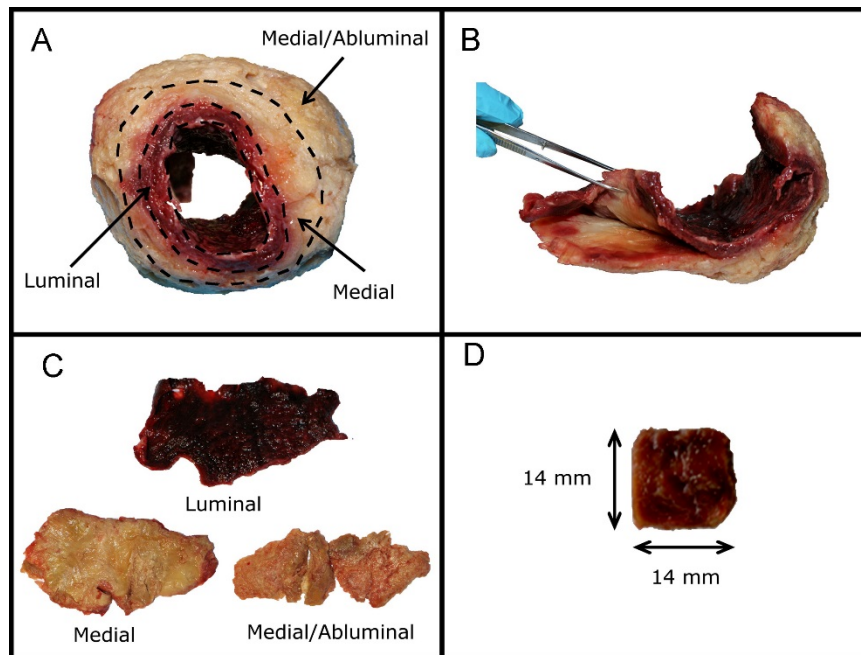
Figure 2-5 ILT tissue preparation for biaxial testing [81].

Unusual for soft biological tissues, ILT exhibited an almost stress-strain linear relation and isotropic properties. Although studies have revealed the inhomogeneity of the tissue, in most FE models, the ILT

has been assumed isotropic and homogeneous [83–86]. Some of the ILT studies in the literature are summarized in Table 2-3.

Table 2-3: ILT tests studies.

Authors	Test	Layers studied	Findings
Di Martino, 1998	Uniaxial	Luminal layers	Linear stress-strain relationship
Wang, 2001	Uniaxial	Luminal and medial layers	Inhomogeneous and isotropic
Vande Geest, 2006	Biaxial	Luminal layer	Isotropic
Tong, 2011	Biaxial	Luminal, medial and abluminal layers	Anisotropy in luminal layer. Medial and abluminal layers isotropic.
O'Leary, 2014	Biaxial	Luminal, medial and abluminal layers	Mild non-linearity stress-strain relationship. Inhomogeneous and isotropic.
Ashton, 2009	Compressive	Luminal, medial and abluminal layers	Inhomogeneous with higher compressive stiffness in abluminal layer

The ILT also affects the AAA wall, which is thinner and shows more frequent signs of inflammation, apoptosis of smooth muscle cells (SMC) and degraded extracellular matrix when it is covered by a thick ILT. This may perturb the structural integrity and stability of the vessel wall [87]. However, the role of ILT in AAA rupture is still controversial, and it is still not clear if an ILT increases or decreases AAA rupture risk.

2.3.4.3 Calcifications

A small commentary should be dedicated to calcifications. Calcification is the process in which calcium builds up in body tissue where there normally is not any calcium. It is commonly found within the aneurysm wall in most AAAs of a clinically relevant size [88]. The calcified deposits primarily occur within the intima and intima-media interface, but can also occur within the ILT.

Determining the material properties of individual AAA calcified deposits is difficult owing to their small size, but it is generally assumed to behave as an isotropic material with higher stiffness than the surrounding arterial wall [84,89,90]. It is also believed that small calcification weakens the wall [91]; nonetheless, its role in numerical analyses is still under debate.

2.3.5 Conclusions

Mechanical properties of AAA tissue have been extensively studied in vivo and ex vivo. Mechanical tests have demonstrated that arterial tissue exhibits highly nonlinear, anisotropic and hyperelastic properties and it is commonly assumed to be incompressible. The main constitutive models used in numerical simulations are the isotropic model derived by Raghavan (Equation 2-26) and the anisotropic models from Vande Geest (Equation 2-28) and Tong (Equation 2-30). However, it is not possible yet to accurately derive the mechanical properties from in vivo studies.

The role of the ILT and calcifications has been studied too, as they have an important effect on the material properties of the tissue. It has been demonstrated that the AAA wall covered by ILT is stiffer and weaker due to the degradation of extracellular matrix; and it is believed that calcifications weaken the wall.

With respect to the AAA wall strength, several uniaxial tests have been carried out until rupture. It has been found that the strength is nonhomogeneous along the AAA wall and the ultimate stress values often range from 0.34 MPa up to 2.35 MPa. To estimate the AAA wall strength in vivo it is also commonly used the model described by Vande

Geest (Equation 2-23) which takes into account the gender, local thrombus thickness, local AAA diameter and AAA family history.

2.4 Numerical approach to predict AAA rupture

As commented in Chapter 1, the current clinical standard used to quantify AAA rupture threat is to measure the maximum diameter and, if possible the growth rate of the aneurysm. However, there is growing concern over the use of these parameters in all AAA cases and extensive biomechanical analyses have been carried out in the literature to develop more robust rupture parameters than size alone.

The use of computational techniques such as the finite element method (FEM) have allowed estimating the wall stresses in these complex 3D AAA structures in order to predict AAA rupture. For a detailed introduction and background into the FEM the reader can be referred to Zienkiewicz el al. [92]. Briefly, the basic approach of the FEM is to divide a complex geometrical structure (AAA) into smaller pieces or elements. These elements are connected by nodes. The entire network of elements and nodes is called a mesh (Figure 2-6). Wall stress is determined by predicting displacement of the nodes which are influenced by material properties of the aneurysm wall (i.e. stiff or elastic) and preset boundary conditions (i.e. blood pressure).
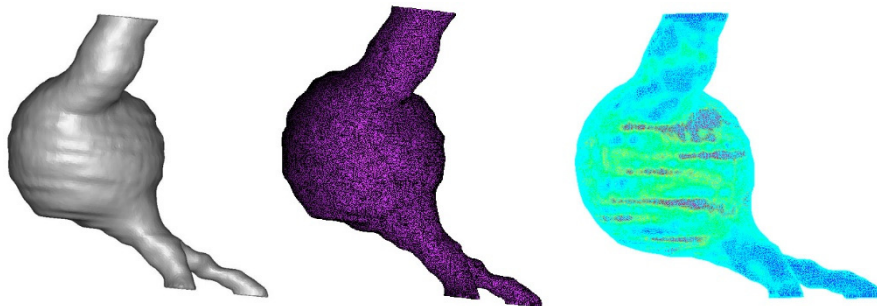
Figure 2-6 Scanned AAA geometry (left), meshed AAA (middle), and AAA stress distribution (right).

For the wall stress calculation three main components are required: the in vivo 3D aneurysm model to create the mesh, the material model describing the mechanical properties of the aneurysm wall and the

boundary conditions. The geometry of the AAA model is acquired by using medical scanners, while the material properties of the AAA have been discussed in the previous section. The standard boundary conditions used throughout the literature when analyzing AAAs using the FEM are 1) applying a static internal pressure of 120 mmHg to the luminal surface and 2) constraining rigidly the proximal and distal regions to represent the tethering to the remainder of the aorta.

Once calculated the stress values on each element of the mesh, an AAA rupture parameter, such as, Peak Wall Stress (PWS) and Finite Element Analysis Rupture Index (FEARI) could be calculated.

2.4.1 Peak Wall Stress

One of the first reports to couple FE analyses together with patient-specific AAA 3D reconstructions was performed by Raghavan et al. [93] where six AAA cases and one healthy control were examined. They found that the PWS among AAA patients was considerably higher than in the nonaneurysmal aorta. Later on, Fillinger et al. [57,59] furthered this work and investigated whether PWS may be superior to diameter in assessing rupture risk of patient-specific AAAs. They first found that PWS was significantly higher for ruptured AAAs than for electively repaired AAAs, even when matched for maximal diameter [59]. In the following study [57], they observed that PWS seems superior to diameter in differentiating patients who later required emergent repair. Specifically, they found differences of 38% (p<0.0001) in PWS between elective repair and emergent repair, while differences in diameter were 3% (p=0.5). Noteworthy is that in this study a large cohort was analyzed: 39 patients who underwent elective repair and 22 patients who required emergent repair. Venkatasubramaniam et al. [56] concluded similar results in a smaller study group (n=27) with mean PWS values equal to 550 kPa and 770 kPa for elective and emergent repair AAAs, respectively. The same conclusions were reported by Truijers et al. [94] in a cohort of 30 small AAAs (diameter < 55 mm).

Additionally, in some of these studies [57,95] they observed that the area of PWS correlated with rupture site. As an example, recently

Doyle et al. [96] studied a case where the exact rupture point was clearly visible on the CT images and it coincided with predicted elevated stress region. However, these findings were challenged by Georgakarakos et al. [95] who found that the location of PWS may not necessarily coincide with the site of rupture. It was reasoned that the wall strength is important to be considered as well. Wall strength is known to vary significantly from region to region, and therefore regions with high wall stress may be safe due to the strength at that location.

2.4.2 RPI, FEARI and PWRI

Next logical step toward rupture risk assessment is to evaluate stress against strength. It is known that AAA rupture occurs when the locally acting wall stress exceeds the locally acting wall strength. Therefore, the AAA tissue strength must play an equal role to AAA wall stress in determining failure. To this end Vande Geest et al. [97] proposed the Rupture Potential Index (RPI) as a metric to quantify AAA rupture risk. The RPI is defined as the ratio of local wall stress to local wall strength, where wall stress distribution was derived from FEM and strength distribution was obtained, as previously described, using a mathematical model (Equation 2-23) developed by Vande Geest et al. [46]. However, in this research where they studied 8 ruptured and 5 nonruptured AAAs, they did not find statistical difference in RPI values between groups. The same index, but called Peak Wall Rupture Index (PWRI) was more recently used by Gasser et al. [60]. In this study PWRI correlated positively with maximum diameter, and a positive rather than negative correlation with ILT volume was observed, indicating the absence of a protective effect of the ILT on rupture risk. They found that when including the ILT and nonhomogeneous wall thickness in the simulations, the PWRI was significantly higher in ruptured than in diameter-matched nonruptured aneurysms. Similar findings indicating RPI values notably higher for ruptured AAAs were found by Maier et al [98].

Doyle et al. [99] developed a similar parameter called FEARI (Finite Element Analysis Rupture Index) to assess the rupture threat. FEARI measures the ratio of wall stress to experimental wall strength, with

values larger than 1 indicating failure. The wall strength values were obtained from previous research on experimental testing of AAA wall specimens [52,54,75]. With all the experimental data from these studies, they divided the AAA in 8 sections and denoted the strength for each section from the experimental data. Then the FEARI approach was used with 42 electively repaired AAAs and 10 ruptured AAAs [100]. FEARI was found to be significantly higher in ruptured AAAs (1.03±0.43 compared to 0.66±0.3 of electively repaired AAAs), as well as diameter and PWS.

2.4.3 SP

Kleinstreuer and Li [101] proposed a patient-specific severity parameter (SP) to estimate the risk of AAA rupture and provide a threshold value when surgical intervention becomes necessary. The SP depends on eight biomechanical factors, to be obtained via patient's pressure and AAA-geometry measurements. It takes into account size, shape, expansion rate, amount of ILT, patient's diastolic pressure, PWS and stiffness change. The authors calculated the SP for three different AAA, and found the highest value for the one AAA that ruptured and found lower values for the other two AAA that were electively repaired. In this work the PWS was calculated via an equation adapted from the Law of Laplace (Equation 2-32) that would likely not work with complexly shaped AAAs.

$$PWS = 0.006 \frac{(1 - 0.68\alpha)e^{0.0123(0.85p_{sys} + 19.5d_{AAA,max})}}{t^{0.63}\beta^{0.125}} \qquad (2\text{-}32)$$

where α is the area ratio of AAA sac to ILT, β the asymmetry parameter, t is the wall thickness, $d_{AAA,max}$ is the maximum transverse diameter and p_{sys} is the systolic blood pressure. Later, Vilalta et al. [102] modified this concept for only considering the main geometric parameters of the aneurysm which can be easily determined by CT or MRI: peak diameter, nondeformed aorta diameter, aneurysm length, anterior and posterior lengths; and the AAA wall thickness. They called the parameter Rupture Index (RI) instead of SP. The basic idea of the method was to correlate the main simple geometric parameters of the aneurysm in order to obtain the morphologic biomechanical

determinants. In their next study [103] they analyzed a set of AAAs and calculated the RI values for each of them. A very interesting point from this study is that the RI values of 95.4% of a group of patients who underwent emergency surgery due to rupture, indicated the high risk of AAA rupture. However, as the maximum diameter of those AAAs were inferior to the threshold value for surgical treatment, they were not repaired until rupture.

Summarizing, in the literature several parameters have been analyzed in order to better predict the AAA rupture risk. The main biomechanical parameters have been presented and the studies have demonstrated that PWS and indexes relating stress-strength have a significant effect on the AAA rupture risk. These studies are illustrated in Table 2-4. Apart from these biomechanical parameters, other researchers have studied the influence on the AAA rupture of some geometric factors (diameter, tortuosity, axisymmetry). For example, Tang et al. [13] revealed that implementing the bulge location and mean averaged area in a predictive model modestly improved the accuracy of detecting aneurysm rupture.

Table 2-4: Biomechanical parameters studied to predict AAA rupture risk. UWT (uniform wall thickness), NUWT (nonuniform wall thickness), MM (material model), R (ruptured AAA), NR (nonruptured AAA).

Authors	FEM assumptions	Parameter Analyzed	Parameter Values
Raghavan, 2000	UWT Without ILT MM: isotropic hyperelastic [55]	PWS	AAA: 290 to 450 kPa AA: 120 kPa
Fillinger, 2003	UWT Without ILT MM: isotropic hyperelastic [55]	PWS	R: 477±60 kPa NR: 369±20 kPa
Venkatasubramaniam, 2004	UWT Without ILT MM: isotropic hyperelastic [55]	PWS	R: 770±209 kPa NR: 550±240 kPa
Vande Geest, 2006	UWT With ILT MM: anisotropic hyperelastic	PWS	R: 0.48±0.05 NR: 0.36±0.03
Kleinstreue, 2006	Equation (no FEM)	PWS	R: 0.75±0.00 NR: 0.55±0.07

Authors	FEM assumptions	Parameter Analyzed	Parameter Values
Truijers, 2007	UWT Without ILT MM: isotropic hyperelastic [55]	PWS	R: 517±24 kPa NR: 397±33 kPa
Gasser, 2010	NUWT With ILT MM: isotropic hyperelastic [55]	PWRI	R: 0.84±0.46 NR: 0.61±0.39
Maier, 2010	UWT With ILT MM: isotropic hyperelastic [55]	RPI	R: 0.47±0.13 NR: 0.33±0.12
Doyle, 2010	UWT With ILT MM: isotropic hyperelastic [55]	FEARI	R: 1.03±0.43 NR: 0.66±0.30

2.4.4 Conclusions

Numerical studies are an alternative tool to predict the AAA rupture. Instead of utilizing the criterion of maximum diameter alone, researchers are suggesting that other parameters could be taken into account when deciding whether to operate or not. The main biomechanical factors studied in the literature which are significant in the AAA rupture are the peak wall stress (PWS) and the rupture potential index (RPI). Also, the influence of different parameters on the wall stress distribution has been extensively studied remarking geometric factors, such as asymmetry and wall thickness, and FEA modeling strategies.

2.5 Experimental approach to predict AAA rupture

Numerical studies can be an important step forward to predict the AAA rupture. However, before clinical implementation, they must be validated. In this subsection, the evolution of the AAA phantoms manufacturing is described and the most important experimental studies related with the AAA phantoms rupture are commented.

2.5.1 AAA phantoms manufacturing

The most common used technologies for manufacturing AAA phantoms are the casting/injection technique and Additive Manufacturing technology.

Regarding casting, many researchers have used the casting technique to manufacture major and minor arteries [104–106] (left of Figure 2-9). Briefly, they used CT scans of patients to transform them to realistic 3D models. After segmentation, the geometry is imported to a CAD software and split into two halves, creating a two-piece mould set. Each patient-specific mould design consists of two sets of moulds. The first mould is designed to produce the casting wax model of the AAA (representing the lumen and called here 'lumen mould'), and the second set to produce the outer silicone model ('outer wall mould'). Once the mould sets have been designed, the files are exported to a CAM software in order to generate the toolpath commands used to

control the milling machine. Then machining is performed by a computer numerical control (CNC) milling machine. When both moulds are machined the wax is casted in the inner mould to make the lumen in wax. Then, the wax model is placed in the outer mould and silicon rubber is injected. After the curing process of the silicone, the wax is melted and the silicone AAA model extracted. The material commonly used in the injection is the silicone rubber which has an isotropic hyperelastic behavior. The whole process is illustrated in Figure 2-7.
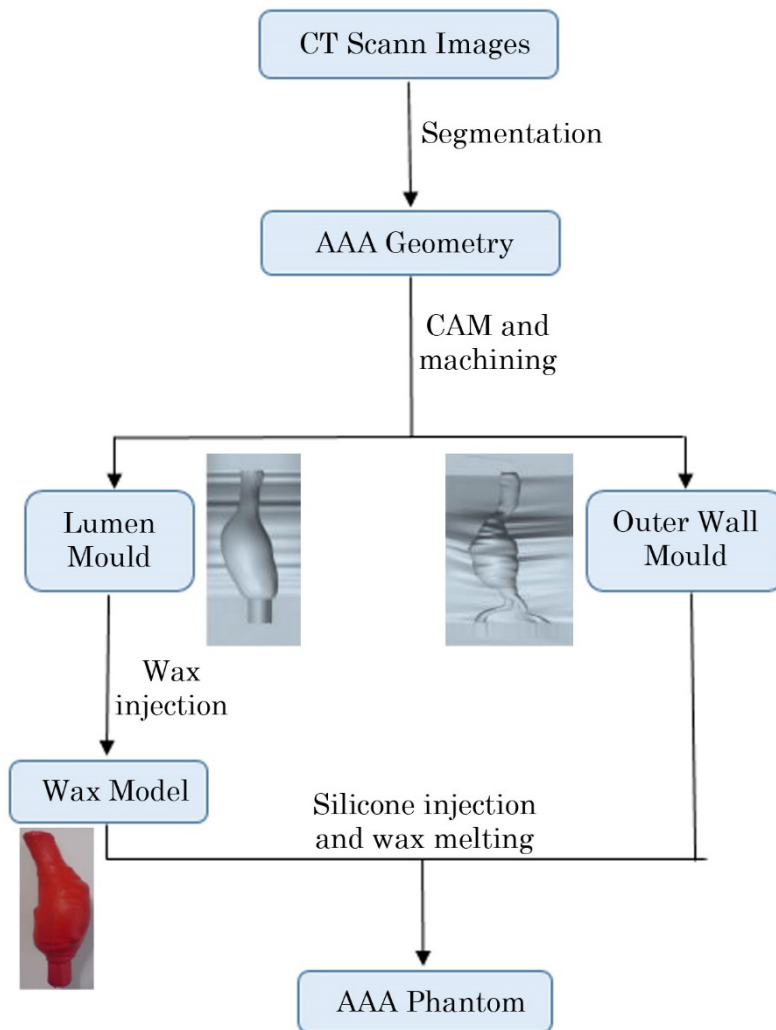
Figure 2-7 Casting technique process.

Following this technique, O'Brien et al. [106] observed the wall thickness error of the phantoms ranged from 20% to 58%, while Doyle et al. [105] achieved an average error equal to 9.21%. Later on, Corbett et al. [107] modified the methodology to make possible the inclusion of ILT in the AAA phantom. This technique is commonly used for AAA phantoms manufacturing, however a drawback of this methodology is that some complex AAA geometries strongly difficult the machining process.

The second technology used for manufacturing AAA is Additive Manufacturing (AM), also known as 3D printing. [108–110] (right of Figure 2-9). AM is an advanced production process that can fabricate physical objects directly from 3D computer-aided design models. This technology enables the fabrication of anatomical models within a short time without tooling. During the process, layers of materials are added until the whole physical object is finished. The process is illustrated in Figure 2-8. In the last decade the technology has greatly improved and currently complex geometries can be printed with a different range of materials. Recently Cloonan et al. [111] showed the potential of 3D printing manufacturing phantoms with flexible materials and recent advances in bioprinting present further possibilities for phantoms [112,113]. The disadvantages of this technology are the high cost - around 100$ for each AAA copy depending on the material and printing technology used-, the printed artery has anisotropy due to the printing process and removing the support material without damaging the flexible AAA phantom can be a challenge.
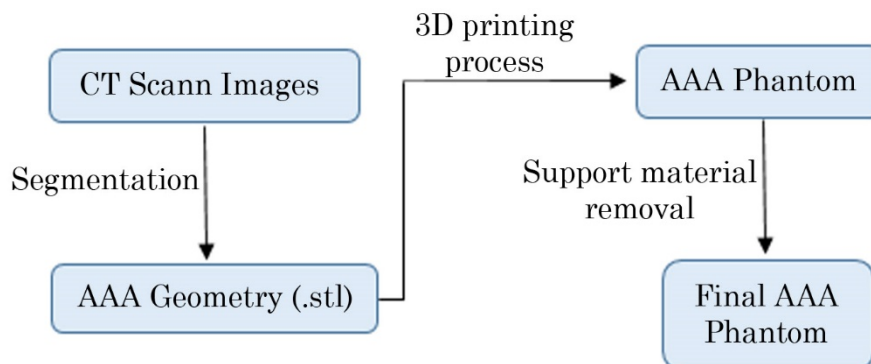
Figure 2-8 AM process.
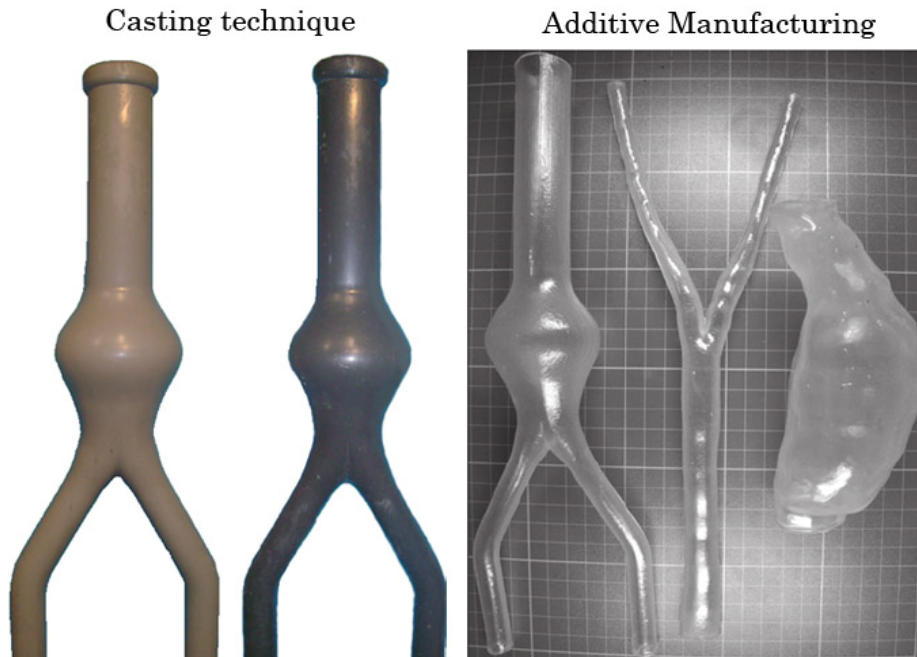
Figure 2-9 AAA replicas manufactured via casting technique (left) [114] and rapid prototyping (right) [115].

Apart from the mentioned techniques, in studies where the AAA wall compliance is not transcendent, different techniques can be used. For instance, Stamatopoulos et al. [116] used a 3D printer for creating an AAA replica and then submerged it in a liquid silicone elastomer material. When the silicone was cured, the 3D printed material was removed using tap water to obtain a silicone mould with a hole inside representing the AAA geometry.

2.5.2 Experimental studies with AAA phantoms

Due to the complexity of manufacturing AAA phantoms, few experimental studies have been carried out in the literature. The principal experimental studies are focused on the prediction of AAA rupture location, the deformation of the AAA wall, the flow behavior along the AAA and pre-clinical testing of endovascular grafts.

Doyle et al. [114] manufactured 4 patient-specific geometries following the casting technique [105] in order to examine whether high stress regions predict the rupture location. They inflated the phantoms until

they burst finding that experimental rupture locations agreed with regions of both peak and high wall stress from Finite Element analyses.

AAA phantoms were also used to measure wall strains under pressure. However, in contrast to engineering parts where strain gauges are placed on the surface of the object, this approach would not be suitable for the AAAs, as attaching them on the surface of the artery is a difficult task due to its complex geometry. Therefore non-contact testing techniques are desired and visual approaches, photoelastic method and stereoscopic technique, have been used in the literature.

Photoelastic fringe analysis is a widely used method for visualizing experimentally the overall surface stress and strain in a structure during static or dynamic loading [117]. The method is based on the property of birefringence. Briefly, a polarized light passes through a photoelastic material and splits into two beams along the principal strain directions with a retardation between them. The primary variables required when measuring strain are the fringe order (N) and the fringe value (f) where f is a combination of the wavelength of the light ($\lambda = 575\,nm$), the thickness of the material (t) and the optical coefficient of the material (K). The formula to calculate f is shown in Equation 2-33 and the difference in principal strains in Equation 2-34.

$$f = \lambda/(2tK) \qquad\qquad (2\text{-}33)$$

$$\varepsilon_x - \varepsilon_y = Nf \qquad\qquad (2\text{-}34)$$

The fringe order is the result of measurements and it is proportional to the difference between the principal strains. The fringes are ordinarily color continuous bands which will be dependent on the retardation value. The complete color sequence is given in Figure 2-10 including, for each color, the relative retardation and the numerical fringe order.
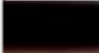
TABLE 1 — ISOCHROMATIC FRINGE CHARACTERISTICS			
Color	Approximate Relative Retardation		Fringe Order
	nm	in x 10⁻⁶	N
Black	0	0.0	0.0
Pale Yellow	345	14.0	0.60
Dull Red	520	20.0	0.90
Red/Blue Transition	575	22.7	1.00
Blue-Green	700	28.0	1.22
Yellow	800	32.0	1.39
Rose Red	1050	42.0	1.82
Red/Green Transition	1150	45.4	2.00
Green	1350	53.0	2.35
Yellow	1440	57.0	2.50
Red	1520	60.0	2.65
Red/Green Transition	1730	68.0	3.00
Green	1800	71.0	3.10

Figure 2-10 Isochromatic fringe characteristics [118].

This technique was applied by Morris et al. [119] to measure experimentally the stress patterns in idealized AAA phantoms (manufactured by the casting technique). However, in this work normal incidence (of the light) was not considered on the curved surfaces on the model which resulted in reduced accuracies. This issue was resolved by Callanan et al. [120] who used the same technique for idealized AAA models, but with normal incidence. The differences in principle strain between numerical studies and experiments were low, ranging from 0.03 to 10.01%. More recently Doyle et al. [121] applied this technique to patient-specific AAA geometries with uniform wall thickness and measured the fringe order in 6 locations; the results showed acceptable errors. An example of this technique is shown in Figure 2-11.

FEA Wall Stress   Photoelastic Wall Stress
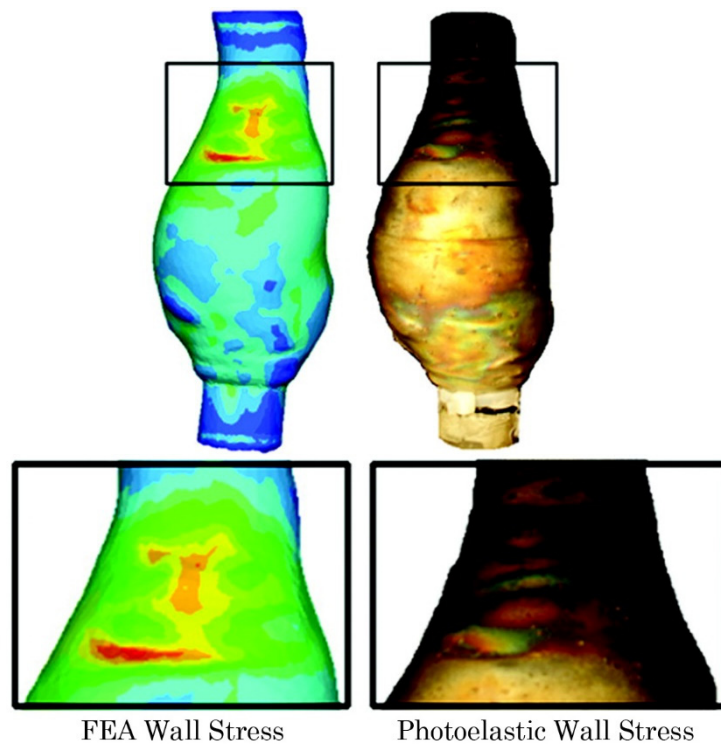
Figure 2-11 FEA and photoelastic AAA wall stress [122].

This methodology only works for perfectly linear elastic photoelastic models and it is not devoid of drawbacks that can affect accuracy. In order to obtain accurate fringe orders that represent the actual strain variation, the normal incidence to the surface is vital. Due to the complex geometries of patient-specific AAAs (irregular structures with several inflection points and changes in curvature on the surface), it would be hard to accurately measure the strain distribution along the whole aneurysm. It has also limitations when trying to visualize low strain regions as the isochromatic fringe orders obtained from the photoelasticity model become less clear. Additionally, the fringe order measurement may vary slightly depending on the user.

The stereoscopic technique is an alternative to photoelasticity that makes possible to measure locations and displacements in three dimensions by utilizing imaging from different perspectives as a basis for the triangulation of 3D positions. The stereoscopic technique has

been utilized inflating arteries in mice by Sutton et al. [123]. They used a microscope system and measured successfully the full 3D displacement and surface strain fields via digital image correlation (DIC). Although DIC is a good technique, it must be noted that DIC typically relies on statistical correlation instead of an exact match of markers and is very dependent on the pattern. To avoid these issues, and as an alternative to DIC, point tracking was used by Meyer et al, [104]. Dots were drawn manually in idealized AAA shapes and recorded by two grayscale cameras in each inflation test for subsequent analysis. The problem with this technique is that to locally measure the strains accurately, the density of markers would have to be very high, complicating the work.

Both methods, DIC and point tracking (Figure 2-12), are valid to measure the wall strain of the outer surface without contact and therefore, avoiding external interactions. However, the problem with using the stereoscopic technique (with both methods) is that in many patient-specific AAA geometries it would not work due to tortuosity; that is, several regions of the artery could not be visible to both cameras.
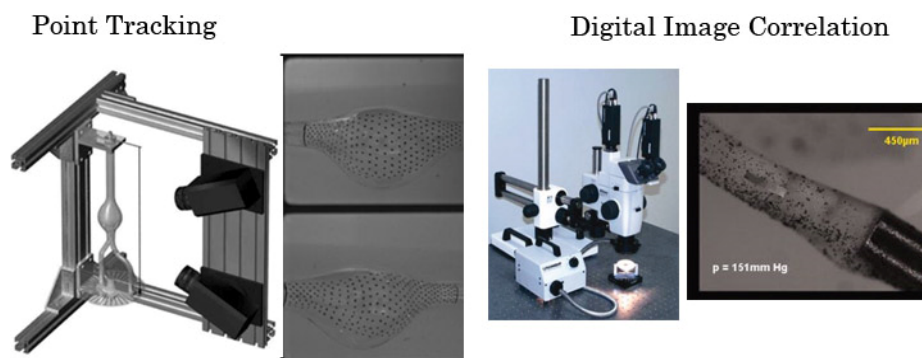
Figure 2-12 Stereoscopic techniques: point tracking [104] (left) and DIC [123] (right).

DIC has been also applied to characterize tissue in bulge inflation tests [45,124,125] (Figure 2-13).
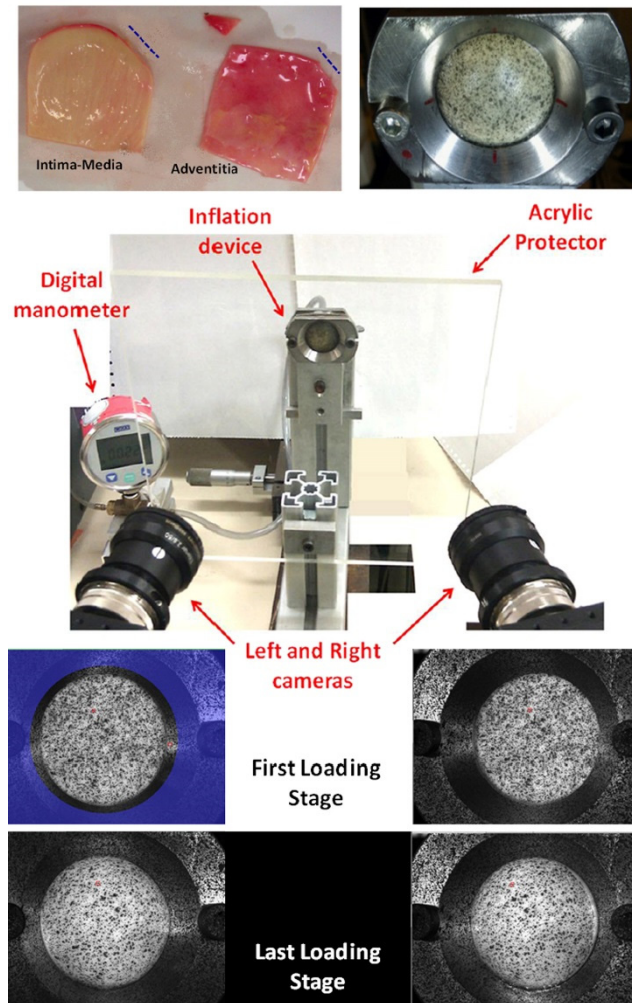
Figure 2-13 Bulge inflation test [125].

AAA phantoms were also used for flow behavior studies. Indeed, the complex hemodynamics observed in the human aorta play important roles in the regulation of vascular homeostasis and therefore has been extensively studied in the literature. Different researchers have experimentally analyzed the hemodynamics of the AAAs in order to study the hemodynamic change after stent-graft implantation [126], the influence on the flow of the aorto-iliac bifurcation [116,127] and the ILT [128]; and to validate numerical simulations [129]. To this end different methodologies have been used to measure flow velocities as phase-contrast magnetic resonance imaging (PCMRI) and particle

image velocimetry (PIV) system. However, these methodologies are limited to bi-dimensional observation planes. Laser Doppler velocimetry can achieve high spatial and temporal resolution but it is a point measurement technique and it is time consuming to fully resolve the 3D velocity field in a large domain such as the human aortic phantom. Recently, Gallo et al. [130] demonstrated that 3D particle tracking velocimetry (PTV) is very suitable for studying complex unsteady flows as in aorta and for validating computational models of aortic hemodynamics.

Finally, phantoms are employed to evaluate new stent-graft design. With the continuous development of new stent grafts and implantation techniques, it has now become technically feasible to treat AAAs with challenging anatomy using EVAR. It is essential to evaluate new stent designs before in vivo testing and in vitro experimentations are very useful to improve the stent-graft design. AAA replicas can help improving surgical planning or training by practicing in the laboratory before the surgery in the operating room. They also could help to understand the limitation of endovascular approaches in those challenging AAA anatomies. For instance, 3D replicas of AAA with complex neck morphology has been tested as an aide to decision making and device delivery [108,131] and also to test whether catheters and stents could be tested in such models [132].

2.5.3 Conclusions

During the last decade a considerable progress has been carried out by numerous researchers with respect to the manufacturing process of AAA phantoms. Nowadays, manufacturing AAA phantoms with isotropic hyperelastic mechanical properties and uniform wall thickness is possible, and even including the ILT to obtain more realistic replicas.

These patient-specific AAA replicas have been proved to be very useful for several applications. However due to the cost and time consuming for the manufacturing process, few experimental studies have been carried out. Creating replicas with a more realistic behavior and

reducing fabrication costs will have a positive impact on various clinical applications such as:

- The validation of numerical studies, medical image-based models and inverse characterization methods.
- In-vitro experiments (as an alternative to computational modeling) for studying overall aneurysm mechanics during blood flow dynamics or for predicting its risk of rupture.
- Pre-clinical testing of endovascular grafts where more realistic in vitro models are needed.
- Experimental assessment of new or existing designs of catheter devices in terms of trackability forces, rigidity of catheter guides and deployment of stent grafts.
- Benchtop testing of endovascular grafts for the detection of endoleaks type III.

2.6 Biomechanical factors influencing the AAA wall stress distribution

It has been demonstrated that the wall stress distribution along the AAA has an important effect on its rupture. In this subsection the effect on the AAA wall stress of different features will be discussed.

2.6.1 Geometry

The mechanics of the AAA wall and the resulting distribution of wall stress are influenced by the individual shape of the aneurysmal aorta. Hence, parameters like asymmetry, wall thickness, and tortuosity should be considered.

Vorp et al. [133] generated 3D computer models of AAA varying the asymmetry with the maximum diameter held constant. The factor of asymmetry ß measures the ratio of the maximum posterior radius (r_p) to the maximum anterior radius (r_a) (Figure 2-14), with ß=1 indicating axisymmetric model. Five models were constructed varying ß and were analyzed with FEA. The results indicated that the asymmetry has a substantial influence on the distribution of wall stress within the

aneurysm, with higher stress values when the asymmetry increases (ß decreases).
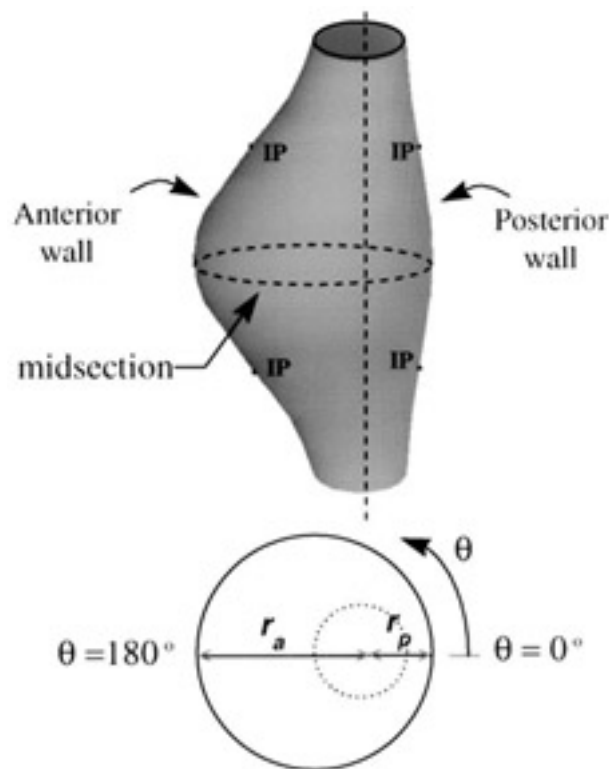
Figure 2-14 Representative 3D virtual AAA model (top) and midesectional cross section (bottom) [133].

A similar study with similar findings was carried out by Rodriguez et al. [134]. They also modeled 3D AAA models with different degrees of asymmetry and their results indicated that for AAAs with the same diameter and relative length, the PWS increases significantly as the aneurysm becomes more asymmetric.

The individual nonuniformity of the wall thickness is another factor of significant importance in the AAA rupture risk prediction. The pathological state of the abdominal aorta results in an overall thicker and weaker wall [49], however, Raghavan et al. [52] observed that AAA rupture occurs at thin regions of the wall, and this is due to local wall mechanics. Previously, in 1993 Mower et al. [135] had

demonstrated that wall thickness is a major parameter influencing wall stress distribution compared to aneurysm maximum diameter alone. More recently, Raut et al. [136] demonstrated (in 28 patient-specific AAA models) that the use of any uniform wall thickness model compared to a patient-specific regionally varying wall thickness results in significantly different biomechanical parameters. Therefore when estimating peak biomechanical parameters, such as stress, it is recommended to use the patient-specific regionally varying wall thickness.

Tortuosity is another geometric parameter that has been demonstrated to be important in the AAA wall mechanics. Tortuosity is expressed as the fractional increase in length of a tortuous vessel in relation to a imaginary straight line (Figure 2-15).
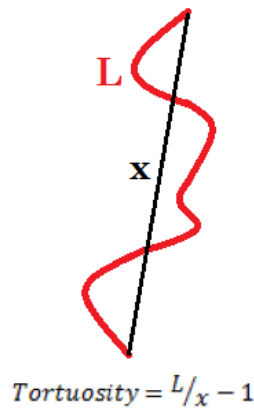
$$Tortuosity = {L}/{x} - 1$$

Figure 2-15 Tortuosity definition.

In 2004 Fillinger et al. [137] suggested that ruptured AAAs had less tortuous anatomy than unruptured. However, more recently Georgarakos et al. [138] observed in 19 patients that the degree of centerline tortuosity correlated significantly and positively with the PWS. Therefore it is still not clear how tortuosity affects AAA rupture.

The mean centerline curvature is another geometrical factor whose influence on the AAA wall stress has been studied by Giannoglou et al. [139]. This group studied 39 patients and surprisingly they did not find a correlation of maximum diameter with PWS. However, their results revealed that the mean centerline curvature of the AAA was a

significant predictor of PWS. Related also with the curvature, it was observed that the maximum stress is located at the inflection point where the aneurysm curvature changes from concave to convex [57]. Moreover it was observed that the location of maximum stress at the posterior wall seems to coincide with peaks in the magnitude of the gaussian curvature [140].

2.6.2 Material Model

An accurate and reliable stress analysis of AAA apart from an accurate 3D description of the aneurysm, it requires an appropriate constitutive law for the material.

Most of the earlier studies on AAA have relied on isotropic models [56,57,60,89,93,94,100] assuming incompressible behavior for the arterial wall. However, the anisotropy found in the AAA tissue [50,68,73,141] is an important property that was not considered in these projects. Considering the anisotropy in FEA models, commonly derives in higher PWS in comparison with isotropic wall models [86,142,143].

2.6.3 Influence of initial AAA configuration

Most computational AAA geometries used for FEA are commonly generated from multiple CT images acquired at one instant (gated) or multiple instants within the cardiac cycle, and therefore these geometries do not correspond to the geometry in the unloaded state. Applying a physiological pressure to the pre-deformed geometry may have a significant effect on the wall stress distribution and therefore it must be taken into account. To this end several studies have proposed algorithms to derive the zero stress configuration [144–146]. Ideally, the physiological pressure conditions should be applied to the unloaded geometry or zero pressure geometry to get physiological stress results.

The effect of considering the initial configuration on the FEA has contradictory results in the literature. While Lu et al. [144] concluded that conventional approach over-predicts the stress, de Putter et al. [147] and Speelman et al. [148] concluded that not accounting for the

zero pressure configuration may lead to an underestimation of the maximum PWS. Gee et al. [149] also found that not considering the initial stress overestimates the displacements and yields to unrealistic large deformations.

2.6.4 Residual stress

Residual stresses are also characteristic of vascular tissues. They can be estimated globally by using the opening angle of an artery [150] or numerically predicted [151]. The effect on the arterial wall is that the inner part of the wall is compressed, whereas the outer part is tensioned. This stress distribution under internal pressure load causes the resultant stress distribution to be roughly homogeneous across the arterial wall, thus neglecting it in the load-free configuration typically leads to significant stress gradients across the wall thickness. The peak stress values are similar, however, if residual stresses are taken into account, the maximal circumferential stress does not appear near the lumen but instead in the media and subjected to higher stresses [150,152].
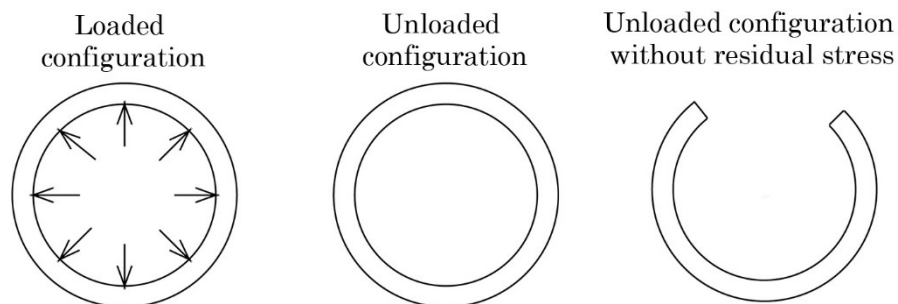
Figure 2-16 Initial configuration of an AAA slice: scanned geometry (left), zero pressure geometry (middle) and residual stress free (right).

2.6.5 Intraluminal thrombus

A common feature in most AAAs is the presence of ILT. From a biomechanics perspective, the relation of the ILT development with the aneurysm rupture is still not clearly understood.

First, it is thought that ILT varies the strength of the tissue. Some studies have suggested that in the AAA wall covered by ILT there is a

degradation of the extracellular matrix due to the hypoxia, making the wall weaker [153]. Also, the AAA wall covered by a thick ILT is thinner and has an increased number of inflammatory cells and smooth muscle cell apoptosis [87].

Apart from these consequences the ILT itself influences mechanical stress of the underlying vessel wall. Various studies have demonstrated that the ILT reduces the wall stress distribution and PWS [84,154,155]. In contrast, other researchers have concluded that the ILT may not reduce wall stress, as it does not reduce both the mean and the pulse pressure near the aneurysmal wall [156,157]. In a more recent study, Polzer et al. [158] found that ILT fissures increase the stress in the underlying wall, whereas other regions remain unaffected.

2.6.6 Calcifications

Most of AAAs exhibit localized calcifications in the media, which have been taken into consideration recently for simulations of AAA biomechanics. However, there are still conflicting reports on whether the presence of calcification increases [159] or decreases [89] wall stress.

2.6.7 Effect of blood flow

Most of the researches analyzing the AAA wall stress distribution have been carried out by applying a uniform pressure on the inner surface of the aneurysm sac, i.e. a computational solid stress - static analysis (CSSs). However, it should be mentioned that this approach does not account for the hemodynamics of the blood flow through the aneurysm and the compliant nature of the AAA wall. To consider the time varying pressure load instead of the steady state load, other researchers followed the computational solid stress, but with a transient analysis (CSSt). Yet, in these cases the pressure load is spatially uniform, while the physiologic intraluminal pressure is spatially nonuniform. Furthermore, this approach disregards the effect of hemodynamics and interaction between the pulsatile blood flow and the compliant arterial wall. To this end, some researchers have carried out *fully coupled* fluid-structure interaction (FSI*)*

analysis in order to study the aneurysmatic fluid-mechanics by accounting both for the instantaneous fluid forces acting on the wall and the effects of the wall motion on the fluid dynamic field.

Although the isolated static structural stress analysis approach captures the gross features of the stress distribution, the results derived from CSSs or CSSt techniques compared to FSI*f* approach, underestimate the PWS on average by 20%-30% for AAAs with variable wall thickness and 10% for uniform wall thickness AAAs [160–162]. The main drawback of the FSI*f* approach is the high computational cost and therefore a partially coupled FSI (FSI*l*) was followed by other researchers [163,164]. Scotti and Finol [160] compared a partially coupled FSI (FSI*l*) with FSI*f* analysis finding differences up to 6.5% in wall stress.

2.7 Conclusions

This chapter summarizes the most important knowledge areas to get the main objective of this research project. Several conclusions can be drawn:

- The AAA diameter is the main parameter used in clinical practice to decide whether a patient should be operated or not. However, diameter criterion is not precise for all the cases, and numerical studies have proved that wall stress has a big impact on the AAA rupture. As the wall stress depends primarily on the patient-specific AAA geometry, various geometrical parameters have been analyzed in the literature, but still there are parameters to be studied that can improve the accuracy of the AAA rupture estimation.
- Due to the time consuming and high cost of manufacturing AAA phantoms, few experimental studies have been carried out in the literature. With the current methodologies proposed for manufacturing AAA replicas, it is possible to create AAA phantoms with uniform wall thickness, isotropic wall properties and inclusion of ILT. However, it has been demonstrated the importance of variable wall thickness and anisotropy on the AAA wall stress

distribution, and therefore more realistic AAA replicas would be of interest for experimental studies.

- The AAA wall stress distribution has been proved to have an impact on the AAA rupture. Due to difficulties of physical experiments, FEA is employed to calculate the AAA wall stress distribution. Although FEA represents an important step, numerical studies must be validated before clinical implementation. Despite the importance of these experimental studies, there is no study that verifies the stress distribution along the entire AAA wall.

Chapter 3

Influence of local curvature on synthetic AAA geometries

3.1 Introduction

Although the maximum diameter criterion is still the most important factor when predicting risk of rupture of AAAs, other parameters should be considered from a purely biomechanical point of view.

Aneurysm rupture occurs when the local stress in the arterial wall exceeds the maximum local strength of the tissue, indicating that the relationship between localized tissue strength and stress should be considered for rupture risk assessment. Although wall stress in AAA walls have been linked to a high risk of aneurysm rupture, yet computing AAA wall stress is still an uncommon clinical practice. Several studies [56,57] have demonstrated that Peak Wall Stress (PWS), predicted by a Finite Element Analysis (FEA), is significantly

higher in symptomatic/ruptured AAAs than in unruptured AAAs. Recently, Doyle et al. [96] showed how the rupture location of a patient-specific AAA can be predicted from high wall stress regions. However, rupture points do not always coincide with the PWS regions [95] because wall stress alone is not sufficient to predict rupture risk and, therefore, regional estimations of wall strength and the parameters that rule the stress distribution such as, maximum diameter, wall thickness, tortuosity and asymmetry, are also necessary [46].

In this chapter the local mean curvature (LMC), in addition to local wall thickness (LWT) is computed from synthetic AAA geometries and the relationship of these metrics with AAA wall stress is assessed. Such assessment can be envisioned as the equivalent of providing geometric surrogates of wall stress, which could be used in future efforts for the development of a computational tool for AAA rupture risk assessment based on individual metrics of AAA geometry. Two studies have been carried out. In the first study (section 3.3) the maximum diameter and uniform wall thickness of the AAA geometries are set to constant, while in the second study (section 3.4) the analysis is made varying these two geometry metrics. First, in section 3.2 the principal curvatures are briefly described.

3.2 Principal curvatures

Consider a surface S defined by the function $z = f(x, y)$ and a point P on the surface S (Figure 3-1). Assume that N is the normal vector to the surface S that passes through the point P; and v a unit vector tangential to the surface S that passes through the point P. Let c be the parameterized curve given by slicing S through the plane spanned by v and N (plane π).
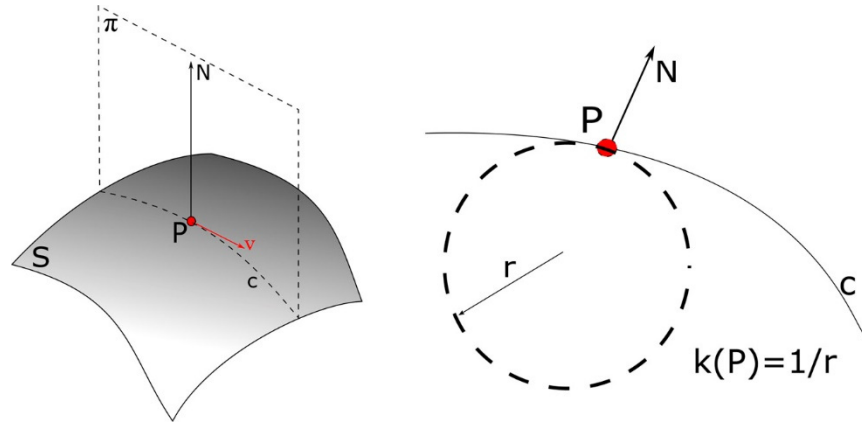
Figure 3-1 Curvature of surface S for a specific point P.

Being c a plane curve, c has a signed curvature k at point P with respect to the unit normal N. The curvature k is the inverse of the radius of the osculating circle to curve c at point P. The curvature k depends on the direction of the tangential vector v. When the directional vector v changes, so does the the curvature k at point P. The principal curvatures of the surface at P (k_1 and k_2) are the largest and smallest possible values of curvature at point P. Positive values for the principal curvatures indicate convex regions, whereas negative values indicate concave regions.

More rigorously, the curve c can be defined as:

$$c(t) = (v_1 t, v_2 t, f(v_1 t, v_2 t)) \tag{3-1}$$

and the curvature k is defined by Equation 3-2

$$c''(s)|_{s=0} = kN(P) \tag{3-2}$$

where $s = s(t)$ represents arc length with $s(0) = 0$ (i.e., $s(t) = \int_0^t |c'(t)| dt$). It can be demonstrated that $c''(s)|_{s=0}$ can be replaced with $c''(t)|_{t=0}$ without loss of generality. Finally using Equation 3-2 it can be obtained Equation 3-3

$$k = f_{xx}(0,0)v_1^2 + 2f_{xy}(0,0)v_1 v_2 + f_{yy}(0,0)v_2^2 \tag{3-3}$$

where f_{xx}, etc. are the partial derivatives of f. Equation 3-3 can be defined in the matrix form with the Hessian matrix as

$$k = \begin{bmatrix} v_1 & v_2 \end{bmatrix} \begin{bmatrix} f_{xx}(0,0) & f_{xy}(0,0) \\ f_{xy}(0,0) & f_{yy}(0,0) \end{bmatrix} \begin{bmatrix} v_1 \\ v_2 \end{bmatrix} \tag{3-4}$$

From linear algebra, the largest and smallest values of curvature (principal curvatures) are the eigenvalues (λ_1 and λ_2) of the Hessian matrix. Since the Hessian matrix is symmetric, the eigenvalues are real and the eigenvectos are orthogonal.

3.3 First study

In this study, seven different AAA geometries with uniform wall thickness and the same maximum diameter are analyzed. First, the synthetic AAA geometries are modelled and simulated with FEA. Subsequently, results are statistically analyzed.

3.3.1 AAA geometry definition and geometry quantification

In this section in order to analyze whether the curvature has a high impact on the AAA wall stress, seven different geometries that replicate an aneurysm in the abdominal aorta are designed with PTC Creo 3.0 (PTC Corporate Headquarters, Needham, USA). They are illustrated in Figure 3-2. Obviously, none of the geometries are equal to a patient-specific AAA geometry, however, the curvature values can be found in regions of patient-specific AAAs. In all the cases, the maximum diameter is set to 40 mm, while the thickness is 1.5 mm throughout the whole aneurysm. The length of the aneurysm is different for each geometry in order to obtain different curvatures along the AAA.
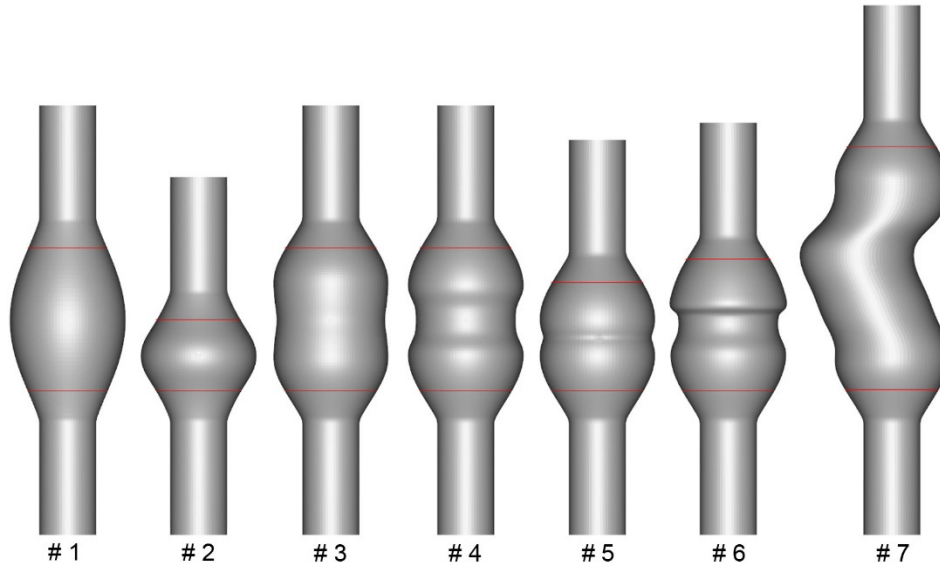
Figure 3-2 Seven different synthetic AAA geometries generated in PTC Creo.

To calculate the geometric indexes, the geometries are exported in the form of stereolitography (.stl) files. An open-source code written in MATLAB (MathWorks, Natick, USA) is used to determine the principal curvatures (k_1 and k_2) [165]. The local mean curvature (LMC) is derived from the principal curvatures as indicated in Equation 3-5.

$$LMC = (k_1 + k_2)/2 \qquad (3\text{-}5)$$

3.3.2 Finite Element Analysis

The geometries are imported to Abaqus (Dassault Systems, Vélizy-Villacoublay, France) and meshed with tetrahedral elements. For each geometry, a mesh independence study is performed so as to select the correct element size in order to balance computer simulation time and result accuracy. The AAA wall is assumed to be hyperelastic, incompressible and defined by an isotropic constitutive material proposed previously by Raghavan and Vorp [55], where the strain energy density function is defined by Equation 3-6

$$W = \alpha(I_1 - 3) + \beta(I_1 - 3)^2 \qquad (3\text{-}6)$$

where I_1 is the first invariant of the left Cauchy-Green tensor and α and β are the material coefficients. The material coefficients were quantified from uniaxial tensile experiments with 69 human AAA specimens ($\alpha = 174$ kPa and $\beta = 1,881$ kPa) [55] and are assumed to be the same for all models. These geometric (thickness) and material parameters (α and β) are fixed for all cases in order to keep them from influencing the results.

The proximal and distal ends of the abdominal aorta are considered to be fixed in order to replicate anatomical tethering of the aorta, while the loading condition is established by applying the uniform pressures of 80 and 140 mmHg to the inner wall of the virtual artery. The Von Mises, circumferential and axial stresses are obtained as the primary outcomes from the FEA simulations (Figure 3-3). All simulations are run on a computer with an Intel Xeon 2.67 GHz processor, with 6 GB RAM, and running Windows 7 64-bit.
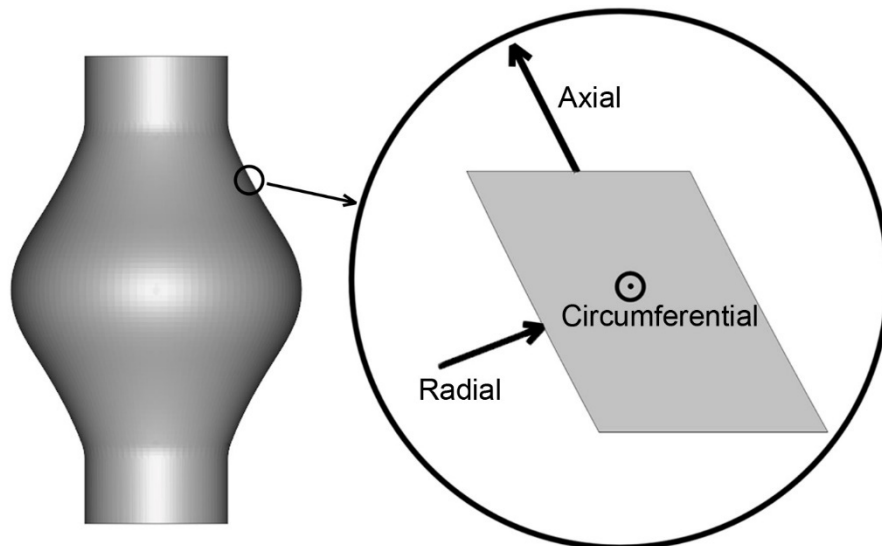
Figure 3-3 Stress directions (axial and circumferential) for each element.

The LMC distribution and stress distribution of the specimens are illustrated in the Appendix A. As an example, the distributions in geometry #4 are illustrated in Figure 3-4.
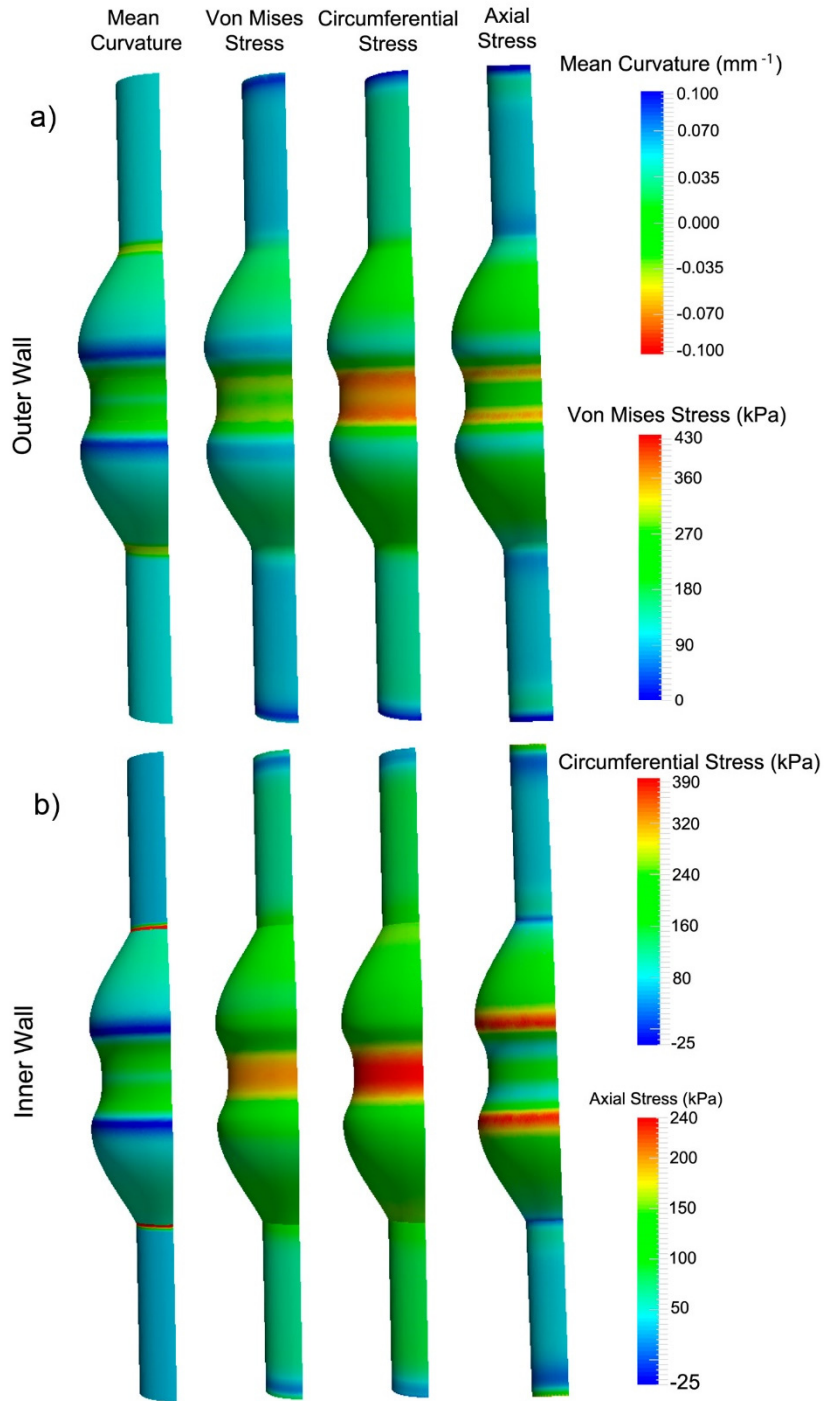
Figure 3-4 Mean Curvature and stress distribution of the a) outer and b) inner wall of geometry #4.

3.3.3 Statistical Analysis

A correlation analysis is carried out using the statistical software Minitab v17 (Minitab Inc., Pennsylvania, USA). For each AAA geometry, two correlation studies are run: the first only considers the outer wall and the second only considers the inner wall. In both studies a Pearson's correlation coefficient and a p-value with a 95% confidence level are obtained. For each study, a sample of 200 random points placed on the corresponding sac surface (outer or inner) of the aneurysm is selected. This number of points is selected as increasing this number does not change the Pearson´s correlation values. The LMC values for these points are calculated in MATLAB, while the corresponding stress values are derived from FEA simulations with Abaqus.

The Pearson's correlation r value and the p-value for each geometry are shown in Table 3-1, while graphic results for some of the geometries are illustrated in Figure 3-5.

Table 3-1: Pearson's correlation and p-values of the LMC with wall stresses for the synthetic AAAs.

Correlation coefficients for wall stresses at the outer wall surface					
AAA	Von Mises		Circumferential		Axial	
No	Pearson's r	p-value	Pearson's r	p-value	Pearson's r	p-value
1	0.423	<0.001	0.283	<0.001	0.821	<0.001
2	-0.995	<0.001	-0.994	<0.001	-0.981	<0.001
3	-0.955	<0.001	-0.950	<0.001	-0.928	<0.001
4	-0.932	<0.001	-0.926	<0.001	-0.981	<0.001
5	-0.854	<0.001	-0.804	<0.001	-0.919	<0.001
6	-0.749	<0.001	-0.737	<0.001	-0.928	<0.001
7	-0.964	<0.001	-0.937	<0.001	-0.751	<0.001
Correlation coefficients for wall stresses at the inner wall surface					
AAA	Von Mises		Circumferential		Axial	
No	Pearson's r	p-value	Pearson's r	p-value	Pearson's r	p-value
1	-0.058	0.412	-0.452	<0.001	0.725	<0.001
2	0.048	0.501	-0.919	<0.001	0.992	<0.001
3	-0.744	<0.001	-0.818	<0.001	0.709	<0.001
4	-0.426	<0.001	-0.587	<0.001	0.921	<0.001
5	-0.439	<0.001	-0.243	<0.001	0.884	<0.001
6	0.043	0.553	-0.257	<0.001	0.885	<0.001
7	-0.593	<0.001	-0.701	<0.001	0.686	<0.001
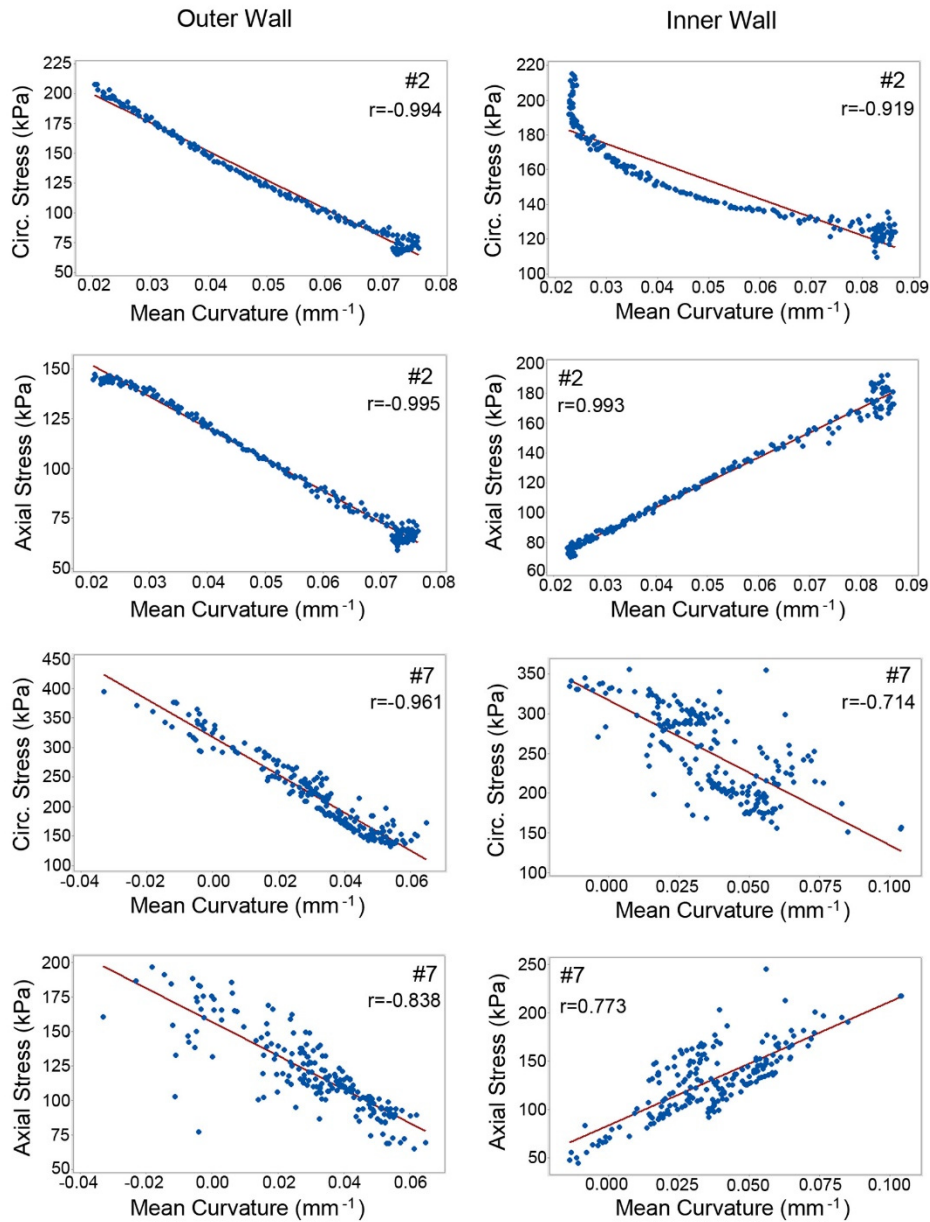
Figure 3-5 Graphic results of the correlation analysis between the circumferential-axial stress and the MC for geometries #2 and #7.

According to those results, in the outer wall the circumferential and the axial stress distributions are negatively correlated with the LMC (r=-0.727 and r=-0.702, respectively). Consequently, the Von Mises stress distribution is negatively correlated with the LMC (r=-0.718).

However, in the inner wall the negative correlation between the LMC and the circumferential stress is lower (r=-0.570) and the axial stress distribution is positively correlated with the LMC (r=0.881). Therefore it cannot be stated that the Von Mises stress is negatively correlated with the LMC as a general rule.

An exception must be pointed out for geometry #1, where the correlations are not congruent with the results obtained with the other six geometries. In this geometry the variation in the LMC along the aneurysm sac is very small (<0.005 mm^{-1}, while in other geometries is around 0.1 mm^{-1}), and therefore other geometrical parameters may have more influence on the stress distribution than the LMC. Apart from this exception, the LMC seems to play an important role in the stress distribution, and therefore it may be taken into account together with the diameter.

3.4 Second study

In the first study, the synthetic AAA geometries were modeled with uniform wall thickness and the same maximum diameter. However, it is known that both, wall thickness and maximum diameter, are related with wall stress. Therefore, in this second study the influence of these parameters are also analyzed together with the LMC in order to evaluate whether LMC is significant when the other 2 factors are contributing to the AAA wall stress.

3.4.1 AAA geometry definition and geometry quantification

Four synthetic AAA geometries with three different maximum diameters (MD) each (30, 50 and 70 mm), for a total of twelve specimens, are designed in PTC Creo. It must be noted that when the maximum diameter is increased the length of the aneurysm is also increased. The geometries are designed with variable wall thickness. Variable thickness is set following studies by other researchers [162] in which thickness is inversely proportional to the local diameter, following Equation 3-7:

$$LWT(\emptyset) = T\, d/\emptyset \tag{3-7}$$

where T and d are the undilated thickness (equal to 2 mm) and diameter (equal to 20 mm), $\emptyset$ is the diameter value for each cross section, and $LWT(\emptyset)$ is the corresponding thickness for each cross section. In Figure 3-6 one quarter of some of the geometries are represented with the wall thickness distribution.
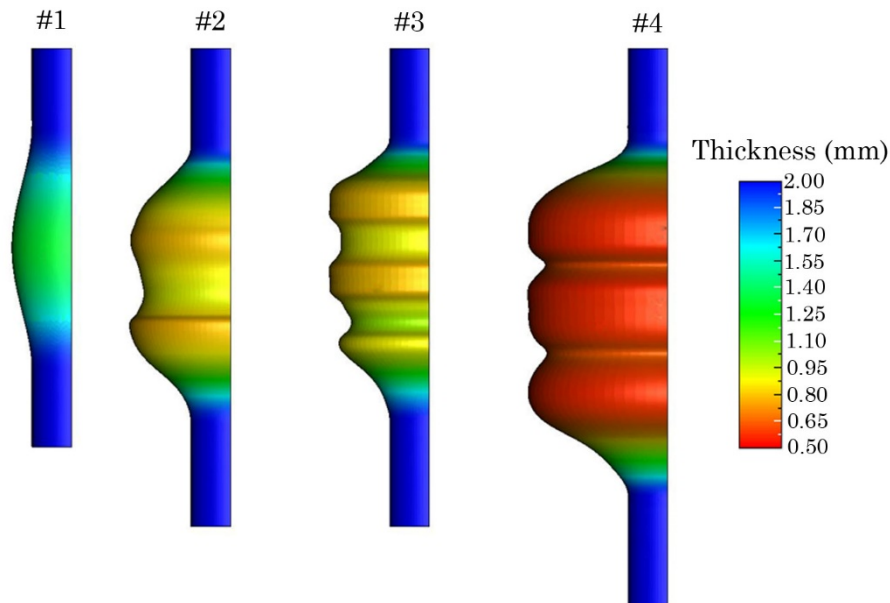
Figure 3-6 Geometries #1 (MD=30 mm), #2 (MD=50 mm), #3 (MD=50 mm) and #4 (MD=70 mm) with the respective wall thickness distribution.

As the geometries are axisymmetric, the local diameter (LD) for each point is calculated using its corresponding coordinates. With the data of the cross sectional diameter, the LWT for each point can be calculated directly with Equation 3-7.

3.4.2 Finite Element Analysis

The geometries are imported again to Abaqus and the same process as in the first study is followed. The same material model and boundary conditions as in the first study are set. The primary outcomes from FEA are also Von Mises, circumferential and axial stress. As an example, the wall stress distribution of some of these geometries is illustrated in Figure 3-7.
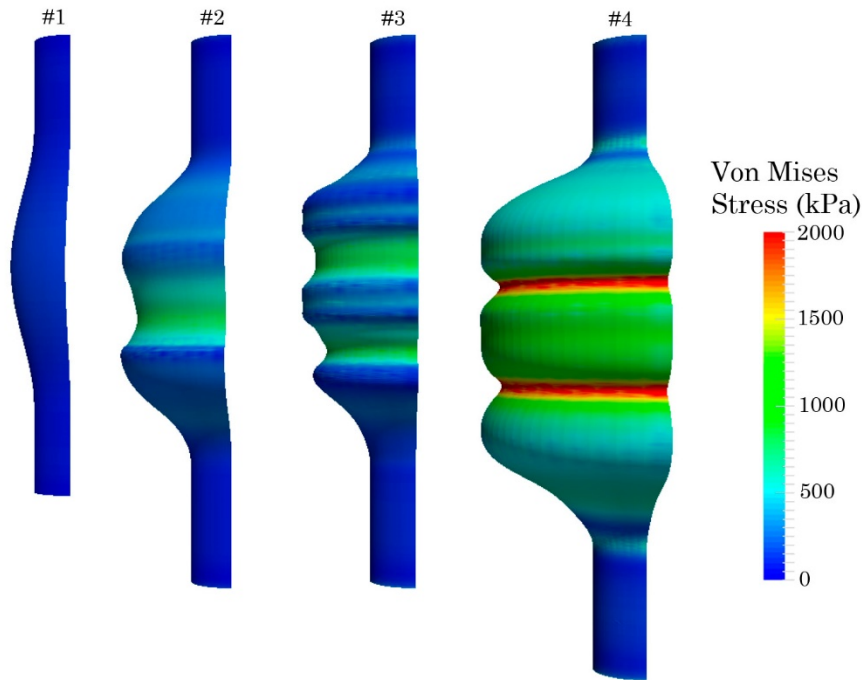
Figure 3-7 Von Mises stress distribution for geometries #1, #2, #3 and #4.

3.4.3 Statistical Analysis

A correlation analysis is carried out with Minitab v17. Again, for each AAA geometry, two correlation studies are run: the first only considers the outer wall and the second only considers the inner wall. In both studies a Pearson's correlation coefficient and a p-value with a 95% confidence level are obtained. For each study, a sample of 500 random points placed on the corresponding sac surface (outer or inner) of the aneurysm is selected. This number of points is selected as increasing this number does not change the Pearson´s correlation values. The LMC values for these points are calculated in MATLAB, while the corresponding stress values are derived from FEA simulations with Abaqus. The LD and LWT are calculated directly with the points' coordinates.

For each geometry, the Pearson's correlation (and p-values) of the geometric indexes and the Von Mises, circumferential and axial stresses are shown in Table 3-2, Table 3-3 and Table 3-4.

As in the first study, on the outer wall surface, LMC appears to be negatively correlated with Von Mises wall stress (in both circumferential and axial direction) except for geometry #1 (as discussed in the previous section, probably due to the small LMC variation along the AAA). The average Pearson's correlation values on the outer wall of the LMC with Von Mises, circumferential and axial stress are -0.383, -0.399 and -0.392 respectively.

On the inner wall there are two cases (geometry #2 with MD equal to 50 and 70 mm) in which the LMC has not statistical significance. For the rest of the geometries the LMC appears to be again negatively correlated with Von Mises wall stress, but with lower Pearson's correlation values (r=-0.077). Similar to the firs study, LMC appears to be negatively correlated with circumferential stress (r=-0.209) and positively correlated with axial stress (r=0.759).

The results of the LD and LWT do not have physical sense, i.e. LD appears to be negatively correlated with wall stress and LWT positively correlated with wall stress. This issue can be due that in the range of study of each AAA, the variation of LD and LWT is not significant and therefore LMC (which in these geometries is negatively correlated with LWT and positively correlated with LD) has a higher effect on wall stress. Figure 3-8 illustrates graphically the correlations between the Von Mises stress and the LMC for the outer and inner wall of geometries #2 MD30, #3 MD50 and #4 MD70.
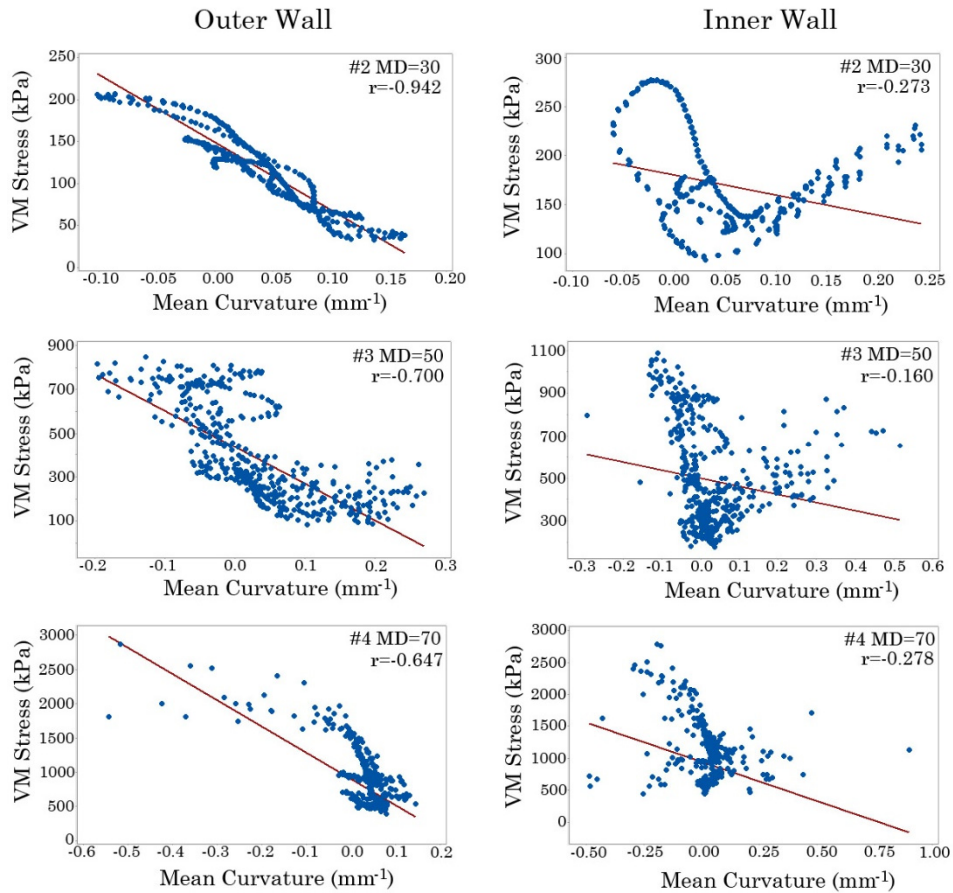
Figure 3-8 Graphic results of the correlation analysis between the Von Mises stress and the MC for geometries #2 MD30, #3 MD50 and #4 MD70.

It can be appreciated in Figure 3-8 that while in the outer wall the correlation between the Von Mises stress and LMC is clearly negative, in the inner wall this is not so clear.

Table 3-2: Pearson's correlation (p-values) of the geometry parameters with Von Mises stress.

AAA	LMC		LD		LWT	
No	Pearson's r	p-value	Pearson's r	p-value	Pearson's r	p-value
Correlation coefficients for Von Mises stresses at the outer surface						
MD=30 mm						
1	0.856	<0.001	0.983	<0.001	-0.992	<0.001
2	-0.942	<0.001	-0.782	<0.001	0.745	<0.001
3	-0.795	<0.001	-0.715	<0.001	0.715	<0.001
4	-0.838	<0.001	-0.930	<0.001	0.933	<0.001
MD=50mm						
1	0.705	<0.001	0.930	<0.001	-0.979	<0.001
2	-0.616	<0.001	0.092	0.039	-0.146	0.001
3	-0.700	<0.001	-0.242	<0.001	0.199	<0.001
4	-0.814	<0.001	-0.247	<0.001	0.180	<0.001
MD=70mm						
1	0.493	<0.001	0.927	<0.001	-0.990	<0.001
2	-0.624	<0.001	0.224	<0.001	-0.292	<0.001
3	-0.679	<0.001	0.240	<0.001	-0.275	<0.001
4	-0.647	<0.001	0.176	<0.001	-0.208	<0.001
Correlation coefficients for Von Mises stresses at the inner surface						
MD=30 mm						
1	0.753	<0.001	0.991	<0.001	-0.997	<0.001
2	-0.273	<0.001	-0.417	<0.001	0.426	<0.001
3	-0.120	<0.001	-0.492	<0.001	0.505	<0.001
4	-0.576	<0.001	-0.854	<0.001	0.865	<0.001
MD=50mm						
1	0.669	<0.001	0.958	<0.001	-0.992	<0.001
2	-0.071	0.112	0.256	<0.001	-0.257	<0.001
3	-0.160	<0.001	0.050	0.268	-0.088	0.049
4	-0.730	<0.001	-0.110	0.014	0.053	0.243
MD=70mm						
1	0.199	<0.001	0.955	<0.001	-0.996	<0.001
2	0.007	0.884	0.384	<0.001	-0.386	<0.001
3	-0.258	<0.001	0.432	<0.001	-0.444	<0.001
4	-0.278	<0.001	0.326	<0.001	-0.344	<0.001

Table 3-3: Pearson's correlation (p-values) of the geometry parameters with circumferential stress.

Correlation coefficients for circumferential stresses at the outer surface						
AAA	LMC		LD		LWT	
No	Pearson's r	p-value	Pearson's r	p-value	Pearson's r	p-value
MD=30 mm						
1	0.851	<0.001	0.980	<0.001	-0.991	<0.001
2	-0.938	<0.001	-0.779	<0.001	0.743	<0.001
3	-0.816	<0.001	-0.715	<0.001	0.716	<0.001
4	-0.842	<0.001	-0.930	<0.001	0.933	<0.001
MD=50mm						
1	0.606	<0.001	0.873	<0.001	-0.943	<0.001
2	-0.590	<0.001	0.054	0.228	-0.107	0.017
3	-0.689	<0.001	-0.250	<0.001	0.207	<0.001
4	-0.804	<0.001	-0.249	<0.001	0.183	<0.001
MD=70mm						
1	0.297	<0.001	0.815	<0.001	-0.932	<0.001
2	-0.625	<0.001	0.141	0.002	-0.213	<0.001
3	-0.638	<0.001	0.213	<0.001	-0.244	<0.001
4	-0.604	<0.001	0.161	<0.001	-0.189	<0.001
Correlation coefficients for circumferential stresses at the inner surface						
AAA	LMC		LD		LWT	
No	Pearson's r	p-value	Pearson's r	p-value	Pearson's r	p-value
MD=30 mm						
1	0.730	<0.001	0.986	<0.001	-0.994	<0.001
2	-0.546	<0.001	-0.602	<0.001	0.596	<0.001
3	-0.224	<0.001	-0.477	<0.001	0.487	<0.001
4	-0.558	<0.001	-0.866	<0.001	0.871	<0.001
MD=50mm						
1	0.447	<0.001	0.849	<0.001	-0.923	<0.001
2	-0.380	<0.001	0.109	0.015	-0.137	0.002
3	-0.372	<0.001	-0.033	0.462	-0.011	0.801
4	-0.746	<0.001	-0.137	0.002	0.073	0.105
MD=70mm						
1	0.081	0.072	0.793	<0.001	-0.915	<0.001
2	-0.193	<0.001	0.173	<0.001	-0.219	<0.001
3	-0.449	<0.001	0.321	<0.001	-0.337	<0.001
4	-0.296	<0.001	0.269	<0.001	-0.286	<0.001

Table 3-4: Pearson's correlation (p-values) of the geometry parameters with axial stress.

AAA No	Correlation coefficients for axial stresses at the outer surface					
	LMC		LD		LWT	
	Pearson's r	p-value	Pearson's r	p-value	Pearson's r	p-value
	MD=30 mm					
1	0.893	<0.001	0.995	<0.001	-0.999	<0.001
2	-0.846	<0.001	-0.571	<0.001	0.523	<0.001
3	-0.913	<0.001	-0.670	<0.001	0.673	<0.001
4	-0.930	<0.001	-0.797	<0.001	0.809	<0.001
	MD=50mm					
1	0.857	<0.001	0.993	<0.001	-0.998	<0.001
2	-0.695	<0.001	0.365	0.039	-0.432	0.001
3	-0.933	<0.001	-0.239	<0.001	0.211	<0.001
4	-0.942	<0.001	-0.223	<0.001	0.163	<0.001
	MD=70mm					
1	0.673	<0.001	0.933	<0.001	-0.988	<0.001
2	-0.302	<0.001	0.766	<0.001	-0.836	<0.001
3	-0.730	<0.001	0.441	<0.001	-0.473	<0.001
4	-0.851	<0.001	0.223	<0.001	-0.268	<0.001
AAA No	Correlation coefficients for axial stresses at the inner surface					
	LMC		LD		LWT	
	Pearson's r	p-value	Pearson's r	p-value	Pearson's r	p-value
	MD=30 mm					
1	0.860	<0.001	0.996	<0.001	-0.989	<0.001
2	0.964	<0.001	0.848	<0.001	-0.817	<0.001
3	0.864	<0.001	0.796	<0.001	-0.784	<0.001
4	0.913	<0.001	0.901	<0.001	-0.897	<0.001
	MD=50mm					
1	0.860	<0.001	0.999	<0.001	-0.979	<0.001
2	0.826	0.112	0.746	<0.001	-0.699	<0.001
3	0.868	<0.001	0.653	<0.001	-0.614	<0.001
4	0.941	<0.001	0.641	<0.001	-0.581	<0.001
	MD=70mm					
1	0.247	<0.001	0.998	<0.001	-0.966	<0.001
2	0.416	<0.001	0.896	<0.001	-0.851	<0.001
3	0.762	<0.001	0.751	<0.001	-0.701	<0.001
4	0.581	<0.001	0.635	<0.001	-0.595	<0.001

To further evaluate whether these geometric indices can be used as predictors of wall stress, the 500 nodes of each geometry are placed in two groups (one for each wall surface) and a linear regression analysis is carried out for both surfaces. The MD of each AAA geometry is added to the analysis. The response variable is expressed using Equation 3-8,

$$Y = \beta_0 + \sum \beta_i X_i \qquad (3\text{-}8)$$

where Y represents the predicted response (wall stress); X_i denotes the independent parameters (MD [mm], LD [mm], LMC [mm^{-1}] and LWT [mm]); β_0 is the intercept term, which is constant; and β_i are the coefficients of each parameter that quantify their linear effect. The potential correlative relationships of the five geometric indices with wall stress are statistically analyzed at a confidence level of 95%.

For the linear regression analysis based on grouping all AAA inner and outer wall surface nodes (6,000 nodes each surface), Table 3-5 describes the model coefficients along with the coefficients of determination (R^2) of the predictive model for each wall surface. The regression analysis yields that the four geometric indexes are statistically significant ($p < 0.001$) in the inner wall (the linear regression function indicates that AAA wall stress has a significant relationship with the four geometric indices); surprisingly, in the outer wall, LWT does not appear to be statistically significant. The model's coefficients of determination for the outer and inner wall surfaces are 0.690 and 0.605, respectively, indicating that 69.0% and 60.5% of the variation in the local wall stress can be explained by the statistical model. Two additional regression analyses are carried out considering only LMC and MD as independent predictive parameters. The predictability of the new models using only LMC is 14.2% and 5.0% for the outer and inner wall surfaces, respectively, while using only MD is, likewise, 52.3% and 50.8%. Combining both LMC and MD as predictive parameters, the predictability increases to 63.2% and 53.0% respectively, for the outer and inner wall surfaces.

Table 3-5: Coefficients (standard errors in parentheses) of the predictive models and their coefficient of determination for the linear regression analysis expressed by Equation 3-8 taking into account all four geometric indices.

AAA Wall Surface	Coefficients of the independent parameters					R^2
	β_0	β_{MD}	β_{LD}	β_{LMC}	β_{LWT}	
Outer	-292.0	6.5	9.5	-1480.4	-	0.690
Inner	-696.9	6.9	15.0	-703.9	231.8	0.605

3.5 Conclusions

It can be inferred from the results of these studies that the LMC has a relevant effect on the stress distribution. As mentioned, from a mechanical point of view, the AAA rupture occurs when the local stress in the artery wall exceeds the maximum strength of the tissue, thus greater stress values along the wall would increase the risk of rupture. Before adopting this statement for all the cases, a larger number of geometries should be analyzed. Nevertheless, these studies are a first step toward suggesting that adding the LMC to the diameter criterion would help physicians make decisions about whether or not to recommend surgery. It is important to note that this parameter, which may have a significant influence on AAA rupture, could be derived from CT scans.

In both studies some simplifications were made: 1) the thrombus and calcifications, present in 75% of AAAs [166,167] have not been considered; 2) although the AAA tissue presents anisotropic behavior [68,70,73], the isotropic model derived by Raghavan and Vorp [55] was implemented; and 3) the studied geometries are not patient-specific, and thickness was kept constant in the first study in order to keep it from having an influence. Despite these simplifications and the low number of geometries that were analyzed, the results suggest that the LMC may play a relevant role in AAA rupture risk, and in some cases it may even have more influence than diameter alone. To illuminate this point, a representative simple example with two different geometries is analyzed.

Geometries #8 and #9 are designed with PTC Creo 3.0 (Figure 3-9(a)), with a maximum diameter equal to 70 mm and 40 mm, and variable

thickness (Equation 3-7). Considering only the diameter, it could be said that the risk of rupture seems to be higher in geometry #8. However, as Figure 3-9(b) shows, the stress distribution in the second geometry has higher stress values under the same blood pressure (140 mmHg). The peak stress value for the first case is 746.64 kPa, whereas for the second case is 1407.32 kPa. Hence, considering that both geometries have the same tissue strength throughout the entire AAA, the rupture risk would be higher in geometry #9. The latter geometry is also analyzed in Minitab v17 and the outcomes are consistent with previous results showing a significant correlation between LMC and stress.
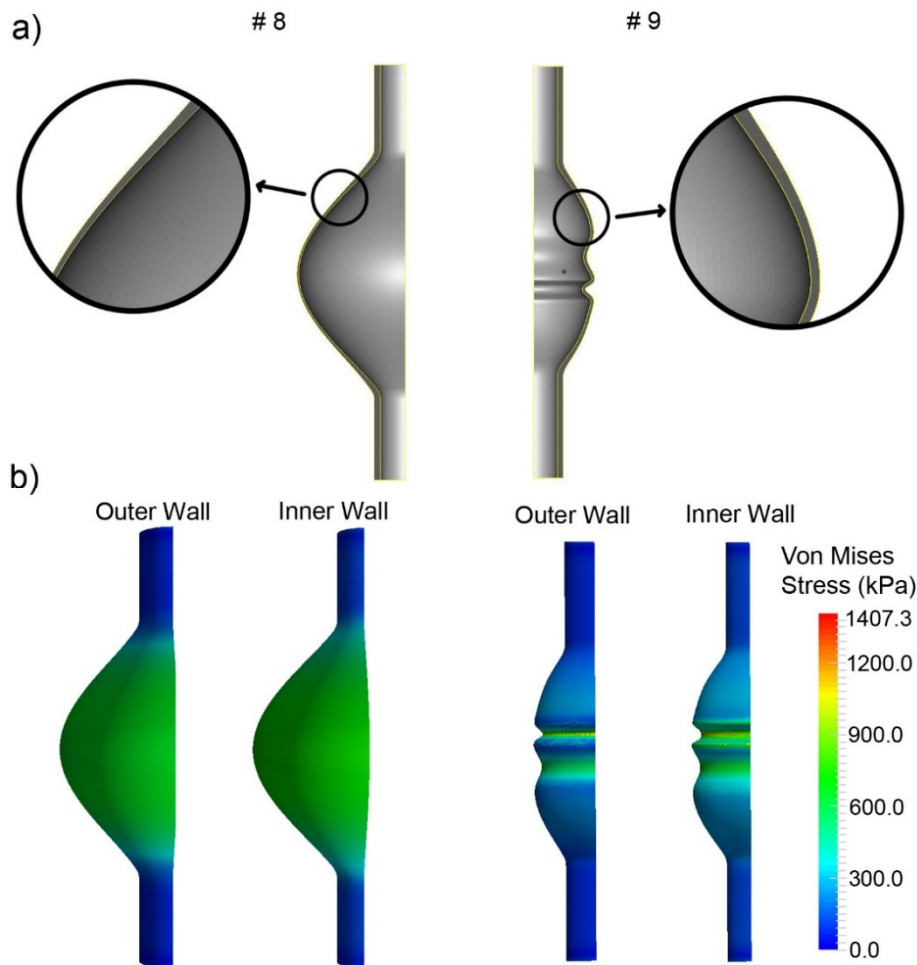
Figure 3-9 (a) Geometries #8 and #9 with variable wall thickness, and (b) stress distribution at 140 mmHg,

These studies are just a first step in the process of including another geometric parameter (LMC) in decisions regarding whether an AAA should be treated. It has been confirmed that there is a significant correlation between LMC and stress in the synthetic AAA geometries, meaning that the LMC may indeed be considered. However more work is still necessary in order to confirm whether these conclusions remain valid when moving to patient-specific geometries. In the next chapter, the LMC will be studied in patient-specific geometries.

Chapter 4

Influence of the local curvature on patient-specific AAA geometries

4.1 Introduction

In Chapter 3, the significant influence of the curvature on the AAA wall stress distribution has been demonstrated. However, this dependence has been only studied in synthetic AAA geometries and it should be verified in patient-specific geometries. To this end, in this chapter 30 AAA patient-specific geometries with different maximum diameters are analyzed.

In this chapter the local mean curvature (LMC) and local Gaussian curvature (LGC), in addition to local wall thickness (LWT) and local cross-sectional diameter (LD) are computed and the relationship of these metrics with AAA wall stress is analyzed. Such assessment can be envisioned as the equivalent of providing geometric surrogates of

wall stress, which could be used in future efforts for the development of a computational tool for AAA rupture risk assessment based on individual metrics of AAA geometry. In section 4.2 the finite element analysis to calculate wall stress is exposed, while in section 4.3 the geometry metrics quantification process is exposed. Finally, in section 4.4 the statistical results are illustrated.

4.2 Finite Element Analysis

Thanks to a collaboration of the University with Dr. Ender Finol, Associate Professor at the University of Texas at San Antonio (UTSA) and Head of the Vascular Biomechanics and Biofluids Laboratory, a set of 30 patient-specific AAA geometries was provided. Briefly, the thirty AAA patient computed tomography angiography (CTA) datasets were acquired retrospectively from existing medical records at Allegheny General Hospital (AGH; Pittsburgh, PA), following approval of the appropriate protocol by the Institutional Review Boards at AGH and UTSA. The CTA images corresponded to the last radiological follow up available prior to a recommendation for interventional treatment. These standard of care images consisted of 3.0 mm slices with an average pixel size of 0.69 mm. The maximum diameter of these AAAs ranged from 30 to 80 mm.
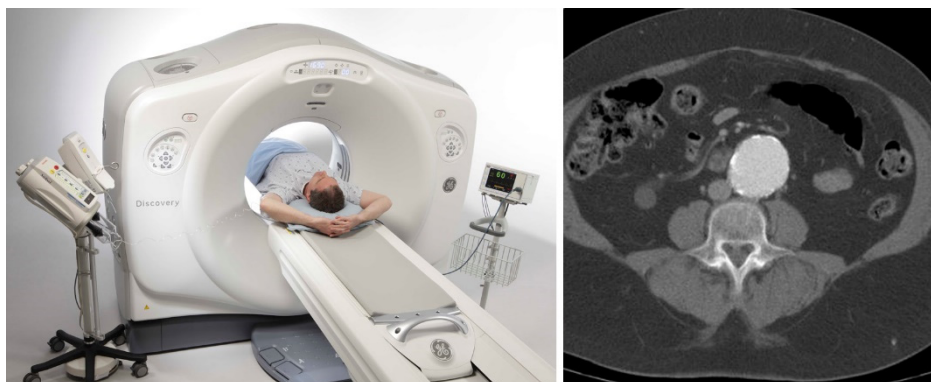
Figure 4-1 Computed tomography angiography scanner (left) [168] and a patient CTA image (right) [169].

Using in-house segmentation and meshing software (AAAVASC, University of Texas at San Antonio [170,171]), the 30 AAA FEA models were generated using quadratic hexahedral elements following the

method and mesh sensitivity analysis described by Raut et al. [172]. One of the important features of this mesh methodology is the ability to model regionally varying wall thickness (Figure 4-2). All this process was carried out by Dr. Finol's group.
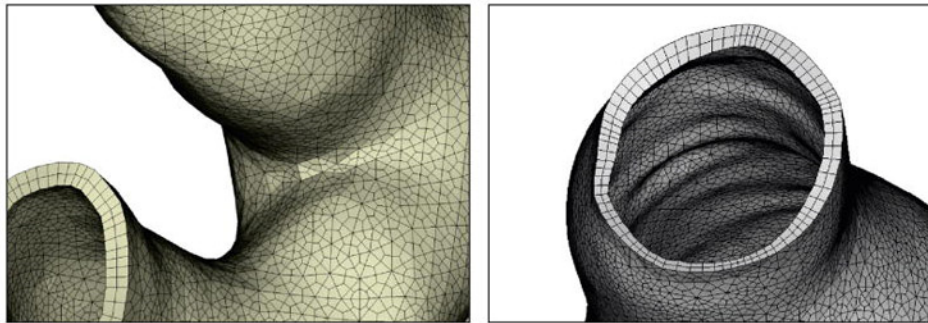
Figure 4-2 AAA hexahedral mesh considering nonuniform wall thickness [172].

The AAA is assumed again to be hyperelastic, incompressible and defined by an isotropic constitutive material proposed previously by Raghavan and Vorp [55] (Equation 3-6) with the same material coefficients ($\alpha = 174$ kPa and $\beta = 1,881$ kPa).

The FEA simulations are performed with the solver ADINA (Adina R&D Inc., Watertown, MA) with an intraluminal loading pressure of 120 mmHg applied in 24 time steps at 5 mmHg intervals. The proximal and distal ends of the abdominal aorta are considered to be fixed in order to replicate anatomical tethering of the aorta. The FE meshes range in size from 90,000 to 200,000 elements, and computational times are in the 4-12 hour range using a Windows workstation with 24 cores and 98 GB of RAM. The first principal stress is the primary outcome of the FEA simulations and used as representative of the AAA wall stress. The Figure 4-3 illustrates the spatial distribution of wall stress obtained as the outcome of FEA simulations completed on three AAAs from the study group. The wall stress distribution of the rest of the geometries is illustrated in the Appendix B.
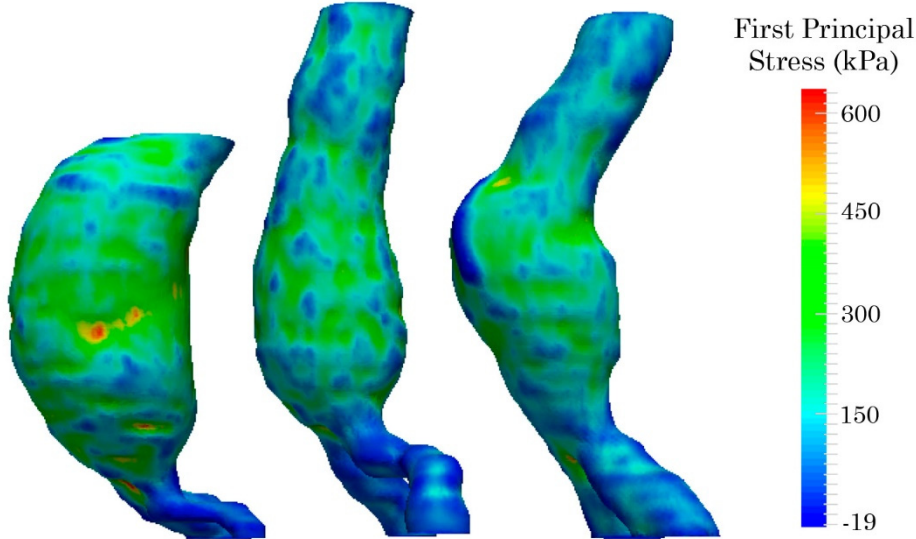
Figure 4-3 Spatial distributions of wall stress computed on the outer wall surface of three exemplary AAA geometries.

4.3 Geometry quantification

To calculate the geometric indices, the pressurized FE meshes are exported in the form of stereolithography (.stl) files. As in Chapter 3, an open-source script written in MATLAB is used to determine the principal curvatures (k_1 and k_2) [165]. The LMC is calculated as shown in Equation 3-5, while the LGC is derived from the principal curvatures according to Equation 4-1. The Figure 4-4 illustrates the spatial distribution of the LMC.

$$LGC = k_1 k_2 \qquad\qquad (4\text{-}1)$$

To calculate the LD for each node of the AAAs, the centerlines are extracted for each AAA using the Vascular Modeling Tool Kit (VMTK) [173], which extracts a centerline as the trace of the maximum inscribed spheres of the vessel surface [174] (Figure 4-5). In this work, the LD is estimated as the diameter of the inscribed spheres and an example for 3 patient-specific geometries is shown in the top frame of Figure 4-6.
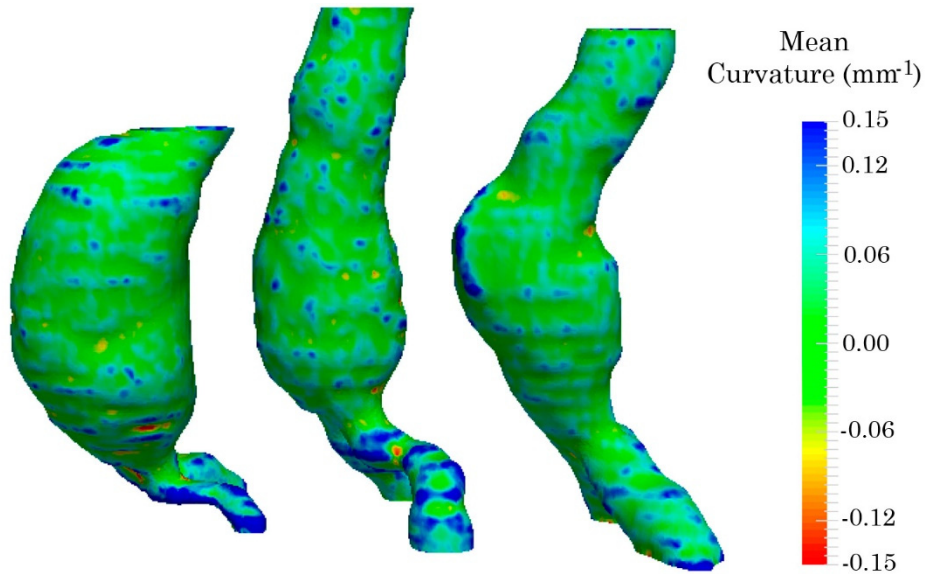
Figure 4-4 Spatial distributions of mean curvature computed on the outer wall surface of three exemplary AAA geometries.
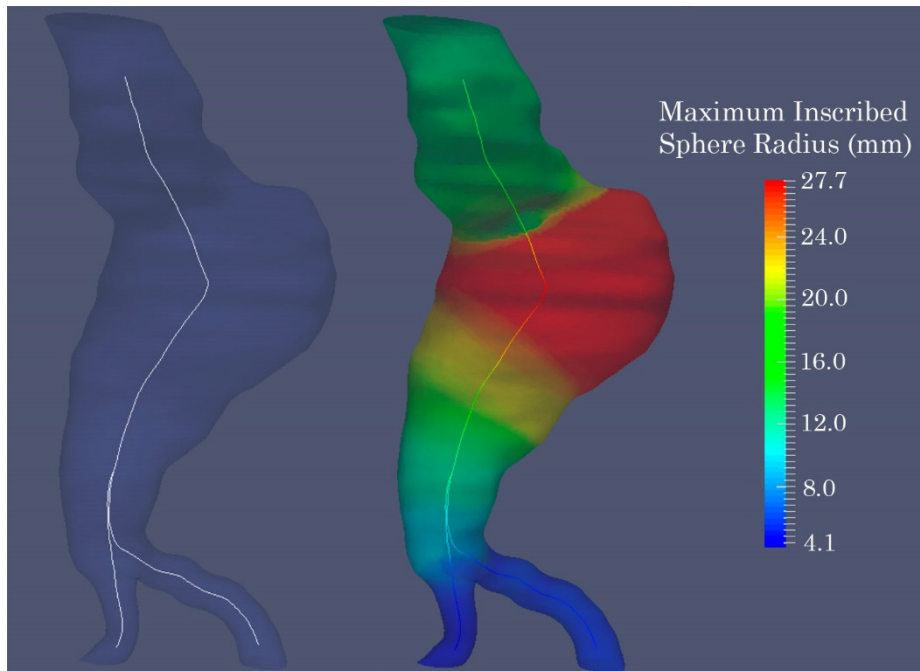
Figure 4-5 Extracted centerline for an exemplary AAA geometry via VMTK.

The last geometric parameter to be calculated for each node is the wall thickness. The LWT is calculated using an in-house script written in

MATLAB. Briefly, the code calculates first the normal for each node of the AAA geometry; then, it finds the triangle of the opposite wall surface where the calculated vector normal crosses; and finally the distance between the node and the cross point is the thickness corresponding to that node. This code is validated in 10 random points with thickness data obtained from MAGICS v19.01 (Materialise, Leuven, Belgium) for the same AAA geometries. The bottom frame of Figure 4-6 illustrates the spatial distribution of LWT.
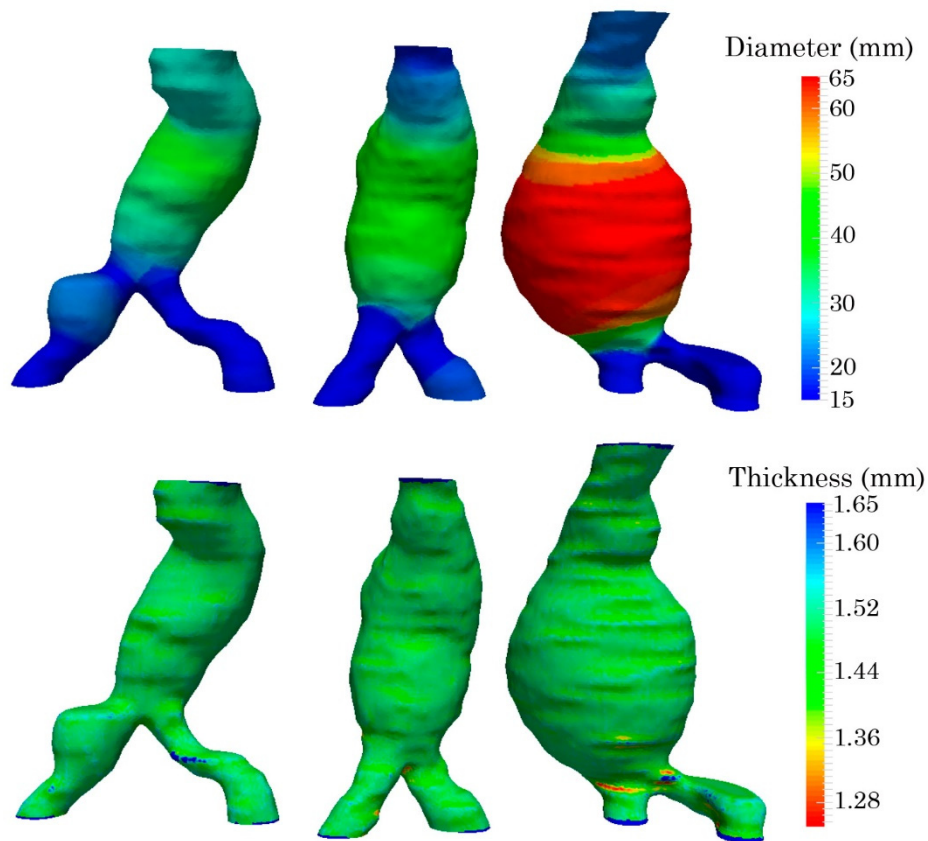
Figure 4-6 Spatial distributions of diameter and local wall thickness (LWT) computed on the outer wall surface of three exemplary AAA geometries.

4.4 Statistical analysis

4.4.1 Individual study

First, a correlation analysis for individual AAAs is carried out. The potential correlations of the geometric indexes (LMC, LGC, LD, and LWT) with wall stress are studied for all AAAs. To this end, a correlation analysis is carried out using the statistical software MINITAB, considering first all the nodes (from the .stl files) that make up the outer wall surface of the AAA sac and then all the nodes from the inner wall surface. Each surface is comprised of approximately 22,000 nodes. In both studies a Pearson's correlation coefficient and a p-value with a 95% confidence level are obtained.

The Pearson's correlation (and p-values) of the geometric indices and wall stresses are shown for each AAA in Table 4-1 for the outer wall and in Table 4-2 for the inner wall surfaces. On the outer wall surface, LMC, LGC and LWT appear to be negatively correlated with wall stress while LD is positively correlated with wall stress: the average Pearson's correlation coefficients for LMC, LGC, LWT and LD are –0.779, –0.417, –0.234, and 0.192, respectively.

Figure 4-7(a) to Figure 4-7(d) illustrate these correlations for all outer wall surface nodes of AAA #9. On the inner wall surface, while LMC and LD are positively correlated with wall stress for all the geometries (the average Pearson's correlations are 0.475 and 0.141, respectively), LWT is negatively correlated with wall stress for all the geometries (the average Pearson's correlation is –0.179) and LGC is positively correlated with wall stress for all but two of the geometries (the average Pearson's correlation for the 28 AAAs where LGC is significant is 0.147). Figure 4-8(a) to Figure 4-8(d) illustrate these correlations for all inner wall surface nodes of AAA #3.

Table 4-1: Pearson's correlation and p-values for independent parameters LMC, LGC, LWT, and LD with wall stress as the dependent parameter for the outer wall surface.

| AAA No. | Correlation coefficients for wall stresses at the outer wall surface | | | | | | | |
| | LMC | | LGC | | LWT | | LD | |
	Pearson's r	p-value	Pearson's r	p-value	Pearson's r	p-value	Pearson's r	p-value
1	-0.815	< 0.001	-0.421	< 0.001	-0.327	< 0.001	0.169	< 0.001
2	-0.787	< 0.001	-0.489	< 0.001	-0.224	< 0.001	0.189	< 0.001
3	-0.794	< 0.001	-0.384	< 0.001	-0.351	< 0.001	0.269	< 0.001
4	-0.738	< 0.001	-0.369	< 0.001	-0.094	< 0.001	0.236	< 0.001
5	-0.829	< 0.001	-0.434	< 0.001	-0.286	< 0.001	0.229	< 0.001
6	-0.740	< 0.001	-0.442	< 0.001	-0.190	< 0.001	0.226	< 0.001
7	-0.804	< 0.001	-0.361	< 0.001	-0.214	< 0.001	0.119	< 0.001
8	-0.706	< 0.001	-0.370	< 0.001	-0.175	< 0.001	0.277	< 0.001
9	-0.817	< 0.001	-0.437	< 0.001	-0.236	< 0.001	0.191	< 0.001
10	-0.738	< 0.001	-0.316	< 0.001	-0.235	< 0.001	0.230	< 0.001
11	-0.740	< 0.001	-0.415	< 0.001	-0.238	< 0.001	0.319	< 0.001

| AAA No. | Correlation coefficients for wall stresses at the outer wall surface | | | | | | | |
| | LMC | | LGC | | LWT | | LD | |
	Pearson's r	p-value	Pearson's r	p-value	Pearson's r	p-value	Pearson's r	p-value
12	-0.812	< 0.001	-0.309	< 0.001	-0.278	< 0.001	0.218	< 0.001
13	-0.779	< 0.001	-0.455	< 0.001	-0.191	< 0.001	0.258	< 0.001
14	-0.702	< 0.001	-0.341	< 0.001	-0.145	< 0.001	0.331	< 0.001
15	-0.794	< 0.001	-0.495	< 0.001	-0.253	< 0.001	0.174	< 0.001
16	-0.794	< 0.001	-0.484	< 0.001	-0.284	< 0.001	0.120	< 0.001
17	-0.731	< 0.001	-0.355	< 0.001	-0.196	< 0.001	0.333	< 0.001
18	-0.798	< 0.001	-0.479	< 0.001	-0.157	< 0.001	0.168	< 0.001
19	-0.804	< 0.001	-0.370	< 0.001	-0.207	< 0.001	0.209	< 0.001
20	-0.796	< 0.001	-0.447	< 0.001	-0.371	< 0.001	0.059	< 0.001
21	-0.726	< 0.001	-0.358	< 0.001	-0.201	< 0.001	0.283	< 0.001
22	-0.805	< 0.001	-0.394	< 0.001	-0.323	< 0.001	0.173	< 0.001

Correlation coefficients for wall stresses at the outer wall surface

AAA No.	LMC		LGC		LWT		LD	
	Pearsons r	p-value	Pearson's r	p-value	Pearson's r	p-value	Pearson's r	p-value
23	-0.782	< 0.001	-0.462	< 0.001	-0.132	< 0.001	0.238	< 0.001
24	-0.815	< 0.001	-0.355	< 0.001	-0.232	< 0.001	-0.070	< 0.001
25	-0.778	< 0.001	-0.403	< 0.001	-0.294	< 0.001	0.113	< 0.001
26	-0.731	< 0.001	-0.416	< 0.001	-0.116	< 0.001	0.169	< 0.001
27	-0.799	< 0.001	-0.501	< 0.001	-0.200	< 0.001	0.216	< 0.001
28	-0.804	< 0.001	-0.380	< 0.001	-0.202	< 0.001	0.188	< 0.001
29	-0.796	< 0.001	-0.504	< 0.001	-0.390	< 0.001	-0.104	< 0.001
30	-0.802	< 0.001	-0.576	< 0.001	-0.285	< 0.001	0.223	< 0.001
Average Pearson's r	-0.779		-0.417		-0.234		0.192	

Table 4-2: Pearson's correlation and p-values for independent parameters LMC, LGC, LWT, and LD with wall stress as the dependent parameter for the inner wall surface.

| AAA No. | Correlation coefficients for wall stresses at the outer wall surface | | | | | | | |
| | LMC | | LGC | | LWT | | LD | |
	Pearson's r	p-value	Pearson's r	p-value	Pearson's r	p-value	Pearson's r	p-value
1	0.666	< 0.001	0.260	< 0.001	-0.248	< 0.001	0.089	< 0.001
2	0.308	< 0.001	0.042	< 0.001	-0.122	< 0.001	0.186	< 0.001
3	0.483	< 0.001	0.182	< 0.001	-0.239	< 0.001	0.188	< 0.001
4	0.586	< 0.001	0.254	< 0.001	-0.085	< 0.001	0.210	< 0.001
5	0.497	< 0.001	0.097	< 0.001	-0.236	< 0.001	0.221	< 0.001
6	0.379	< 0.001	0.092	< 0.001	-0.187	< 0.001	0.208	< 0.001
7	0.722	< 0.001	0.249	< 0.001	-0.282	< 0.001	0.118	< 0.001
8	0.513	< 0.001	0.243	< 0.001	-0.225	< 0.001	0.178	< 0.001
9	0.680	< 0.001	0.338	< 0.001	-0.219	< 0.001	0.147	< 0.001
10	0.577	< 0.001	0.171	< 0.001	-0.252	< 0.001	0.189	< 0.001
11	0.511	< 0.001	0.297	< 0.001	-0.203	< 0.001	0.270	< 0.001

Correlation coefficients for wall stresses at the outer wall surface

AAA No.	LMC		LGC		LWT		LD	
	Pearson's r	p-value	Pearson's r	p-value	Pearson's r	p-value	Pearson's r	p-value
12	0.708	< 0.001	0.294	< 0.001	-0.242	< 0.001	0.206	< 0.001
13	0.392	< 0.001	0.128	< 0.001	-0.155	< 0.001	0.289	< 0.001
14	0.302	< 0.001	0.022	0.001	-0.119	< 0.001	0.215	< 0.001
15	0.285	< 0.001	0.026	< 0.001	-0.167	< 0.001	0.103	< 0.001
16	0.456	< 0.001	0.111	< 0.001	-0.048	< 0.001	0.086	< 0.001
17	0.485	< 0.001	0.162	< 0.001	-0.044	< 0.001	0.292	< 0.001
18	0.316	< 0.001	-0.005	0.545	-0.147	< 0.001	0.098	< 0.001
19	0.653	< 0.001	0.316	< 0.001	-0.199	< 0.001	0.139	< 0.001
20	0.459	< 0.001	0.121	< 0.001	-0.154	< 0.001	-0.067	< 0.001
21	0.507	< 0.001	0.046	< 0.001	-0.048	< 0.001	0.180	< 0.001
22	0.665	< 0.001	0.232	< 0.001	-0.280	< 0.001	0.085	< 0.001

Correlation coefficients for wall stresses at the outer wall surface

AAA No.	LMC		LGC		LWT		LD	
	Pearsons r	p-value	Pearson's r	p-value	Pearson's r	p-value	Pearson's r	p-value
23	0.379	< 0.001	0.102	< 0.001	-0.118	< 0.001	0.229	< 0.001
24	0.426	< 0.001	-0.004	0.711	-0.263	< 0.001	-0.103	< 0.001
25	0.548	< 0.001	0.134	< 0.001	-0.175	< 0.001	0.015	< 0.001
26	0.284	< 0.001	-0.036	< 0.001	-0.211	< 0.001	0.047	< 0.001
27	0.467	< 0.001	0.187	< 0.001	-0.092	< 0.001	0.222	< 0.001
28	0.536	< 0.001	0.107	< 0.001	-0.285	< 0.001	0.061	< 0.001
29	0.156	< 0.001	-0.155	< 0.001	-0.180	< 0.001	-0.170	< 0.001
30	0.307	< 0.001	0.107	< 0.001	-0.134	< 0.001	0.285	< 0.001
Average Pearson's r	0.475		0.147		-0.179		0.141	
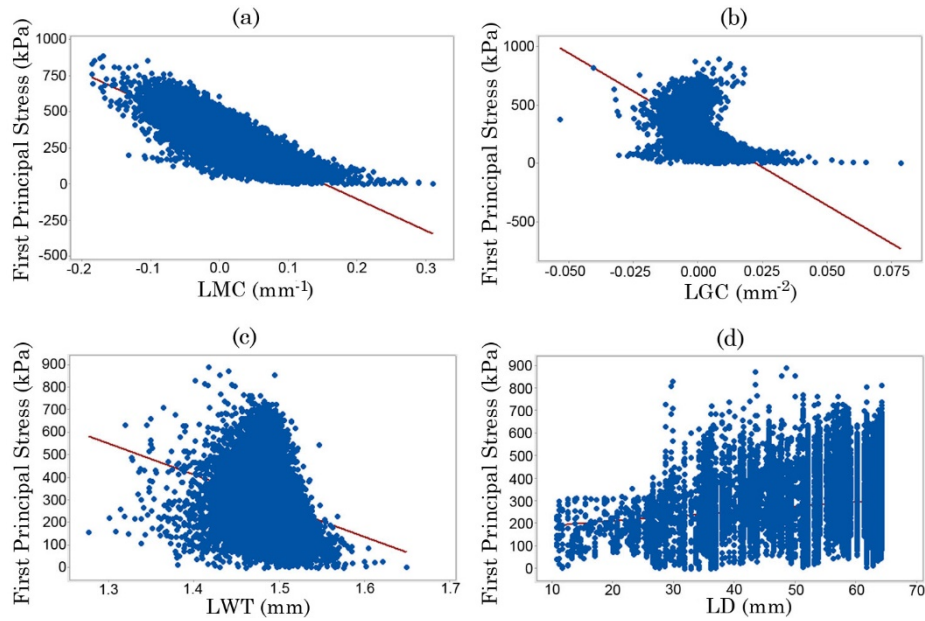
Figure 4-7 Graphical representation of the correlation analyses of wall stress with (a) LMC, (b) LGC, (c) LWT, and (d) LD for the outer wall surface nodes of AAA #9. The Pearson's r correlation coefficients were −0.817, −0.437, −0.236, and 0.191, respectively.
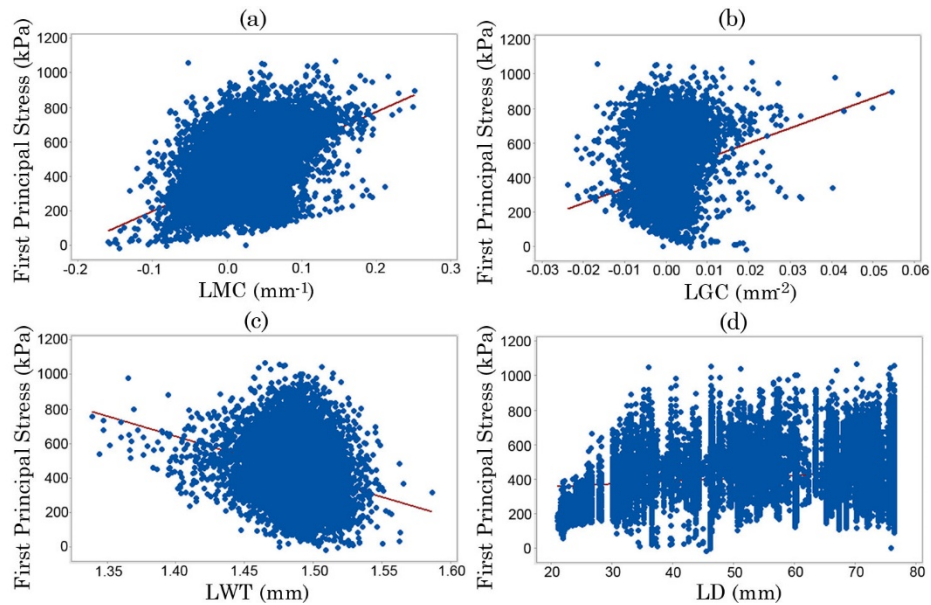
Figure 4-8 Graphical representation of the correlation analyses of wall stress with (a) LMC, (b) LGC, (c) LWT, and (d) LD for the inner wall surface nodes of AAA #3. The Pearson's r correlation coefficients were 0.483, 0.182, −0.239, and 0.188, respectively.

As an example to visualize these results, Figure 4-9 illustrates the wall stress, LMC and LWT distribution in two regions of the outer surface of the geometry #19.

In region #1, five zones are selected. Zones 'a' and 'b' have a peak stress that corresponds to negative values of LMC and low thickness, whereas zone 'c', which has low stress values, matches with high positive curvature and a thick wall. Zones 'd' and 'e' have similar thicknesses, but different mean curvatures. While the zone 'd' has positive curvature, the zone 'e' has negative curvature yielding to a higher wall stress.

In region #2, two zones with similar MC are selected. In this case, the wall in zone 'f' is thinner than in zone 'g', yielding higher wall stresses in zone 'f'. These observations, which are repeated for other regions of the AAA phantoms, are consistent with the results derived from the statistical analyses.
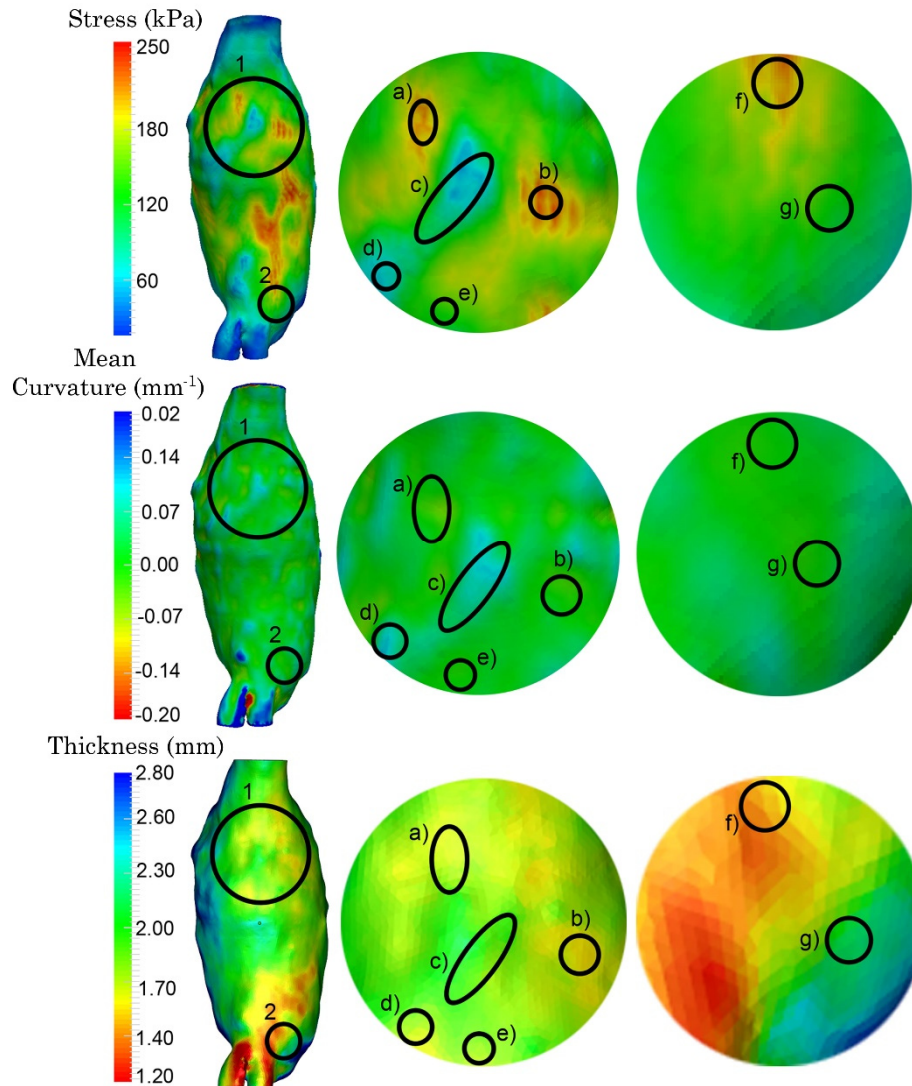
Figure 4-9 Stress, mean curvature and wall thickness distributions for the geometry #19. Regions #1 and #2 enclose seven representative zones (a-g) that explain the statistical results.

4.4.2 Regression analysis for all AAAs

To further evaluate whether these geometric indexes can be used as predictors of wall stress, all the nodes that make up the 30 AAA geometries (approximately 660,000 each for the inner and outer wall surfaces) are placed in two groups (one for each wall surface) and a linear regression analysis is carried out for both surfaces. The

maximum diameter (MD) of each AAA is added to the analysis. The response variable is expressed using Equation 3-8. In this case the independent parameters are MD [mm], LD [mm], LMC [mm^{-1}], LGC [mm^{-2}] and LWT [mm]. The potential correlative relationships of the five geometric indices with wall stress are statistically analyzed at a confidence level of 95%.

The regression analysis yields that the five geometric indices are statistically significant (p < 0.001); the linear regression function indicates that AAA wall stress has a significant relationship with the five geometric indices. Table 4-3 describes the model coefficients along with the coefficients of determination (R^2) of the predictive model for each wall surface. The model's coefficients of determination for the outer and inner wall surfaces are 0.712 and 0.516, respectively, indicating that 71.2% and 51.6% of the variation in the local wall stress can be explained by the statistical model.

Table 4-3: Coefficients (standard errors in parentheses) of the predictive models and their coefficient of determination for the linear regression analysis expressed by Equation 3-8 taking into account all five geometric indices.

AAA Wall Surface	Coefficients of the independent parameters						R^2
	β_0	β_{MD}	β_{LD}	β_{LMC}	β_{LGC}	β_{LWT}	
Outer	-194.8 (5.0)	1.7 (0.01)	2.2 (0.01)	-2233.0 (2.57)	4903.3 (21.30)	197.7 (3.37)	0.712
Inner	32.7 (5.12)	3.3 (0.01)	2.2 (0.01)	1536.4 (3.04)	-6059.8 (24.00)	-34.6 (3.40)	0.516

In order to observe the effect of adding the LMC to predict the wall stress, two additional regression analyses are carried out considering only LMC and MD as independent predictive parameters. The predictability of the new models using only LMC is 47.7% and 12.0% for the outer and inner wall surfaces, respectively, while using only MD is, likewise, 23.5% and 27.7%. Combining both LMC and MD as predictive parameters, the predictability increases to 64.9% and 44.7%, respectively, for the outer and inner wall surfaces.

4.5 Conclusions

This chapter assesses the statistical significance of the relationships of five geometric indexes (LD, MD, LMC, LGC, and LWT) with AAA wall stress using a collection of thirty patient-specific aneurysms reconstructed from CTA images collected retrospectively. Wall stress was estimated using quasi-static FEA simulations at peak systole while the aforementioned geometry metrics were computed using algorithms applied to FE meshes representative of the native AAAs. Statistical analyses were based on correlations of the geometric indices and wall stress for the individual AAA inner and outer wall surfaces, as well as regression analyses inclusive of all AAA wall surfaces.

For the analysis of individual AAAs, it was found that LMC exhibited the highest average correlation coefficient with wall stress compared to the other geometry metrics. Moreover, LWT had a negative correlation with wall stress for both inner and outer wall surfaces, which has an intuitive physical meaning in classical structural mechanics. A remarkable finding was that LD had the lowest average correlation coefficient with wall stress compared to LMC, LGC and LWT. This indicates that local wall thickness and surfaces curvatures (mean and Gaussian) correlate better with wall stress than the local aneurysm diameter alone. The predictability of the regression models for the wall stress estimated at the outer and inner wall surfaces as a function of all the indices was 71.2% and 51.6%, respectively. The present work highlights the importance of computing LMC (a geometric indicator that has been studied scarcely despite its strong statistical correlation with AAA wall mechanics) with the other four geometric indices as predictive of AAA wall stress. These statistical correlations are similar in nature to other predictive correlations based on tortuosity, asymmetry and wall thickness [175].

Noteworthy is that the accuracy of the AAA surface curvatures is likely to be sensitive to the clinical image segmentation protocol. While this work does not specifically quantify such sensitivity, it is important to consider that thresholding-based segmentation methods and subsequent smoothing of the vessel luminal and wall surfaces can result in unrealistic surface curvatures. In addition, local variations in

the mean curvature of blood vessels with complex surfaces, e.g. with sharp changes in concavity and convexity, may not be accurately detected (and, subsequently, segmented) by standard of care 3.0 mm CTA slices. While this represents a limitation of the present work, future improvements in clinical imaging technology and segmentation algorithms are expected to mitigate such shortcomings. Some simplifications were made in the present study, which could limit the findings of the work to other AAA population groups: 1) although AAA tissue exhibits anisotropic behavior [73], the isotropic nonlinear model postulated by Raghavan and Vorp [55] was implemented in the FEA models; 2) thrombus and calcifications are usually present in 75% of AAAs [77,176], but were not included in the FEA models; 3) the initial stresses due to the diastolic pressure acting on the AAA wall during clinical imaging were not considered; and 4) the residual stresses and prestretch conditions [177] were also not modeled.

Despite these limitations, the segmentation and mesh generation algorithms used in this work have been previously validated [170,171] and it is believed the geometric indices are accurately representative of the native, individual AAAs. To this end, LMC was found to be the most statistically significant index for predictability of wall stress, which appears to indicate that LMC should be taken into account to estimate AAA rupture risk. Nevertheless, it is important to quantify additional geometric characteristics that can significantly predict AAA wall stress. It is unlikely that any one of the herein proposed geometric indices alone would be a reliable surrogate for rupture risk. However, by including all the significant geometry metrics and evaluating them in a larger patient cohort, a more accurate predictive model could be derived yielding a rupture risk prediction based on geometric surrogates of wall stress.

Chapter 5

Manufacturing of AAA replicas with isotropic behavior

5.1 Introduction

Several projects have indicated through extensive use of numerical simulations via FEA that the diameter rupture criterion needs to be complemented with AAA wall stress [96,98,178–180], and therefore factors such as geometry and biomechanics must be also considered [181–185]. Nonetheless, these virtual results must be experimentally validated against either data obtained from in-vitro experiments with AAA arteries or against experiments with synthetic-made AAA replicas.

Several studies have been carried out to artificially create phantoms by combining images from medical scanners in order to acquire the geometry with existing manufacturing processes as Additive

Manufacturing (AM) and injection molding in order to obtain the physical replica. The most common technique is the one described by Doyle et al. [186] and used by others [187,188]. This technique, explained in the state of the art, provides isotropic AAA replicas with uniform wall thickness. The materials used in this method are silicones (whose behavior has been studied [189]) with a hyperelastic behavior similar to the AAA behavior. One drawback of this methodology is that for performing the two aluminum molds machining is needed, with the corresponding time and production costs.

The purpose of this chapter is to describe a new modeling and manufacturing process for patient-specific artery replicas with nonuniform wall thickness, with a focus on developing physiologically realistic AAA phantoms. In the section 5.2 the methodology for manufacturing the AAA is described and in section 5.3 the material characterization is exposed.

5.2 Synthetic AAA manufacturing methodology

The vacuum casting technique is chosen as the preferred manufacturing method to build an arterial replica. The process involves pouring liquid polyurethane (PUR) resins under vacuum into a silicon mold that contains a hollow cavity with the desired shape. The mold is previously obtained by taking as a reference a master model printed with an AM technology. The steps for creating the artery replica are illustrated in Figure 5-1.

The patient-specific AAA geometry (provided by Dr. Ender Finol) is obtained from CT images as explained in section 4.2. Once the .stl file of the AAA geometry is obtained, it is manipulated using MAGICS to prepare a virtual model for AM. With MAGICS, the artery is cut along several partition lines, while assuring the correct positioning of each part relative to the other parts with the use of connector pins, to facilitate the vacuum casting process (Figure 5-2).
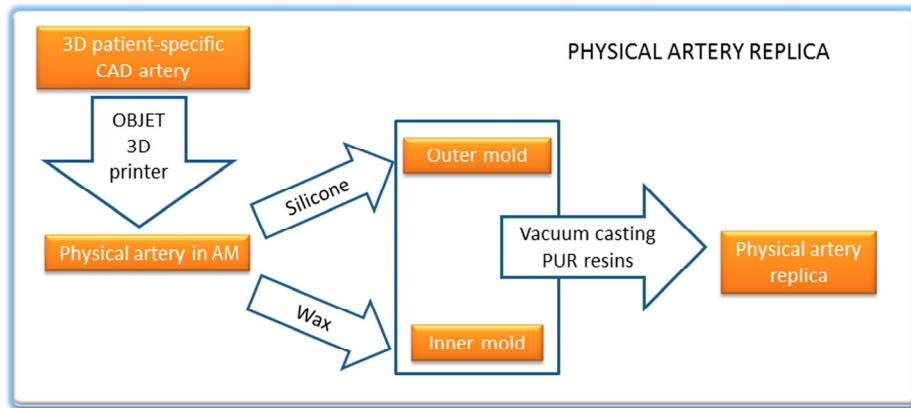
Figure 5-1 Flow chart describing the artery replication process.
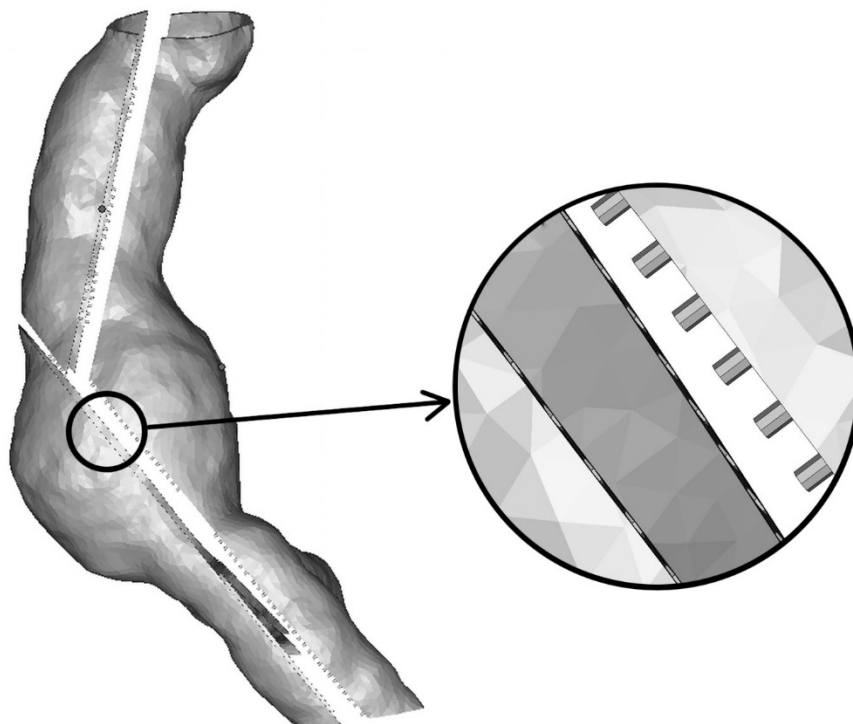
Figure 5-2 Partition lines for the artery with their proper connector pins.

The prepared AAA geometry is printed using the AM printer OBJET EDEN 330 (Stratasys Ltd., Minneapolis, MN, USA), which is based on the PolyJet technology featuring print resolutions of 42-, 84- and 16-

microns in the X, Y and Z-axis, respectively (Figure 5-3). The printing material for the artery is the general purpose Fullcure 720.
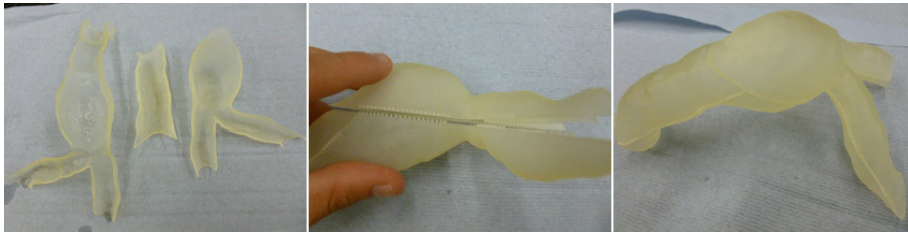
Figure 5-3 Printed AM artery.

Once printed and the support material removed, the outer and the inner mold are built by using the AM artery as the master mold. For the outer mold (see Figure 5-4), the printed artery, with its proximal and distal boundary openings blocked with Plasticine®, is rigidly fit inside a methacrylate frame. A viscous mix of silicone and a catalyst (SLM VTX 950, SLM Solutions GmbH, Lübeck, Germany) at a 10:1 ratio is poured inside the frame until the frame is completely filled and the artery entirely covered. The frame is then placed inside an oven at 45ºC to cure for 24 hours. Once cured, the mold is cut open and the artery is removed leaving the mold cavity, which accurately replicates the outer surface of the artery. Two ports are made in the mold to enable the subsequent steps of wax and resin injections, one in the proximal region for the wax injection and the second one close to the artery's maximum diameter for the resin injection.
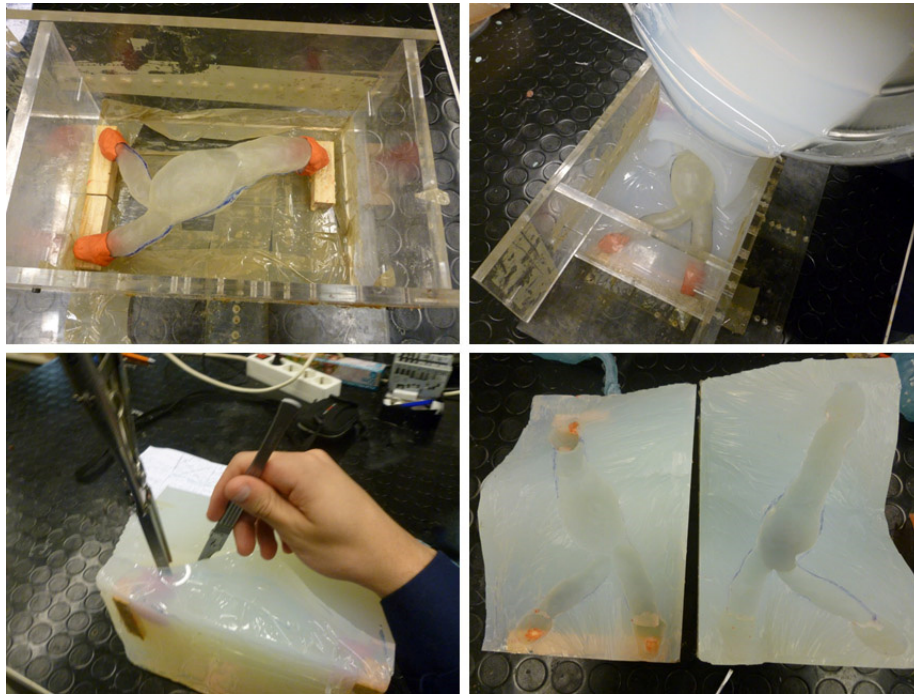
Figure 5-4 Process for the outer mold: AM artery within the mold (top-left) filling the frame with silicon (top-right), opening the silicon mold (bottom-left), and the final outer mold (bottom-right).

The inner mold (Figure 5-5) is made of WA-70 wax (SLM) with a melting point between 68ºC and 70ºC. To build this wax mold, the AM artery is placed into the silicone mold and both are pre-heated at 40ºC for 24 hours. The wax is in a liquid state after being melted in an oven at 70ºC and it is poured through the silicon mold's upper port. Once poured, the silicone mold containing the additive manufactured artery and the liquid wax inside it is placed inside the oven at 40ºC to slowly solidify the wax. Once in a solid state, the silicone mold is opened and the wax is removed from the interior of the AM artery.
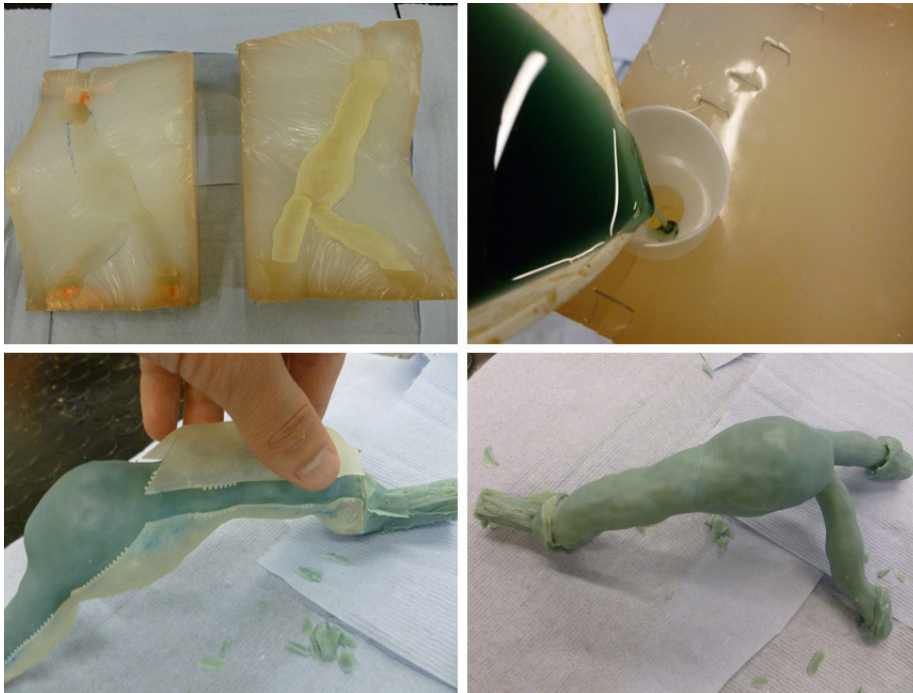
Figure 5-5 Process for the inner mold: silicone mold with the AM artery (top-left), filling the mold with liquid wax (top-right), opening the AM artery to remove the wax mold (bottom-left), and the final inner mold (bottom-right).

With the outer and inner molds created, a casting process is followed using the MCP 4/01 vacuum casting machine (SLM Solutions GmbH, Lübeck, Germany). The raw material used to replicate the artery is a PUR resin commercialized by SLM. It is a transparent rubber with high resistance to UV light.

The first step of the casting process is to place the silicone (outer) mold with the wax (inner) mold together with the two components (A and B) of the PUR in the vacuum chamber (see Figure 5-6). The resin is degassed, mixed and poured into the mold. When the mold is filled, the vacuum is released and the mold is placed in an oven at 45ºC to cure the resin. After 24 hours of curing, the oven temperature is increased to 85ºC to melt the inner wax. At the end of the melting process (approximately 3 hours), the silicone mold is opened and the rubber-like artery removed.

Figure 5-6 Vacuum casting process for the artery: silicone mold with the wax mold inside (top-left), mold and PUR resins ready for casting inside the MCP 4/01 vacuum casting machine (top-right), wax melting (bottom-left), and opening the mold to remove the artery (bottom-right).

The entire process, illustrated in Figure 5-1, can be completed in less than 4 days. The approximate cost of fabricating an artery replica (i.e., the AAA phantom) with this protocol, not including the cost of machine-hours and man-hours, is 135€ that is the sum of 80€ for the 3D printing, 40€ for the silicone material and 15€ for the PUR resins. In Figure 5-7 some AAA phantoms achieved with this methodology are shown.

Figure 5-7 AAA phantoms.

Finally, the phantom is inspected to quantify its geometric accuracy. Towards this end, 30 rectangular samples randomly distributed from the artery replica are cut with a scalpel and from each sample ten thicknesses are randomly measured by using a digital caliper with a resolution of 10 microns. Simultaneously, twelve thicknesses from each of the corresponding samples of the virtual aorta model are computationally measured. Samples are shown in Figure 5-8.
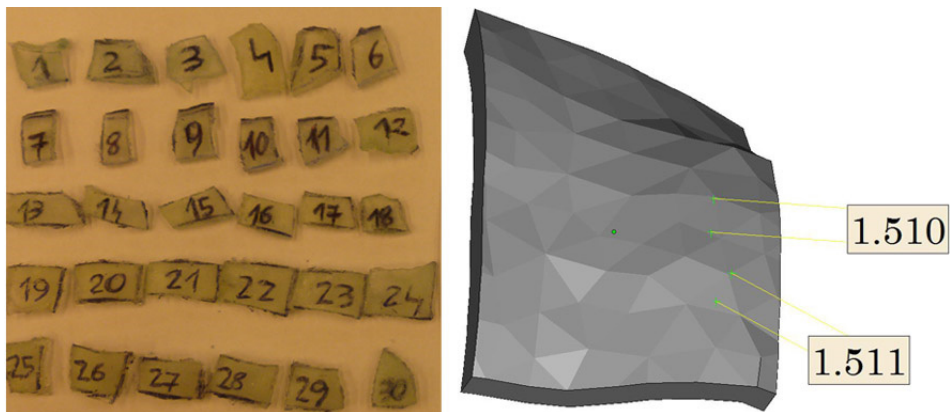
Figure 5-8 Rectangular samples to measure wall thickness of the real (left) and virtual (right) artery.

These measurements are statistically analyzed by calculating the mean and standard deviation for each sample and a comparison between the real and virtual aorta model is made. The mean and

standard deviation for each physical and virtual sample are calculated using the ten real and twelve virtual measurements respectively.

Two different geometries are analyzed. The average and standard deviations of the wall thicknesses for the first geometry are shown in Table 5-1 while the statistical data for the second artery is shown in Table 5-2. Percentage differences refer to the difference between the wall thickness of the physical replica (phantom) and the virtual model. According to these results, the physical artery has thicker walls with the average difference for all the samples at 11.14% for the first geometry and 30.65% for the second geometry.

Table 5-1: Thicknesses of the physical and virtual arteries. Geometry #1.

| | Artery replica #1 | | | | |
| | Virtual | | Real | | Diff. |
Sample	Avg. (mm)	Std. (mm)	Avg. (mm)	Std. (mm)	(%)
1	1.842	0.45	1.956	0.23	6.18
2	1.724	0.26	1.912	0.23	10.90
3	1.617	0.12	1.948	0.19	20.50
4	1.577	0.08	1.899	0.22	20.40
5	1.628	0.09	2.017	0.24	23.90
6	1.712	0.27	1.948	0.35	13.80
7	1.531	0.04	1.546	0.32	1.01
8	1.561	0.07	1.571	0.22	0.65
9	1.546	0.08	1.644	0.25	6.36
10	1.591	0.09	1.645	0.28	3.42
11	1.752	0.21	1.750	0.28	-0.09
12	1.658	0.18	1.699	0.31	2.47
13	1.624	0.14	1.648	0.25	1.51
14	1.583	0.10	1.618	0.21	2.22
15	1.530	0.05	1.641	0.4	7.27
16	1.565	0.06	1.685	0.37	7.67
17	1.644	0.14	1.797	0.36	9.31
18	1.893	0.38	1.914	0.26	1.14
19	1.949	0.53	2.038	0.29	4.57
20	1.703	0.21	2.209	0.35	29.68
21	1.575	0.08	2.299	0.21	45.93
22	1.602	0.10	2.113	0.16	31.95
23	1.599	0.12	2.127	0.28	33.03
24	1.964	0.58	2.296	0.37	16.88
25	1.550	0.06	1.550	0.40	0.03
26	1.535	0.06	1.538	0.25	0.21
27	1.662	0.21	1.681	0.28	1.16
28	1.644	0.18	1.654	0.21	0.60
29	1.597	0.10	1.877	0.39	17.52
30	1.536	0.05	1.752	0.27	14.07
	Average difference (%)				11.14

Table 5-2: Thicknesses of the physical and virtual arteries. Geometry #2.

	Artery replica #2				
	Virtual		**Real**		Diff.
Sample	Avg. (mm)	Std. (mm)	Avg. (mm)	Std. (mm)	(%)
1	1.502	0.05	1.356	0.18	-9.72
2	1.665	0.22	1.734	0.21	4.13
3	1.293	0.41	1.745	0.15	34.93
4	1.547	0.08	2.021	0.28	30.66
5	1.585	0.11	2.500	0.24	57.71
6	1.545	0.04	2.057	0.28	33.18
7	1.602	0.17	1.668	0.27	4.12
8	1.656	0.17	1.775	0.26	7.22
9	1.661	0.12	1.884	0.26	13.41
10	1.661	0.11	1.798	0.21	8.28
11	1.603	0.13	1.726	0.14	7.67
12	1.526	0.06	2.157	0.38	41.34
13	1.531	0.04	1.985	0.36	29.68
14	1.603	0.17	1.667	0.17	3.97
15	1.620	0.14	1.672	0.23	3.22
16	1.603	0.15	1.885	0.30	17.56
17	1.578	0.08	1.838	0.14	16.45
18	1.556	0.06	1.657	0.17	6.50
19	1.767	0.41	2.631	0.26	48.90
20	1.531	0.04	2.510	0.11	63.98
21	1.583	0.11	2.372	0.26	49.89
22	1.574	0.06	2.220	0.28	41.00
23	1.670	0.18	2.374	0.22	42.16
24	1.810	0.19	2.125	0.09	17.39
25	1.777	0.21	2.866	0.26	61.31
26	1.786	0.22	3.143	0.22	75.97
27	1.752	0.17	3.075	0.27	75.56
28	1.728	0.16	2.791	0.35	61.52
29	1.689	0.12	2.561	0.30	51.63
30	1.864	0.25	2.234	0.23	19.88
	Average difference (%)				30.65

This thickness difference between virtual and physical arteries is acceptable and in the range of other works. The next step is to characterize the behavior of the PUR resins.

5.3 Material characterization

With the manufacturing protocol defined, the next step is to measure the mechanical properties of phantom material candidates to yield stress-strain curves that can be compared to the known healthy and aneurysmal abdominal aorta properties [54]. To this end, various rubber-like materials are created using the commercially available SLM bi-component PUR SLM 7140, 7160 and 7190 (A and B) as the base material. The A and B components were mixed in various ratios to obtain a range of diverse resins. With this range of materials, several tensile specimens are created and tested to obtain stress-strain curves that are as physiologically realistic as possible. The tensile test specimens are designed in accordance with ASTM D412 Type B. All specimens are pre-conditioned at 20ºC (± 1ºC) and 40% (± 5%) relative humidity prior to testing. The tensile tests are performed on the specimens to generate force-extension data using an INSTRON MINI 44 (Instrom Worldwide, Norwood, MA) tensile test machine Figure 5-9.
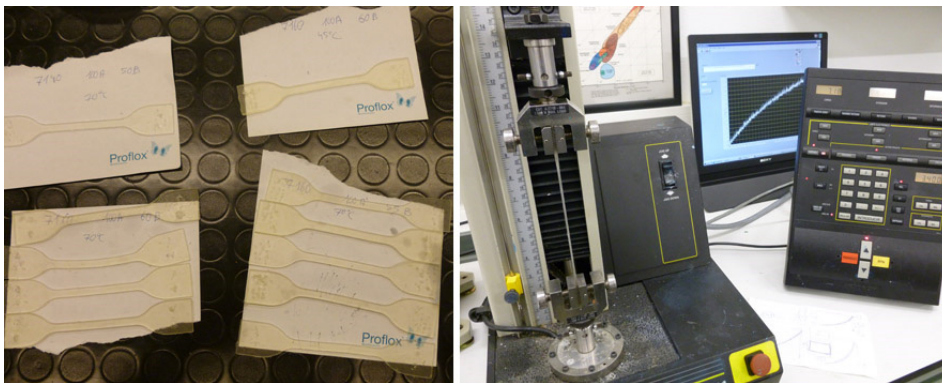
Figure 5-9 Tensile test specimens (left) and tensile test machine (right).

Each sample is subjected to a cross-head speed of 3.4 mm/min until failure with pre-conditioning of 10 cycles to 7.5% of the gauge length to avoid the Mullins effect [51]. The load-displacement outputs from the tensile test machine were normalized to stress-strain data. The strain is defined in Equation 5-1

$$\varepsilon = \frac{\Delta l}{l_0} \qquad\qquad (5\text{-}1)$$

where Δl is the change in length of the specimen at any time and l_0 was its original length. The true stress (Cauchy) is used assuming that the testing materials are incompressible and that the volume do not change during the tests:

$$\sigma = \frac{F}{A^*} \qquad\qquad (5\text{-}2)$$

$$A^* = \frac{A_0 l_0}{l_0 + \Delta l} \qquad\qquad (5\text{-}3)$$

where F is the force required and A^* the area at any instant.

The polyurethane resins tested in this research exhibit almost linear stress-strain curves. For each material, six specimens are tested, and the Young's modulus is derived. In Table 5-3 the average Young's modulus for each material together with the standard deviation is displayed and in Figure 5-10 the stress-strain curves for one specimen of each material are illustrated. As it can be appreciated, the noise is more perceptible for softer materials (materials 6 and 7) as the uniaxial tensile machine is not perfectly suitable for so soft materials.

Table 5-3: Average Young modulus (R^2) of tested PUR resins and standard deviation; and strength.

Material #	PUR resin	Mixing ratio A:B	Young's modulus (R^2) [kPa]	Standard deviation [kPa]	Strength (kPa)
1	7190	100:90	13955.50(0.96)	966.98	12094
2	7190	100:85	6925.50(0.99)	808.60	9665
3	7190	100:75	3411.83(0.97)	759.13	5509
4	7160	100:69	2863.73(0.95)	101.02	2780
5	7160	100:60	1668.67(0.91)	155.24	1946
6	7140	100:45	1108.28(0.90)	57.09	1521
7	7140	100:38	554.61(0.67)	96.88	986
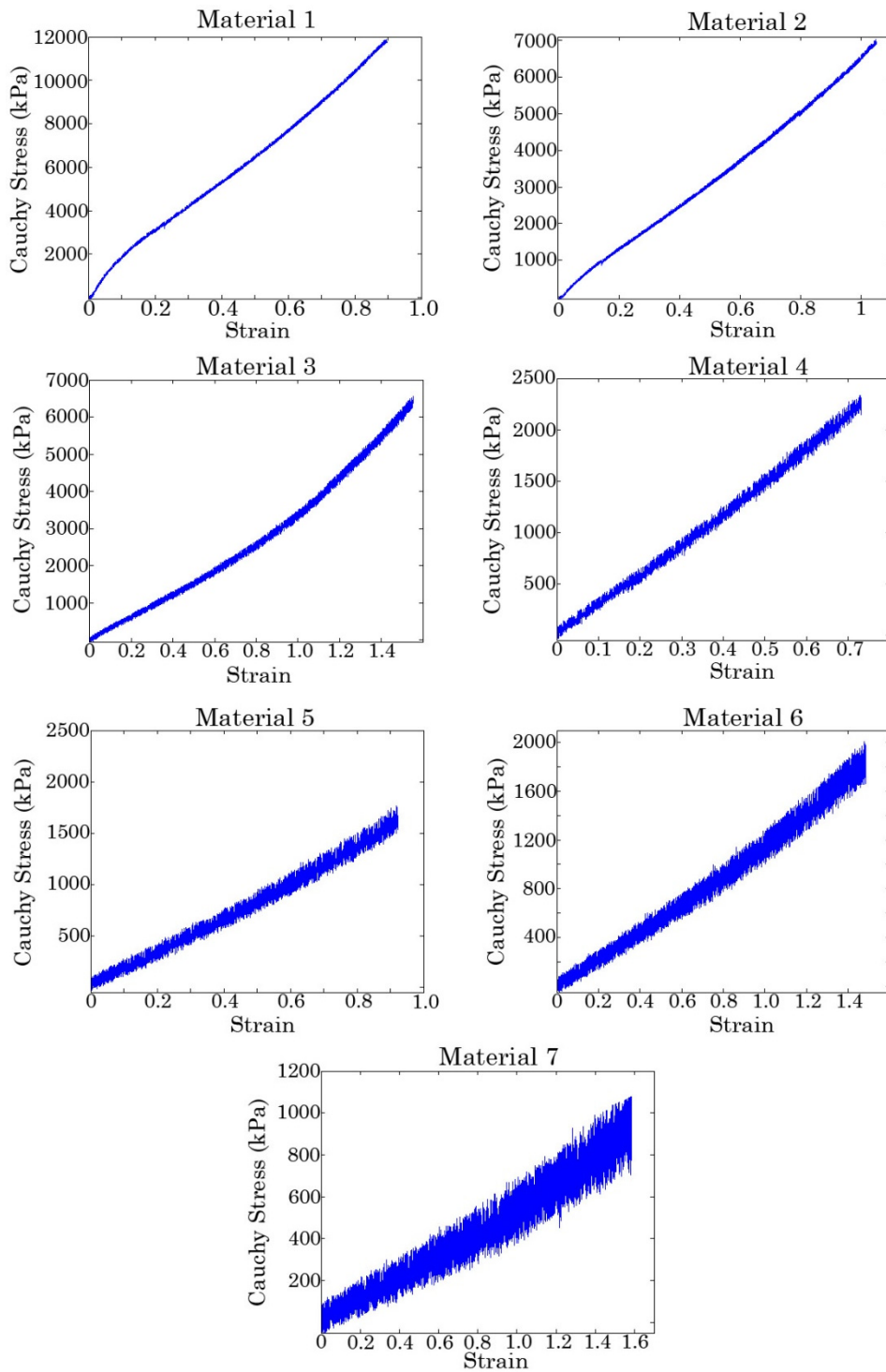
Figure 5-10 Stress-strain curves of the tested specimens.

The results are exported to stress-strain graphs and compared with artery behavior. In addition, another sample of the specimen is printed, with the 3D printer using the rubber-like material Fullcure 980 Tango Black Plus, and is tested. As explained in the state of the art, large human arteries, as most soft tissues, present a non-linear mechanical behavior characterized by a stress-strain curve with convexity toward the horizontal axis; small increases in stress result in large stretches (toe region) and are followed by a quasi linear behavior (at moderate strains) as illustrated in Figure 5-11. As commented, the PUR resins tested in this research exhibit almost linear stress-strain curves. While it is not possible to replicate the entire hyperelastic soft tissue behavior, it was obtained a reasonably analogous behavior of the resins in the toe region of both the normal and the aneurysmal abdominal aorta [54]. Some of the stress strain curves resulting from the uniaxial tensile testing are shown in Figure 5-11. The response of a typical healthy abdominal aorta and an AAA obtained by Raghavan et al. [54] under zero-stress conditions and at room temperature are superimposed in this chart for comparison purposes.
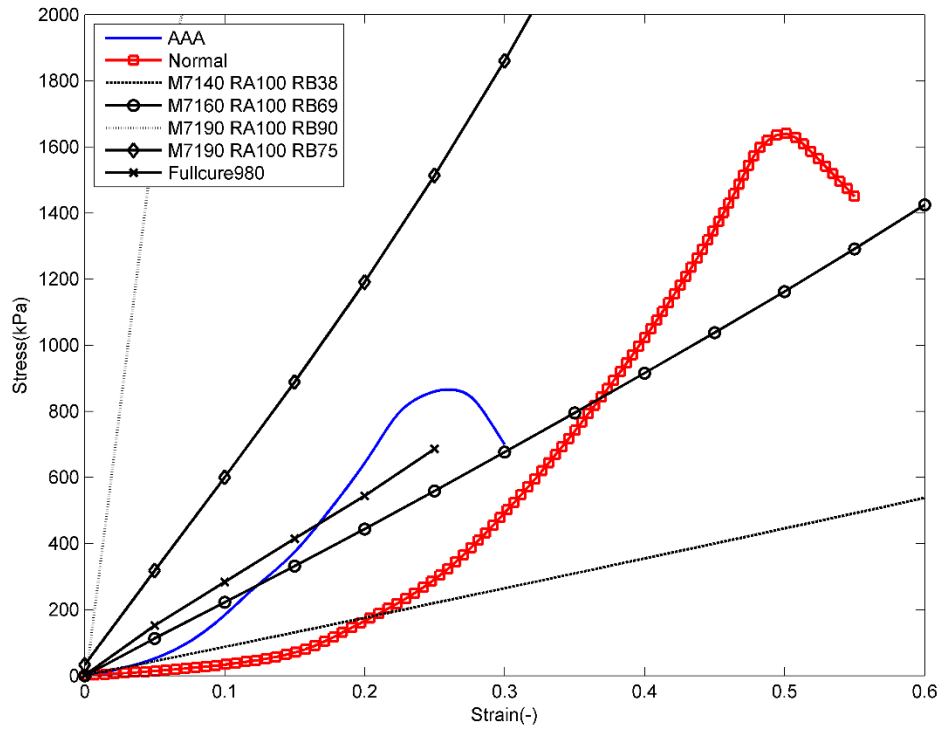
Figure 5-11 Stress-strain curves for PUR resins and 3D printing vs. ex-vivo experiments for normal and AAA arteries from Raghavan and Vorp [54].

With the available resins and the proper mixing ratio, it is possible to achieve a good correlation with the population-averaged healthy aorta and AAA tissues. To better compare the artery behavior with the PUR resins, the root mean square (RMS) error of the stress and the stiffness is analyzed. In the case of the healthy aortic tissue, the toe region (0-0.2 strain) is approximated with the M7140 resin (RA100 RB38) with a RMS error for the stress and the stiffness (slope of stress-strain curves:$E = \sigma/\varepsilon$) of 42.86 kPa and 0.660 MPa respectively, based on 200 data points. Similarly, the response of the AAA tissue is also reasonably approximated with the M7160 resin (RA100 RB69), but only up to a 0.15 strain. The RMS error for the stress of this correlation is 42.75 kPa while the RMS error for the stiffness is 1.28 MPa based on 150 data points.

However, noteworthy is that the Raghavan and Vorp curves were obtained under a zero-stress condition, while in vivo tissue is exposed to a stressed configuration. Some studies [18-20] have analyzed the

stressed configuration obtaining mean values between 130 kPa and 180 kPa depending on the case of study. If 50 kPa is considered as the mean value of the state of stress in-vivo, the present methodology is still appropriate since the AAA tissue can be represented by the linear region of the stress-strain curve and a good approximation could be obtained for any patient-specific artery by modifying the PUR mixing ratio. In the Table 5-4 the RMS errors of the PUR resins for this case are shown.

Table 5-4: RMS errors of the tested PUR resins.

PUR resin	Mixing ratio A:B	Stress RMS error [kPa] with AA/AAA	Stiffness RMS error [MPa] with AA/AAA
7140	100:38	536.20/345.21	4.41/4.47
7140	100:45	454.01/297.37	3.89/3.93
7160	100:60	371.27/249.01	3.38/3.39
7160	100:69	198.95/146.47	2.37/2.28
7190	100:75	126.82/100.21	1.97/1.81
7190	100:85	433.21/210.45	2.67/2.27
7190	100:90	1484.70/818.89	9.37/9.11

For this particular patient, the 7190 (RA100RB75) resin is the resin which better approximates the AA and AAA tissue with a RMS error for stiffness of 1.97 MPa and 1.81 MPa respectively and a RMS error for stress of 126.82 kPa and 100.21 kPa respectively. These values are the lowest ones for the tested PUR resins for both stress and stiffness RMS and for both AA and AAA arteries. Considering that the range of values of the stiffness for each point varies from 2.18 MPa to 7.39 MPa in these points, the RMS error is acceptable. With different components and mixing ratios different results can be achieved, and errors can be reduced.

In summary, although the stress-strain dependency is not linear in an in-vivo loading condition, for small strain ranges a linear stress-strain relationship is a reasonably good approximation. This methodology allows us to match that linearity with a synthetic material.

5.4 Conclusions

This chapter presents the development and application of a novel methodology for building AAA replicas with patient-specific, regionally varying, nonuniform wall thickness and isotropic material properties at small strains. The AAA phantoms will have a positive impact on various clinical applications such as:

- The validation of numerical studies, medical image-based models and inverse characterization methods.
- In vitro experiments (as an alternative to computational modeling) for studying overall aneurysm mechanics coupled with blood flow dynamics or for predicting rupture risk.
- Pre-clinical testing of endovascular grafts.
- Benchtop testing o of endovascular grafts for the detection of type III endoleaks.
- Experimental assessment of new or existing designs of cathether devices in terms of trackability forces, rigidity of catheter guides and deployment of stent grafts.
- Use in hospital simulation centers for honing professionals' skills and refining advanced techniques.

The applied method is fast, relatively inexpensive, and can be easily reproduced for other applications. Liquid polyurethane resins have shown to be appropriate materials to characterize the mechanical behavior of healthy arteries and aneurysmal aortas, in both in-vitro (with no pre-stretch) and in-vivo conditions (with pre-stretch).

The thickness differences obtained from the comparison of the virtual and physical arteries are due to two main sources. On the one hand, the process for measuring the wall thickness in the physical artery was the most suitable to the model and is one that was followed similarly by Doyle and colleagues [186]. The methodology is not devoid of measuring errors. Depending on the user's skill, the material of the phantom could be more or less compressed when measuring the thickness. This limitation was evaluated with the help of 5 volunteers who were asked 10 times to measure the thickness of a rectangular sample of the 7140 material with a uniform thickness of 2.5 mm. The fifth volunteer was the author who measured the thickness values of

the artery in this paper. The ANOVA analysis was performed and showed that there is no statistically significant differences between the mean values for the thickness (p value=0.586) meaning that the person who measured the thickness is not critical. With this in mind, our results showed that the error of the author measuring with the caliper is 1.64%. It seems reasonable for the authors to expect the same error when measuring the artery thickness.

On the other hand, it seems that the greater wall thickness of the phantom was due to the expansion of the silicone and the contraction of the wax. Wax contraction was mitigated by pre-heating the silicone mold and the RP artery inside it to 45ºC. The expansion of the silicone was difficult to minimize because each time the mold was used it exhibited some expansion. In vacuum casting, the silicone mold is normally discarded after 15-20 trials because of geometrical and dimensional tolerance differences. The phantom that was measured was obtained at the 3rd trial, such that the molds had undergone the casting process few times and thus had reasonable accuracy, as Table 5-1 and Table 5-2 illustrate.

The cost of manufacturing the artery replicas is relatively low when one considers that the main investment is the 3D printer, around 20,000€ for a 3D printer which uses the rigid material Fullcure 720. However, once the artery is printed and the silicone mold is made, the cost of a new replica is only 15€. Nevertheless, a limitation of the methodology is that after approximately 5-10 casting processes, a new silicone mold should be created to avoid possible dimensional inaccuracies in the resulting artery replica. Yet, in this worst case scenario in which it would be necessary to build both the artery with PUR resins and a new silicone mold in every casting, the cost would only increase to 55€. If AM technology is used to manufacture AAAs with flexible material, as recently done by Cloonan et al. [115], the investment for 3D printer increases up to 40,000€ (Objet30 Prime).

Regarding the rubber-like material available of the 3D printing, the response of the Fullcure 980 seems to be in range to AAA and AA arteries, and in addition, it presents a better dimensional accuracy in the artery with respect to the methodology presented in this paper.

However, the artery made of Fullcure 980 has four main disadvantages which were solved in this research with the PUR approach. First, its stiffness is fixed, that is, the user cannot control it and, in consequence, cannot mimic the response of different patients with different AAA properties. With the methodology explained in this study the stiffness can be modified to any artery by changing the mixing ratio of the PUR resins. Secondly, due to the printing process the AM artery has anisotropy in the three directions of impression which cannot be controlled. Thirdly it is the price. For more than one AAA model, the AM process is considerably more expensive (70€ each copy), because the artery needs to be printed every time, while the artery from the PUR approach is just 15€. The last issue is that when using Poly-jet technology for 3-D printing, one requires applying water pressure to remove the support material. Removing all the support material for complicated geometries, as AAAs, is a difficult task, and furthermore, geometries could be damaged due to the water jet. In the future, a new soluble 'support material', that Stratasys is developing and that avoids the water jetting, could be used.

Additionally, it must be pointed out that the presented methodology to get realistic AAA replicas was focused on arteries with isotropic mechanical properties. Having control of the wall thickness and the stress-strain curve is a new step forward to achieve the exact artery fidelity and the next step could be addressing the anisotropic behavior of the real arteries.

The temperature deserves a final comment. The current tests and methodology was carried out at room temperature close to 20ºC and the future experimental tests should be performed at that temperature. Beyond that temperature, for instance if the phantom needs to be analyzed at body temperature (37ºC), the presented methodology to build the physical replica is also valid, but the tensile tests should be repeated at 37ºC, in order to take into account the new softer behavior of the PUR resins and, in the end, to select the proper PUR resin.

Manufacturing of AAA replicas with anisotropic behavior

6.1 Introduction

In the previous chapter, a methodology for manufacturing isotropic AAA phantoms with nonuniform wall thickness was developed and applied. However, various studies [50,68,70,73] have tested the AAA tissues biaxially, revealing an increase of the mechanical anisotropy in the tissue due to degradation of the AAA, with preferential stiffening in the circumferential direction. The consideration of the anisotropy parameter plays an important role in the results of numerical simulations and this parameter must be taken into account for further works [86,142,143,190–192]. Within the context of physical replicas, this consideration points to a step forward in the manufacturing of phantoms with arterial anisotropic behavior.

The purpose of this chapter is to describe and apply a new methodology for manufacturing physiologically realistic AAA replicas that display anisotropic behavior. This is the first time that a methodology is reported for developing arterial replicas with nonuniform wall thickness and defined anisotropy. The process is based on the previous chapter; addressing the anisotropic behavior by manufacturing the arteries with a set of ring-shaped PUR fibers placed inside the artery walls. First, in section 6.2 the composite material is characterized; and then, in section 6.3 the process of manufacturing the AAA phantoms with anisotropic behavior is explained.

6.2 Material characterization

In Chapter 5, the materials were uniaxially tested (Table 5-3). In this chapter, to characterize an anisotropic composite, biaxial testing is carried out. First, the procedure to manufacture the composite specimens is explained and then the biaxial tests are displayed.

6.2.1 Composite specimens preparation

To achieve the anisotropic behavior in the specimens, a series of fibers are embedded in the matrix forming a composite (Figure 6-1).
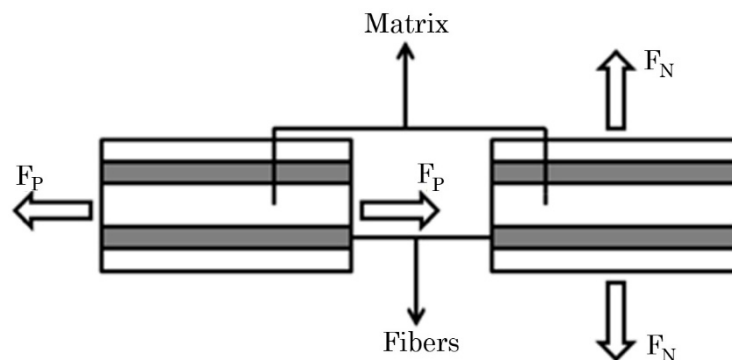
Figure 6-1 Matrix component with embedded fibers.

Equations 6-1 and 6-2, that can be easily derived from composite material theory [193], describe the approximate behavior of a composite.

$$E_P = (1 - f) \cdot E_m + f \cdot E_f \qquad\qquad (6\text{-}1)$$

$$E_N = \frac{E_m \cdot E_f}{(1 - f) \cdot E_f + f \cdot E_m} \qquad\qquad (6\text{-}2)$$

where E_P and E_N are the Young's modulus of the composite material in the direction parallel and normal to the fibers; E_m and E_f are the elastic modulus of the matrix and the fibers respectively, and f is the volume fraction of fibers in the composite i.e. fiber volume/total volume ratio. Therefore, it can be appreciated that increasing the fiber proportion (from f=0 to f=0.5) will lead to an increase in the ratio E_P/E_N and an increase of the Young´s modulus in both directions (assuming E_f>E_m).

Usually, composite specimens for biaxial testing have a square or cross shape geometry. When biaxially testing in vivo samples, square shapes are more commonly used [68,70,73]. Therefore, in this work the composite specimens are squares of 25 x 25 mm and 3 mm in thickness. Different composites are fabricated altering the proportion of fibers, the matrix elastic modulus and the fiber elastic modulus.

The procedure to obtain the square specimens with the fibers in the inside is as follows. Once defined the proportion of fibers, the fibers are modeled using CREO 2.0 and are printed with the OBJET EDEN 330 printer. The AM fibers are used as a reference to create the mold of silicone. Finally, pouring the PUR resins into the mold in the vacuum machine and after curing, the fibers are obtained with the desired fiber elastic modulus. This process is illustrated in Figure 6-2.

Figure 6-2 Fiber manufacturing process: AM fibers (left), silicone mold (center) and final PUR resins fibers (right).

Once the fibers are fabricated, a similar procedure is followed to obtain the silicone mold that defines the external shape of the specimen (top-left image of Figure 6-3). Then the fibers are attached to the mold (bottom-left image of Figure 6-3), the PUR resin selected for the matrix is poured to fill the mold, and when cured the silicone mold is opened and the squared anisotropic specimen removed (bottom-right image of Figure 6-3).
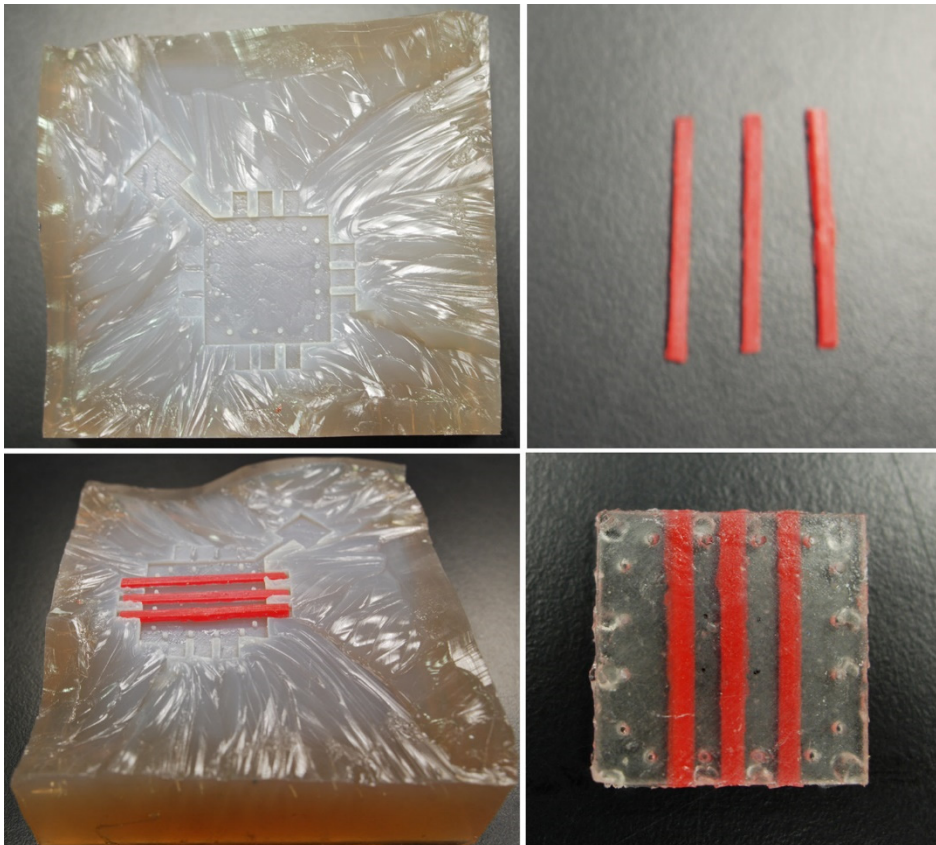
Figure 6-3 Anisotropic specimen manufacturing process: mold (top-left), fibers (top-right), fibers placed in the mold before vacuum casting (bottom-left), and final composite specimen with the markers (bottom-right).

Five different composites are fabricated with the properties showed in Table 6-1.

Table 6-1: Specimens tested biaxially.

# Specimen	Matrix Material	Fiber Material	Proportion of fibers
1	6	3	0.25
2	7	4	0.30
3	7	4	0.15
4	7	5	0.15
5	7	6	0.15

6.2.2 Biaxial testing procedure and constitutive modelling

Tests on each specimen are conducted using a custom-made planar biaxial testing system. The device, illustrated in Figure 6-4, is fabricated with aluminum profiles forming a quadrangular frame. Each sample is loaded with the help of sixteen hooks (four at each side) that are connected to sixteen containers able to hold weights via plastic wires that run over sixteen pulleys of 20 mm in diameter. The load at each point is controlled by gradually placing controlled weights into the containers. Four loading scenarios (240 grams, 480 grams, 720 grams and 960 grams) are considered. The stress data is derived from the force, as done in other studies. In this biaxial machine, sand particles are used as weights. Prior to load the specimen, the amount of necessary sand is calculated using a centigram-precision scale. That means that the load error would be very small.
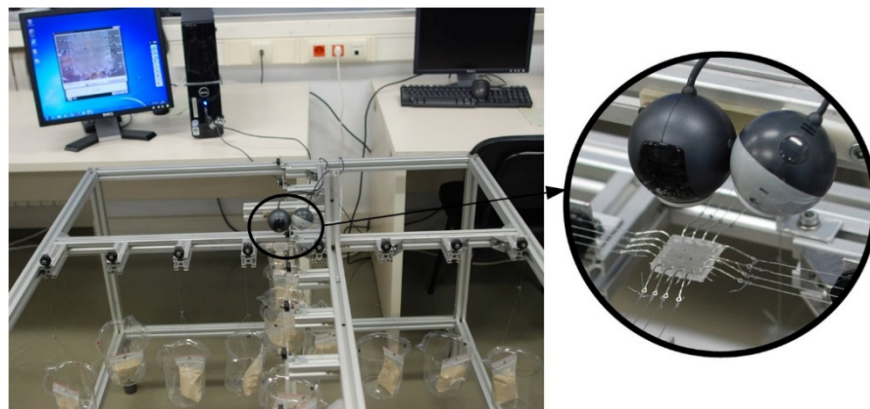
Figure 6-4 Complete biaxial testing system (left) and stereovision system (right).

The strain measurement is calculated through the binocular stereovision technique [194]. Four small markers forming a 5 mm x 5 mm square are placed in the center of the testing specimen for optical tracking (Figure 6-5). This technique allows the markers' 3D coordinates to be computed by triangulation from a pair of images (Figure 6-6). To this end, a pair of Logitech QuickCam E3500 webcams (resolution ~0.03 mm/pixel) are mounted at the top of the device.
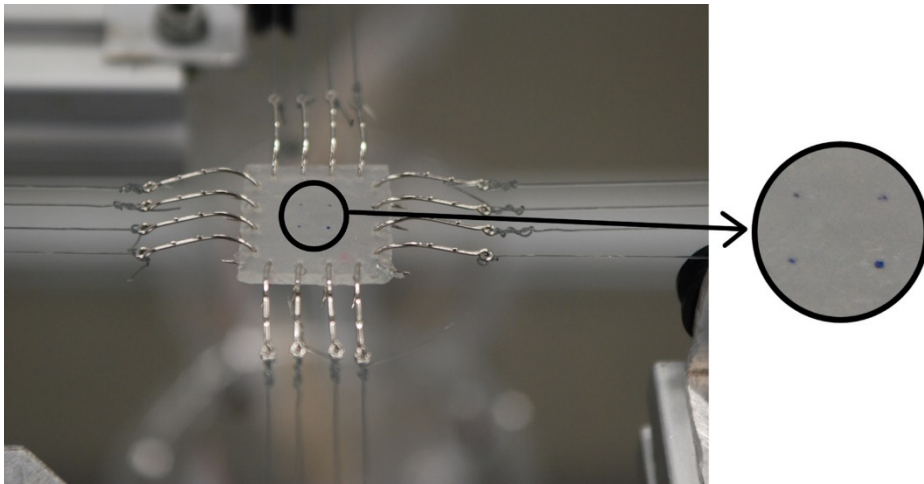
Figure 6-5 Tested specimen with the four markers.

Before running the biaxial tensile tests, the cameras are calibrated in order to ensure accuracy. An open-source code in MATLAB language is used to define the intrinsic and extrinsic parameters of the cameras [195]. With these known parameters and the relative position of one camera with respect to the other, the 3D coordinates of the marker points can be obtained and then, the strain can be calculated.
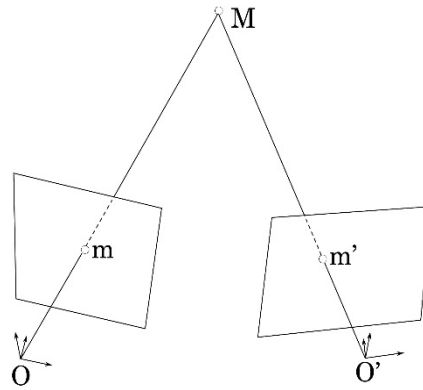
Figure 6-6 Binocular stereovision.

After the calibration process, in order to inspect the accuracy of the stereovision system, the same template used for the calibration is recorded in six different positions. For each position, eight measurements are taken in different directions. The known distances are compared to the ones calculated via stereovision and the errors are calculated as a percentage:

$$e(\%) = |D_R - D_M|/D_R \tag{6-3}$$

where e is the error, D_R is the real distance between the selected points and D_M is the distance measured by the stereovision system. The average error (SD) of the stereovision system is equal to 0.58% (0.37%), i.e. a maximum error of 48 μm for 5 mm lengths (distance between markers).

The inter-operator variability when measuring the strain is found non critical after statistically perform an ANOVA analysis with three volunteers aside from the author. Results show that there are no statistically significant differences between the measured strains (p value=0.950).

The thickness of the specimens is measured several times with a digital caliper prior to testing, and the average thickness is used in subsequent stress calculations. The specimen is tested using a stress-controlled protocol, where the first Piola-Kirchoff stresses (i.e. the

engineering stresses) serve as a measure. The non-zero components of the first Piola-Kirchoff stress tensor **P** have the form:

$$P_{\theta\theta} = f_\theta/TX_L, \qquad P_{LL} = f_L/TX_\theta \qquad (6\text{-}4)$$

where f_θ and f_L denote the forces in each direction, T is the thickness in the unloaded configuration, and X_θ and X_L are the dimensions between the hooks along the circumferential and longitudinal directions of the square specimen , i.e. 20 mm.

Each biaxial specimen is tested in the following order: $P_{\theta\theta}:P_{LL}$=1:1, 0.75:1, 1:0.75, 0.5:1, 1:0.5, 1:1, keeping the ratio $P_{\theta\theta}:P_{LL}$ constant for each protocol. For instance, the loading protocol 1:0.75 means that the specimen is charged with 240 grams, 480 grams, 720 grams and 960 grams in the circumferential direction, and with 180 grams, 360 grams, 540 grams and 720 grams in the longitudinal direction. The last equibiaxial tension protocol (i.e., $P_{\theta\theta}:P_{LL}$=1:1) is performed to confirm that no structural damage occurs in the specimen as a result of the mechanical testing. Each specimen is preconditioned through six loading and unloading cycles, and the seventh cycle is used for the subsequent analysis.

From the recorded marker positions, the deformation gradient tensor **F** is calculated at each measured value of imposed load [196]. The Green strain tensor **E** is calculated as denoted in Equation 6-5. The shear components of the deformation gradient tensor **F** are found to be negligible, so the in-plane Green strain tensor components are determined with Equation 6-6.

$$\boldsymbol{E} = \tfrac{1}{2}(\boldsymbol{F}^T\boldsymbol{F} - 1) \qquad (6\text{-}5)$$

$$E_{\theta\theta} = \tfrac{1}{2}(\lambda_\theta^2 - 1), \qquad E_{LL} = \tfrac{1}{2}(\lambda_L^2 - 1) \qquad (6\text{-}6)$$

with λ_θ and λ_L denoting the stretches in both directions.

To model the mechanical response of the tested materials, a strain energy function W (Equation 6-7) developed by Choi and Vito [197] for the canine pericardium and used by Vande Geest et al. [68] for both aneurysmal and non-aneurysmal abdominal aortic tissue is used:

$$W = b_0(e^{(1/2)b_1 E_{\theta\theta}^2} + e^{(1/2)b_2 E_{LL}^2} + e^{b_3 E_{\theta\theta} E_{LL}} - 3) \qquad (6\text{-}7)$$

where b_0, b_1, b_2 and b_3 are the material coefficients to be determined.

From Equation 6-7 the in-plane second Piola-Kirchoff stresses (Equations 6-9 and 6-10) can be determined applying Equation 6-8.

$$S = \frac{\partial W}{\partial E} \qquad (6\text{-}8)$$

$$S_{\theta\theta} = b_0(b_1 E_{\theta\theta} e^{(1/2)b_1 E_{\theta\theta}^2} + b_3 E_{LL} e^{b_3 E_{\theta\theta} E_{LL}}) \qquad (6\text{-}9)$$

$$S_{LL} = b_0(b_2 E_{LL} e^{(1/2)b_2 E_{LL}^2} + b_3 E_{\theta\theta} e^{b_3 E_{\theta\theta} E_{LL}}) \qquad (6\text{-}10)$$

The data from the five biaxial protocols ($P_{\theta\theta}$: P_{LL}=1:1, 0.75:1, 1:0.75, 0.5:1, 1:0.5) for each specimen are fit to this model using the Generalized Reduced Gradient method and the material coefficients are derived for individual samples. In order to derive a single constitutive model, data from each protocol is averaged to obtain a single dataset of the composite.

Additionally, the anisotropy parameter [68,197]:

$$AI = \sqrt{b_1/b_2} \qquad (6\text{-}11)$$

is calculated in order to compare the PUR resins behavior with AAA tissue data.

6.2.3 Biaxial testing results

After the tensile tests, the representative **S-E** plots are obtained for each specimen (Figure 6-7). Then, the specimens are modeled calculating the material coefficients (b_0, b_1, b_2 and b_3) of Equation 6-7.
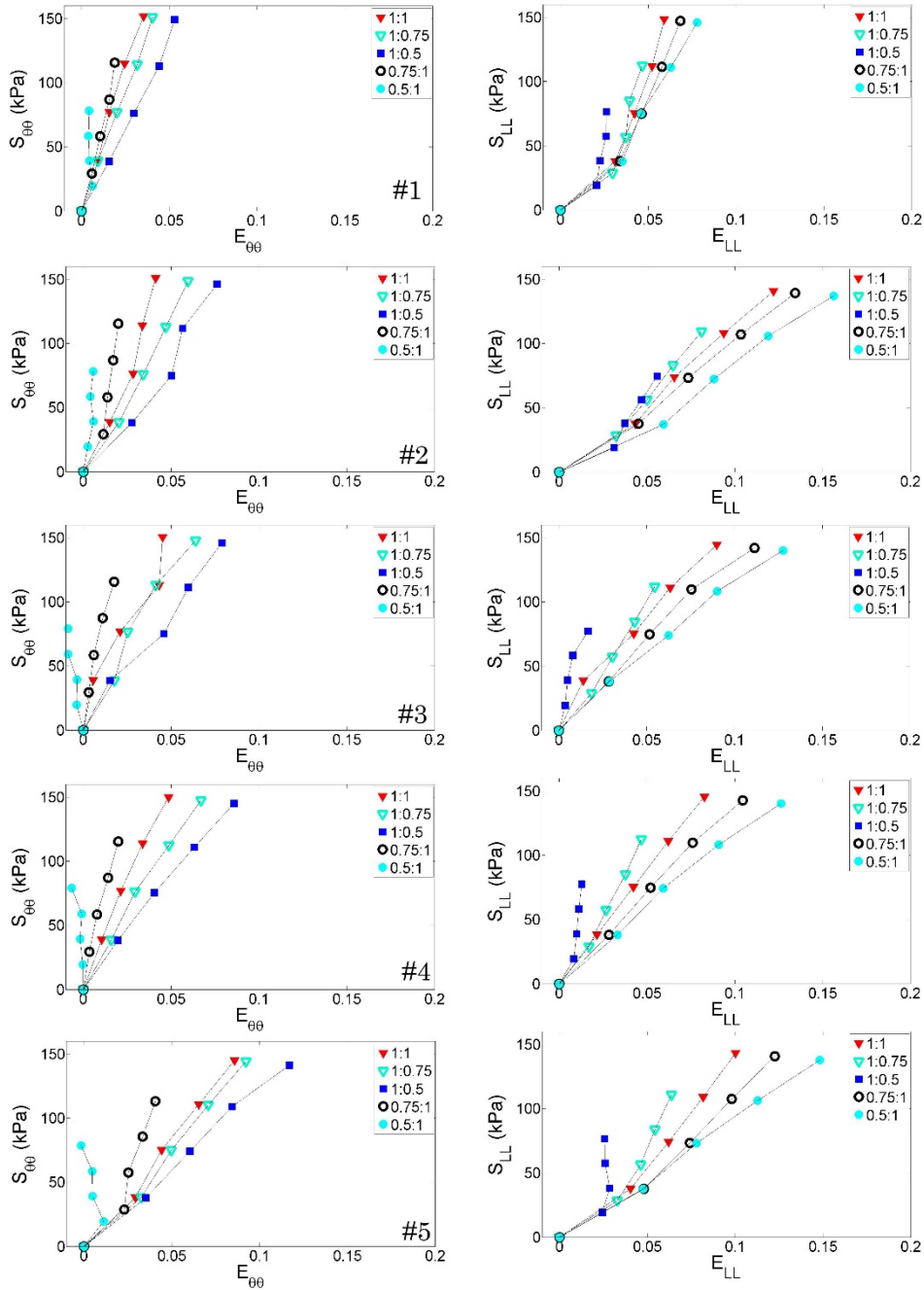
Figure 6-7 S-E plots of the 5 tested specimens.

Once the material coefficients are calculated for each specimen, the composite behavior is compared to the AAA tissue behavior (using Vande Geest's data [68]). To this end, three parameters are selected:

the anisotropic index parameter *AI*, the peak Green strain ratio ($E_{LL,max}/E_{\theta\theta,max}$) and the strain energy at an equibiaxial nominal stress of 60 kPa (W_{60}). The comparison of these parameters are shown in Table 6-2.

Table 6-2: *AI*, Green strain ratio and *W* comparison between Vande Geest's data and composite specimen.

Specimen	AI	$E_{LL,max}/E_{\theta\theta,max}$	W_{60}
Vande Geest	1.13	1.61	1.25
#1	1.54	3.81	0.91
#2	1.32	2.87	1.64
#3	1.30	2.50	1.72
#4	1.09	1.43	1.29
#5	1.11	1.25	2.29

Considering the results of the biaxial tests, the specimen #4 is selected as a candidate to mimic the AAA tissue behavior. Therefore six new specimens (named V1 to V6) with the same properties, *f*=0.15, E_m=0.54 MPa (Material 7) and E_f=1.64 MPa (Material 5), are fabricated and biaxially tested.

For all tested specimens, the results from the first and last equibiaxial protocol coincide and thus suggest that no structural damage of the tissue occurs as a result of testing. The circumferential and longitudinal experimental results for these specimens are shown in Table 6-3 and Table 6-4 respectively.

Table 6-3: Nominal Stress–Stretch response of specimens in the circumferential direction.

Loading Protocol $P_{\theta\theta}:P_{LL}$	Nominal Stress (kPa)	Stretch						Aver. Stretch	Stand. Dev.
		V1	V2	V3	V4	V5	V6		
1:1	39.24	1.014	1.006	1.005	1.008	1.017	1.013	1.010	0.005
	78.48	1.028	1.008	1.014	1.028	1.025	1.023	1.021	0.008
	117.72	1.043	1.018	1.024	1.039	1.043	1.032	1.033	0.011
	156.96	1.059	1.031	1.036	1.053	1.067	1.040	1.048	0.014
1:0.75	39.24	1.020	1.011	1.008	1.016	1.025	1.016	1.016	0.006
	78.48	1.036	1.018	1.018	1.028	1.044	1.029	1.029	0.010
	117.72	1.057	1.031	1.029	1.054	1.074	1.041	1.048	0.017
	156.96	1.075	1.045	1.043	1.072	1.094	1.061	1.065	0.020
1:0.5	39.24	1.025	1.019	1.007	1.020	1.026	1.020	1.019	0.007
	78.48	1.051	1.032	1.023	1.045	1.055	1.032	1.040	0.013
	117.72	1.073	1.050	1.036	1.066	1.086	1.057	1.061	0.018
	156.96	1.098	1.067	1.056	1.090	1.110	1.074	1.082	0.020

Loading Protocol $P_{\theta\theta}:P_{LL}$	Nominal Stress (kPa)	Stretch						Aver. Stretch	Stand. Dev.
		V1	V2	V3	V4	V5	V6		
0.75:1	29.43	0.990	1.005	0.998	1.007	1.011	1.008	1.003	0.008
	58.86	1.002	1.002	1.002	1.013	1.018	1.010	1.008	0.007
	88.29	1.012	1.009	1.004	1.019	1.029	1.010	1.014	0.009
	117.72	1.020	1.008	1.010	1.025	1.036	1.020	1.020	0.010
0.5:1	19.62	0.996	1.006	1.000	0.993	1.000	1.003	1.000	0.005
	39.24	0.990	1.000	0.998	0.998	0.999	1.004	0.998	0.005
	58.86	0.990	0.999	0.999	0.998	1.006	1.003	0.999	0.005
	78.48	0.984	0.992	0.991	1.000	0.999	0.994	0.993	0.006

Table 6-4: Nominal Stress–Stretch response of specimens in the longitudinal direction.

Loading Protocol $P_{\theta\theta}:P_{LL}$	Nominal Stress (kPa)	Stretch						Aver. Stretch	Stand. Dev.
		V1	V2	V3	V4	V5	V6		
1:1	39.24	1.021	1.027	1.021	1.011	1.028	1.021	1.021	0.006
	78.48	1.047	1.049	1.041	1.028	1.051	1.031	1.041	0.010
	117.72	1.068	1.064	1.058	1.049	1.075	1.047	1.060	0.011
	156.96	1.101	1.079	1.074	1.065	1.101	1.057	1.080	0.018
1:0.75	29.43	1.014	1.025	1.018	1.007	1.023	1.014	1.017	0.006
	58.86	1.024	1.034	1.026	1.015	1.037	1.022	1.026	0.008
	88.29	1.045	1.046	1.037	1.022	1.044	1.029	1.037	0.010
	117.72	1.061	1.054	1.041	1.030	1.056	1.033	1.046	0.013
1:0.5	19.62	1.006	1.018	1.008	1.002	1.007	1.009	1.008	0.005
	39.24	1.005	1.018	1.011	1.004	1.012	1.009	1.010	0.005
	58.86	1.012	1.021	1.011	1.001	1.014	1.008	1.011	0.006
	78.48	1.016	1.021	1.013	1.002	1.019	1.006	1.013	0.008

Loading Protocol $P_{\theta\theta}:P_{LL}$	Nominal Stress (kPa)	Stretch						Aver. Stretch	Stand. Dev.
		V1	V2	V3	V4	V5	V6		
0.75:1	39.24	1.033	1.036	1.021	1.020	1.033	1.022	1.028	0.007
	78.48	1.069	1.052	1.049	1.037	1.058	1.040	1.051	0.012
	117.72	1.094	1.073	1.068	1.054	1.090	1.060	1.073	0.016
	156.96	1.127	1.098	1.090	1.082	1.124	1.072	1.100	0.022
0.5:1	39.24	1.030	1.037	1.036	1.025	1.039	1.028	1.033	0.005
	78.48	1.068	1.060	1.055	1.046	1.071	1.047	1.058	0.010
	117.72	1.105	1.094	1.076	1.074	1.107	1.068	1.087	0.017
	156.96	1.156	1.113	1.105	1.098	1.151	1.093	1.119	0.028

The model for each specimen is derived and the experimental data of the six specimens is averaged. The material coefficients together with the three parameters used for comparison, are shown in Table 6-5.

Table 6-5: Model parameters for average and individual specimen, Anisotropy factor (AI), peak Green strain ratio and W values.

Specimen	b_0(kPa)	b_1	b_2	b_3	*AI*	E_{LLmax} /$E_{\theta\theta max}$	W_{60} (kPa)	R^2
V1	2787.43	0.48	0.35	0.24	1.18	1.76	1.91	0.98
V2	2482.89	0.83	0.50	0.34	1.29	2.62	1.48	0.92
V3	1278.27	1.96	1.10	0.74	1.33	2.06	1.31	0.97
V4	3205.90	0.51	0.47	0.27	1.04	1.25	1.41	0.98
V5	2590.61	0.45	0.36	0.21	1.12	1.54	2.13	0.97
V6	3784.70	0.51	0.42	0.25	1.09	1.43	1.29	0.97
Composite Average	3716.25	0.45	0.33	0.21	1.17	1.77	1.58	0.98

Also the **S-E** plot of the composite average (experimental data and material model) is displayed in Figure 6-8.
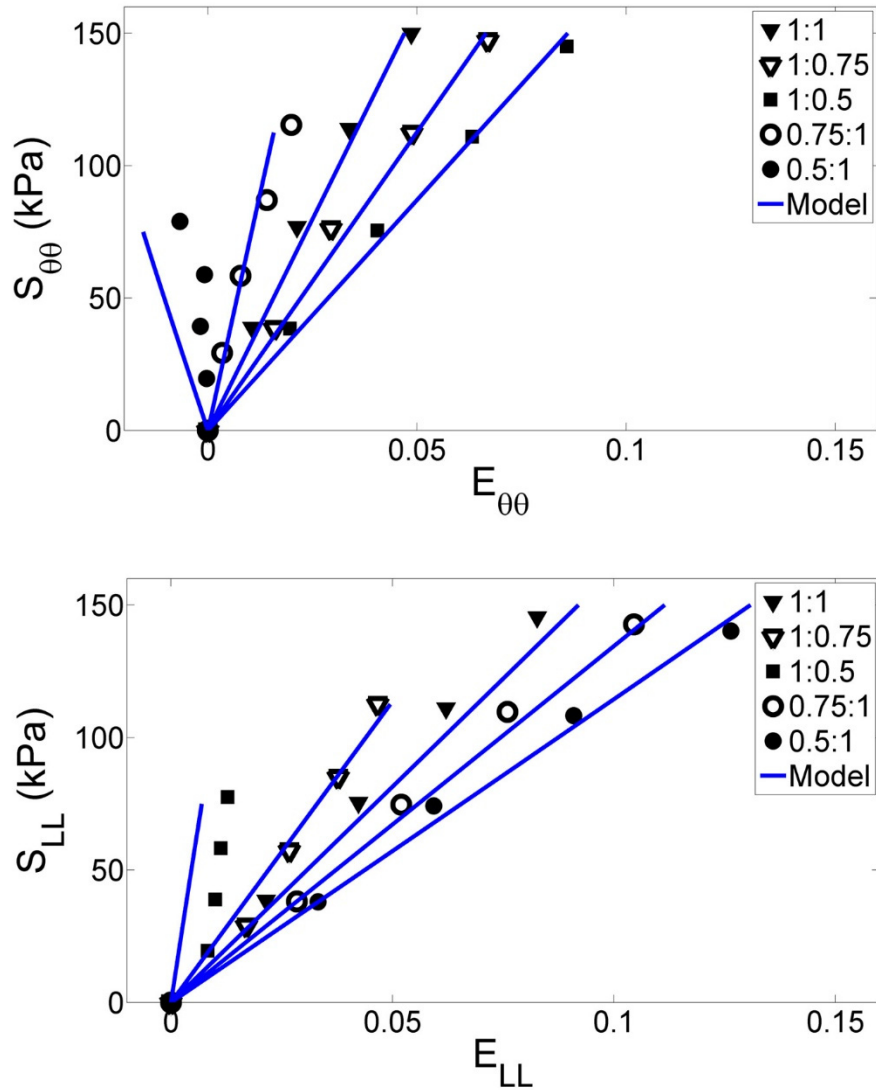
Figure 6-8 S-E plots of the composite average with the corresponding material model for the circumferential (left) and longitudinal (right) direction.

Prior to manufacture the AAA phantom, the influence of the fiber diameter is analyzed. To this end, two specimens are manufactured with the same composite parameters but a different number of fibers (Figure 6-9).
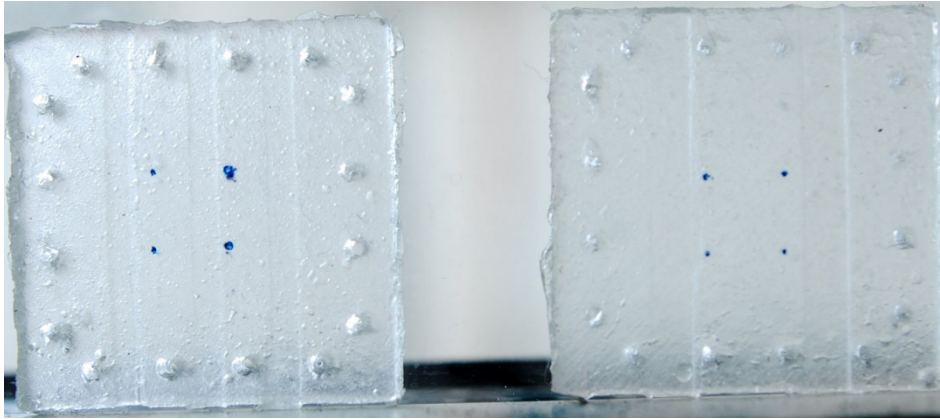
Figure 6-9 Composite specimens with three (left) and two (right) embedded fibers.

Both specimens are biaxially tested and the models, illustrated in Figure 6-10, are derived from the experimental data. As it can be appreciated in Table 6-6, the results are similar, indicating that fiber diameter is not as critical as the other composite parameters. Therefore, the anisotropy would be mainly defined by the fiber proportion and increasing the number of fibers (reducing the fiber diameter) would make the anisotropy more local.

Table 6-6: *AI*, Green strain ratio and W comparison for composite specimens with two and three fibers.

# fibers specimen	*AI*	$E_{LLmax}/E_{\theta\theta max}$	W_{60} (kPa)
2	1.33	1.96	1.32
3	1.24	1.89	1.28
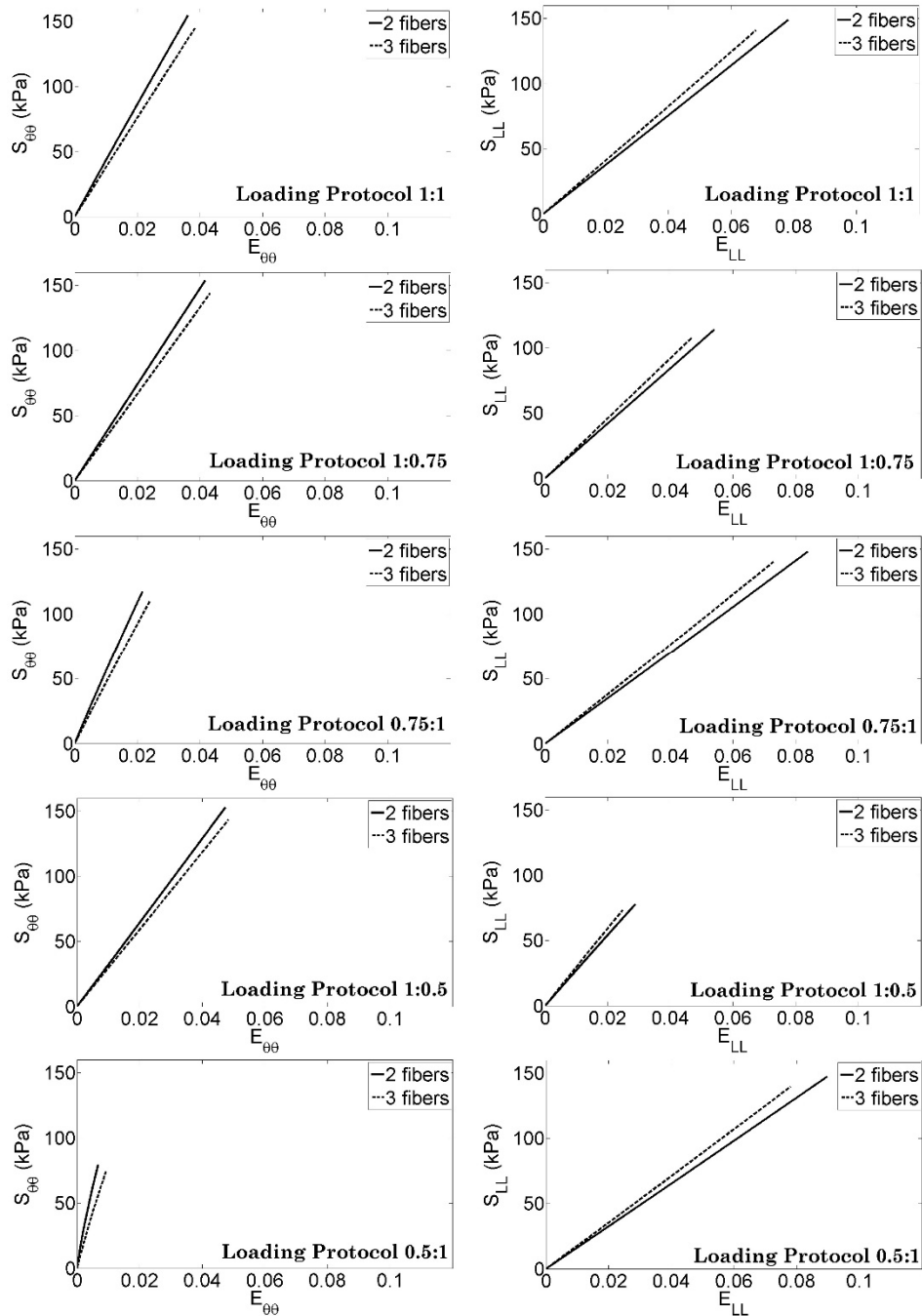
Figure 6-10 Comparison of material model for specimens with two and three fibers for the different loading protocols.

6.3 Synthetic AAA manufacturing methodology

Once the desired properties of the composite are selected, i.e. fiber proportion, and matrix and fiber components, the process for creating anisotropic AAA phantoms is carried out.

First, the dimensions of the fibers need to be calculated. Due to the nonuniformity of the AAA wall thickness, the fiber dimensions should be variable in order to achieve the desired f along the whole AAA phantom. To this end the following process (Figure 6-11) is followed:

- The AAA geometry is divided into 10 mm slices using MAGICS v16.02 (Materialise, Leuven, Belgium).
- Each slice is divided into eight parts. For each part, the average thickness is measured.
- Finally, the appropriate fiber dimensions for each slice is designed by considering the selected value of f.
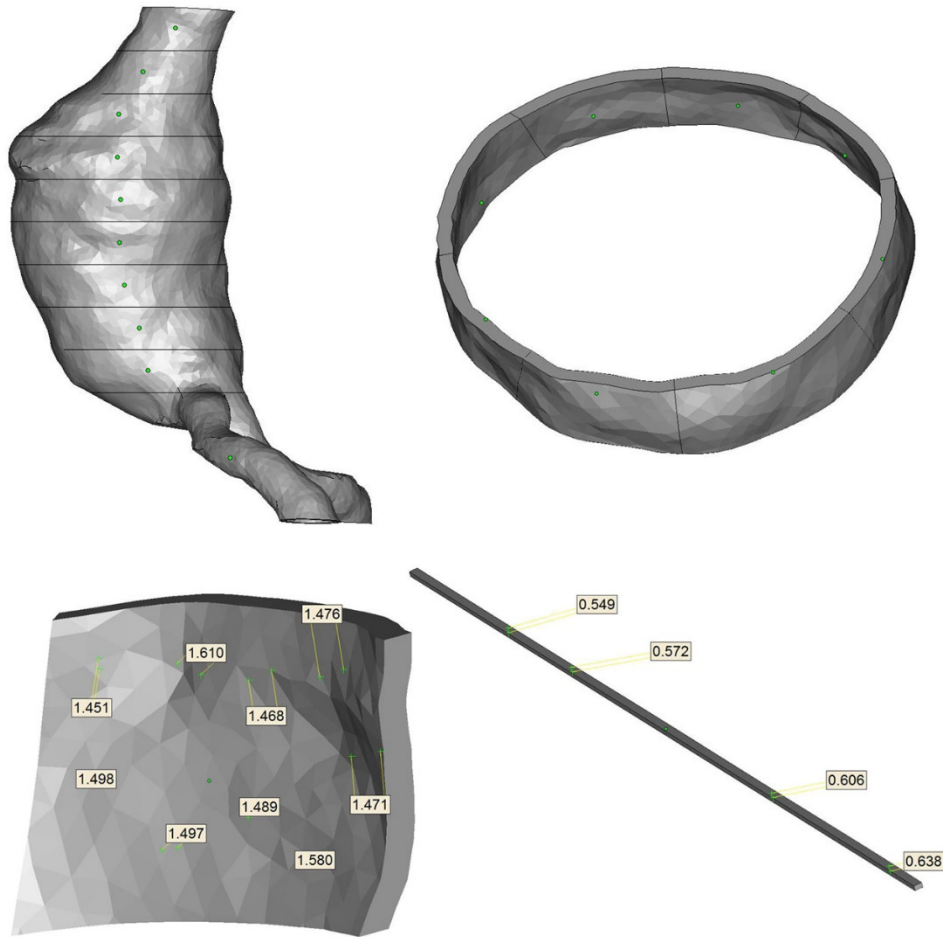
Figure 6-11 Process for designing the fibers: AAA geometry divided into 10 mm slices (top-left), slices divided into eight parts (top-right), thickness measurement (bottom-left) and fiber design (bottom-right).

Then, to manufacture the anisotropic AAA phantom, the procedure is similar to the one explained in Chapter 5, but with some intermediate steps to embed the fibers. The inclusion of the fibers precedes the vacuum casting with PUR resin. Each fiber is attached to the external surface of the wax mold by gluing its two ends with cyanoacrylate glue, i.e. Superglue 3 (Loctite, Düsseldorf, Germany). Each fiber is fixed along the circumferential direction, as illustrated in Figure 6-12. Next, the wax mold with its fibers is placed inside the silicone mold. The process continues with the casting, the subsequent curing process inside an oven at 45ºC, and the wax melting process at 85ºC to finally

obtain the anisotropic AAA replica. The entire process can be completed in less than 3 days.

Figure 6-12 PUR fibers attached to the wax inner mold (left) and as a part of the final anisotropic AAA physical replica (right).

The AAA phantom is created with the same properties of the tested specimen #4. To analyze whether the behavior of the AAA phantom is similar to the composite, two square specimens (P1 and P2) are cut for subsequent biaxial analysis. Prior to tensile tests, the sample thickness is averaged by measuring it ten times with a digital caliper. The same protocol, as defined previously, is followed for the biaxial analysis. The experimental results and material model of these two specimens are illustrated in Figure 6-13 together with the average composite behavior.
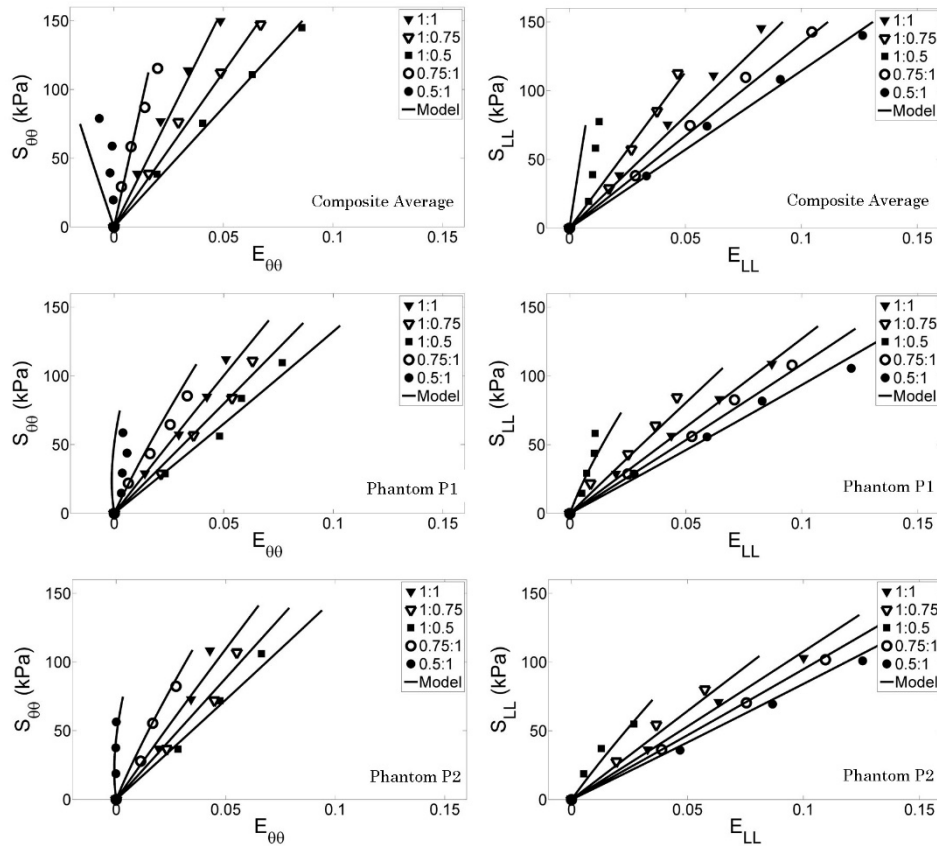
Figure 6-13 S-E plots of the composite average (top) and phantom specimen experimental data with the corresponding material model for the circumferential (left) and longitudinal (right) direction.

The material parameters of the phantom specimens are shown in Table 6-7. The results derived from the AAA phantom specimens are similar and the differences in AI, $E_{LL,max}/E_{\theta\theta,max}$ and W_{60} between the composite specimens and AAA phantom specimens are not statistically significant, with p-values equal to 0.871, 0.764 and 0.053, respectively.

Table 6-7: Model parameters for average and phantom specimens, Anisotropy factor (AI), peak Green strain ratio and W values.

Specimen	b_0(kPa)	b_1	b_2	b_3	*AI*	$E_{LLmax}/E_{\theta\theta max}$	W_{60} (kPa)	R^2
Composite Average	3716.25	0.45	0.33	0.21	1.17	1.77	1.58	0.98
P1	2696.18	0.45	0.35	0.19	1.14	1.81	2.15	0.96
P2	3906.77	0.33	0.21	0.12	1.24	1.98	2.29	0.96

6.4 Conclusions

This chapter describes a methodology for manufacturing patient-specific replicas of arteries with regionally varying wall thickness and anisotropic behavior. By varying the composite parameters (f, E_m and E_f), different mechanical properties and grades of anisotropy can be achieved. Once the desired composite parameters are defined, the AAA phantom can be fabricated with similar mechanical properties, always considering a small deviation.

Two simplifications were made in this study. The first one is the omission of the thrombus and calcifications, present in 75% of AAAs [167,198], as they are beyond the scope of this study. However, the inclusion of the thrombus in idealized AAA replicas was studied by Corbett et al. [189] and could be implemented in this methodology in an analogous way. The second simplification is that AAA tissue behavior was mimicked as quasi linear, while several studies [64,68,70,73,199] have revealed the nonlinear behavior of AAA tissue. However, the stress-strain curves reported in those studies were obtained under a zero-stress condition, and such conditions neglect the fact that in-vivo tissue is exposed to a stressed configuration [148,149]. The residual strain [151] when tissue is excised was not contemplated either. Thus taking these factors into consideration, a realistic AAA replica should mimic the second region of the curve, which explains why the material properties of the manufactured phantoms were contrasted with that region. Furthermore, small strain ranges in a hyperelastic material can be considered linear since the physiological strain ranges due to the pulsatile hemodynamics are small; thus mimicking the anisotropic range linearly is a first good approach. In

order to compare the grade of anisotropy in the AAA tissue [68] and the selected composite , two parameters were selected: *AI* and the mean peak Green strain ratio ($E_{LL,max}/E_{\theta\theta,max}$). As a measure of overall stiffness, the strain energy at an equibiaxial nominal stress of 60 kPa (W_{60}) was also compared. As mentioned above, in-vivo, the realistic material properties correspond to the linear region of the stress-strain curves (Figure 6-14) (this study has considered that it was above 10 kPa).
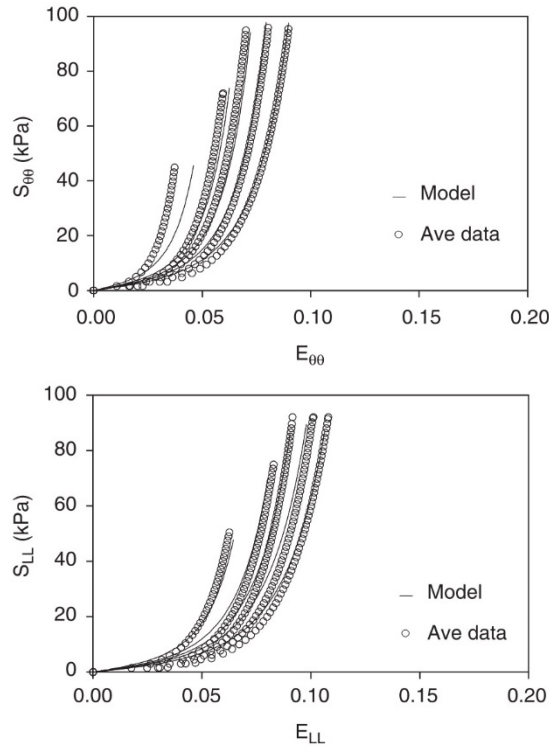
Figure 6-14 Average AAA model derived by Vande Geest et al. [68].

Hence, in order to estimate W_{60} from Vande Geest's data, Equation 6-12 is used.

$$W_{60} = (W_{70} - W_{10}) - \sum_{i=\theta,L}[S_{i,P_I=10}(E_{i,P_i=70} - E_{i,P_i=10})] \qquad (6\text{-}12)$$

As can be observed in Table 6-8, the differences between the AAA samples and the data from the curves obtained in this study are small.

Table 6-8: *AI*, Green strain ratio and *W* compared against Vande Geest's data, composite specimens and AAA phantom specimens.

	AI	$E_{LL,max}/E_{\theta\theta,max}$	W_{60}
Vande Geest (n=26)	1.13±0.27	1.61±1.08	1.25±0.47
Composite (n=6)	1.19±0.07	1.77±0.50	1.58±0.35
AAA Phantoms (n=2)	1.29±0.09	1.89±0.12	2.22±0.09
Composite vs. Van de Geest (%)	3.54	9.94	26.40
Composite vs. Phantom (%)	1.71	6.78	40.51

Comparing the tested composite with Vande Geest's data, the derived differences are relatively low (Table 6-8) and acceptable, with a maximum difference equal to 26.40% in the W_{60} parameter. The differences in the factors measuring the grade of anisotropy are lower than 10%.

As the manufactured AAA phantom has the patient-specific geometry and nonuniform wall thickness, it is not surprising that the difference between the composite and the AAA replica specimens exists because the experiments were not carried out under the same conditions. That is, while the composite specimens were completely planar and had a uniform thickness, the AAA phantom specimens were not perfectly planar due to curvature, and the thickness varied due to the patient-specific AAA geometry. Both factors influenced the experimental results. Another influential factor is the thickness error of the phantom due to the manufacture process (average dimensional mismatch of 180 microns, Chapter 5), which changes the proportion of the fibers and thus the mechanical properties. These issues are responsible of differences between AAA phantom specimens and composite specimens. The factor W_{60} is different between them (p=0.053) with an average difference equal to 40.51%. AI index and Green strain ratio do not differ significantly between the phantom and composite specimens (p=0.871 and p=0.764), with differences lower than 7%.

It must be pointed out that the fibers employed in this study do not want to imitate the wavy and dispersed distribution of collagen fibers and neither its thickness (0.8-2.4 μm); that cannot be achieved even with a 3D printer. The purpose of including the fibers is to provide the AAA phantom with anisotropic behavior at a macro scale, which was verified with the experiments.

Finally, Additive Manufacturing is a promising alternative technology, and the considerable evolution over the last decade now makes multi-material 3D printing possible. The development of the multi-material technology may allow anisotropic AAA phantoms to be printed and this issue will be studied in Chapter 7. However, as commented in Chapter 5, this technology still has some drawbacks as the initial investment (around 120,000€ for multi-material 3D printers) and the issue with removing the support material.

Anisotropic AAA replicas via Additive Manufacturing

7.1 Introduction

In the last two chapters, an affordable methodology has been developed to manufacture isotropic and anisotropic AAA phantoms via vacuum casting technique. The purpose of this chapter is to use the multi-material additive manufacturing (also known as 3D printing) strategy for manufacturing idealized AAA replicas with anisotropic behavior. The 3D printer used in this study is the Objet260 Connex 2 (Stratasys Ltd., Minneapolis, MN, USA) based on the Poly-Jet technology.

In section 7.2, the characterization process of the anisotropic specimens is explained, while the process of design and manufacturing

of the AAA phantom with anisotropic behavior is described in section 7.3.

7.2 Material characterization

In his section, the available flexible materials of the 3D printer are uniaxially tested. Then, following a similar procedure as in the previous chapter, different anisotropic composite specimens are manufactured and biaxially tested.

7.2.1 Uniaxial tensile tests

As in Chapter 5, tensile test specimens are designed in accordance with ASTM D412 Type B. The dog-bone specimens are designed in CREO 3.0 and printed with the Objet 260 Connex 2 with the available flexible materials. The flexible material TangoPlus (codename Fullcure 930) is mixed in different proportions with the rigid material Vero Clear (codename Fullcure 810) to obtain seven different flexible materials (Table 7-1). For each material, two specimens are manufactured.

Table 7-1: Materials selected for manufacturing the specimens.

Material #	3D Printer Material
1	Tango Plus FLX930
2	FLX9940-DM
3	FLX9950-DM
4	FLX9960-DM
5	FLX9970-DM
6	FLX9985-DM
7	FLX9995-DM

All specimens are pre-conditioned at 20ºC (± 1ºC) and 40% (± 5%) relative humidity prior to testing. Tensile tests are performed on the specimens to generate force-extension data using the INSTRON MINI 44 tensile test machine. Each specimen is subjected to a cross-head speed of 3.4 mm/min until failure with pre-conditioning for 10 cycles to 7.5% of the gauge length. The load-displacement outputs from the tensile test machine are normalized to stress-strain data.

The stress-strain curves for one of the specimens of each material is shown in Figure 7-1. Several points should be commented. Firstly, all the materials present a quasi linear behavior, with the exception of the material FLX9995, that present two different slopes, one until 0.1 strains and the second one beyond that point. The second point to mention is the noise recorded when testing: the softer is the material, the higher the noise.

Mechanical properties for each material are reported in Table 7-2:

- The mean stiffness and the standard deviation is calculated by averaging the slope of the two linear trend lines that fit experimental data of the two specimens. The worst R^2 value among all specimens is 0.88 (FLX9995) since it does not have a linear behavior.
- The strength for each material is calculated averaging the individual strength values from the experimental curves of the two specimens.
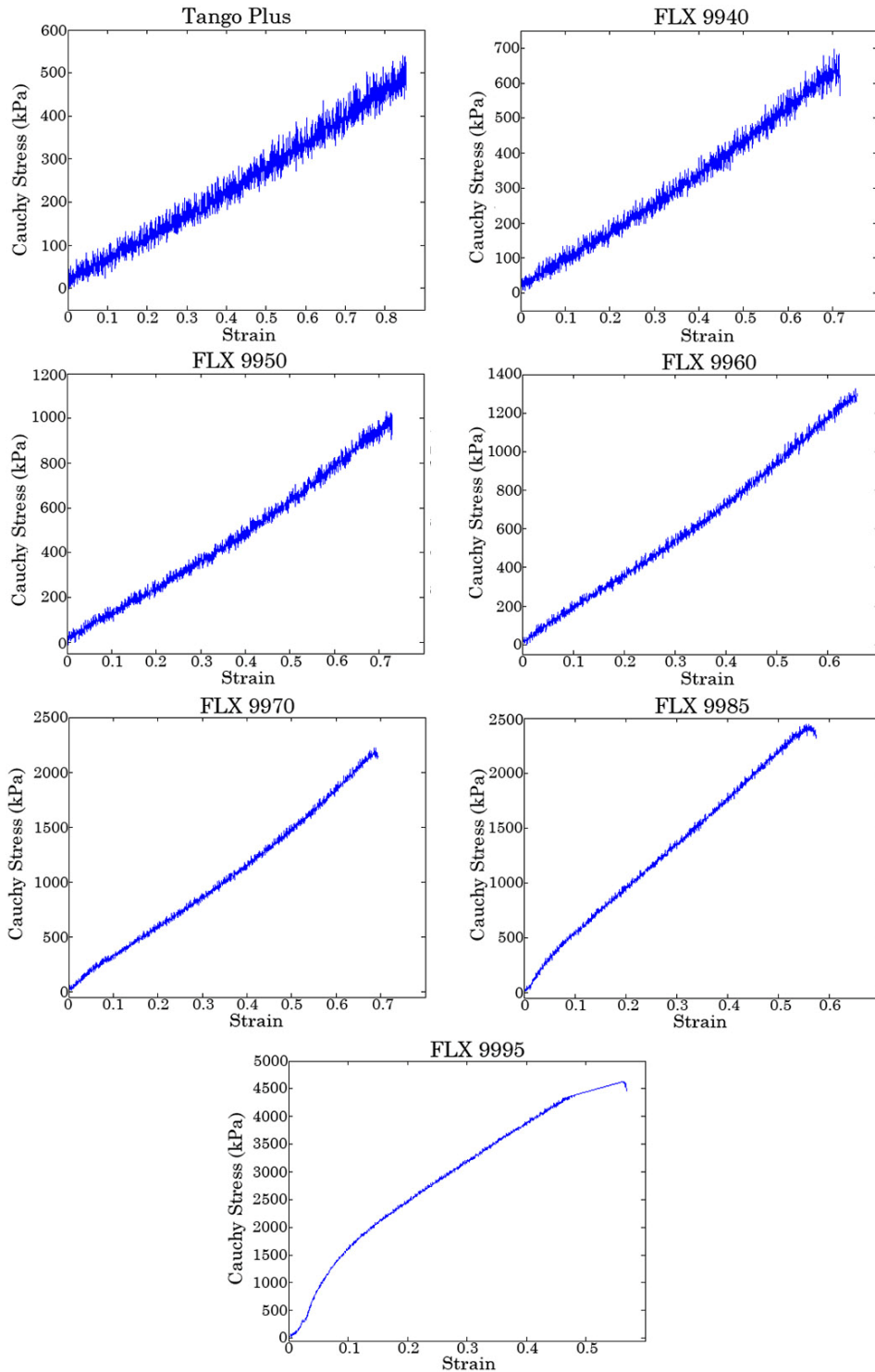
Figure 7-1 Stress-strain curves of the available flexible materials.

Table 7-2: Average Young modulus of tested digital materials and standard deviation; and strength.

Material #	Young's modulus (kPa)		Strength (kPa)
	Mean (R^2)	STD	
1	566.70 (0.98)	1.98	561
2	875.95 (0.99)	2.47	735
3	1275.00 (0.99)	23.33	1010
4	1908.20 (0.99)	22.06	1335
5	2961.25 (0.99)	78.56	2033
6	4482.05 (0.99)	68.24	2464
7	9328.35 (0.88)	383.32	4635

7.2.2 Biaxial tensile tests

Once the available flexible materials for the 3D printer are uniaxially tested, the anisotropic composite specimens can be considered. The composite specimens have a quadrangular shape of 25 x 25 mm with 2 mm in thickness. Various fibers are embedded in the inside of each specimen (Figure 7-2).
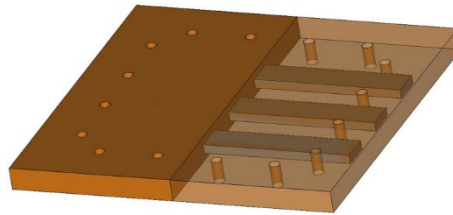
Figure 7-2 Composite specimen featuring three fibers.

In this study, two different composites (C1 and C2) are fabricated varying the proportion of fibers *f,* the matrix material and the fiber material. The properties of each composite are displayed in Table 7-3. These properties will define the mechanical behavior of the composite. For each composite, two specimens (a and b) are manufactured and tested; and their results compared against the response of AAA human tissue published by Vande Geest [68].

Table 7-3: Composite properties: fiber proportion *f*, matrix material and fiber material.

Composite #	Matrix Material	Fiber Material	*f*
1	2	4	0.15
2	3	4	0.15

Biaxial tests on each specimen are conducted in a similar way than the explained in Chapter 6; and the strain energy function *W* developed by Choi and Vito (Equation 6-7) is used for modelling the response of the tested composites. The representative ***S-E*** plots of the experimental data and the corresponding material model, are illustrated in Figure 7-3 for each tested specimen.

The material parameters for the composite specimens and the respective coefficient of determination (R^2) are reported in Table 7-4. In addition, as done in Chapter 6, three additional parameters are added in this table: the anisotropic factor *AI* (Equation 6-11), the ratio between the maximum Green strain in the longitudinal and circumferential directions ($E_{LL,max}/E_{\theta\theta,max}$); and as a measure of overall stiffness, the strain energy at an equibiaxial nominal stress of 60 kPa (W_{60}).

Table 7-4: Model parameters for individual composite specimens fits to Equations (6-7)-(6-10), Anisotropy factor (*AI*), peak Green strain ratio and *W* values.

Specimen	b_0(kPa)	b_1	b_2	b_3	*AI*	$E_{LLmax}/E_{\theta\theta max}$	W_{60} (kPa)	R^2
C1-a	4685.50	0.40	0.24	0.15	1.31	2.31	1.67	0.98
C1-b	5988.11	0.25	0.18	0.11	1.17	1.68	1.76	0.98
C2-a	7718.04	0.27	0.22	0.10	1.12	1.38	1.29	0.95
C2-b	8977.08	0.24	0.19	0.11	1.12	1.44	1.22	0.95
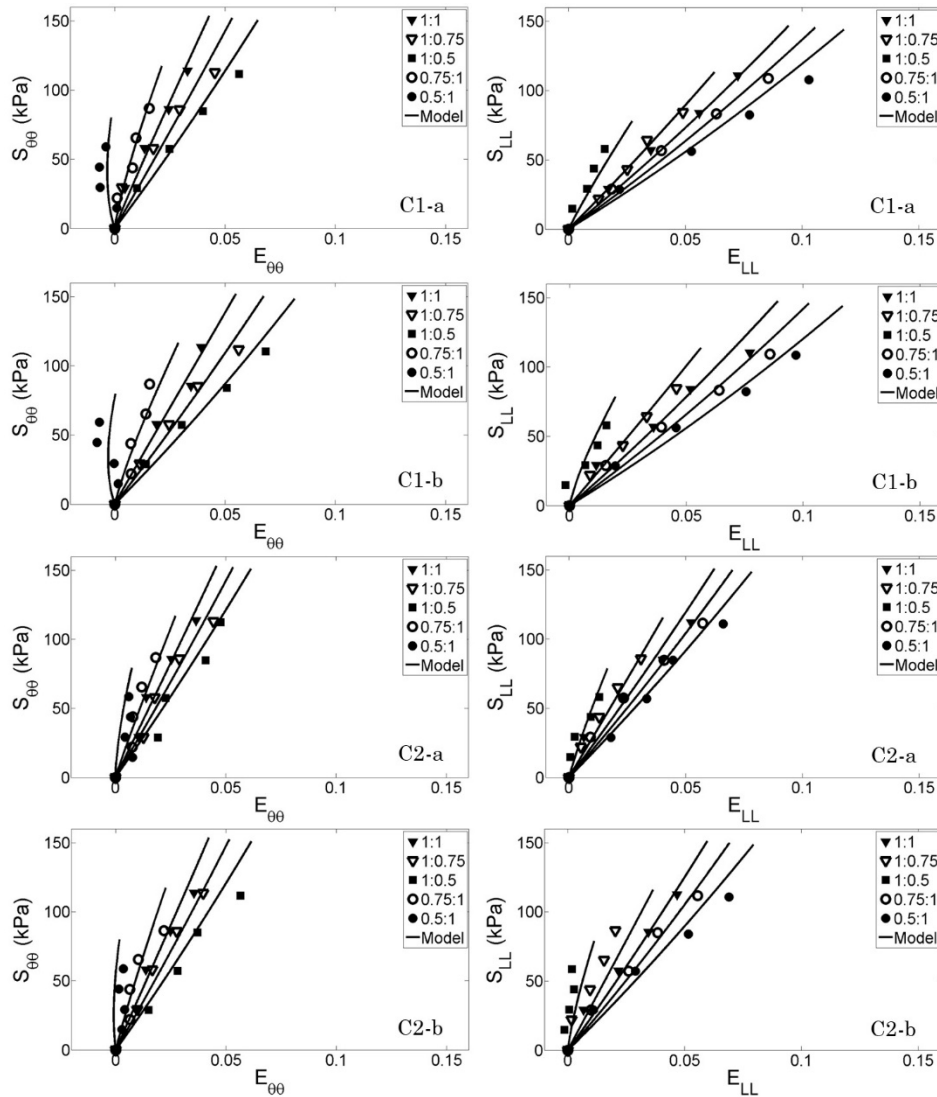
Figure 7-3 S-E plots of the four tested specimens with the experimental data points and material model.

Considering the results of the biaxial tests and comparing them with the AAA tissue behavior from Vande Geest data, as done in the previous chapter, the selected composite to represent the AAA tissue is the composite 2, i.e. f=0.15, Em=1.275 MPa and Ef=1.908 MPa.

With the composite properties defined, the idealized AAA phantom can be designed and manufactured.

7.3 Idealized AAA phantom manufacturing

As a first step, an idealized AAA phantom is manufactured to check whether the anisotropic behavior is equivalent to the composite specimen when the properties of the composite (*f, Em* and *Ef*) are maintained.

To this end, an idealized AAA geometry with a maximum diameter equal to 50 mm, aneurysm length equal to 90 mm and wall thickness equal to 2 mm (as done in previous studies [106,200]) is designed in CREO 3.0. With the fiber volume fraction defined (*f*=0.15), the section of the fiber is calculated. The section of the fiber, which depends on the number of fibers, is constant along the AAA due to the uniform wall thickness of the AAA. The design of the idealized AAA is illustrated in the top image of Figure 7-4. Once the printing process is over, the support material is removed with pressurized water. The resultant printed AAA is shown in the bottom row of Figure 7-4.
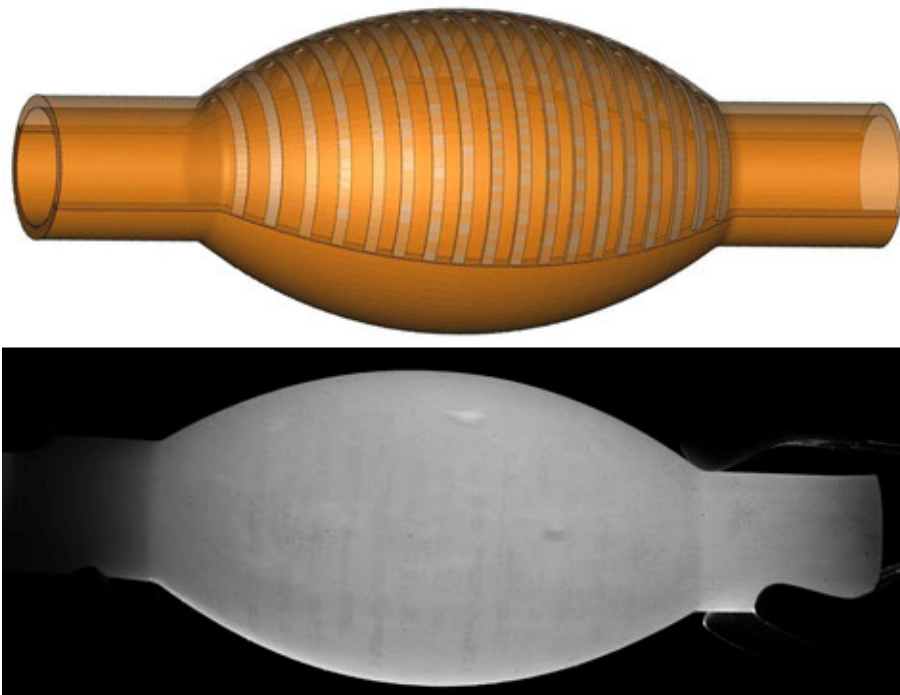
Figure 7-4 Virtual AAA (top), printed AAA (middle) and printed AAA with a flashlight to see the fibers (bottom).

In order to compare the AAA properties with the composite properties, two square specimens are cut from the phantom for subsequent biaxial analysis (Figure 7-5).
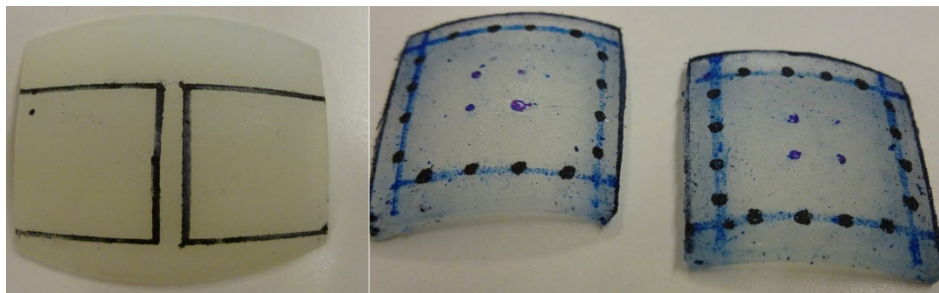
Figure 7-5 AAA phantom specimens.

Both specimens are biaxially tested following the same procedure explained in section 6.1.2. The representative **S-E** plots of the AAA phantom specimens are displayed in Figure 7-6 and the material coefficients are reported in Table 7-5.

Table 7-5: Model parameters for phantom specimens fits to Equations (6-7)-(6-10), Anisotropy factor (*AI*), peak Green strain ratio and *W* values.

Specimen	b_0(kPa)	b_1	b_2	b_3	*AI*	$E_{LLmax}/E_{\theta\theta max}$	W_{60} (kPa)	R^2
P1	8262.29	0.23	0.18	0.10	1.13	1.50	1.37	0.96
P2	7991.49	0.22	0.18	0.09	1.10	1.35	1.48	0.96
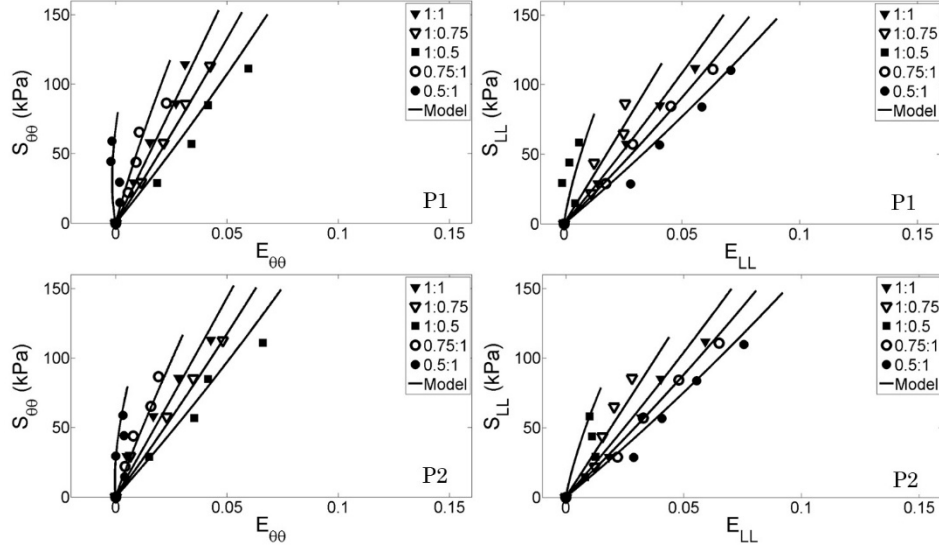
Figure 7-6 S-E plots of the phantom specimens with the corresponding material model for the circumferential (left) and longitudinal (right) direction.

Finally, the experimental results are compared with the data of human AAA tissue from Vande Geest's study. As done in Chapter 6, when comparing the overall stiffness (W_{60}), the second region of the Vande Geest curves (above 10 kPa) is considered. The differences between the selected composite (C2) and the human AAA tissue, as well as the differences between the composite specimens and the phantom specimens are reported in Table 7-6.

Table 7-6: *AI*, peak Green strain ratio and *W* compared against Vande Geest's data, composite specimens and AAA phantom specimens.

	AI	$E_{LL,max}/E_{\theta\theta,max}$	W_{60}
Vande Geest (n=26)	1.13±0.27	1.61±1.08	1.25±0.47
Composite (n=2)	1.11±0.01	1.41±0.04	1.26±0.05
AAA Phantoms (n=2)	1.10±0.01	1.43±0.11	1.43±0.08
Composite vs. Van de Geest (%)	2.21	12.42	0.40
Composite vs. Phantom (%)	0.91	1.05	11.93

The differences of the tested composite and Vande Geest's data are relatively low with a maximum difference equal to 12.42% in the peak Green strain ratio parameter. There also exists an acceptable difference between the tested composite and AAA phantom specimens (maximum difference of 11.93% in W_{60} parameter). One of the reasons of the latter difference could be that while the composite specimens are completely planar, the AAA phantom specimens have a curvature (it can be appreciated in Figure 7-5) that may have an influence on the experimental tests.

7.4 Conclusions

This chapter presents the potential of multi-material additive manufacturing technologies to manufacture AAA phantoms with anisotropic behavior. It should be noted, that as in the previous chapter, the fibers employed in this study are not intended to imitate the wave and dispersed distribution of collagen fibers nor their thickness. The actual purpose of including the fibers is to provide the AAA phantom with anisotropic behavior at a macro scale, which has been verified by the experimental tests. It must be said that due to the printing process (layer by layer) the AM artery has anisotropy in the three directions of impression which cannot be controlled. Nonetheless, in this study this kind of anisotropy has not been detected (it may be negligible).

In this work, only two composite materials have been tested. One of them resembles very well the second region of the actual AAA tissue (Table 7-6). Nonetheless, by varying the composite parameters (*f*, *Em* and *Ef*) different composites with different mechanical properties can be obtained. For instance, for mimicking the first region of the stress-strain curves, the material 1 could be selected as the matrix material. It also should be noted that, in this study, only two specimens are tested for each composite. In order to be more confident with the results and to have a more accurate average response of the composites, more specimens should be tested for each composite.

As a first step, this methodology has been applied to manufacture phantoms with idealized AAA geometries. The following steps will be to apply the methodology to patient-specific AAA geometries with

uniform wall thickness; and then to apply it to patient-specific AAA geometries with nonuniform wall thickness. For these two steps, the design process would be more laborious since the trajectory of the fibers would not be simple circumferences, and in the latter case, the section of the fiber would vary along the AAA wall depending on the local wall thickness.

Additionally, implementing the inclusion of intraluminal thrombus in the AAA phantoms would be an easy task, once the geometry of the thrombus is got in .stl format. The only step to follow is to select for the thrombus a material distinct to the AAA wall's. However, the problem is that currently the material with lowest stiffness is material #1 (E=0.567 MPa), while the thrombus stiffness has been demonstrated to be much lower, in ranges close to 0.060 MPa [201]. Nevertheless, in the future, printing materials with stiffness in that range could be developed.

The main disadvantages of additive manufactured phantoms are the ones commented in preceding chapters. First, the high initial investment for acquiring a multi-material 3D printer (around 120,000€) added to the high cost of flexible materials (around 275€/kg). For instance, the cost of the printed AAA phantom in this study is 67.03€ considering only the material costs. Another drawback concerns the support material; removing it from complicated geometries can be a difficult task, but as commented in Chapter 5, Stratasys is developing a new soluble support material, which will avoid the water jetting.

Experimental verification of AAA wall stress distribution

8.1 Introduction

In the last three chapters different methodologies for manufacturing AAA phantoms with isotropic and anisotropic behavior have been explained. One of the applications where the AAA phantoms have been used among researchers was to predict the AAA rupture site. Doyle et al. [114] confirmed that the actual rupture site of a patient's artery matched the region of peak wall stress predicted by simulations.

There are some options in engineering for directly measuring strains and displacements in a geometric component in order have the strain distribution and to visualize the weakest point of that geometry in terms of strength. However, some of these options are difficult to apply for the AAA phantom:

- One possibility is to use strain gauges on the surface of the artery and, later, obtain the stresses from the strains. However, this approach has several limitations, beginning with the difficulty of attaching the gauge to the surface of an artery. In addition, obtaining the stresses for the inside wall surface would have been complicated as well, due to space limitations to place the gauges.

- 'Photoelasticity' is another strategy. This method was used by Doyle et al. [121] to experimentally measure strain at some points of the AAA model. However, this methodology has drawbacks that can affect accuracy. Firstly, the method only works for perfectly linear elastic photoelastic models. Then, in order to obtain accurate fringe orders that represent the actual strain variation, the normal incidence to the surface is vital. Due to the complex geometries of patient-specific AAAs (irregular structures with several inflection points and changes in curvature on the surface), it would be complex to accurately measure the strain distribution on the entire aneurysm. Additionally, the fringe order measurement may vary slightly depending on the user. Similar to the strain gauges strategy, this method cannot measure the strain on the inner wall.

- Another option is to use a stereoscopic technique, which makes possible to measure locations and displacements in three dimensions by utilizing imaging from different perspectives as a basis for the triangulation of 3D positions. The stereoscopic technique has been utilized with digital image correlation (DIC), for example, in inflating arteries in mice [123]. However, DIC typically relies on statistical correlations instead of an exact match of markers and is dependent on the pattern. Point-tracking was used by Meyer et al. [104], where dots were drawn manually in idealized AAA shapes to measure experimentally strains. The problem with this technique is that to locally measure the strains accurately, the density of markers would have to be high. Stereoscopic techniques would be difficult to apply in many patient-specific AAA geometries that are highly tortuous; that is, there would be regions of the artery not visible

to both cameras. Again, only the outer wall strain can be measured.

As these methodologies have considerable limitations, the purpose of this chapter is to describe and apply a new methodology to numerically verify the predicted AAA wall stress against its counterpart obtained from experimental testing. To this end, a mix of experimental and numerical strategies based on an already validated algorithm [146] is used. To carry out this methodology, four main steps are followed. The first one is manufacturing the AAA phantoms via the vacuum casting technique (section 8.2). The second one will be the scanning of the AAA phantoms -inflated at various pressures- with the help of a Micro Computed Tomography (μCT) scanner (section 8.3). In the third one (section 8.4), the stress distribution in the scanned AAA geometries is going to be calculated via two different approaches: Finite Element Analyses with ADINA and a zero pressure algorithm developed by Riveros et al. [146]. Finally, the numerical AAA stress distribution from ADINA is compared against the AAA stress distribution from the algorithm (section 8.5). The whole process is illustrated in Figure 8-1.
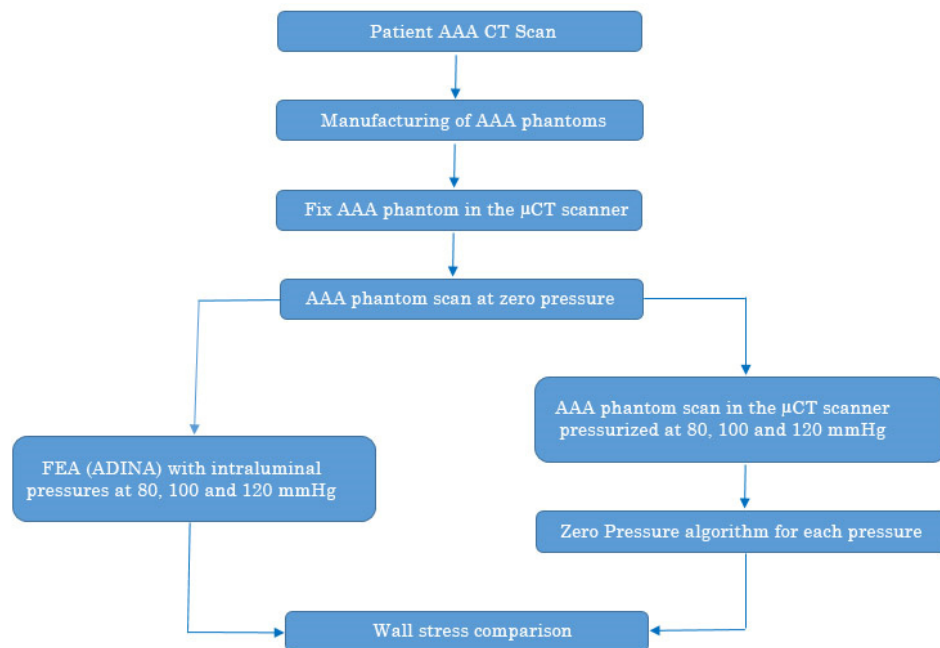
Figure 8-1 Flowchart for the verification of wall stresses.

8.2 AAA phantoms manufacturing

Four AAA isotropic phantoms with variable wall thickness are fabricated using the methodology explained in Chapter 5. To select the appropriate polymers and mixing ratios, the AAA stress-strain data from Raghavan and Vorp [55] is used (Figure 8-2). In that study, the stress-strain data shows a highly nonlinear behavior, with two remarkable regions: the soft region (toe of the stress-strain curve) and a stiffer region (quasi linear). In contrast to Raghavan and Vorp data [55], where AAA data was obtained under a zero-stress condition, in-vivo tissue is always exposed to a stressed configuration ranged between 50 kPa and 200 kPa [148,149]. Considering this pre-stressed configuration, the initial region of the stress-strain curve (from 0 to 50 kPa) is not considered in this work. Thus, the first material to select (soft region) would represent the strain region from 0.05 up to 0.10, while the second material (stiff region) would have to mimic the strain region from 0.10 up to 0.15.
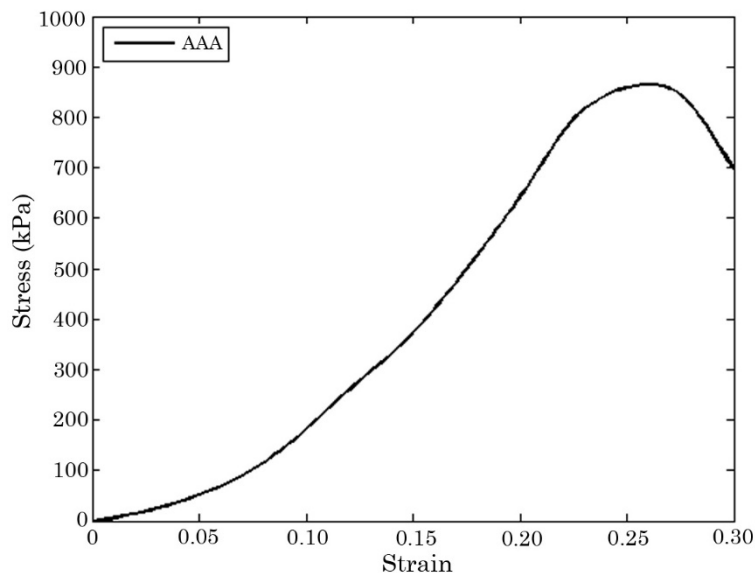
Figure 8-2 Stress strain curves for AAA arteries from Raghavan and Vorp [55].

In order to make the choice of both materials, all polymers uniaxially tested in Chapter 5 are compared against Raghavan and Vorp data. The tested materials with the mixing ratio are shown in Table 5.3. To

this end, the stiffness (slope of stress-strain curves) RMS errors are calculated based on n=100 data points as indicated in Equation 8-1. The polymer and mixing ratio with the lowest RMS error is selected for each of the regions.

$$\text{RMS} = \sqrt[2]{\frac{\sum_{i=1}^{n}(Raghavan\ Stiffness_i - Polymer\ Stiffness_i)^2}{n}} \qquad (8\text{-}1)$$

The material #4 (PUR 7160) is selected for the soft region with an stiffness RMS error equal to 0.39 MPa, while the material #3 (PUR 7190) is selected to represent the stiff region of the curve with a stiffness RMS error equal to 0.12 MPa. The Figure 8-3 illustrates the Raghavan and Vorp AAA stress-strain curve together with the selected materials.
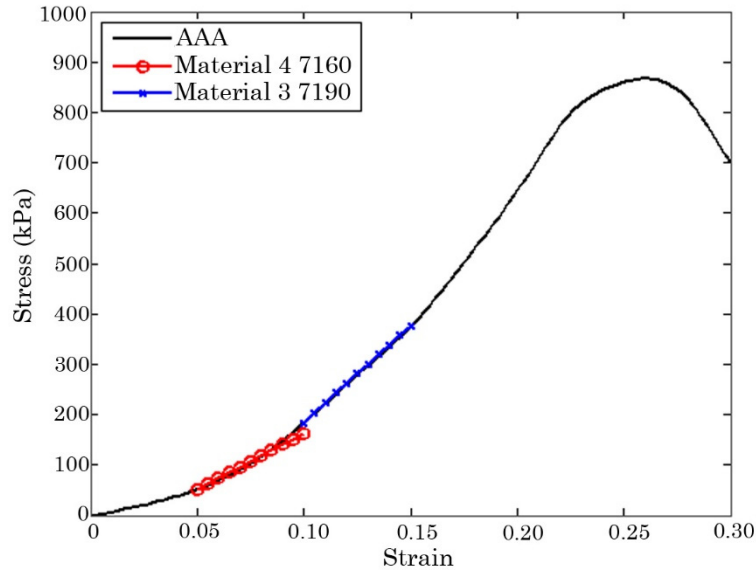
Figure 8-3 Stress strain curves for materials 3 and 4 and ex-vivo experiments for AAA arteries from Raghavan and Vorp [55].

Although each material is close to a linear elastic behaviour, in this work they are defined by the hyperelastic and isotropic two-term Mooney-Rivlin constitutive relation [202] expressed by Equation 8-2

$$W = C_1(I_1 - 3) + C_2(I_2 - 3) \qquad (8\text{-}2)$$

where W is the strain energy, I_1 and I_2 are the first and second invariants of the right Cauchy-Green deformation tensor $\mathbf{C}$, and C_1 and C_2 are the material constants. The experimental data is fit to this model (Figure 8-4) and the model coefficients are derived for each material. The material parameters C_1 and C_2 for the 7160 material are 279.17 and 94.43 kPa respectively, while for the 7190 material are equal to 44.52 and 624.18 kPa respectively. The goodness-of-fit (R^2 values) of the mathematical model are 0.9940 and 0.9506 respectively.
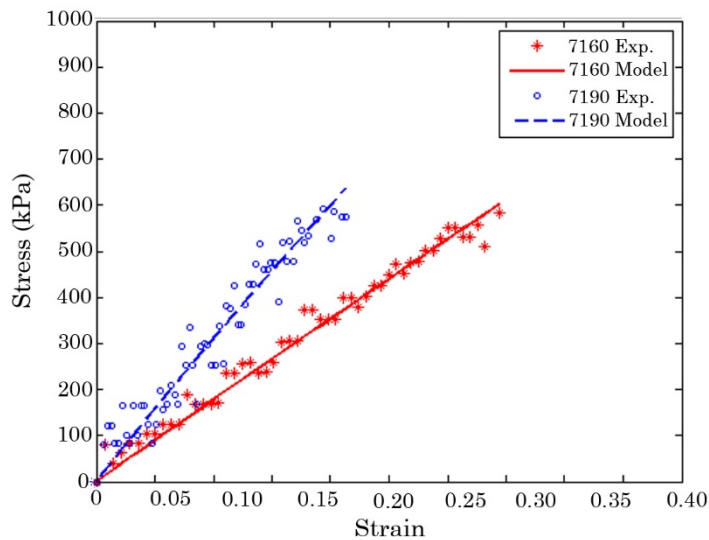
Figure 8-4 Conventional stress-strain diagrams for the 7160 (material #4) and 7190 (material #3) obtained with uniaxial tensile experiments.

Following the procedure explained in Chapter 5, two AAA copies (a and b) are manufactured for each material (Figure 5-7)

8.3 Scanning

Once the AAA phantoms are manufactured, they are tested with a SkyScan 1076 µCT scanner (SkyScan Kontich, Belgium) that features a 3D spatial resolution down to 9 microns (Figure 8-5).

Figure 8-5 SkyScan 1076 µCT scanner.

The proximal neck of each AAA model is connected to a sphygmomanometer while the iliac artery ends are blocked with two plastic caps to avoid any air leakage (Figure 8-6).
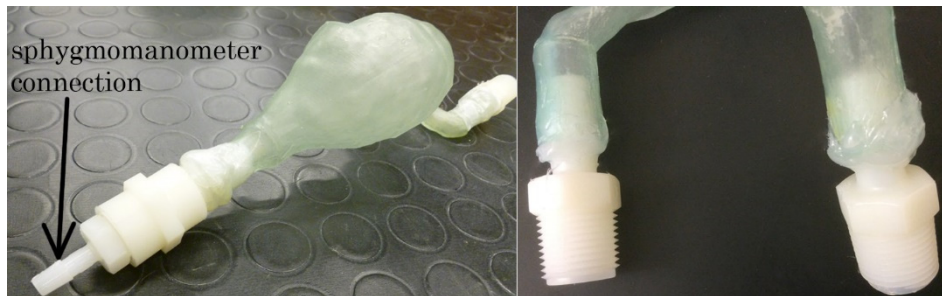
Figure 8-6 AAA phantom with the neck prepared to be connected to the sphygmomanometer (left); and iliac artery ends blocked (right).

Before the scanning process, AAA phantoms are pressurized with the sphygmomanometer for four hours to detect any air leakage. The pressure loss is below 1%. When no air leakage is detected, each phantom is fixed in the scanner (Figure 8-7) and scanned at a pressure of 0, 80, 100 and 120 mmHg with a resolution of 35 µm.
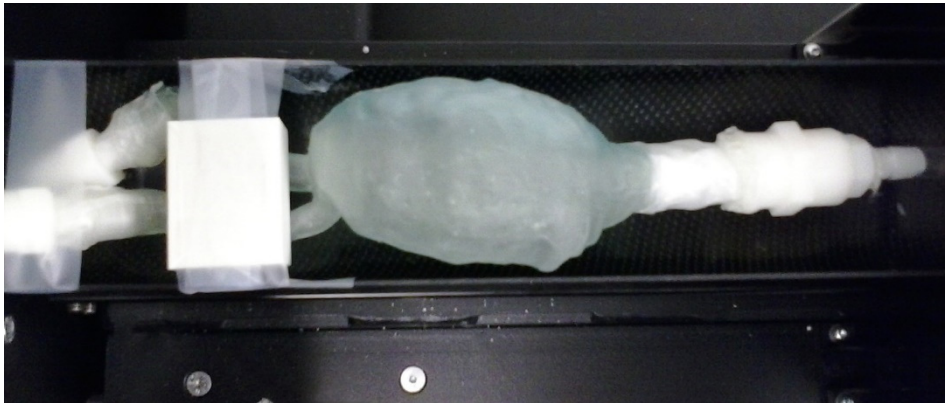
Figure 8-7 AAA phantom fixed in the μCT scanner.

The output from the scanning process is a collection of DICOM files representing cross-sections of the phantom geometry (Figure 8-8). These files are imported to Mimics 11.0 (Materialise, Leuven, Belgium) for segmentation (Figure 8-9).
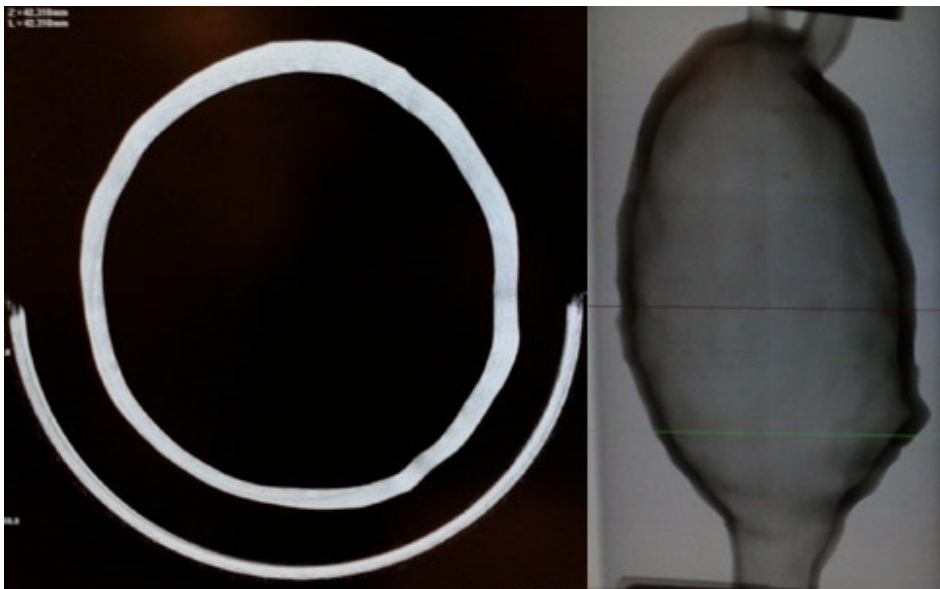
Figure 8-8 DICOM files from the scanning process.
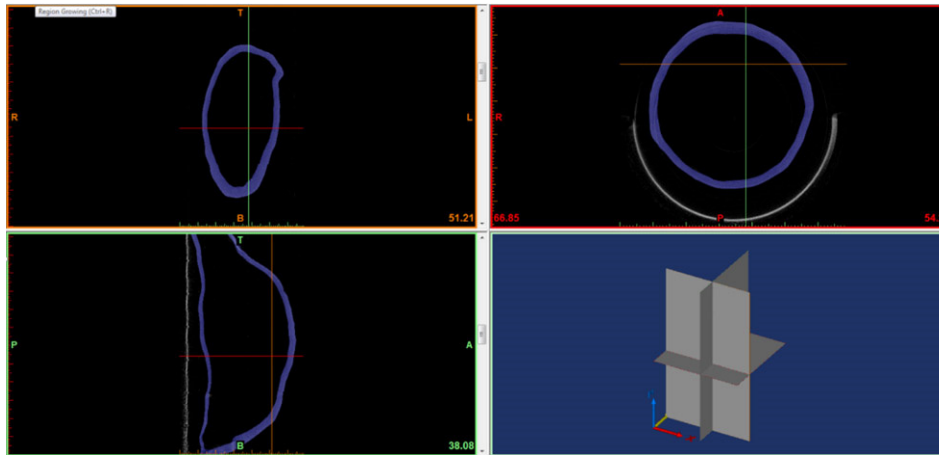
Figure 8-9 Segmentation in Mimics.

After the segmentation process, the files are prepared in 3-Matic (Materialise, Leuven, Belgium) and finally sixteen .stl files are obtained, i.e. two copies of each material scanned at four intraluminal pressures.

8.4 Structural analysis

The .stl files containing the scanned geometries are imported to ANSYS ICEM v14.0 (ANSYS Inc., Canonsburg, PA) for meshing purposes. All geometries are meshed using 4-node tetrahedral elements (Figure 8-10). In order to find the optimal number of elements, a mesh independence study is carried out with one of the geometries scanned at zero pressure. Several simulations are run for different mesh densities by applying a uniform pressure of 120 mmHg to the inner surface of the model. The mesh refinement is done until the average stress difference between the two meshes is negligible (<1%). The mesh independence study indicates the suitability of a 700,000 tetrahedral element mesh for this study, and so forth, the sixteen .stl files are meshed with approximately 700,000 elements.
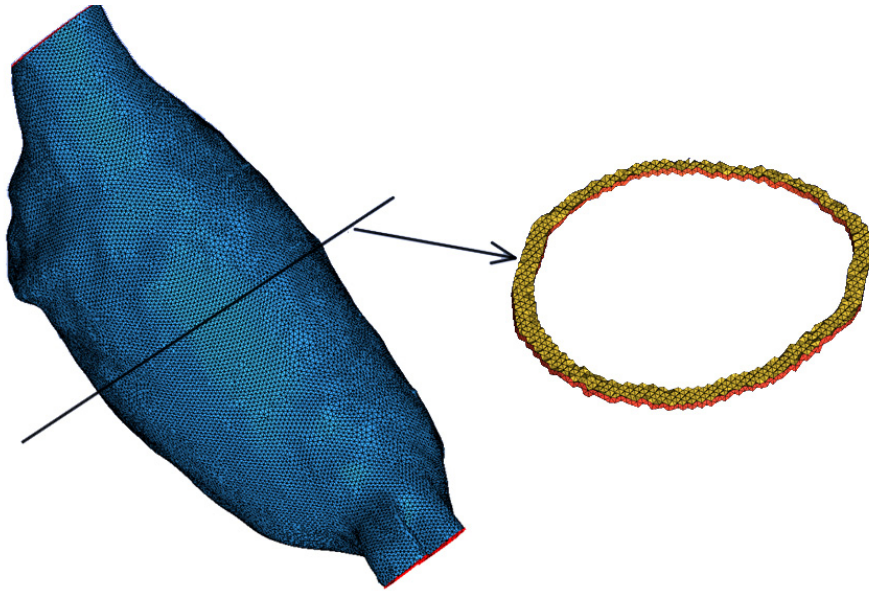
Figure 8-10 Phantom 7160a scanned at 0 mmHg once meshed in ICEM.

After meshing, the Nastran files are imported to ADINA v8.8 (ADINA R&D Inc., Cambridge, MA) for structural analysis. First the numerical analysis via FEA is carried out with the AAA geometries scanned at 0 mmHg; and then the zero pressure algorithm is applied to the AAA geometries scanned at the different intraluminal pressures (80, 100 and 120 mmHg).

8.4.1 Numerical analysis

The Mooney-Rivlin material model (Equation 8-2) is applied to the four geometries with their corresponding material coefficients. To define the near incompressibility of the material, the bulk modulus is calculated for each material using Equation 8-3

$$k = \frac{E}{3(1 - 2\nu)} \tag{8-3}$$

where E is the small strain Young's modulus and ν is the Poisson's ratio, which is 0.49 for both materials.

The computational analyses are performed by constraining the proximal and distal ends to represent the tethering of the aorta. These

are standard boundary conditions used throughout the literature [84,203,204] when analyzing AAAs using FEA. In this work the proximal and distal ends are also fixed during the scanning of the AAA phantoms. The loading condition is established by applying uniform pressures of 80, 100 and 120 mmHg to the inner surface of the FEA model. The Von Mises stress is the primary outcome of the FEA simulations.

8.4.2 Zero pressure algorithm

The stress distribution of the numerical studies should be compared with the experimental data. However, from the experiments only the inflated AAA geometry is available. To obtain the stress distribution in those inflated geometries, a zero pressure iterative algorithm is used. This algorithm was developed by Riveros et al. [146] for isotropic and anisotropic behaviors and it has been employed in other studies [175,205] to derive the zero pressure geometry of patient-specific AAAs. This algorithm was validated by Chandra et al. [206] using an idealized AAA phantom of known constitutive material properties and subjecting it to different intraluminal pressures.

Briefly, this algorithm utilizes the scanned mesh of the pressurized phantom to make an initial approximation of the zero-pressure state by extrapolating the nodal displacements of the outer wall mesh. Then, this zero-pressure mesh is loaded in ADINA to the corresponding pressure and the resulting inflated geometry is compared to the initial scanned mesh. If both meshes are dissimilar, a fixed point iterative algorithm is implemented to make incremental corrections to the nodal coordinates and calculate a new zero-pressure mesh. This new mesh is then inflated and the results compared again with the scanned mesh. If the error is low relative to a prescribed relative percentage difference, the iteration stops. Otherwise, the point fixed algorithm is again implemented and another zero-pressure mesh created. The process continues until the error is lower than the prescribed threshold (0.05%). When the iterative process ends, the wall stress distribution is taken from the last FEA simulation. A representative schema of this algorithm is illustrated in Figure 8-11.
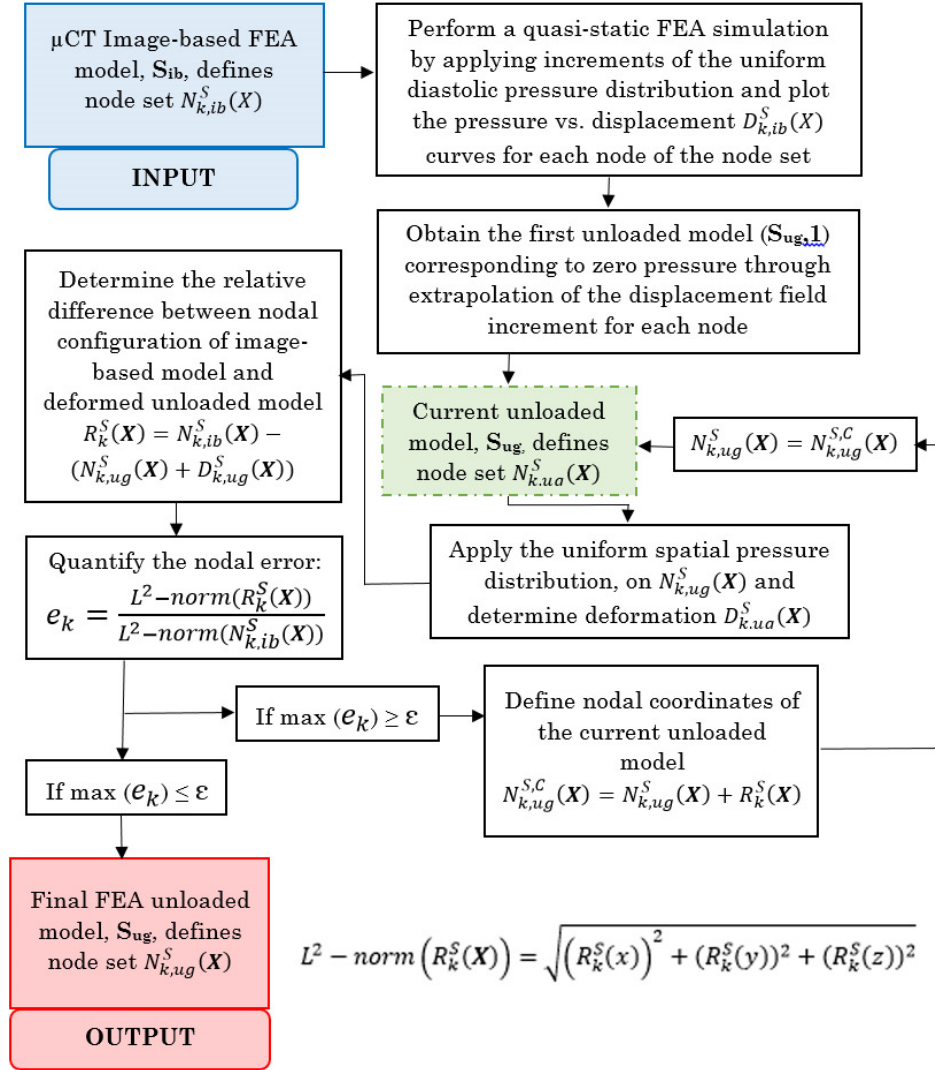
Figure 8-11 Modified flowchart of the zero pressure iterative algorithm to generate a predicted unloaded geometry of the solid domain (S_ug) [206].

This algorithm is applied to the four phantoms scanned at 80, 100 and 120 mmHg to obtain the different unloaded geometries. When applying the corresponding intraluminal pressure to the unloaded geometries ($\boldsymbol{S_{ug}}$), the resultant deformed configuration corresponds to the scanned geometries ($\boldsymbol{S_{ib}}$). This way, the stress distribution data is available for all the scanned AAA phantoms.

8.5 Wall stress verification

In this subsection the wall stress comparison between the outcomes from the numerical studies and the outcomes from the zero-pressure algorithm is made. As an example, Figure 8-12 shows two different viewpoints of the wall stress distribution for the 'a' specimens for both the numerical and experimental studies at an intraluminal pressure of 120 mmHg. The wall stress distribution for the 'b' specimens is similar.
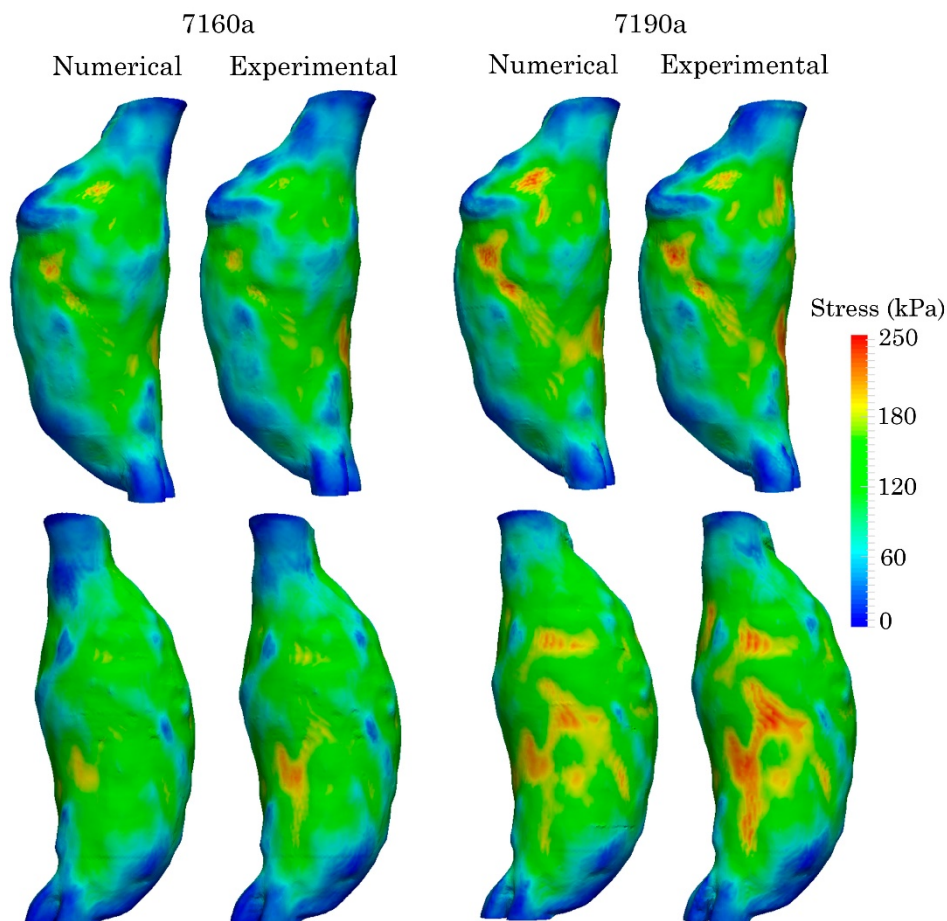
Figure 8-12 Numerical and experimental wall stress distributions for the 7160a and 7190a models with an intraluminal pressure of 120 mmHg.

Two comparisons are made between the experimental and numerical studies.

The first one analyzes the overall differences regarding the average stress of the AAAs. To this end, the 99th percentile wall stress of the mesh elements is taken as an input. The differences are shown in Table 8-1. As it can be observed, the differences between the numerical and experimental studies are negligible: an average difference of 0.26% in the 7160 models and 2.04% in the 7190 models. The maximum difference for the 7160 models is 0.55%, corresponding to the 7160a-P100 (7160a model at a pressure equal to 100 mmHg) phantom. For this case, the average stress in the numerical study is 72.60 kPa while for the experimental one it is 72.21 kPa. For the 7190 models, a difference of 2.59% is the maximum and it is found in the 7190b-P120 phantom. In this case, the numerical and experimental average wall stresses are 94.71 kPa and 97.23 kPa, respectively.

Table 8-1: Differences in 99th percentile wall stress between numerical and experimental studies.

Pressure (mmHg)	99th percentile wall stress difference (%)			
	7160a	7160b	7190a	7190b
80	0.14	0.05	2.01	1.61
100	0.55	0.04	1.73	2.12
120	0.53	0.26	2.18	2.59

The second comparison analyzes the differences of the stress at the Gaussian points of 30 elements located in stress concentration regions (Figure 8-13): 15 are placed on the outer surface and 15 on the inner surface.
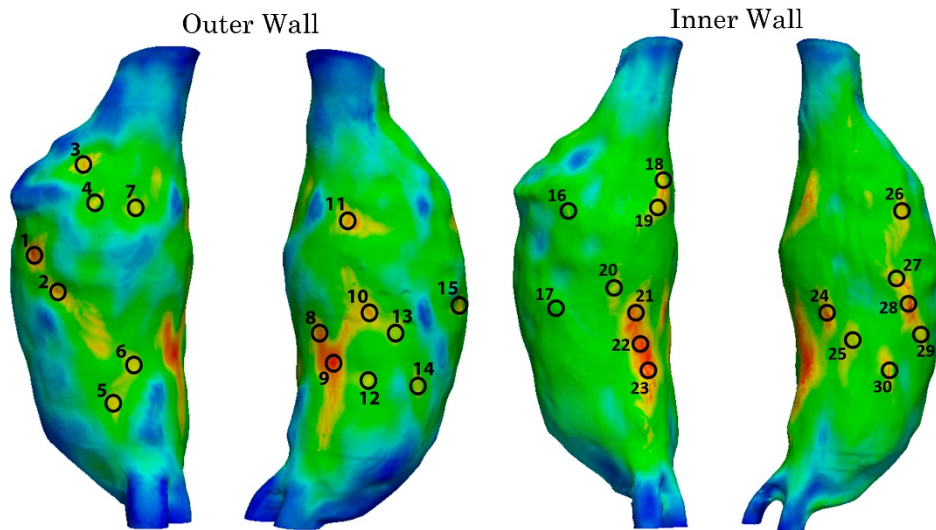
Figure 8-13 The thirty regions of wall stress concentration on the outer (left) and inner (right) wall used for the comparison study.

The comparison is made manually, selecting the peak stress elements for each region. These differences are on average 5.08% and 5.23% in the 7160 and 7190 models respectively. The maximum error is equal to 15.15% and it is found in region #29 of phantom 7160a. Part of this error can be attributed to the manual process to select the element from each of the stress concentration regions: the element is not located at the same coordinates as in the physical phantom. This uncertainty, together with the fact that the elements are found in regions with high stress gradients introduces uncertainty in the estimation of the average relative difference. The average error for each model and pressure is reported in Table 8-2, while in the Appendix C it can be found the difference for all the points.

Table 8-2: Average and standard deviation differences in local wall stresses between numerical and experimental studies.

	Pressure (mmHg)	Average (%) and Standard Deviation (%) for local wall stresses							
		7160a		7160b		7190a		7190b	
		Avg.	SD	Avg.	SD	Avg.	SD	Avg.	SD
Outer Wall	80	5.42	2.90	6.08	3.40	5.51	3.63	5.14	3.37
	100	5.91	3.14	4.93	3.14	4.26	3.68	5.32	3.43
	120	4.68	3.06	5.66	3.99	4.26	3.14	5.77	2.72
Inner Wall	80	5.05	3.94	4.08	3.28	4.66	2.27	5.33	3.68
	100	4.29	2.63	4.38	3.12	6.26	3.74	5.60	3.58
	120	5.44	2.08	5.08	3.47	4.68	3.04	5.91	3.80

8.6 Conclusions

This chapter describes a methodology to experimentally verify the numerical stress analysis using physical tests with AAA phantoms. Due to the high spatial resolution of the µCT scanner (35 microns), the geometry used for the numerical analyses is identical to the one used for the experimental study. In this work, the manufactured AAA phantoms have an isotropic and hyperelastic behavior. However, large human arteries exhibit a more complex biomechanical behavior such as anisotropy. In addition, most AAAs of clinically relevant size have an intraluminal thrombus. As it has been demonstrated in Chapter 6 and 7, the anisotropy can be addressed to the physical phantoms including fibers inside the AAA wall. Also the inclusion of thrombus has been avoided in this work. However, it is possible to introduce it in the physical phantoms: via vacuum casting technique following the steps displayed by Corbett et al. [189]; while via additive manufacturing could be directly implemented. Therefore, in future studies this methodology could be applied with more realistic AAA phantoms, as the zero pressure algorithm developed by Riveros et al. [146] allows considering the anisotropic hyperelastic behavior of the

aortic wall, its thickness and accounts for the presence of the intraluminal thrombus.

An additional simplification in this work is related to the stress-free configuration of the model. The in-vivo AAA was scanned in a loaded configuration and then the phantoms were manufactured. So, in this work the loaded geometry was used; however, the unloaded geometry could have been obtained via different methods [144–146] and used to manufacture the AAA replicas. Subsequently, the same verification methodology could be carried out. Finally, due to the manufacturing process, the AAA phantoms have a variable wall thickness that does not match exactly the patient-specific wall thickness measured from the CT images. This shortcoming does not influence the verification protocol as both numerical and experimental studies were carried out with the AAA phantom geometry obtained from µCT images and, therefore, the wall thickness distribution of the numerical and experimental models is identical. It should be noted that manufacturing the phantoms via additive manufacturing (Chapter 7) would fix the shortcoming related to the wall thickness error.

As a final comment, the explained methodology in this chapter, apart from verifying the AAA wall stress distribution, it could be also appropriate to validate material models. In the last decade, there has been an evolution in AAA manufacturing processes and a variety of materials are now available. When utilizing complex materials, these have to be assessed experimentally to derive a constitutive model. The present work could be useful to test the validity of these models.

Chapter 9:

Conclusions and future work

This chapter presents the main contributions of this thesis project, as well as suggests future lines of research that could complement this work.

9.1 Conclusions

This project makes contributions to three topics: the study of new geometry metrics that can influence AAA wall stress distribution, research on new methodologies for manufacturing AAA replicas and the application of an experimental protocol for verifying AAA wall stress distribution.

The main contributions are:

- We found that the local mean curvature is closely related to wall stress in 30 patient-specific AAA geometries. This work underscores the importance of evaluating AAA mean wall

curvature as a potential surrogate for wall stress, which in turn is related to AAA rupture risk. The predictability of the models using only the maximum diameter is 23.5% and 27.7% for the outer and inner wall surfaces, respectively. By adding the local mean curvature to the predictive model, the predictability increases to 64.9% and 44.7%, respectively, for the outer and inner wall surfaces.

- We developed an affordable vacuum casting technique for manufacturing patient-specific AAA phantoms with regionally varying wall thickness and isotropic material properties. Different materials were uniaxially tested and compared with the AAA tissue. The materials with mechanical properties similar to the AAA tissue were used to manufacture AAA phantoms.

- We implemented a new methodology that uses vacuum casting to manufacture patient-specific AAA replicas with non-uniform wall thickness and an overall anisotropic behavior. A custom-made planar biaxial testing system was designed and fabricated in order to biaxially test different composites. All the composites were compared against the human AAA tissue, and the one that best mimics a prescribed region of the stress-strain curves of the human tissue was selected for the manufacture of anisotropic AAA phantoms. It was verified that the mechanical properties of the phantom correspond to the chosen composite's mechanical behavior.

- The multi-material additive manufacturing (AM) strategy was applied to the manufacture of idealized AAA geometries with anisotropic properties. Different composites were fabricated and biaxially tested, and again, the one that best mimics tissue behavior was selected for the manufacture of the idealized AAA phantom. It was verified that the mechanical properties of the phantom correspond to the composite's mechanical behavior. This strategy requires a bigger investment, but its geometry is more accurate and the mechanical properties are less variable.

- A new experimental methodology was developed for verifying AAA wall stress distribution. This procedure was applied to patient-specific AAA phantoms with isotropic properties. It

uses a µCT scanner to accurately capture the geometry of the AAA phantoms in different loading conditions and a validated zero pressure algorithm to obtain the wall stress distribution in the scanned geometries. Once the wall stress distribution was verified, the influence of the curvature and wall thickness was analyzed confirming the results presented in the conclusion given at the beginning of this list.

9.2 Future work

Work on the three topics covered in this thesis can be continued over several possible future research lines.

Concerning the geometric indices influencing wall stress distribution, these are the proposed future studies:

- In the current research, the local mean curvature was analyzed in 30 patient-specific AAA geometries. This study can be extended to more AAA geometries in order to be more confident of the results.
- In order to get more realistic results, more complex structural studies can be carried out in order to confirm the influence of this geometric parameter. These studies could consider 1) the anisotropic behavior of the AAA; 2) the inclusion of intraluminal thrombus (ILT) in the models; 3) the unloaded configuration of the AAA; and 4) the residual stresses and prestretch conditions.
- A wall stress predictive model that considers the curvature as well as other parameters that have been demonstrated to have influence on wall stress, such as wall thickness, asymmetry, tortuosity, diameter, systolic and diastolic pressure, etc., can be developed. The accuracy of this model could be evaluated with different AAA geometries. With the resulting local wall stress predictive model and a local wall strength predictive model [36], an index like FEARI (considering the wall stress/wall strength ratio) can be calculated and whether it correctly discriminates between ruptured and unruptured AAAs can be verified.

Relative to the manufacture of realistic AAA replicas, the following future lines can be considered:

- Modifying the vacuum casting strategy in order to manufacture anisotropic AAA phantoms that include the ILT in order to get more realistic phantoms. This concern could be addressed similar to the approach explained by Corbett et al. [72].
- The inclusion of electrospun fibers could be of interest, as their diameter could match the range of collagen fiber diameters. However, it should be said that implementing them in a manufacturing process would be a challenging task.
- In this work the multi-material AM technology was applied to fabricate idealized AAA phantoms with anisotropic properties. Apart from testing other composites, the next step would be to apply this technology to patient-specific AAA geometries with regional varying wall thickness.
- Including the ILT in the AM technology could be interesting. However, future flexible materials with stiffness that is similar to the ILT's stiffness should be developed for 3D printing.

Finally, with respect to the experimentation with the AAA phantoms:

- The described methodology for verifying the wall stress distribution can be applied to more realistic AAA phantoms, i.e. considering the anisotropic behavior and the inclusion of ILT (phantoms with these properties could be manufactured).
- Other experiments can be carried out with the AAA phantoms, for instance, benchtop studies with induced flows. The use of transparent materials would make it possible to perform particle image velocimetry (PIV) studies. These experiments could be useful, for example, for verifying the wall shear stress of the numerical fluid structure interaction (FSI) studies.

The role of ILT is still very controversial. While ILT is considered to generate a cushioning effect on the aneurysmal wall stress, it is also known that the wall behind the ILT is weaker and stiffer. Experimental studies with AAA phantoms may help to better understand its effect. Additionally, when manufacturing the

phantoms via AM technology, a different material—one which is stiffer—can be designated for the wall behind the ILT.

Appendix A: Wall stress and mean curvature distribution of synthetic AAAs

This appendix shows the wall stress and mean curvature distribution of the rest of the synthetic AAAs that have not been illustrated in the first study of Chapter 3.
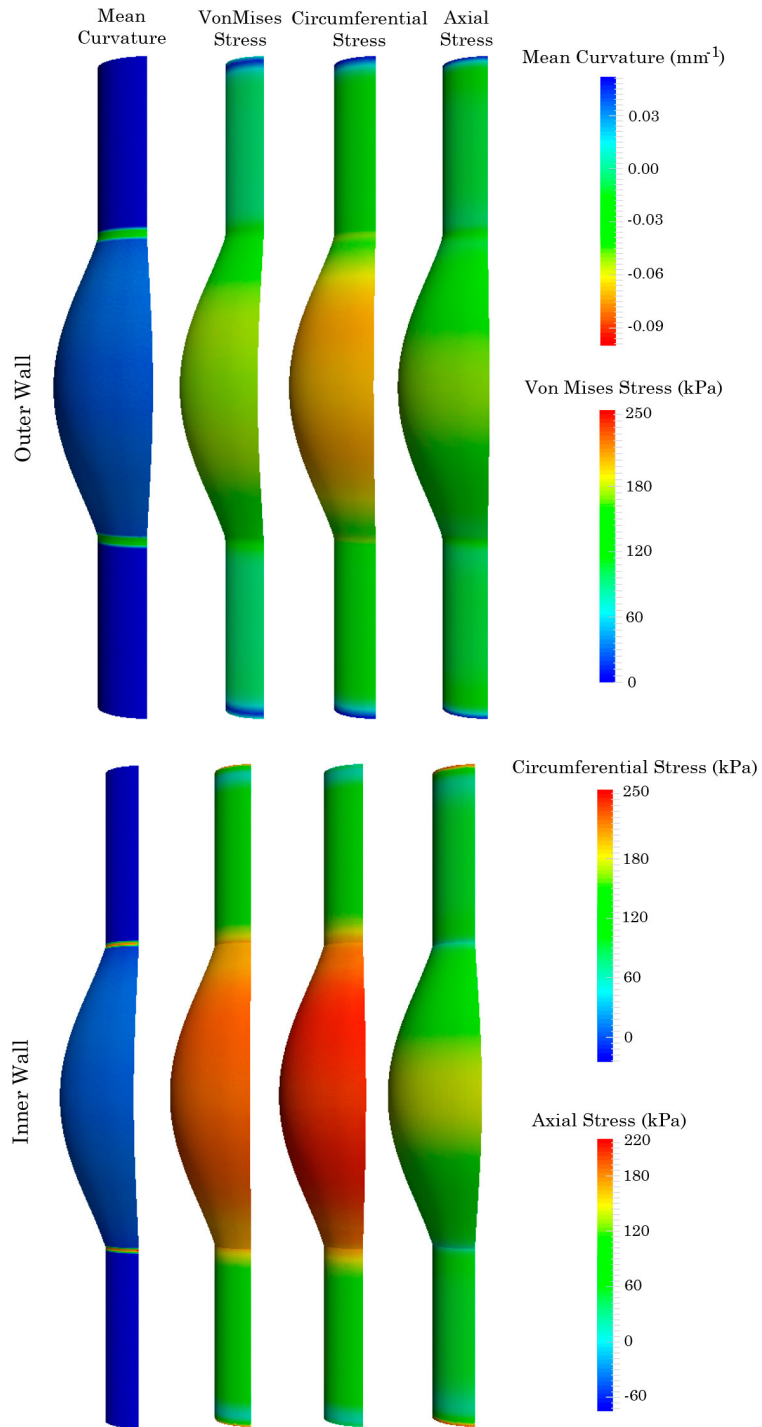
Figure A-1 Mean Curvature and stress distribution of the outer and inner wall of geometry #1.
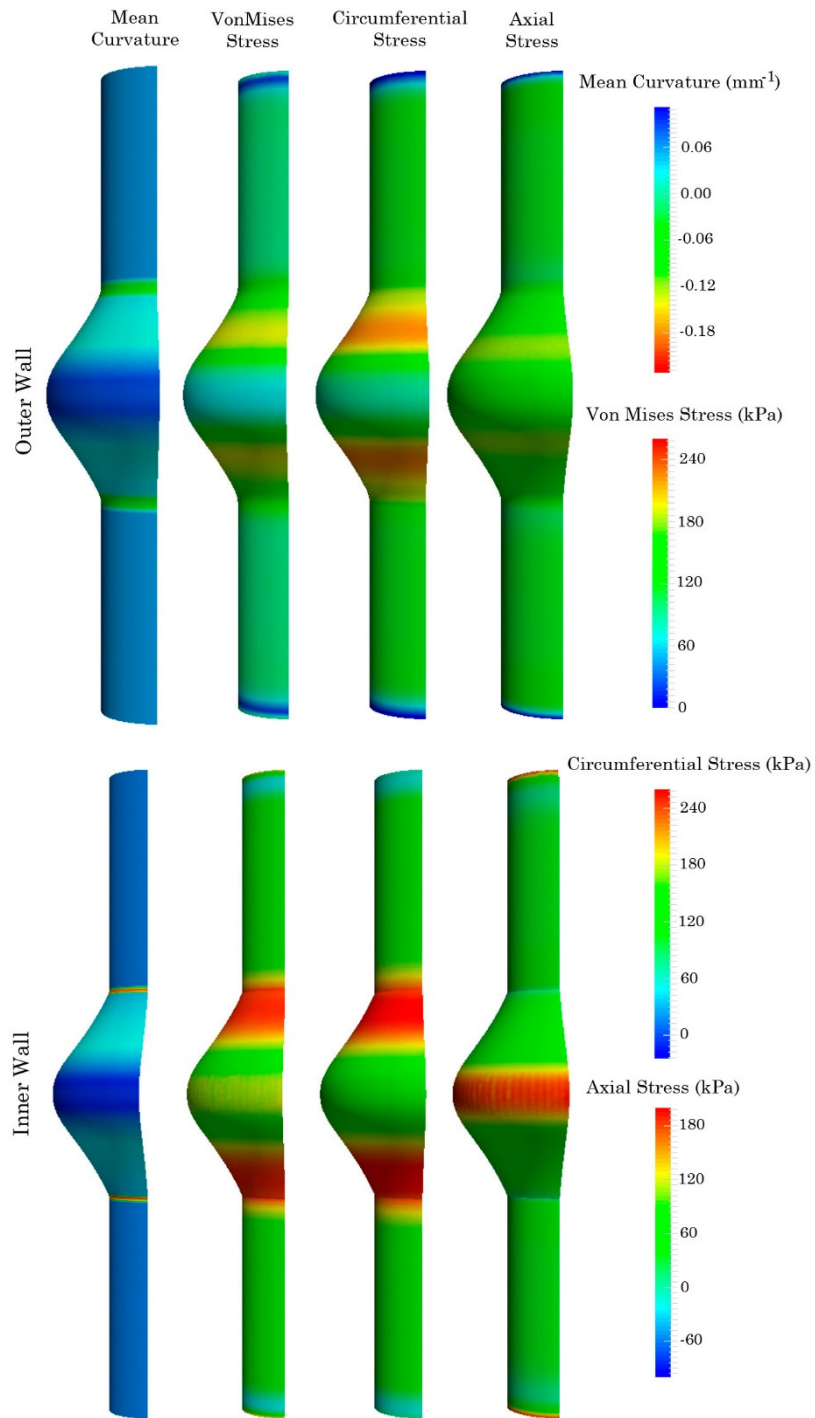
Figure A-2 Mean Curvature and stress distribution of the outer and inner wall of geometry #2.
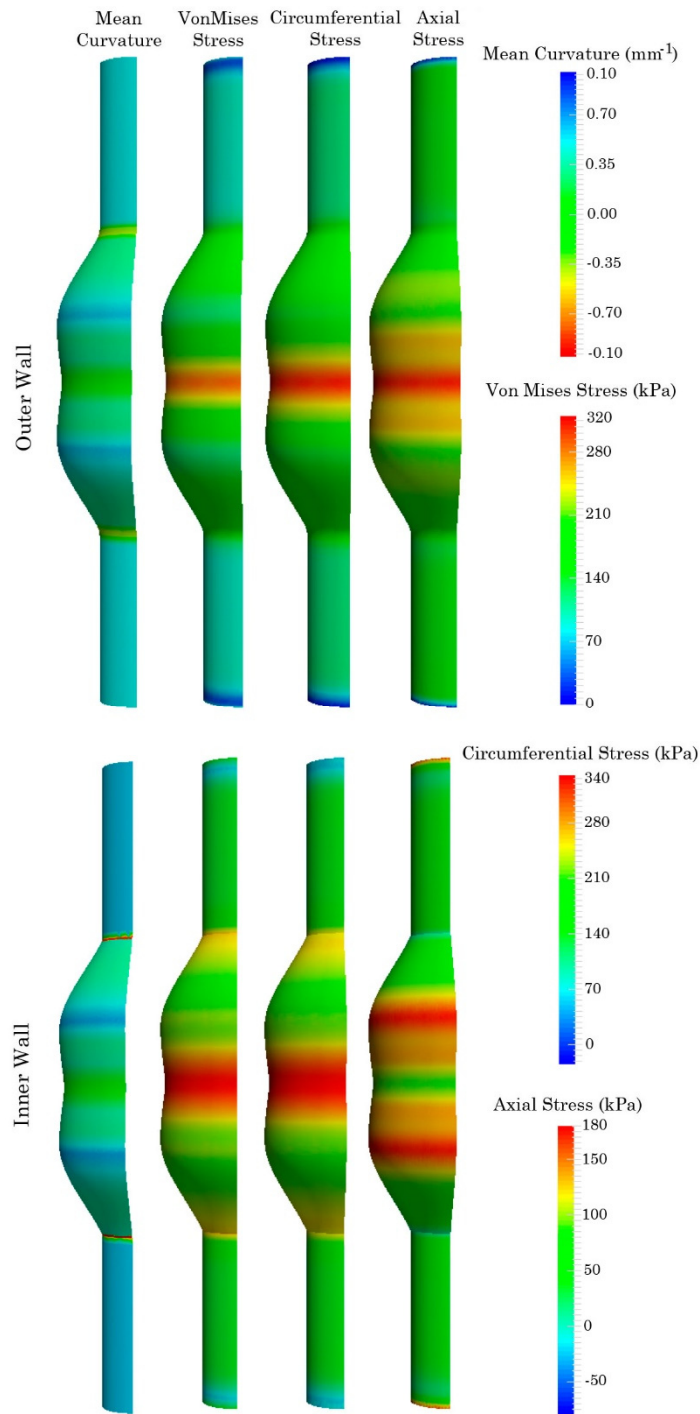
Figure A-3 Mean Curvature and stress distribution of the outer and inner wall of geometry #3.
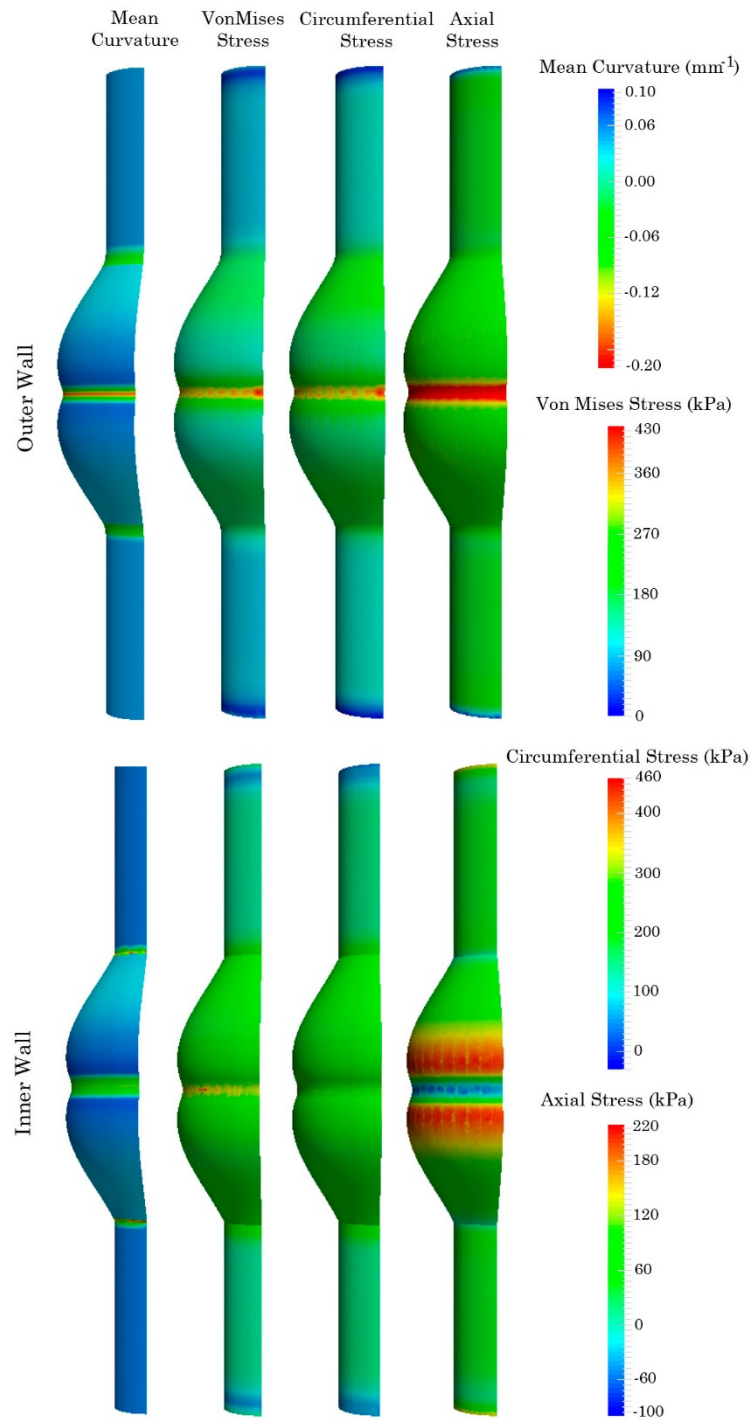
Figure A-4 Mean Curvature and stress distribution of the outer and inner wall of geometry #5.

Figure A-5 Mean Curvature and stress distribution of the outer and inner wall of geometry #6.
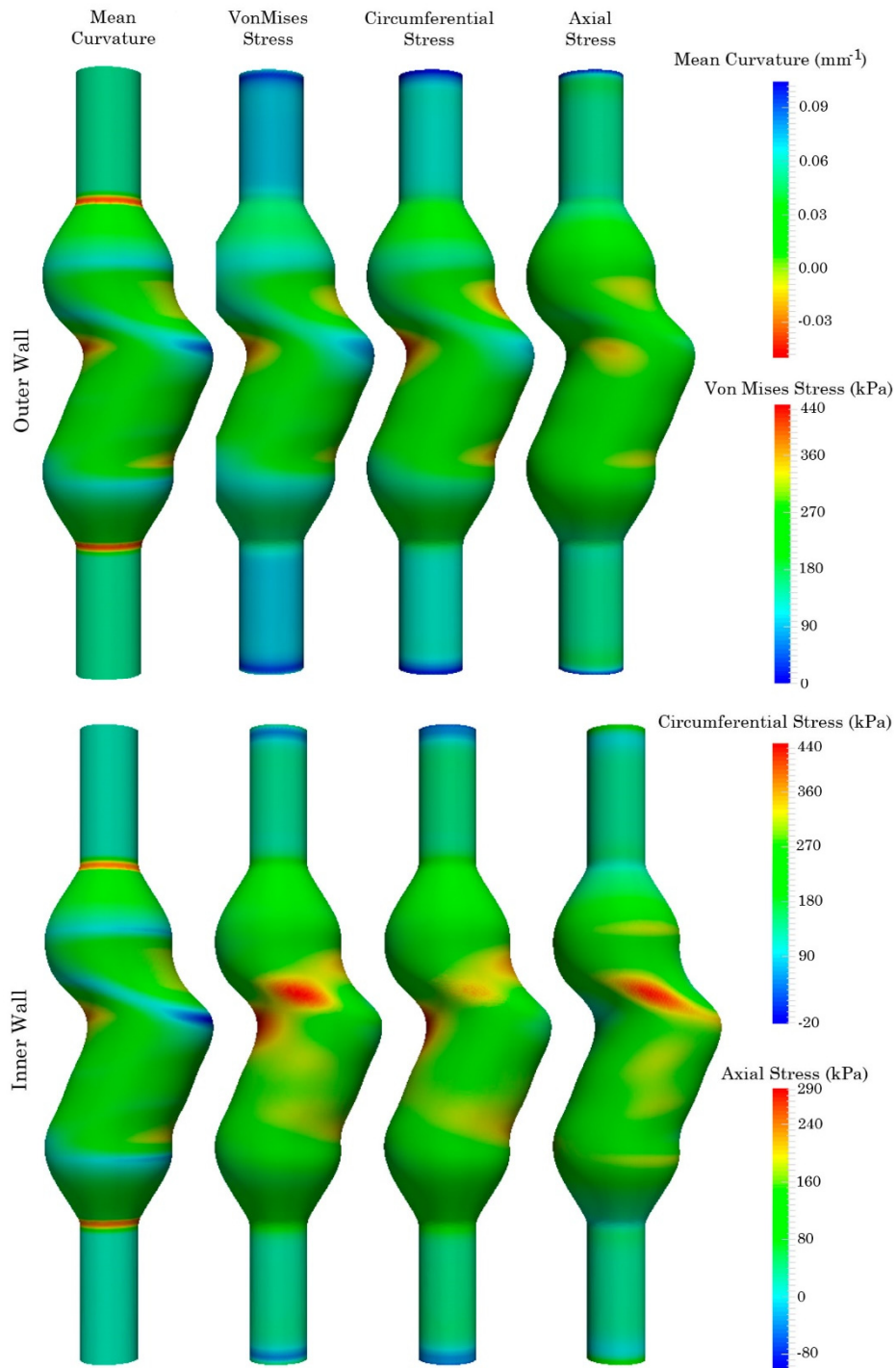
Figure A-6 Mean Curvature and stress distribution of the outer and inner wall of geometry #7.

Appendix B: First principal stress distribution of the 30 patient-specific AAAs

This appendix shows the first principal wall stress distribution of the 30 patient-specific AAA geometries studied in the Chapter 4.
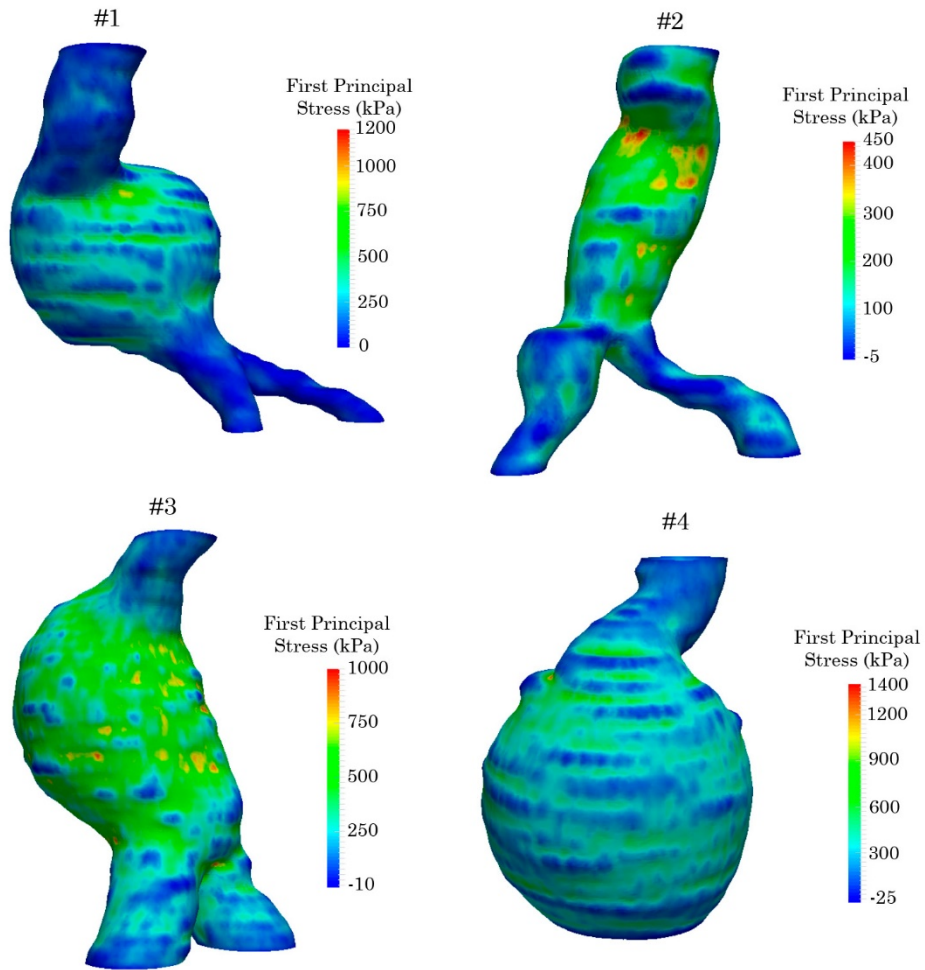
Figure B-1 First principal stress distribution of patient-specific geometries: #1 to #4.
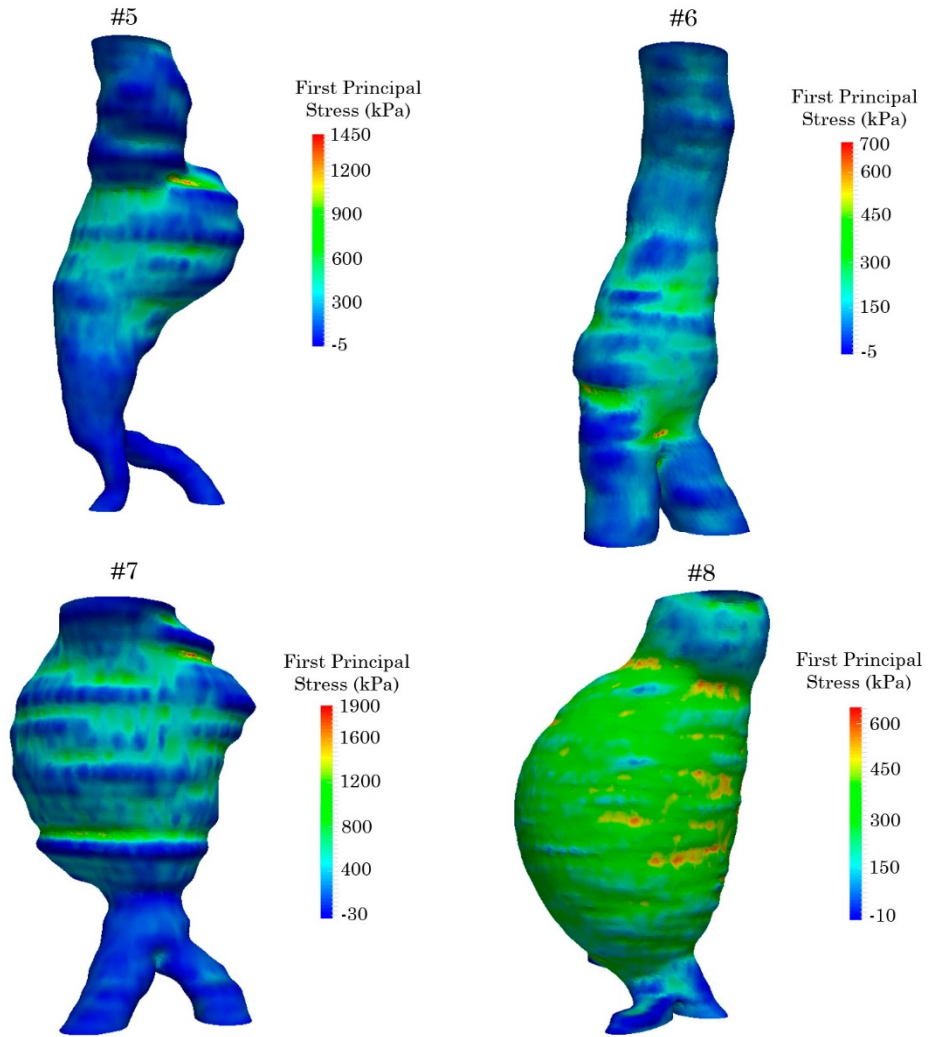
Figure B-2 First principal stress distribution of patient-specific geometries: #5 to #8.
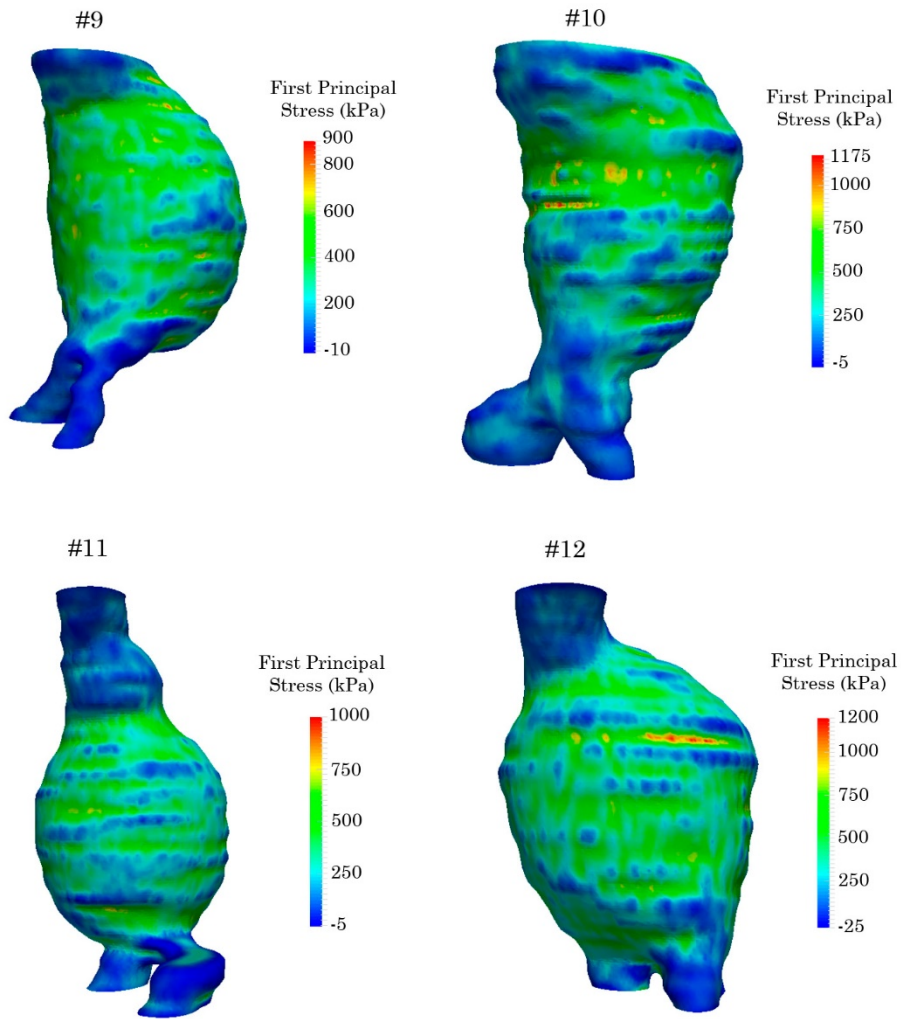
Figure B-3 First principal stress distribution of patient-specific geometries: #9 to #12.
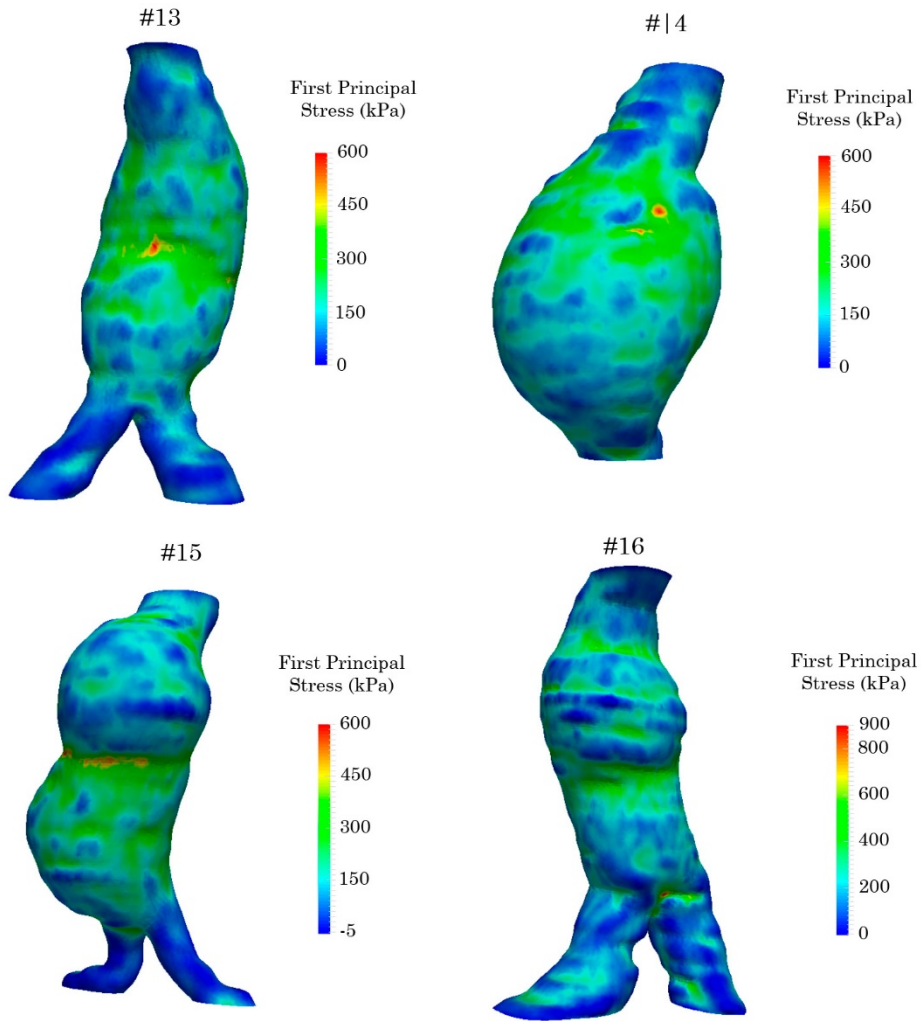
Figure B-4 First principal stress distribution of patient-specific geometries: #13 to #16.

Figure B-5 First principal stress distribution of patient-specific geometries: #17 to #20.
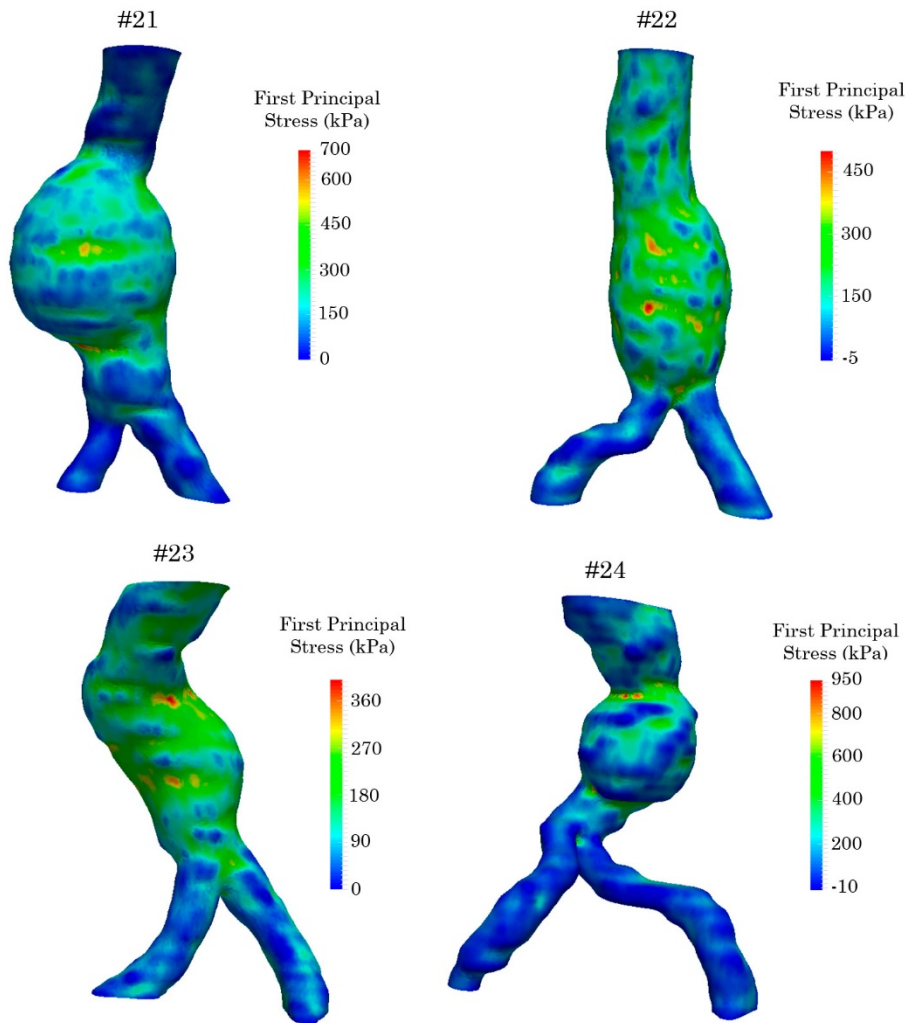
Figure B-6 First principal stress distribution of patient-specific geometries: #21 to #24.

Figure B-7 First principal stress distribution of patient-specific geometries: #25 to #28.
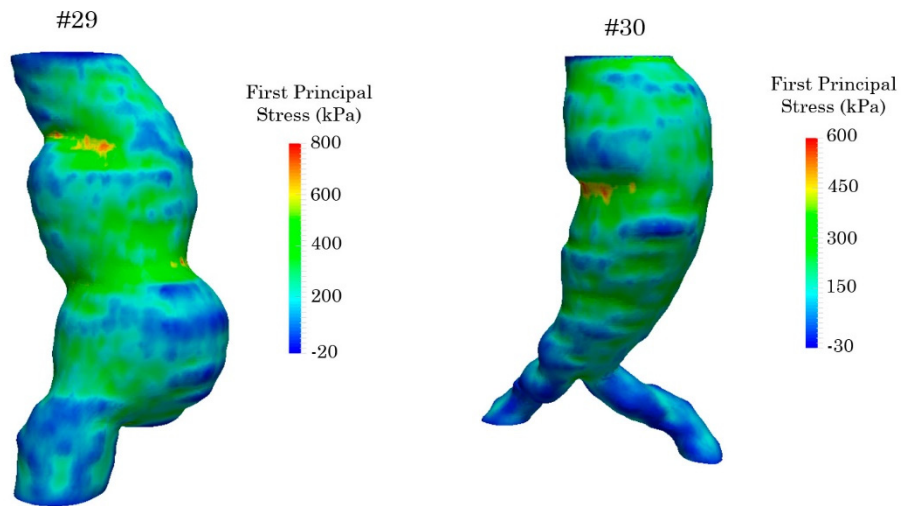
Figure B-8 First principal stress distribution of patient-specific geometries: #29 and #30.

Appendix C: Wall stress comparison between experimental and numerical studies

In this appendix the differences between the experimental and numerical studies of the 30 representative points for the four geometries at the corresponding pressures are reported.

Table C-1: Difference in local wall stresses between numerical and experimental studies of the 30 representative regions for geometry 7160a with an intraluminal pressure equal to 80 mmHg.

# Region	Numerical Stress (kPa)	Experimental Stress (kPa)	Difference (%)
1	131.87	131.77	0.07
2	117.86	112.40	4.85
3	116.80	120.52	3.08
4	105.68	94.98	11.26
5	110.08	112.96	2.55
6	114.01	118.13	3.49
7	107.68	100.92	6.70
8	137.27	132.18	3.85
9	149.85	138.13	8.49
10	126.48	119.11	6.19
11	115.87	108.72	6.57
12	126.81	122.15	3.81
13	98.22	104.58	6.07
14	91.25	101.01	9.66
15	109.65	115.02	4.66
16	105.27	104.43	0.79
17	97.52	92.26	5.39
18	127.14	127.86	0.57
19	115.61	125.51	7.89
20	117.07	112.07	4.27
21	147.67	147.99	0.22
22	170.29	162.07	4.82
23	135.45	130.21	3.87
24	134.95	136.72	1.29
25	128.50	133.46	3.71
26	113.20	108.58	4.08
27	105.80	116.17	8.93
28	133.88	123.61	7.67
29	120.46	102.20	15.15
30	110.00	102.21	7.09

Table C-2: Difference in local wall stresses between numerical and experimental studies of the 30 representative regions for geometry 7160a with an intraluminal pressure equal to 100 mmHg.

# Region	Numerical Stress (kPa)	Experimental Stress (kPa)	Difference (%)
1	159.04	156.82	1.42
2	143.93	150.91	4.63
3	140.16	147.36	4.88
4	131.67	127.15	3.56
5	140.48	134.86	4.17
6	148.56	150.97	1.60
7	135.15	127.86	5.70
8	170.99	162.86	4.99
9	194.42	171.49	13.37
10	157.14	146.44	7.31
11	147.07	138.55	6.15
12	153.53	140.06	9.62
13	121.80	111.57	9.17
14	120.17	130.09	7.63
15	137.00	143.45	4.50
16	130.20	122.93	5.58
17	124.54	120.40	3.33
18	155.53	169.10	8.03
19	162.24	160.69	0.96
20	134.05	138.55	3.25
21	181.15	179.90	0.69
22	202.73	204.28	0.76
23	168.79	158.82	5.90
24	164.86	179.05	7.93
25	163.26	171.99	5.08
26	143.76	133.00	7.48
27	146.34	151.14	3.17
28	157.25	153.66	2.28
29	142.84	132.58	7.18
30	130.23	133.94	2.77

Table C-3: Difference in local wall stresses between numerical and experimental studies of the 30 representative regions for geometry 7160a with an intraluminal pressure equal to 120 mmHg.

# Region	Numerical Stress (kPa)	Experimental Stress (kPa)	Difference (%)
1	187.75	193.80	3.12
2	178.62	177.69	0.52
3	168.60	166.62	1.18
4	157.84	168.47	6.31
5	170.02	157.29	8.10
6	181.31	183.17	1.02
7	163.02	157.93	3.23
8	200.74	186.90	7.41
9	225.42	206.26	9.29
10	188.10	175.32	7.29
11	177.16	164.48	7.71
12	195.42	182.71	6.95
13	159.53	156.26	2.09
14	147.07	154.70	4.94
15	162.62	160.90	1.07
16	159.12	153.89	3.29
17	141.89	149.50	5.09
18	184.03	197.82	6.97
19	181.97	186.46	2.41
20	175.97	167.10	5.04
21	189.94	206.70	8.11
22	258.80	238.21	7.96
23	232.91	217.28	6.71
24	212.08	217.64	2.56
25	195.54	206.92	5.50
26	170.80	161.33	5.54
27	179.49	187.32	4.18
28	201.42	182.57	9.36
29	169.25	175.54	3.58
30	170.97	162.02	5.23

Table C-4: Difference in local wall stresses between numerical and experimental studies of the 30 representative regions for geometry 7160b with an intraluminal pressure equal to 80 mmHg.

# Region	Numerical Stress (kPa)	Experimental Stress (kPa)	Difference (%)
1	127.54	129.60	1.60
2	113.68	117.89	3.57
3	114.35	125.42	8.83
4	108.43	117.36	7.61
5	105.68	111.18	4.95
6	108.80	112.02	2.88
7	108.07	101.26	6.73
8	129.43	119.74	8.09
9	138.12	125.08	10.42
10	120.23	109.19	10.12
11	117.44	109.59	7.16
12	107.79	99.55	8.27
13	101.46	105.77	4.07
14	103.25	106.97	3.47
15	108.48	116.95	7.24
16	103.79	108.07	3.96
17	95.79	93.28	2.62
18	125.17	135.41	7.57
19	123.22	127.45	3.32
20	112.70	111.35	1.20
21	140.75	134.11	4.72
22	145.20	142.50	1.86
23	127.27	127.04	0.18
24	137.14	135.95	0.87
25	115.05	128.32	10.35
26	125.82	115.91	7.88
27	126.37	114.52	9.38
28	139.39	135.42	2.85
29	121.87	126.92	3.98
30	118.09	117.52	0.48

Table C-5: Difference in local wall stresses between numerical and experimental studies of the 30 representative regions for geometry 7160b with an intraluminal pressure equal to 100 mmHg.

# Region	Numerical Stress (kPa)	Experimental Stress (kPa)	Difference (%)
1	156.58	158.00	0.90
2	136.72	148.49	7.93
3	141.23	148.68	5.01
4	133.90	128.14	4.49
5	132.36	131.68	0.52
6	135.06	130.41	3.57
7	135.37	129.30	4.69
8	158.50	148.37	6.82
9	172.71	158.11	9.23
10	142.16	131.16	8.39
11	148.67	140.10	6.12
12	136.24	124.76	9.20
13	130.52	123.39	5.78
14	132.95	132.15	0.61
15	139.60	138.73	0.62
16	129.42	123.86	4.30
17	124.93	116.96	6.38
18	162.44	169.36	4.09
19	149.90	149.94	0.03
20	144.49	144.75	0.18
21	172.28	170.99	0.75
22	188.98	180.16	4.66
23	154.65	151.17	2.25
24	169.46	178.96	5.31
25	143.51	160.74	10.72
26	153.58	147.74	3.80
27	142.57	138.16	3.09
28	172.91	155.22	10.23
29	166.56	157.72	5.31
30	154.55	147.48	4.58

Table C-6: Difference in local wall stresses between numerical and experimental studies of the 30 representative regions for geometry 7160b with an intraluminal pressure equal to 120 mmHg.

# Region	Numerical Stress (kPa)	Experimental Stress (kPa)	Difference (%)
1	185.15	201.86	8.28
2	171.54	166.45	3.05
3	167.90	190.01	11.64
4	160.27	168.20	4.71
5	159.26	160.26	0.62
6	165.55	159.55	3.76
7	162.99	154.55	5.46
8	190.78	175.28	8.84
9	206.99	185.85	11.37
10	178.20	162.80	9.46
11	178.19	164.92	8.05
12	165.52	153.63	7.74
13	154.01	154.91	0.58
14	160.06	160.06	0.01
15	166.14	168.42	1.35
16	157.43	152.73	2.98
17	152.26	143.13	6.00
18	182.12	202.05	9.86
19	178.67	193.15	7.50
20	172.55	177.27	2.66
21	209.68	204.51	2.47
22	222.79	219.47	1.49
23	188.12	195.40	3.73
24	206.53	207.50	0.47
25	174.75	195.90	10.80
26	189.19	167.99	11.21
27	174.44	186.32	6.38
28	207.73	196.76	5.28
29	176.60	179.50	1.61
30	179.84	173.07	3.76

Table C-7: Difference in local wall stresses between numerical and experimental studies of the 30 representative regions for geometry 7190a with an intraluminal pressure equal to 80 mmHg.

# Region	Numerical Stress (kPa)	Experimental Stress (kPa)	Difference (%)
1	151.98	149.79	1.46
2	133.46	143.41	6.94
3	131.49	147.05	10.58
4	117.75	128.66	8.48
5	116.53	112.74	3.36
6	118.78	118.30	0.41
7	112.84	110.94	1.71
8	136.97	126.15	8.58
9	149.21	135.03	10.50
10	153.58	139.61	10.01
11	142.35	133.22	6.85
12	126.11	133.30	5.39
13	132.51	133.22	0.53
14	125.57	130.99	4.14
15	107.74	111.92	3.74
16	127.03	120.77	4.93
17	101.11	109.68	7.81
18	149.96	156.62	4.25
19	154.42	148.53	3.81
20	133.69	139.52	4.18
21	152.18	159.11	4.35
22	168.73	164.00	2.81
23	136.40	142.20	4.07
24	136.10	150.18	9.38
25	139.22	145.52	4.33
26	141.74	132.16	6.76
27	148.30	140.86	5.02
28	163.37	164.26	0.54
29	143.96	153.57	6.25
30	130.52	132.42	1.43

Table C-8: Difference in local wall stresses between numerical and experimental studies of the 30 representative regions for geometry 7190a with an intraluminal pressure equal to 100 mmHg.

# Region	Numerical Stress (kPa)	Experimental Stress (kPa)	Difference (%)
1	187.78	174.82	7.42
2	165.81	160.43	3.35
3	159.86	166.65	4.07
4	144.68	147.48	1.90
5	141.60	138.74	2.06
6	149.54	155.06	3.56
7	147.27	130.11	13.19
8	167.54	163.11	2.71
9	177.88	172.28	3.25
10	190.82	173.18	10.18
11	177.89	165.87	7.25
12	158.56	163.25	2.87
13	157.47	159.25	1.12
14	153.03	152.22	0.53
15	133.54	132.95	0.44
16	155.03	145.60	6.08
17	121.63	127.31	4.46
18	184.86	161.44	12.67
19	183.33	187.16	2.04
20	175.71	164.96	6.12
21	180.35	189.74	4.95
22	205.92	183.01	11.12
23	173.04	173.98	0.54
24	174.30	183.06	4.79
25	180.88	187.38	3.47
26	167.48	154.44	7.79
27	182.40	160.22	12.16
28	195.29	175.99	9.89
29	183.43	173.78	5.26
30	171.68	176.08	2.50

Table C-9: Difference in local wall stresses between numerical and experimental studies of the 30 representative regions for geometry 7190a with an intraluminal pressure equal to 120 mmHg.

# Region	Numerical Stress (kPa)	Experimental Stress (kPa)	Difference (%)
1	217.19	212.70	2.11
2	198.15	204.46	3.09
3	190.85	215.11	11.28
4	174.39	190.08	8.25
5	165.57	170.86	3.09
6	180.84	184.06	1.75
7	175.98	167.37	5.14
8	195.14	194.38	0.39
9	220.11	202.52	8.68
10	221.52	210.52	5.22
11	213.52	201.34	6.05
12	193.08	196.00	1.48
13	179.49	176.29	1.81
14	190.46	194.25	1.96
15	160.67	166.61	3.57
16	183.80	179.14	2.54
17	153.67	154.72	0.68
18	224.07	233.01	3.84
19	213.64	230.26	7.22
20	205.99	202.60	1.64
21	234.71	229.69	2.14
22	243.44	224.21	7.90
23	247.90	224.21	9.56
24	211.48	219.79	3.78
25	220.17	223.20	1.36
26	217.62	195.71	10.07
27	220.05	230.94	4.71
28	227.65	226.03	0.71
29	205.42	177.71	13.49
30	213.88	212.52	0.64

Table C-10: Difference in local wall stresses between numerical and experimental studies of the 30 representative regions for geometry 7190b with an intraluminal pressure equal to 80 mmHg.

# Region	Numerical Stress (kPa)	Experimental Stress (kPa)	Difference (%)
1	148.78	139.55	6.62
2	141.15	141.70	0.39
3	130.07	131.88	1.38
4	125.38	128.13	2.14
5	115.34	109.98	4.87
6	112.42	112.81	0.34
7	114.66	106.99	7.17
8	102.26	115.54	11.49
9	131.05	121.95	7.46
10	129.60	118.23	9.62
11	123.09	121.26	1.51
12	122.26	114.19	7.07
13	104.47	110.37	5.34
14	112.39	118.86	5.44
15	96.94	103.36	6.21
16	121.41	122.39	0.80
17	105.12	105.47	0.34
18	131.04	134.91	2.87
19	148.67	144.58	2.75
20	129.34	125.95	2.62
21	159.31	153.20	3.84
22	173.48	155.09	10.60
23	154.63	145.60	5.84
24	133.24	145.53	8.44
25	137.32	148.47	7.51
26	123.71	114.83	7.17
27	128.48	122.18	4.90
28	151.96	137.55	9.48
29	112.85	127.84	11.72
30	115.24	116.56	1.14

Table C-11: Difference in local wall stresses between numerical and experimental studies of the 30 representative regions for geometry 7190b with an intraluminal pressure equal to 100 mmHg.

# Region	Numerical Stress (kPa)	Experimental Stress (kPa)	Difference (%)
1	182.83	182.03	0.44
2	176.68	159.54	10.75
3	155.41	165.65	6.18
4	155.17	163.56	5.13
5	132.88	128.00	3.81
6	143.83	145.01	0.81
7	146.68	134.35	9.18
8	136.36	140.39	2.87
9	165.28	151.79	8.88
10	168.78	153.82	9.72
11	160.00	154.91	3.29
12	156.31	148.58	5.20
13	134.90	136.50	1.17
14	142.92	156.46	8.66
15	122.29	127.06	3.76
16	162.46	145.80	10.26
17	132.87	131.57	0.98
18	183.81	181.09	1.48
19	187.29	182.79	2.40
20	158.15	158.46	0.19
21	197.44	192.07	2.72
22	202.75	188.43	7.06
23	177.09	160.91	9.14
24	169.82	189.07	10.18
25	174.25	184.43	5.52
26	154.85	143.95	7.04
27	160.77	153.92	4.26
28	177.27	160.06	9.71
29	174.99	159.06	9.10
30	145.94	140.07	4.02

Table C-12: Difference in local wall stresses between numerical and experimental studies of the 30 representative regions for geometry 7190b with an intraluminal pressure equal to 120 mmHg.

# Region	Numerical Stress (kPa)	Experimental Stress (kPa)	Difference (%)
1	216.22	212.45	1.77
2	209.10	217.71	3.95
3	184.61	195.62	5.63
4	185.41	202.21	8.31
5	169.69	174.09	2.53
6	170.66	180.37	5.39
7	175.40	164.00	6.95
8	171.78	178.33	3.68
9	201.39	182.29	10.48
10	201.88	182.09	10.87
11	192.91	181.40	6.34
12	187.21	176.72	5.94
13	160.63	149.42	7.50
14	176.98	182.42	2.98
15	146.25	152.80	4.29
16	189.07	172.90	8.55
17	159.50	163.92	2.69
18	200.63	199.69	0.47
19	228.84	219.40	4.13
20	193.64	185.01	4.46
21	234.53	227.28	3.09
22	250.67	227.43	9.27
23	217.21	209.61	3.50
24	203.14	228.61	11.14
25	211.88	231.71	8.56
26	183.77	166.50	9.40
27	192.47	184.93	3.92
28	220.12	193.03	12.31
29	183.99	183.57	0.23
30	184.90	172.09	6.93

Appendix D: Publications

This appendix includes the front page of the articles that have already been published by the author of this thesis in scientific journals. Submitted articles that are currently under review are also included.

D.1 Accepted Articles

Ruiz de Galarreta, S., Cazón, A., Antón, R., and Finol, E. A., 2014, "Abdominal Aortic Aneurysm: From Clinical Imaging to Realistic Replicas.," J. Biomech. Eng., 136(January), pp. 14502–14505.

Ruiz de Galarreta, S., Cazón, A., Antón, R., and Finol, E., 2016, "A Methodology for Verifying Abdominal Aortic Aneurysm Wall Stress," J. Biomech. Eng., **139**(1)

Ruiz de Galarreta, S., Antón, R., Cazon, A., Larraona, G. S., and Finol, E. A., 2016, "Anisotropic abdominal aortic aneurysm replicas with biaxial material characterization," Med. Eng. Phys., **38**(12)

D.2 Submitted Articles

Ruiz de Galarreta, S., Antón, R., Cazón, A., and Pradera, A., 2016, "Influence of the Local Mean Curvature on the Abdominal Aortic Aneurysm Stress Distribution", Journal of Mechanics in Medicine and Biology (Under review)

Ruiz de Galarreta, S., Cazón, A., Antón, R., and Finol, E. A., 2016, "The Relationship between Surface Curvature and Abdominal Aortic Aneurysm Wall Stress", J. Biomech. Eng (Under review)

Abdominal Aortic Aneurysm: From Clinical Imaging to Realistic Replicas

Sergio Ruiz de Galarreta
Mechanical Department,
Tecnun,
Universidad de Navarra,
San Sebastián 20018, Spain

Aitor Cazón[1]
CEIT and Mechanical Department,
Tecnun,
Universidad de Navarra,
San Sebastián 20018, Spain
e-mail: acazon@tecnun.es

Raúl Antón
Mechanical Department,
Tecnun,
Universidad de Navarra,
San Sebastián 20018, Spain

Ender A. Finol
Department of Biomedical Engineering,
The University of Texas at San Antonio,
San Antonio, TX 78249

The goal of this work is to develop a framework for manufacturing nonuniform wall thickness replicas of abdominal aortic aneurysms (AAAs). The methodology was based on the use of computed tomography (CT) images for virtual modeling, additive manufacturing for the initial physical replica, and a vacuum casting process and range of polyurethane resins for the final rubberlike phantom. The average wall thickness of the resulting AAA phantom was compared with the average thickness of the corresponding patient-specific virtual model, obtaining an average dimensional mismatch of 180 μm (11.14%). The material characterization of the artery was determined from uniaxial tensile tests as various combinations of polyurethane resins were chosen due to their similarity with ex vivo AAA mechanical behavior in the physiological stress configuration. The proposed methodology yields AAA phantoms with nonuniform wall thickness using a fast and low-cost process. These replicas may be used in benchtop experiments to validate deformations obtained with numerical simulations using finite element analysis, or to validate optical methods developed to image ex vivo arterial deformations during pressure-inflation testing. [DOI: 10.1115/1.4025883]

Keywords: AAA replica, additive manufacturing, vacuum casting, tensile strength

Introduction

An abdominal aortic aneurysm (AAA) is a permanent focal dilatation of the abdominal aorta in the infrarenal segment to 1.5 times its normal diameter [1], causing 1.3% of all deaths among men aged 65–85 in developed countries. The ability to predict the rupture of the abdominal aorta is a concern for both vascular sur-

geons and patients, since it is based on statistical in vivo data [2] and numerical patient-specific analysis. An AAA rupture is associated with the diameter of the aneurysm, but the use of finite element analysis has indicated that an AAA rupture is also highly related to peak wall stress [3–6]. Patient-specific aneurysm phantoms have been created in fabrication laboratories to replicate the response of the abdominal aorta. These replicas are built by combining medical images and conventional manufacturing techniques such as additive manufacturing (AM) and injection molding [7–9]. To achieve reliable outcomes from both numerical and in vitro experiments, materials whose mechanical properties have a stress-strain curve similar to those of the aneurysm wall should be used to build the replicas [10]. These curves change spatially along the aorta and are dependent on the patient's age, gender, and the ratio of elastin and collagen; the aneurysmal aorta is stiffer compared to the healthy aorta [11].

The primary objective of this work is to develop and apply a new modeling and manufacturing process for patient-specific artery replicas with nonuniform wall thickness, with a focus on developing physiologically realistic AAA phantoms. This is the first time, to the authors' knowledge, that a methodology is reported for manufacturing arteries with nonuniform wall thickness distributions. Artery replicas were manufactured by using computed tomography (CT) images to generate virtual models, AM to make the initial physical model, and vacuum casting in combination with commercially available polyurethane resins (PURs) and casting wax, to build the final phantom. The material characterization was assessed from uniaxial tensile experiments. These replicas can be useful to validate deformations obtained with numerical simulations with the small deformations that occur in a phantom placed in a benchtop apparatus subject to pulsatile flow and pressure. To this end, the compliance of the patient-specific replicas will be accurate at small strain ranges and they will have individual geometric characteristics, including regional variations of wall thickness.

Methods

The vacuum casting technique was chosen as the preferred manufacturing method to build an arterial replica. The process involves pouring liquid polyurethane resins (PURs) under vacuum into a silicon mold that contains a hollow cavity with the desired shape. The mold was previously obtained by taking as a reference a master model printed with an AM technology. The steps for creating the artery replica are illustrated in Fig. 1.

Virtual Abdominal Aorta. The patient-specific AAA geometry was obtained following the acquisition of the subject's contrast-enhanced CT images from Allegheny General Hospital (Pittsburgh, PA) following an Institutional Review Board approved protocol. The medical images were segmented using in-house image segmentation software (AAAVASC, University of Texas at San Antonio, San Antonio, TX), which is capable of identifying the boundaries of the lumen inner and outer wall surfaces [12]. The segmentation algorithms have been extensively validated [12,13] and used to quantify the geometry of patient-specific AAA models [14,15], identify classifiers of ruptured/
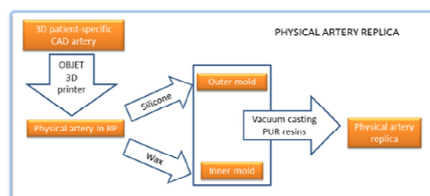
Fig. 1 Flow chart describing the artery replication process

Research Papers

A Methodology for Verifying Abdominal Aortic Aneurysm Wall Stress

Sergio Ruiz de Galarreta, Aitor Cazón, Raúl Antón and Ender A. Finol
[+] Author and Article Information

ARTICLE | REFERENCES | FIGURES | TABLES

Abstract

Abstract | Introduction | Methodology | Results | Discussion | Conclusion | Acknowledgements | References

An abdominal aortic aneurysm (AAA) is a permanent focal dilatation of the abdominal aorta of at least 1.5 times its normal diameter. Although the criterion of maximum diameter is still used in clinical practice to decide on a timely intervention, numerical studies have demonstrated the importance of other geometric factors. However, the major drawback of numerical studies is that they must be validated experimentally before clinical implementation. This work presents a new methodology to verify wall stress predicted from the numerical studies against the experimental testing. To this end, four AAA phantoms were manufactured using vacuum casting. The geometry of each phantom was subject to microcomputed tomography (µCT) scanning at zero and three other intraluminal pressures: 80, 100, and 120 mm Hg. A zero-pressure geometry algorithm was used to calculate the wall stress in the phantom, while the numerical wall stress was calculated with a finite-element analysis (FEA) solver based on the actual zero-pressure geometry subjected to 80, 100, and 120 mm Hg intraluminal pressure loading. Results demonstrate the moderate accuracy of this methodology with small relative differences in the average wall stress (1.14%). Additionally, the contribution of geometric factors to the wall stress distribution was statistically analyzed for the four phantoms. The results showed a significant correlation between wall thickness and mean curvature (MC) with wall stress.

ARTICLE IN PRESS

Contents lists available at ScienceDirect

Medical Engineering and Physics

journal homepage: www.elsevier.com/locate/medengphy

Technical note

Anisotropic abdominal aortic aneurysm replicas with biaxial material characterization

Sergio Ruiz de Galarreta[a], Raúl Antón[a,*], Aitor Cazon[a], Gorka S. Larraona[a], Ender A. Finol[b]

[a] Department of Mechanical Engineering, Tecnun, University of Navarra, Paseo Manuel de Lardizabal, 13, 20018 San Sebastián, Spain
[b] Department of Biomedical Engineering, The University of Texas at San Antonio, One UTSA Circle, AET 1.360, San Antonio, TX 78249-0669, United States

ARTICLE INFO

ABSTRACT

An Abdominal Aortic Aneurysm (AAA) is a permanent focal dilatation of the abdominal aorta at least 1.5 times its normal diameter. The criterion of maximum diameter is still used in clinical practice, although numerical studies have demonstrated the importance of other biomechanical factors. Numerical studies, however, must be validated experimentally before they can be clinically implemented. We have developed a methodology for manufacturing anisotropic AAA replicas with non-uniform wall thickness. Different composites were fabricated and tested, and one was selected in order to manufacture a phantom with the same properties. The composites and the phantom were characterized by biaxial tensile tests and a material model was fit to the experimental data. The experimental results were compared with data from the literature, and similar responses were obtained. The anisotropic AAA replicas with non-uniform wall thickness can be used in benchtop experiments to validate deformations obtained with numerical simulations or for pre-intervention testing of endovascular grafts. This is a significant step forward considering the importance of anisotropy in numerical simulations.

© 2016 IPEM. Published by Elsevier Ltd. All rights reserved.

1. Introduction

An Abdominal Aortic Aneurysm (AAA) is a permanent dilatation of the abdominal aorta, and its rupture remains a significant cause of death in developed countries among men aged 65–85 [1]. In clinical practice, uncertainty still remains about the correct time to operate, but the criterion of maximum diameter is commonly accepted as a rupture prediction factor, meaning that medical doctors recommend surgical interventions when AAA diameters are greater than 55 mm [2]. When studying AAA rupture, numerical simulations via Finite Element Analysis (FEA) have proved to be very useful in indicating that this rupture criterion needs to be complemented with AAA wall stress data [3–5], meaning that factors such as geometry and biomechanics must also be considered [6,7].

In vitro experiments with AAA phantoms have been shown to be very useful in several applications [8–10]. These phantoms ranged from totally idealized geometries to real AAA geometries generally with uniform [11,12] but also with non-uniform thickness [13]. However, the anisotropy found in the AAA tissue [14–17] is an important property that was not considered in these projects. When using inverse analysis the mechanical properties

* Corresponding author. Fax: +34 943 31 14 42.
E-mail address: ranton@tecnun.es (R. Antón).

are not critical [18,19], but the consideration of the anisotropy parameter plays an important role in the results of numerical simulations with a forward approach, and it must be taken into account for further studies [20–22]. Within the context of physical replicas, this consideration points to a step forward in the manufacturing of phantoms with arterial anisotropic behavior.

The purpose of the present work is to describe and apply a new methodology for manufacturing AAA replicas that display anisotropic behavior. To the best of the authors' knowledge, this is the first time that a methodology is reported for creating arterial replicas with non-uniform wall thickness and defined anisotropy.

2. Materials and methods

2.1. Uniaxial testing of isotropic specimens

Tensile tests were carried out following ASTM D412 Type B. Specimens were manufactured via the vacuum casting technique by using the bi-components PUR SLM 7140, 7160 and 7190 at seven different mixing ratios.

Tensile tests were performed on the specimens to generate force-extension data using an INSTRON MINI 44 (Instrom Worldwide, Norwood, MA) tensile test machine. Each specimen was subjected to a cross-head speed of 3.4 mm/min until failure with pre-conditioning for 10 cycles to 7.5% of the gauge length. The

INFLUENCE OF THE LOCAL MEAN CURVATURE ON THE ABDOMINAL AORTIC ANEURYSM STRESS DISTRIBUTION

S. RUIZ DE GALARRETA, R. ANTON*, A. CAZON and A. PRADERA

Department of Mechanical Engineering, Tecnun, University of Navarra
San Sebastián, Paseo Manuel de Lardizabal, 13, 20018, San Sebastián, Spain.
sruiz@tecnun.es
ranton@tecnun.es
acazon@tecnun.es
apradera@tecnun.es

An abdominal aortic aneurysm (AAA) is a permanent focal dilatation of the abdominal aorta of at least 1.5 times its normal diameter. Although the criterion of maximum diameter is still used in clinical practice to decide when to proceed with surgical intervention, numerical studies have demonstrated the importance of other geometric factors. In this work, the influence of the local mean curvature on AAA stress distribution has been analyzed in synthetic AAA geometries via finite element analysis. The results show a significant correlation between this geometric parameter and stress, suggesting that local mean curvature should also be considered along with the diameter criterion when making decisions about surgery.

Keywords: Finite Element, AAA, mean curvature, stress analysis, simulation

1. Introduction

An abdominal aortic aneurysm (AAA) is a localized dilatation of the abdominal aorta causing around 1.3% of the deaths in developed countries among men aged 65-85[1], and when rupture occurs the mortality risk is high [2]. AAA rupture can be prevented either by an open-repair, which involves making a large incision in the abdomen in order to directly view the aneurysm, or by a minimally-invasive procedure called endovascular repair.

Currently, the method that medical doctors most often use when deciding whether to operate is based on the diameter of the patient's AAA: if the AAA diameter is greater than 55mm, the risk of rupture is considered to be sufficiently high and surgery is recommended[2]. However, this criterion's fails in 10% to 25% of the cases[3].

Independently of the criterion and from a purely mechanical point of view, rupture occurs when the local stress in the artery wall exceeds the maximum strength of the tissue, indicating that the relationship between tissue strength and stress distribution is a key element and thus should be analyzed.

The purpose of this study is to determine whether the shape or geometry of AAAs can have a significant influence on AAA rupture and whether it is another factor that should be considered when making decisions about surgical intervention. To that end, this study analyzes the correlation between a geometric parameter, the local mean curvature (MC), and the stresses in seven different AAA geometries by means of running finite element analyses in Abaqus FEA and Pearson's statistical method in Minitab.

2. Materials and Methods

Seven different geometries that replicate an aneurysm in the abdominal aorta were designed with PTC Creo 3.0 (PTC Corporate Headquarters, Needham, USA) (Fig. 1). In all the cases, the maximum diameter was set to 40 mm, while the thickness was 1.5 mm throughout the whole aneurysm.

THE RELATIONSHIP BETWEEN SURFACE CURVATURE AND ABDOMINAL AORTIC ANEURYSM WALL STRESS

Sergio Ruiz de Galarreta
Mechanical Department
Tecnun
University of Navarra
20018, San Sebastián, Spain

Aitor Cazón[1]
Mechanical Department
Tecnun
University of Navarra
20018, San Sebastián, Spain
Email: acazon@tecnun.es

Raúl Antón
Mechanical Department
Tecnun
University of Navarra
20018, San Sebastián, Spain

Ender A. Finol
Department of Biomedical Engineering
The University of Texas at San Antonio
San Antonio, TX 78249-0669

The maximum diameter criterion is the most important factor when predicting risk of rupture of abdominal aortic aneurysms (AAA). An elevated wall stress has also been linked to a high risk of aneurysm rupture, yet is an uncommon clinical practice to compute AAA wall stress. The purpose of this study is to assess whether other characteristics of the AAA geometry are statistically correlated with wall stress. Using in-house segmentation and meshing algorithms, thirty patient-specific AAA models were generated for finite element analysis. These models were subsequently used to estimate wall stress and maximum diameter, and to evaluate the spatial distributions of wall thickness, cross-sectional diameter, mean curvature, and Gaussian curvature. Data analysis consisted of statistical correlations of the aforementioned geometry metrics with wall stress for the thirty AAA inner and outer wall surfaces. In addition, a linear regression analysis was performed with all the AAA wall surfaces to quantify the relationship of the geometric indices with wall stress. These analyses indicated that while all geometry metrics have statistically significant correlations with wall stress, the local mean curvature (LMC) exhibits the highest average Pearson's correlation coefficient for both inner and outer wall surfaces. The linear regression analysis revealed coefficients of determination for the outer and inner wall surfaces of 0.712 and 0.516, respectively, with LMC having the largest effect on the linear regression equation with wall stress. This work underscores the importance of evaluating AAA mean wall curvature as a potential surrogate for wall stress.

Keywords: Local mean curvature; thickness; regression; AAA; geometry.

INTRODUCTION

An Abdominal Aortic Aneurysm (AAA) is a localized dilatation of the abdominal aorta that causes around 1.3% of deaths in developed countries among men aged 65-85 [1], with a high mortality risk when it ruptures [2]. AAA rupture can be prevented either by an open surgical repair, which involves a large incision in the abdomen to access the diseased abdominal aorta, or by the minimally invasive, catheter-based, endovascular aneurysm repair. To evaluate the risk of aneurysm rupture, the diameter of the aneurysm is a universally accepted factor and the general consensus is that AAAs larger than $50 - 55$ mm in maximum diameter are at a high risk of rupture, for which repair is recommended [2]. However, the rate of failure of this criterion ranges from 10% to 25% [3]. In an autopsy study of 473 non-operated aneurysms, 13% of aneurysms with a maximum diameter under 50 mm ruptured, while 60% of aneurysms with diameters over 50 mm remained intact [4]. Hence, the maximum diameter criterion is not always sufficient to assess the *individual* risk of aneurysm rupture and alternative criteria for this assessment are warranted.

Several studies [5,6] have demonstrated that Peak Wall Stress (PWS), predicted by a finite element analysis (FEA), is significantly higher in symptomatic/ruptured AAAs than in unruptured AAAs. Recently, Doyle et al. [7] showed how the rupture location of a patient-specific AAA can be predicted from high wall stress regions. However, noteworthy is that wall stress alone is not sufficient to predict rupture risk and that regional estimations of wall strength are also necessary [8]. From a purely biomechanical point of view, aneurysm rupture occurs when the local stress in the arterial wall exceeds the maximum local strength of the tissue, indicating that the relationship between localized tissue strength and stress should be considered for rupture risk assessment. To this end, Gasser et al. [9]

List of nomenclature

Acronyms and definitions

AM	Additive Manufacturing
AI	Anisotropy Index factor
ILT	Intraluminal Thrombus
LD	Local Diameter
LGC	Local Gaussian Curvature
LMC	Local Mean Curvature
LWT	Local Wall Thickness
MD	Maximum Diameter
PUR	Polyurethane
.STL	Stereolitography

List of symbols

$\mathbf{B}$	Left Cauchy-Green deformation tensor
$\mathbf{C}$	Right Cauchy-Green deformation tensor
E	Young's modulus
E_m	Matrix elastic modulus
E_f	Fiber elastic modulus
$\mathbf{E}$	Green-Lagrange finite strain tensor
$\mathbf{F}$	Deformation gradient tensor
f	fiber volume fraction
G	Shear modulus
k_1, k_2	Principal curvatures
I_1, I_2	First and second invariant of $\mathbf{B}$
$\mathbf{P}$	First Piola-Kirchhoff stress tensor
$\mathbf{S}$	Second Piola-Kirchhoff stress tensor
W	Strain energy density function
γ	Shear strain
ε	Strain
κ	Bulk modulus
λ	Stretch
σ	Cauchy stress

τ   Tangential force

Bibliography

[1]   Neto, A., de Oliveira, L., de Andrade Alves, G., Da Penha Andrade, G., and de Faria, E., 2014, "Two-stage hybrid open-endovascular repair of a Crawford type IV aortic aneurysm: Therapeutic challenge," J. Vasc. Bras., **13**(2), pp. 131–136.

[2]   Johnston, K. W., Rutherford, R. B., Tilson, M. D., Shah, D. M., Hollier, L., and Stanley, J. C., 1991, "Suggested standards for reporting on arterial aneurysms," J. Vasc. Surg., **13**, pp. 452–458.

[3]   Liddington, M. I., and Heather, B. P., 1992, "The relationship between aortic diameter and body habitus," Eur. J. Vasc. Surg., **6**, pp. 89–92.

[4]   Mozaffarian, D., Benjamin, E. J., Go, A. S., Arnett, D. K., Blaha, M. J., Cushman, M., De Ferranti, S., Després, J. P., Fullerton, H. J., Howard, V. J., Huffman, M. D., Judd, S. E., Kissela, B. M., Lackland, D. T., Lichtman, J. H., Lisabeth, L. D., Liu, S., Mackey, R. H., Matchar, D. B., McGuire, D. K., Mohler, E. R., Moy, C. S., Muntner, P., Mussolino, M. E., Nasir, K., Neumar, R. W., Nichol, G., Palaniappan, L., Pandey, D. K., Reeves, M. J., Rodriguez, C. J., Sorlie, P. D., Stein, J., Towfighi, A., Turan, T. N., Virani, S. S., Willey, J. Z., Woo, D., Yeh, R. W., and Turner, M. B., 2015, Heart disease and stroke statistics-2015 update : A report from the American Heart Association.

[5]   Nordon, I. M., Hinchliffe, R. J., Loftus, I. M., and Thompson, M.

M., 2011, "Pathophysiology and epidemiology of abdominal aortic aneurysms.," Nat. Rev. Cardiol., **8**(2), pp. 92–102.

[6]   2016, "Abdominal Aortic Aneurysm" [Online]. Available: http://www.patienteducationcenter.org/articles/abdominal-aortic-aneurysm/.

[7]   Sommer, G., Regitnig, P., Költringer, L., Holzapfel, G. a, Koltringer, L., and Holzapfel, G. a, 2010, "Biaxial mechanical properties of intact and layer-dissected human carotid arteries at physiological and supraphysiological loadings.," Am. J. Physiol. Heart Circ. Physiol., **298**(3), pp. H898–H912.

[8]   Wagenseil, J. E., and Mecham, R. P., 2009, "Vascular Extracellular Matrix and Arterial Mechanics," Physiol. Rev., **89**, pp. 957–989.

[9]   "Aortic aneurysm and dissection" [Online]. Available: https://www.northwell.edu/find-care/conditions-we-treat/aortic-aneurysm-and-dissection#/figure-1-12341.

[10]   Carrell, T. W. G., Burnand, K. G., Wells, G. M. a, Clements, J. M., and Smith, A., 2002, "Stromelysin-1 (matrix metalloproteinase-3) and tissue inhibitor of metalloproteinase-3 are overexpressed in the wall of abdominal aortic aneurysms," Circulation, **105**, pp. 477–482.

[11]   Eriksson, P., Jones, K. G., Brown, L. C., Greenhalgh, R. M., Hamsten, a., and Powell, J. T., 2004, "Genetic approach to the role of cysteine proteases in the expansion of abdominal aortic aneurysms," Br. J. Surg., **91**, pp. 86–89.

[12]   Matthew Longo, G., Xiong, W., Greiner, T. C., Zhao, Y., Fiotti, N., and Timothy Baxter, B., 2002, "Matrix metalloproteinases 2 and 9 work in concert to produce aortic aneurysms," J. Clin. Invest., **110**(5), pp. 625–632.

[13]   Thompson, R. W., Geraghty, P. J., and Lee, J. K., 2002, "Abdominal aortic aneurysms: Basic mechanisms and clinical implications," Curr. Probl. Surg., **39**(February), pp. 110–230.

[14]   Tamarina, N. a., McMillan, W. D., Shively, V. P., and Pearce, W. H., 1997, "Expression of matrix metalloproteinases and their inhibitors in aneurysms and normal aorta," Surgery, **122**, pp. 264–272.

[15] Raut, S. S., 2012, "Patient-Specific 3D Vascular Reconstruction and Computational Assessment of Biomechanics – an Application to Abdominal Aortic Aneurysm," Carnegie Mellon University.

[16] Sokolis, D. P., Kefaloyannis, E. M., Kouloukoussa, M., Marinos, E., Boudoulas, H., and Karayannacos, P. E., 2006, "A structural basis for the aortic stress-strain relation in uniaxial tension," J. Biomech., **39**(9), pp. 1651–1662.

[17] Wolinsky, H., and Glagov, S., 1967, "A Lamellar Unit of Aortic Medial Structure and Function in Mammals," Circ. Res., **20**(1), pp. 99–111.

[18] Avolio, A., Jones, D., and Tafazzoli-Shadpour, M., 1998, "Quantification of alterations in structure and function of elastin in the arterial media.," Hypertension, **32**(1), pp. 170–175.

[19] Fleming, C., Whitlock, E. P., Beil, T. L., and Lederle, F. A., 2014, "Screening for Abdominal Aortic Aneurysm: A Best-Evidence Systematic Review for the U.S. Preventive Services Task Force," Ann. Intern. Med., **142**(3), pp. 4–6.

[20] Reimerink, J. J., Van Der Laan, M. J., Koelemay, M. J., Balm, R., and Legemate, D. A., 2013, "Systematic review and meta-analysis of population-based mortality from ruptured abdominal aortic aneurysm," Br. J. Surg., **100**(11), pp. 1405–1413.

[21] 2016, "Stabilizing Minimally Invasive Procedures For AAA" [Online]. Available: http://www.endostaple.com/treatment-challenge/.

[22] 2016, "Endovascular repair of abdominal aortic aneurysms" [Online]. Available: http://www.mayoclinic.org/medical-professionals/clinical-updates/general-medical/endovascular-repair-abdominal-aortic-aneurysms.

[23] Investigators, T. U. K. E. T., 2010, "Endovascular versus Open Repair of Abdominal Aortic Aneurysm," N. Engl. J. Med., **362**(20), pp. 1863–1871.

[24] Hinterseher, I., Kuffner, H., Koch, R., Gabel, G., Saeger, H. D., and Smelser, D., 2012, "Comparison of survival rates for

abdominal aortic aneurysm treatment methods.," World J. Surg., **36**, pp. 917–922.

[25] Mohler, E. R., 2016, "Patient information: Abdominal aortic aneurysm (Beyond the Basics)," UpToDate [Online]. Available: http://www.uptodate.com/contents/abdominal-aortic-aneurysm-beyond-the-basics.

[26] Nicholls, S. C., Gardner, J. B., Meissner, M. H., and Johansen, K. H., 1998, "Rupture in small abdominal aortic aneurysms," J. Vasc. Surg., **28**, pp. 884–888.

[27] Choke, E., Cockerill, G., Wilson, W. R. W., Sayed, S., Dawson, J., Loftus, I., and Thompson, M. M., 2005, "A review of biological factors implicated in abdominal aortic aneurysm rupture," Eur. J. Vasc. Endovasc. Surg., **30**, pp. 227–244.

[28] Powell, J. T., and Brady, A. R., 2004, "Detection, Management, and Prospects for the Medical Treatment of Small Abdominal Aortic Aneurysms," Arterioscler. Thromb. Vasc. Biol., **24**(2), pp. 241–245.

[29] Scott, R., 2002, "The Multicentre Aneurysm Screening Study (MASS) into the effect of abdominal aortic aneurysm screening on mortality in men: a randomised controlled trial," Lancet, **360**(9345), pp. 1531–1539.

[30] Lederle, F. a, Johnson, G. R., Wilson, S. E., Ballard, D. J., Jordan, W. D., Blebea, J., Littooy, F. N., Freischlag, J. a, Bandyk, D., Rapp, J. H., and Salam, A. a, 2002, "Rupture rate of large abdominal aortic aneurysms in patients refusing or unfit for elective repair.," JAMA, **287**(22), pp. 2968–2972.

[31] Hirsch, A. T., Haskal, Z. J., Hertzer, N. R., Bakal, C. W., Creager, M. a, Halperin, J. L., Hiratzka, L. F., Murphy, W. R. C., Olin, J. W., Puschett, J. B., Rosenfield, K. a, Sacks, D., Stanley, J. C., Taylor, L. M., White, C. J., White, J., White, R. a, Antman, E. M., Smith, S. C., Adams, C. D., Anderson, J. L., Faxon, D. P., Fuster, V., Gibbons, R. J., Hunt, S. a, Jacobs, A. K., Nishimura, R., Ornato, J. P., Page, R. L., Riegel, B., American Association for Vascular Surgery, Society for Vascular Surgery, Society for Cardiovascular Angiography and Interventions, Society for Vascular Medicine and Biology, Society of Interventional Radiology, ACC/AHA Task Force on Practice Guidelines Writing Committee to Develop Guidelines

for the Management of Patients With Peripheral Arterial Disease, American Association of Cardiovascular and Pulmonary Rehabilitation, National Heart, Lung, and Blood Institute, Society for Vascular Nursing, TransAtlantic Inter-Society Consensus, and Vascular Disease Foundation, 2006, "ACC/AHA 2005 Practice Guidelines for the management of patients with peripheral arterial disease (lower extremity, renal, mesenteric, and abdominal aortic): a collaborative report from the American Association for Vascular Surgery/Society for Vascular Sur," Circulation, **113**, pp. e463–654.

[32]   McMillan, W. D., and Pearce, W. H., 1999, "Increased plasma levels of metalloproteinase-9 are associated with abdominal aortic aneurysms.," J. Vasc. Surg. Off. Publ. Soc. Vasc. Surg. [and] Int. Soc. Cardiovasc. Surgery, North Am. Chapter, **29**, pp. 122–127; discussion 127–129.

[33]   Cohen, J. R., Sarfati, I., Ratner, L., and Tilson, D., 1990, "Alpha 1-antitrypsin phenotypes in patients with abdominal aortic aneurysms," J Surg Res, **49**, pp. 319–321.

[34]   Rydén Ahlgren, a., Länne, T., Sonesson, B., and Eriksson, S., 1999, "Is there a relationship between abdominal aortic aneurysms and alpha1-antitrypsin deficiency (PiZ)?," Eur. J. Vasc. Endovasc. Surg., **17**, pp. 149–154.

[35]   Athanasiou, K., and Natoli, R., 2008, Introduction to Continuum Biomechanics, Morgan & Claypool Publishers.

[36]   Länne, T., Sonesson, B., Bergqvist, D., Bengtsson, H., and Gustafsson, D., 1992, "Diameter and compliance in the male human abdominal aorta: Influence of age and aortic aneurysm," Eur. J. Vasc. Surg., **6**(2), pp. 178–184.

[37]   MacSweeney, S., Young, G., Greenhalgh, R., and Powell, J., 1992, "Mechanical properties of the aneurysmal aorta," Br. J. Surg., **79**, pp. 1281–1284.

[38]   Sonesson, B., Hansen, F., and Lanne, T., 1997, "Abdominal aortic aneurysm: A general defect in the vasculature with focal manifestations in the abdominal aorta?," J. Vasc. Surg., **26**(2), pp. 247–254.

[39]   Sonesson, B., Sandgren, T., and Länne, T., 1999, "Abdominal aortic aneurysm wall mechanics and their relation to risk of

rupture," Eur. J. Vasc. Endovasc. Surg., **18**(6), pp. 487–493.

[40] Vorp, D., Mandarino, W., Webster, M., and Gorcsan III, J., 1996, "Potential influence of intraluminal thrombus on abdominal aortic aneurysm as assessed by a new non-invasive method," Cardiovasc. Surg., **4**(6), pp. 732–739.

[41] Wilson, K., 1999, "The relationship between abdominal aortic aneurysm wall compliance, maximum diameter and growth," Cardiovasc. Surg., **7**(2), pp. 208–213.

[42] Wilson, K. A., Lee, A. J., Hoskins, P. R., Fowkes, F. G. R., Ruckley, C. V., and Bradbury, A. W., 2003, "The relationship between aortic wall distensibility and rupture of infrarenal abdominal aortic aneurysm," J. Vasc. Surg., **37**(1), pp. 112–117.

[43] Long, A., 2005, "Compliance of abdominal aortic aneurysms evaluated by tissue Doppler imaging: correlation with aneurysm size," J. Vasc. Surg., **42**(1).

[44] Ganten, M. K., Krautter, U., Von Tengg-Kobligk, H., Böckler, D., Schumacher, H., Stiller, W., Delorme, S., Kauczor, H. U., Kauffmann, G. W., and Bock, M., 2008, "Quantification of aortic distensibility in abdominal aortic aneurysm using ECG-gated multi-detector computed tomography," Eur. Radiol., **18**(5), pp. 966–973.

[45] Trabelsi, O., Duprey, A., Favre, J. P., and Avril, S., 2016, "Predictive Models with Patient Specific Material Properties for the Biomechanical Behavior of Ascending Thoracic Aneurysms," Ann. Biomed. Eng., **44**(1), pp. 84–98.

[46] Vande Geest, J. P., Wang, D. H. J., Wisniewski, S. R., Makaroun, M. S., and Vorp, D. a., 2006, "Towards a noninvasive method for determination of patient-specific wall strength distribution in abdominal aortic aneurysms," Ann. Biomed. Eng., **34**(7), pp. 1098–1106.

[47] Sonesson, B., Hansen, F., Stale, H., and Lanne, T., 1993, "Compliance and diameter in the human abdominal aorta-the influence of age and sex," Eur. J. Vasc. Surg., **7**, pp. 690–697.

[48] Kontopodis, N., Georgakarakos, E., Metaxa, E., Pagonidis, K., Papaharilaou, Y., and Ioannou, C. V., 2013, "Estimation of wall properties and wall strength of aortic aneurysms using modern

imaging techniques. One more step towards a patient-specific assessment of aneurysm rupture risk," Med. Hypotheses, **81**(2), pp. 212–215.

[49] Di Martino, E. S., Bohra, A., Vande Geest, J. P., Gupta, N., Makaroun, M. S., and Vorp, D. a., 2006, "Biomechanical properties of ruptured versus electively repaired abdominal aortic aneurysm wall tissue," J. Vasc. Surg., **43**, pp. 570–576.

[50] Iliopoulos, D. C., Deveja, R. P., Kritharis, E. P., Perrea, D., Sionis, G. D., Toutouzas, K., Stefanadis, C., and Sokolis, D. P., 2009, "Regional and directional variations in the mechanical properties of ascending thoracic aortic aneurysms," Med. Eng. Phys., **31**, pp. 1–9.

[51] Mullins, L., 1969, "Softening of Rubber by Deformation," Rubber Chem. Technol., **42**(1), pp. 339–362.

[52] Raghavan, M. L., Kratzberg, J., Castro de Tolosa, E. M., Hanaoka, M. M., Walker, P., and da Silva, E. S., 2006, "Regional distribution of wall thickness and failure properties of human abdominal aortic aneurysm.," J. Biomech., **39**, pp. 3010–3016.

[53] He, C., and Roach, M., 1994, "The composition and mechanical properties of abdominal aortic aneurysms," J. Vasc. Surg., **20**(1), pp. 6–13.

[54] Raghavan, M. L., Webster, M. W., and Vorp, D. a, 1996, "Ex vivo biomechanical behavior of abdominal aortic aneurysm: assessment using a new mathematical model.," Ann. Biomed. Eng., **24**, pp. 573–582.

[55] Raghavan, M. L., and Vorp, D. A., 2000, "Toward a biomechanical tool to evaluate rupture potential of abdominal aortic aneurysm: Identification of a finite strain constitutive model and evaluation of its applicability," J. Biomech., **33**, pp. 475–482.

[56] Venkatasubramaniam, A. K., Fagan, M. J., Mehta, T., Mylankal, K. J., Ray, B., Kuhan, G., Chetter, I. C., and McCollum, P. T., 2004, "A comparative study of aortic wall stress using finite element analysis for ruptured and non-ruptured abdominal aortic aneurysms," Eur. J. Vasc. Endovasc. Surg., **28**, pp. 168–176.

[57]   Fillinger, M. F., Marra, S. P., Raghavan, M. L., and Kennedy, F. E., 2003, "Prediction of rupture risk in abdominal aortic aneurysm during observation: Wall stress versus diameter," J. Vasc. Surg., **37**, pp. 724–732.

[58]   Di Martino, E. S., and Vorp, D. a., 2003, "Effect of variation in intraluminal thrombus constitutive properties on abdominal aortic aneurysm wall stress," Ann. Biomed. Eng., **31**, pp. 804–809.

[59]   Fillinger, M. F., Raghavan, M. L., Marra, S. P., Cronenwett, J. L., and Kennedy, F. E., 2002, "In vivo analysis of mechanical wall stress and abdominal aortic aneurysm rupture risk," J. Vasc. Surg., **36**, pp. 589–597.

[60]   Gasser, T. C., Auer, M., Labruto, F., Swedenborg, J., and Roy, J., 2010, "Biomechanical rupture risk assessment of abdominal aortic aneurysms: Model complexity versus predictability of finite element simulations," Eur. J. Vasc. Endovasc. Surg., **40**(2), pp. 176–185.

[61]   Hyhlik-Dürr, A., Krieger, T., Geisbüsch, P., Kotelis, D., Able, T., and Böckler, D., 2011, "Reproducibility of deriving parameters of AAA rupture risk from patient-specific 3D finite element models.," J. Endovasc. Ther., **18**(3), pp. 289–298.

[62]   Marini, G., Maier, A., Reeps, C., Eckstein, H.-H., Wall, W. A., and Gee, M. W., 2012, "A continuum description of the damaga process in the arterial wall of abdominal aortic aneurysms," Int. j. numer. method. biomed. eng., **28**, pp. 87–99.

[63]   Ogden, R. W., 1972, "Large deformation isotropic elasticity: on the correlation of theory and experiment for compressible rubberlike solids," Proc. R. Soc. Lond. A. Math. Phys. Sci., **328**.

[64]   Reeps, C., Maier, a., Pelisek, J., Härtl, F., Grabher-Meier, V., Wall, W. a., Essler, M., Eckstein, H. H., and Gee, M. W., 2013, "Measuring and modeling patient-specific distributions of material properties in abdominal aortic aneurysm wall," Biomech. Model. Mechanobiol., **12**, pp. 717–733.

[65]   Raghavan, M. L., Hanaoka, M. M., Kratzberg, J. a., Higuchi, M. D. L., and da Silva, E. S., 2011, "Biomechanical failure properties and microstructural content of ruptured and unruptured abdominal aortic aneurysms," J. Biomech., **44**(13),

pp. 2501–2507.

[66]   Xiong, J., Wang, S. M., Zhou, W., and Wu, J. G., 2008, "Measurement and analysis of ultimate mechanical properties, stress-strain curve fit, and elastic modulus formula of human abdominal aortic aneurysm and nonaneurysmal abdominal aorta," J. Vasc. Surg., **48**(1), pp. 189–195.

[67]   Kamenskiy, A., 2015, "Biaxial Testing of Arterial Wall" [Online].   Available: https://www.youtube.com/watch?v=35kJSoOpJG0.

[68]   Vande Geest, J. P., Sacks, M. S., and Vorp, D. A., 2006, "The effects of aneurysm on the biaxial mechanical behavior of human abdominal aorta," J. Biomech., **39**, pp. 1324–1334.

[69]   Choi, H. S., and Vito, R. P., 1990, "Two-dimensional stress-strain relationship for canine pericardium," J. Biomech. Eng., **112**(2), pp. 153–159.

[70]   Tong, J., Cohnert, T., Regitnig, P., and Holzapfel, G. A., 2011, "Effects of age on the elastic properties of the intraluminal thrombus and the thrombus-covered wall in abdominal aortic aneurysms: Biaxial extension behaviour and material modelling," Eur. J. Vasc. Endovasc. Surg., **42**(2), pp. 207–219.

[71]   Holzapfel, G. a, Sommer, G., Gasser, C. T., and Regitnig, P., 2005, "Determination of layer-specific mechanical properties of human coronary arteries with nonatherosclerotic intimal thickening and related constitutive modeling," Am. J. Physiol. Heart Circ. Physiol., **289**(5), pp. 2048–2058.

[72]   Holzapfel, G. A., Gasser, T. C., and Ogden, R. W., 2000, "A new constitutive framework for arterial wall mechanics and a comparative study of material models," J. Elast., **61**(1-3), pp. 1–48.

[73]   O'Leary, S. A., Healey, D. A., Kavanagh, E. G., Walsh, M. T., McGloughlin, T. M., and Doyle, B. J., 2014, "The Biaxial Biomechanical Behavior of Abdominal Aortic Aneurysm Tissue," Ann. Biomed. Eng., **42**(12), pp. 2440–2450.

[74]   Carew, T. E., Vaishnav, R. N., and Patel, D. J., 1968, "Compressibility of the arterial wall.," Circ. Res., **23**, pp. 61–68.

[75]   Thubrikar, M., Labrosse, M., Robicsek, F., and Al-Soudi, J., 2001, "Mechanical properties of abdominal aortic aneurysm wall," J. Med. Eng. Technol., **25**, pp. 133–142.

[76]   Kobielarz, M., and Jankowski, L. J., 2013, "Experimental characterization of the mechanical properties of the abdominal aortic aneurysm wall under uniaxial tension.," J. Theor. Appl. Mech., **51**, pp. 949–958.

[77]   Hans, S. S., Jareunpoon, O., Balasubramaniam, M., and Zelenock, G. B., 2005, "Size and location of thrombus in intact and ruptured abdominal aortic aneurysms," J. Vasc. Surg., **41**, pp. 584–588.

[78]   Di Martino, E., Mantero, S., Inzoli, F., Melissano, G., Astore, D., Chiesa, R., and Fumero, R., 1998, "Biomechanics of abdominal aortic aneurysm in the! presence of endoluminal thrombus: Experimental characterisation and structural static computational analysis," Eur. J. Vasc. Endovasc. Surg., **15**(4), pp. 290–299.

[79]   Wang, D., Makaroun, M., Webster, M., and Vorp, D., 2001, "Mechanical properties and microstructure of intraluminal thrombus from abdominal aortic aneurysm," J. Biomech. Eng., **123**(6).

[80]   Vande Geest, J. P., Sacks, M. S., and Vorp, D. A., 2006, "A planar biaxial constitutive relation for the luminal layer of intraluminal thrombus in abdominal aortic aneurysms," J. Biomech., **39**(13), pp. 2347–2354.

[81]   O'Leary, S. A., Kavanagh, E. G., Grace, P. A., McGloughlin, T. M., and Doyle, B. J., 2014, "The biaxial mechanical behaviour of abdominal aortic aneurysm intraluminal thrombus: Classification of morphology and the determination of layer and region specific properties," J. Biomech., **47**(6), pp. 1430–1437.

[82]   Ashton, J. H., Geest, J. P. Vande, Simon, B. R., and Darren, G., 2009, "Compressive mechanical properties of the intraluminal thrombus in abdominal aortic aneurysms and fibrin-based thrombus mimics," J. Biomech., **42**(3), pp. 197–201.

[83]   Georgakarakos, E., Ioannou, C. V, Volanis, S., Papaharilaou, Y., Ekaterinaris, J., and Katsamouris, A. N., 2009, "The Influence of intraluminal thrombus on abdominal aortic aneurysm wall

stress," Int. Angiol., **28**(4), pp. 325–333.

[84] Li, Z. Y., U-King-Im, J., Tang, T. Y., Soh, E., See, T. C., and Gillard, J. H., 2008, "Impact of calcification and intraluminal thrombus on the computed wall stresses of abdominal aortic aneurysm," J. Vasc. Surg., **47**, pp. 928–935.

[85] Doyle, B. J., Callanan, A., Grace, P. A., and Kavanagh, E. G., 2013, "On the influence of patient-specific material properties in computational simulations: a case study of a large ruptured abdominal aortic aneurysm," Int. j. numer. method. biomed. eng., **29**, pp. 150–164.

[86] Vande Geest, J. P., Schmidt, D. E., Sacks, M. S., and Vorp, D. A., 2008, "The effects of anisotropy on the stress analyses of patient-specific abdominal aortic aneurysms," Ann. Biomed. Eng., **36**(6), pp. 921–932.

[87] Kazi, M., Thyberg, J., Religa, P., Roy, J., Eriksson, P., Hedin, U., and Swedenborg, J., 2003, "Influence of intraluminal thrombus on structural and cellular composition of abdominal aortic aneurysm wall," J. Vasc. Surg., **38**(6), pp. 1283–1292.

[88] Sakalihasan, N., and Michel, J. B., 2009, "Functional Imaging of Atherosclerosis to Advance Vascular Biology," Eur. J. Vasc. Endovasc. Surg., **37**(6), pp. 728–734.

[89] Maier, A., Gee, M. W., Reeps, C., Eckstein, H. H., and Wall, W. A., 2010, "Impact of calcifications on patient-specific wall stress analysis of abdominal aortic aneurysms," Biomech. Model. Mechanobiol., **9**(5), pp. 511–521.

[90] Speelman, L., Bohra, A., Bosboom, E. M. H., Schurink, G. W. H., van de Vosse, F. N., and Makaroun, M. S., 2007, "Effects of wall calcifications in patient-specific wall stress analyses of abdominal aortic aneurysms," J. Biomech. Eng., **129**, pp. 105–109.

[91] Xenos, M., Rambhia, S., Alemu, Y., Einav, S., Ricotta, J. J., Labropoulos, N., Tassiopoulos, A., and Bluestein, D., 2010, "Patient based Abdominal Aortic Aneurysm rupture risk prediction combining clinical visualizing modalities with fluid structure interaction numerical simulations," 2010 Annu. Int. Conf. IEEE Eng. Med. Biol. Soc. EMBC'10, pp. 5173–5176.

[92]   Zienkiewicz, O., Taylor, R., and Zhu, J., 2013, The Finite Element Method: Its Basis and Fundamentals, Elsevier Ltd.

[93]   Raghavan, M. L., Vorp, D. a, Federle, M. P., Makaroun, M. S., and Webster, M. W., 2000, "Wall stress distribution on three-dimensionally reconstructed models of human abdominal aortic aneurysm.," J. Vasc. Surg. Off. Publ. Soc. Vasc. Surg. [and] Int. Soc. Cardiovasc. Surgery, North Am. Chapter, **31**, pp. 760–769.

[94]   Truijers, M., Pol, J. a., SchultzeKool, L. J., van Sterkenburg, S. M., Fillinger, M. F., and Blankensteijn, J. D., 2007, "Wall Stress Analysis in Small Asymptomatic, Symptomatic and Ruptured Abdominal Aortic Aneurysms," Eur. J. Vasc. Endovasc. Surg., **33**, pp. 401–407.

[95]   Georgakarakos, E., Ioannou, C. V., Papaharilaou, Y., Kostas, T., Tsetis, D., and Katsamouris, a. N., 2010, "Peak Wall Stress Does Not Necessarily Predict the Location of Rupture in Abdominal Aortic Aneurysms," Eur. J. Vasc. Endovasc. Surg., **39**(3), pp. 302–304.

[96]   Doyle, B. J., McGloughlin, T. M., Miller, K., Powell, J. T., and Norman, P. E., 2014, "Regions of high wall stress can predict the future location of rupture of abdominal aortic aneurysm," Cardiovasc. Intervent. Radiol., **37**, pp. 815–818.

[97]   Vande Geest, J. P., Di Martino, E. S., Bohra, A., Makaroun, M. S., and Vorp, D. A., 2006, "A biomechanics-based rupture potential index for abdominal aortic aneurysm risk assessment: Demonstrative application," Ann. N. Y. Acad. Sci., **1085**, pp. 11–21.

[98]   Maier, A., Gee, M. W., Reeps, C., Pongratz, J., Eckstein, H. H., and WA, W., 2010, "A comparison of diameter, wall stress, and rupture potential index for abdominal aortic aneurysm rupture risk prediction.," Ann. Biomed. Eng., **38**(10), pp. 3124–3134.

[99]   Doyle, B. J., Callanan, A., Walsh, M. T., Grace, P. A., and Mcgloughlin, T. M., 2009, "A Finite Element Analysis Rupture Index (FEARI) as an Additional Tool for Abdominal Aortic Aneurysm Rupture Prediction," Vasc. Dis. Prev., **6**, pp. 114–121.

[100] Doyle, B. J., Coyle, P., Kavanagh, E. G., Grace, P. A., and Mcgloughlin, T. M., 2010, "A Finite Element Analysis Rupture Index (FEARI) Assessment of Electively Repaired and

Symptomatic / Ruptured Abdominal Aortic Aneurysms," IFMBE Proc., pp. 883–886.

[101] Kleinstreuer, C., and Li, Z., 2006, "Analysis and computer program for rupture-risk prediction of abdominal aortic aneurysms," Biomed. Eng. Online, **5**(1), p. 19.

[102] Vilalta, G., Nieto, F., Vaquero, C., Vilalta, J. A., and Pérez, M. Á., 2011, "Patient-Specific Clinical Assessment of Abdominal Aortic Aneurysm Rupture Risk based on its Geometric Parameters," Biomed. Eng. (NY)., **4**(APRIL 2011), pp. 459–466.

[103] Vilalta, G., Nieto, F., Vaquero, C., Vilalta, J. A., Lipsa, L. M., and Gutierrez, V., 2013, "V Latin American Congress on Biomedical Engineering CLAIB 2011 May 16-21, 2011, Habana, Cuba," IFMBE Proc., **33**, pp. 939–942.

[104] Meyer, C., Bertrand, E., Boiron, O., and Deplano, V., 2011, "Stereoscopically Observed Deformations of a Compliant Abdominal Aortic Aneurysm Model," J. Biomech. Eng., **133**.

[105] Doyle, B. J., Morris, L. G. L. G. ., Callanan, A., Kelly, P., Vorp, D. A., and McGloughlin, T. M., 2008, "3D reconstruction and manufacture of real abdominal aortic aneurysms: from CT scan to silicone model.," J. Biomech. Eng., **130**(June 2008), p. 034501.

[106] O'Brien, T., Morris, L., O'Donnell, M., Walsh, M., and McGloughlin, T., 2005, "Injection-moulded models of major and minor arteries: the variability of model wall thickness owing to casting technique.," Proc Inst Mech Eng H, **219**(5), pp. 381–386.

[107] Corbett, T. J., Doyle, B. J., Callanan, A., Walsh, M. T., and McGloughlin, T. M., 2011, "Engineering Silicone Rubbers for In vitro Studies: Models and ILT Analogues with Physiological Properties," J. Biomech. Eng., **132**(1), pp. 1–25.

[108] Tam, M. D. B. S., Laycock, S. D., Brown, J. R. I., and Jakeways, M., 2013, "3D printing of an aortic aneurysm to facilitate decision making and device selection for endovascular aneurysm repair in complex neck anatomy.," J. Endovasc. Ther., **20**, pp. 863–7.

[109] Winder, R. J., Sun, Z., Kelly, B., Ellis, P. K., and Hirst, D., 2002, "Abdominal aortic aneurysm and stent graft phantom manufactured by medical rapid prototyping.," J. Med. Eng.

Technol., **26**(2), pp. 75–78.

[110] Wilasrusmee, C., Suvikrom, J., Suthakorn, J., Lertsithichai, P., Sitthiseriprapip, K., Proprom, N., and Kittur, D. S., 2008, "Three-dimensional aortic aneurysm model and endovascular repair: An educational tool for surgical trainees," Int. J. Angiol., **17**(3), pp. 129–133.

[111] J., C. A., Danial, S., X., L. R., J., D. B., E., K. E., and M., M. T., 2014, "3D-Printed Tissue-Mimicking Phantoms for Medical Imaging and Computational Validation Applications," 3D Print. Addit. Manuf., **1**(1), pp. 14–23.

[112] Fedorovich, N. E., Kuipers, E., Gawlitta, D., Dhert, W. J. a., and Alblas, J., 2011, "Scaffold Porosity and Oxygenation of Printed Hydrogel Constructs Affect Functionality of Embedded Osteogenic Progenitors," Tissue Eng. Part A, **17**(19-20), pp. 2473–2486.

[113] Schuurman, W., Khristov, V., Pot, M. W., van Weeren, P. R., Dhert, W. J. a, and Malda, J., 2011, "Bioprinting of hybrid tissue constructs with tailorable mechanical properties.," Biofabrication, **3**(2), p. 021001.

[114] Doyle, B. J., Cloonan, A. J., Walsh, M. T., Vorp, D. a., and McGloughlin, T. M., 2010, "Identification of rupture locations in patient-specific abdominal aortic aneurysms using experimental and computational techniques," J. Biomech., **43**(7), pp. 1408–1416.

[115] Cloonan, A. J., Shahmirzadi, D., Li, R. X., Doyle, B. J., Konofagou, E. E., and McGloughlin, T. M., 2014, "3D-Printed Tissue-Mimicking Phantoms for Medical Imaging and Computational Validation Applications," 3D Print. Addit. Manuf., **1**(1), pp. 14–23.

[116] Stamatopoulos, C., Mathioulakis, D. S., Papaharilaou, Y., and Katsamouris, A., 2011, "Experimental unsteady flow study in a patient-specific abdominal aortic aneurysm model," Exp. Fluids, **50**(6), pp. 1695–1709.

[117] Kuske, A., and Robertson, G., 1974, Photoelastic Stress Analysis, John Wiley London.

[118] Inc, V. P. G., 2005, "Introduction to Stress Analysis by the

PhotoStress ® Method by by TN-702-2 the PhotoStress."

[119] Morris, L., O'Donnell, P., Delassus, P., and McGloughlin, T., 2004, "Experimental assessment of stress patterns in abdominal aortic aneurysms using the photoelastic method," Strain, **40**(4), pp. 165–172.

[120] Callanan, A., Morris, L. G. L. G. ., and McGloughlin, T. M., 2012, "Finite element and photoelastic modelling of an abdominal aortic aneurysm: A comparative study," Comput. Methods Biomech. Biomed. Engin., **15**(10), pp. 1111–1119.

[121] Doyle, B. J., Killion, J., and Callanan, A., 2012, "Use of the photoelastic method and finite element analysis in the assessment of wall strain in abdominal aortic aneurysm models," J. Biomech., **45**(10), pp. 1759–1768.

[122] McGloughlin, T. M., and Doyle, B. J., 2010, "New approaches to abdominal aortic aneurysm rupture risk assessment: Engineering insights with clinical gain," Arterioscler. Thromb. Vasc. Biol., **30**(9), pp. 1687–1694.

[123] Sutton, M., Ke, X., Lessner, S., Goldbach, M., Yost, M., Zhao, F., and Schreier, H., 2008, "Strain field measurements on mouse carotid arteries using microscopic three-dimensional digital image correlation," J. Biomed. Mater. Res. A, **84**, pp. 178–190.

[124] Kim, J.-H., Badel, P., Duprey, A., Favre, J. P., and Avril, S., 2011, "Characterisation of failure in human aortic tissue using digital image correlation," Comput. Methods Biomech. Biomed. Engin., **14**(January 2015), pp. 73–74.

[125] Romo, A., Badel, P., Duprey, A., Favre, J. P., and Avril, S., 2014, "In vitro analysis of localized aneurysm rupture," J. Biomech., **47**(3), pp. 607–616.

[126] Frauenfelder, T., Lotfey, M., Boehm, T., and Wildermuth, S., 2006, "Computational fluid dynamics: Hemodynamic changes in abdominal aortic aneurysm after stent-graft implantation," Cardiovasc. Intervent. Radiol., **29**(4), pp. 613–623.

[127] Deplano, V., Meyer, C., Guivier-Curien, C., and Bertrand, E., 2012, "New insights into the understanding of flow dynamics in an in vitro model for abdominal aortic aneurysms," Med. Eng. Phys., **35**(6), pp. 800–809.

[128] Chen, C.-Y., Antón, R., Hung, M., Menon, P., Finol, E. a, and Pekkan, K., 2014, "Effects of intraluminal thrombus on patient-specific abdominal aortic aneurysm hemodynamics via stereoscopic particle image velocity and computational fluid dynamics modeling.," J. Biomech. Eng., **136**(3), p. 031001.

[129] Kung, E. O., Les, A. S., Medina, F., Wicker, R. B., McConnell, M. V, and Taylor, C. a, 2011, "In vitro validation of finite-element model of AAA hemodynamics incorporating realistic outlet boundary conditions.," J. Biomech. Eng., **133**(4), p. 041003.

[130] Gallo, D., G??lan, U., Di Stefano, A., Ponzini, R., L??thi, B., Holzner, M., and Morbiducci, U., 2014, "Analysis of thoracic aorta hemodynamics using 3D particle tracking velocimetry and computational fluid dynamics," J. Biomech., **47**(12), pp. 3149–3155.

[131] Tam, M. D., Latham, T., Brown, J. R. I., and Jakeways, M., 2014, "Use of a 3D printed hollow aortic model to assist EVAR planning in a case with complex neck anatomy: Potential of 3D printing to improve patient outcome," J. Endovasc. Ther., **21**(5), pp. 760–764.

[132] Itagaki, M. W., 2015, "Using 3D printed models for planning and guidance during endovascular intervention: a technical advance," Diagnostic Interv. Radiol., **21**(4), pp. 338–341.

[133] Vorp, D. a., Raghavan, M. L., and Webster, M. W., 1998, "Mechanical wall stress in abdominal aortic aneurysm: Influence of diameter and asymmetry," J. Vasc. Surg., **27**, pp. 632–639.

[134] Rodríguez, J. F., Ruiz, C., Doblaré, M., and Holzapfel, G. A., 2008, "Mechanical stresses in abdominal aortic aneurysms: influence of diameter, asymmetry, and material anisotropy.," J. Biomech. Eng., **130**(2), p. 021023.

[135] Mower, W. R., Baraff, L. J., and Sneyd, J., 1993, "Stress distributions in vascular aneurysms: factors affecting risk of aneurysm rupture.," J. Surg. Res., **55**, pp. 155–61.

[136] Raut, S. S., Jana, A., De Oliveira, V., Muluk, S. C., and Finol, E. A., 2013, "The importance of patient-specific regionally varying wall thickness in abdominal aortic aneurysm biomechanics.," J.

Biomech. Eng., **135**(8), p. 81010.

[137] Fillinger, M. F., Racusin, J., Baker, R. K., Cronenwett, J. L., Teutelink, A., Schermerhorn, M. L., Zwolak, R. M., Powell, R. J., Walsh, D. B., and Rzucidlo, E. M., 2004, "Anatomic characteristics of ruptured abdominal aortic aneurysm on conventional CT scans: Implications for rupture risk," J. Vasc. Surg., **39**, pp. 1243–1252.

[138] Georgakarakos, E., Ioannou, C. V., Kamarianakis, Y., Papaharilaou, Y., Kostas, T., Manousaki, E., and Katsamouris, A. N., 2010, "The Role of Geometric Parameters in the Prediction of Abdominal Aortic Aneurysm Wall Stress," Eur. J. Vasc. Endovasc. Surg., **39**(1), pp. 42–48.

[139] Giannoglou, G., Giannakoulas, G., Soulis, J., Chatzizisis, Y., Perdikides, T., Melas, N., Parcharidis, G., and Louridas, G., 2006, "Predicting the Risk of Rupture of Abdominal Aortic Aneurysms by Utilizing Various Geometrical Parameters: Revisiting the Diameter Criterion," Angiology, **57**(4), pp. 487 – 494.

[140] Nyilas, R. D., Ng, S. M. L., Leung, J., and Xu, X. Y., 2005, "Towards a new geometric approach to assess the risk of rupture of abdominal aortic aneurysms using patient specific modelling," Proceedings of the 2005 Summer Bioengineering Conference, Vail, CO.

[141] Pasta, S., Phillippi, J. A., Tsamis, A., D'Amore, A., Raffa, G. M., Pilato, M., Scardulla, C., Watkins, S. C., Wagner, W. R., Gleason, T. G., and Vorp, D. A., 2015, "Constitutive modeling of ascending thoracic aortic aneurysms using microstructural parameters," Med. Eng. Phys., **000**, pp. 1–10.

[142] Rodríguez, J., Martufi, G., Doblaré, M., and Finol, E. A., 2009, "The effect of material model formulation in the stress analysis of abdominal aortic aneurysms," Ann. Biomed. …, **37**(11), pp. 1–7.

[143] Rodríguez, J. F., Ruiz, C., Doblaré, M., and Holzapfel, G. a, 2008, "Mechanical stresses in abdominal aortic aneurysms: influence of diameter, asymmetry, and material anisotropy.," J. Biomech. Eng., **130**(April 2008), p. 021023.

[144] Lu, J., Zhou, X., and Raghavan, M. L., 2007, "Inverse

elastostatic stress analysis in pre-deformed biological structures: Demonstration using abdominal aortic aneurysms," J. Biomech., **40**, pp. 693–696.

[145] Raghavan, M. L., Ma, B., and Fillinger, M. F., 2006, "Non-invasive determination of zero-pressure geometry of arterial aneurysms," Ann. Biomed. Eng., **34**(9), pp. 1414–1419.

[146] Riveros, F., Chandra, S., Finol, E. a., Gasser, T. C., and Rodriguez, J. F., 2013, "A pull-back algorithm to determine the unloaded vascular geometry in anisotropic hyperelastic AAA passive mechanics," Ann. Biomed. Eng., **41**(4), pp. 694–708.

[147] de Putter, S., Wolters, B. J. B. M., Rutten, M. C. M., Breeuwer, M., Gerritsen, F. a., and van de Vosse, F. N., 2007, "Patient-specific initial wall stress in abdominal aortic aneurysms with a backward incremental method," J. Biomech., **40**, pp. 1081–1090.

[148] Speelman, L., Bosboom, E. M. H., Schurink, G. W. H., Buth, J., Breeuwer, M., Jacobs, M. J., and van de Vosse, F. N., 2009, "Initial stress and nonlinear material behavior in patient-specific AAA wall stress analysis," J. Biomech., **42**, pp. 1713–1719.

[149] Gee, M. W., Reeps, C., Eckstein, H. H., and Wall, W. a., 2009, "Prestressing in finite deformation abdominal aortic aneurysm simulation," J. Biomech., **42**, pp. 1732–1739.

[150] Alastrué, V., Peña, E., Martínez, M. Á., and Doblaré, M., 2007, "Assessing the use of the 'opening angle method' to enforce residual stresses in patient-specific arteries," Ann. Biomed. Eng., **35**(10), pp. 1821–1837.

[151] Polzer, S., Bursa, J., Gasser, T. C., Staffa, R., and Vlachovsky, R., 2013, "A numerical implementation to predict residual strains from the homogeneous stress hypothesis with application to abdominal aortic aneurysms," Ann. Biomed. Eng., **41**(7), pp. 1516–1527.

[152] Rachev, a., and Greenwald, S. E., 2003, "Residual strains in conduit arteries," J. Biomech., **36**, pp. 661–670.

[153] Vorp, D. A., Lee, P. C., Wang, D. H. J., Makaroun, M. S., Nemoto, E. M., Ogawa, S., and Webster, M. W., 2001, "Association of intraluminal thrombus in abdominal aortic

aneurysm with local hypoxia and wall weakening," J. Vasc. Surg., **34**(2), pp. 291–299.

[154] Mower, W. R., Quinones, W. J., and Gambhir, S. S., 1997, "Effect of intraluminal thrombus on abdominal aortic aneurysm wall stress," J. Vasc. Surg., **26**, pp. 602–608.

[155] Wang, D., Makaroun, M., Webster, M., and Vorp, D. A., 2002, "Effect of intraluminal thrombus on Wall Stress in Patient Specific Models of Abdominal Aortic Aneurysm," J. Vasc. Surg., **36**, pp. 598–604.

[156] Schurink, G. W. H., van Baalen, J. M., Visser, M. J. T., and van Bockel, J. H., 2000, "Thrombus within an aortic aneurysm does not reduce pressure on the aneurysmal wall," J. Vasc. Surg., **31**(3), pp. 501–506.

[157] Hinnen, J. W., Koning, O. H. J., Visser, M. J. T., and Van Bockel, H. J., 2005, "Effect of intraluminal thrombus on pressure transmission in the abdominal aortic aneurysm," J. Vasc. Surg., **42**(Fig 1), pp. 1176–1182.

[158] Polzer, S., Gasser, T. C., Swedenborg, J., and Bursa, J., 2011, "The impact of intraluminal thrombus failure on the mechanical stress in the wall of abdominal aortic aneurysms," Eur. J. Vasc. Endovasc. Surg., **41**(4), pp. 467–473.

[159] Speelman, L., Bohra, A., Bosboom, E. M., Schurink, G. W., \mboxvan de Vosse, F. N., Makaroun, M. S., and Vorp, D. A., 2007, "Effects of wall calcifications in patient- specific wall stress analyses of abdominal aortic aneurysms," J. Biomech. Eng., **129**(February 2007), pp. 105–109.

[160] Scotti, C. M., and Finol, E. A., 2007, "Compliant biomechanics of abdominal aortic aneurysms: A fluid-structure interaction study," Comput. Struct., **85**(11-14), pp. 1097–1113.

[161] Scotti, C. M. C. M. ., Jimenez, J. J. . J., Muluk, S. C. S. C. ., and Finol, E. A. . E. a, 2008, "Wall stress and flow dynamics in abdominal aortic aneurysms: finite element analysis vs. fluid-structure interaction.," Comput. Methods Biomech. Biomed. Engin., **11**(3), pp. 301–322.

[162] Scotti, C. M., Shkolnik, A. D., Muluk, S. C., and Finol, E. a, 2005, "Fluid-structure interaction in abdominal aortic aneurysms:

effects of asymmetry and wall thickness.," Biomed. Eng. Online, **4**, p. 64.

[163] Papaharilaou, Y., Ekaterinaris, J. A., Manousaki, E., and Katsamouris, A. N., 2007, "A decoupled fluid structure approach for estimating wall stress in abdominal aortic aneurysms," J. Biomech., **40**(2), pp. 367–377.

[164] Wolters, B. J. B. M., Rutten, M. C. M., Schurink, G. W. H., Kose, U., De Hart, J., and Van De Vosse, F. N., 2005, "A patient-specific computational model of fluid-structure interaction in abdominal aortic aneurysms," Med. Eng. Phys., **27**(10), pp. 871–883.

[165] Kroon, D. J., 2011, "Patch Curvature" [Online]. Available: http://www.mathworks.com/matlabcentral/fileexchange/32573-patch-curvature.

[166] Harter, L., Gross, B., and Callen, P., 1982, "Ultrasonic evaluation of abdominal aortic thrombus," J. Ultrasound Med., **1**(8), pp. 315–318.

[167] Buijs, R. V. C., Willems, T. P., Tio, R. A., Boersma, H. H., Tielliu, I. F. J., Slart, R. H. J. A., and Zeebregts, C. J., 2013, "Calcification as a risk factor for rupture of abdominal aortic aneurysm," Eur. J. Vasc. Endovasc. Surg., **46**(5), pp. 542–548.

[168] Dave, 2010, "The Radiology Portal" [Online]. Available: https://radiologyportal.wordpress.com/ct-resources-portal/.

[169] Radvany, M., 2015, "Abdominal Aortic Aneurysm Imaging," Medscape [Online]. Available: http://emedicine.medscape.com/article/416266-overview.

[170] Shum, J., Di Martino, E. S., Goldhammer, A., Goldman, D. H., Acker, L. C., Patel, G., Ng, J. H., Martufi, G., and Finol, E. A., 2010, "Semiautomatic vessel wall detection and quantification of wall thickness in computed tomography images of human abdominal aortic aneurysms," Med. Phys., **37**, pp. 638–648.

[171] Shum, J., Xu, A., Chatnuntawech, I., and Finol, E. A., 2011, "A framework for the automatic generation of surface topologies for abdominal aortic aneurysm models," Ann. Biomed. Eng., **39**(1), pp. 249–259.

[172] Raut, S. S., Liu, P., and Finol, E. a., 2015, "An approach for patient-specific multi-domain vascular mesh generation featuring spatially varying wall thickness modeling," J. Biomech., **48**(10), pp. 1972–1981.

[173] Antiga, L., 2006, "VMTK - Vascular modeling toolkit" [Online]. Available: http://www.vmtk.org.

[174] Antiga, L., Ene-Iordache, B., and Remuzzi, A., 2003, "Computational geometry for patient-specific reconstruction and meshing of blood vessels from MR and CT angiography," IEEE Trans. Med. Imaging, **22**(5), pp. 674–684.

[175] Raut, S. S., Chandra, S., Shum, J., and Finol, E. A., 2013, "The role of geometric and biomechanical factors in abdominal aortic aneurysm rupture risk assessment," Ann. Biomed. Eng., **41**(7), pp. 1459–1477.

[176] Sakalihasan, N., Limet, R., and Defawe, O., 2005, "Abdominal aortic aneurysm.," Lancet, **365**, p. 1577; author reply 1577–1589.

[177] Barocas, V. H., 2007, "Multiscale, Structure-Based Modeling for the Elastic Mechanical Behavior of Arterial Walls," J. Biomech. Eng., **129**(August), pp. 611–618.

[178] Doyle, B. J., Callanan, A., Walsh, M. T., Grace, P. A., and McGloughlin, T. M., 2009, "A Finite Element Analysis Rupture Index (FEARI) as an Additional Tool for Abdominal Aortic Aneurysm Rupture Prediction," Vasc. Dis. Prev., **6**, pp. 114–121.

[179] McGloughlin, T. M., and Doyle, B. J., 2010, "New approaches to abdominal aortic aneurysm rupture risk assessment: Engineering insights with clinical gain," Arterioscler. Thromb. Vasc. Biol., **30**, pp. 1687–1694.

[180] Vande Geest, J. P., Di Martino, E. S., Bohra, A., Makaroun, M. S., and Vorp, D. a., 2006, "A biomechanics-based rupture potential index for abdominal aortic aneurysm risk assessment: Demonstrative application," Ann. N. Y. Acad. Sci., **1085**, pp. 11–21.

[181] Antón, R., Chen, C., Hung, M., Finol, E., and Pekkan, K., 2015, "Experimental and computational investigation of the patient-specific abdominal aortic aneurysm pressure field," Comput.

Methods Biomech. Biomed. Engin., **18**(9), pp. 981–992.

[182] Vorp, D. a., 2007, "Biomechanics of abdominal aortic aneurysms," J. Biomech., **40**(9), pp. 1887–1902.

[183] Raut, S. S., Jana, A., De Oliveira, V., Muluk, S. C., and Finol, E. A., 2013, "The Importance of Patient-Specific Regionally Varying Wall Thickness in Abdominal Aortic Aneurysm Biomechanics," J. Biomech. Eng., **135**(8).

[184] Raut, S. S., Jana, A., De Oliveira, V., Muluk, S. C., and Finol, E. A., 2013, "The Importance of Patient-Specific Regionally Warying Wall Thickness in Abdominal Aortic Aneurysm Biomechanics," J. Biomech. Eng., **135**(8).

[185] Doyle, B. J., Callanan, A., Burke, P. E., Grace, P. A., Walsh, M. T., Vorp, D. A., and McGloughlin, T. M., 2009, "Vessel asymmetry as an additional diagnostic tool in the assessment of abdominal aortic aneurysms," J. Vasc. Surg., **49**(2), pp. 443–454.

[186] Doyle, B. J., Morris, L. G., Callanan, A., Kelly, P., Vorp, D. A., and McGloughlin, T. M., 2008, "3D reconstruction and manufacture of real abdominal aortic aneurysms: from CT scan to silicone model.," J. Biomech. Eng., **130**(June 2008), p. 034501.

[187] Ene, F., Gachon, C., Delassus, P., Carroll, R., Stefanov, F., O'Flynn, P., and Morris, L., 2011, "In vitro evaluation of the effects of intraluminal thrombus on abdominal aortic aneurysm wall dynamics," Med. Eng. Phys., **33**(8), pp. 957–966.

[188] Corbett, T. J., Molony, D. S., Callanan, A., and McGloughlin, T. M., 2011, "The effect of vessel material properties and pulsatile wall motion on the fixation of a proximal stent of an endovascular graft," Med. Eng. Phys., **33**(1), pp. 106–111.

[189] Corbett, T. J., Doyle, B. J., Callanan, A., Walsh, M. T., and McGloughlin, T. M., 2009, "Engineering Silicone Rubbers for In Vitro Studies: Creating AAA Models and ILT Analogues With Physiological Properties," J. Biomech. Eng., **132**(1).

[190] Rissland, P., Alemu, Y., Einav, S., Ricotta, J. J., and Bluestein, D., 2009, "Abdominal Aortic Aneurysm Risk of Rupture: Patient-Specific FSI Simulations Using Anisotropic Model," J. Biomech. Eng., **131**.

[191] Xenos, M., Rambhia, S. H., Alemu, Y., Einav, S., Labropoulos, N., Tassiopoulos, A., Ricotta, J. J., and Bluestein, D., 2010, "Patient-based abdominal aortic aneurysm rupture risk prediction with fluid structure interaction modeling," Ann. Biomed. Eng., **38**(11), pp. 3323–3337.

[192] Zeinali-Davarani, S., Choi, J., and Baek, S., 2009, "On parameter estimation for biaxial mechanical behavior of arteries," J. Biomech., **42**, pp. 524–530.

[193] Eckold, G. C., 1994, Design and Manufacture of Composite Structures, Woodhead Publishing.

[194] Garcia, D., Orteu, J. J., and Penazzi, L., 2002, "A combined temporal tracking and stereo-correlation technique for accurate measurement of 3D displacements: Application to sheet metal forming," J. Mater. Process. Technol., **125-126**, pp. 736–742.

[195] Bouguet, J., 2013, "Camera Calibration Toolbox for Matlab" [Online]. Available: http://www.vision.caltech.edu/bouguetj/calib_doc/index.html#ref.

[196] Sacks, M. S., 2000, "Biaxial mechanical evaluation of planar biological materials," J. Elast., **61**, pp. 199–246.

[197] Choi, H. S., and Vito, R. P., 1990, "Two-dimensional stress-strain relationship for canine pericardium," J. Biomech. Eng., **112**(2).

[198] Harter, L., Gross, B., and Callen, P., 1982, "Ultrasonic evaluation of abdominal aortic thrombus," J. Ultrasound Med., **1**(8), pp. 315–318.

[199] Martufi, G., Satriano, A., Moore, R. D., Vorp, D. A., and Martino, E. S. Di, 2015, "Local Quantification of Wall Thickness and Intraluminal Thrombus Offer Insight into the Mechanical Properties of the Aneurysmal Aorta," Ann. Biomed. Eng.

[200] Soudah, E., Vilalta, G., Bordone, M., Vilalta, J. A., Nieto, F., Pérez, M. A., and Vaquero, C., 2012, "Idealized abdominal aortic aneurysm (AAA) geometry as predictor of hemodynamics stresses," ECCOMAS 2012 - Eur. Congr. Comput. Methods Appl. Sci. Eng. E-b. Full Pap., (Eccomas), pp. 4385–4395.

[201] Gasser, T. C., Görgülü, G., Folkesson, M., and Swedenborg, J., 2008, "Failure properties of intraluminal thrombus in abdominal aortic aneurysm under static and pulsating mechanical loads," J. Vasc. Surg., **48**(1), pp. 179–188.

[202] Mooney, M., 1940, "A theory of large elastic deformation," J. Appl. Phys., **11**(9), pp. 582–592.

[203] Leung, J. H., Wright, A. R., Cheshire, N., Crane, J., Thom, S. a, Hughes, A. D., and Xu, Y., 2006, "Fluid structure interaction of patient specific abdominal aortic aneurysms: a comparison with solid stress models.," Biomed. Eng. Online, **5**, p. 33.

[204] Raut, S. S., Jana, A., De Oliveira, V., Muluk, S. C., and Finol, E. a., 2014, "The Effect of Uncertainty in Vascular Wall Material Properties on Abdominal Aortic Aneurysm Wall Mechanics," Comput. Biomech. Med. Fundam. Sci. Patient-specific Appl.

[205] Riveros, F., Martufi, G., Gasser, T. C., and Rodriguez, J. F., 2014, "Influence of Ilt Mechanical Behavior in Abdominal Aortic Aneurysms Passive Mechanics," 11th World Congr. Comput. Mech. (WCCM XI) Barcelona, Spain, (Wccm Xi), pp. 3–4.

[206] Chandra, S., Gnanaruban, V., Riveros, F., Rodriguez, J. F., and Finol, E. A., 2016, "A Methodology for the Derivation of Unloaded Abdominal Aortic Aneurysm Geometry With Experimental Validation," J. Biomech. Eng., **138**(10), p. 101005.